Technical Evaluation Report
Diablo Canyon Nuclear Power Plant
Tsunami Hazard Reevaluation Review

Technical Evaluation Report
Diablo Canyon Nuclear Power Plant
Tsunami Hazard Reevaluation Review

Prepared for the

U.S. Nuclear Regulatory Commission

By

TAYLOR ENGINEERING, INC.

November 2017

TECHNICAL EVALUATION REPORT

DIABLO CANYON NUCLEAR POWER PLANT

TSUNAMI HAZARD REEVALUATION REVIEW

EXECUTIVE SUMMARY

Taylor Engineering performed an independent review and confirmatory analysis of the tsunami hazard at the Diablo Canyon Power Plant (DCPP) site, beginning in January 2015. Analysis results were compared to those in the Pacific Gas and Electric Company (PG&E), the licensee, Flood Hazard Reevaluation Report (FHRR) submitted to the Nuclear Regulatory Commission on March 11, 2015. Taylor Engineering's independent analysis includes geophysical characterization of potential distant and local earthquake and landslide tsunami sources as well as detailed numerical simulation of potential tsunamis from these sources. Source characterizations included all available geophysical data, including post-2011 estimations of maximum earthquake slip. The numerical simulations utilized state-of-the-art models executed on large computer clusters. Key DCPP structures and their elevations for the purposes of the tsunami flood hazard analysis are provided in Table 1.

Table 1: Summary of Key DCPP Site Feature Elevations

DCPP Site Feature	Elevation
Reactor Powerblock Area (nominal plant grade)	87.9 ft (NAVD88)
Service Water Intake Structure (SWIS) Snorkel Openings	48.5 to 52.3 ft (NAVD88)
SWIS Pump System Deck	20.4 ft (NAVD88)
SWIS pump minimum operating water level	-20.0 ft (NAVD88)

The potential tsunami sources can be categorized as: 1) local earthquakes, 2) distant earthquakes, 3) local landslides, and 4) distant landslides. Expected tsunami elevations from local earthquakes, such as those originating along the Hosgri Fault, are estimated by computer modeling to be minimal. Local earthquake-induced submarine landslides may produce larger (higher) tsunami flow elevations, and these landslide sources are addressed here. Table 2 summarizes the Taylor Engineering tsunami flood hazard estimates for distant earthquakes, and local and distant landslides.

Table 2: Summary of the Independent Taylor Engineering Tsunami Hazard Assessment.

Tsunami Source Type	Tsunami Source Location	Tsunami Source Parameters	Expected Recurrence Period	Maximum Runup / Minimum Drawdown
Earthquake Generated (distant and local)	Aleutian Arc source produces largest tsunami	Earthquake Magnitude = M_w9.6 Initial tsunami condition generated using standard Okada model	>10,000 years; according to published literature, the largest earthquake that could occur along this subduction zone	Near SWIS : +34.7 ft / -18.0 ft (MSL) +37.6 ft / -15.1 ft (NAVD88)
Distant Landslide	Flank collapse of Kilauea Volcano, Hawaii produces largest tsunami	Subaerial Landslide with a volume of ~1000 km^3 Slide failure and generated tsunami modeled with 3D multi-material mechanics model	>100,000 years; Last known similar event ~120,000 years ago; this analysis assumes an unlikely coherent slide	Near SWIS: +23.0 ft / -10.8 ft (MSL) +25.9 ft / -7.9 ft (NAVD88)
Local Landslide	Goleta-type landslide, occurring near the reactor site produces largest tsunami	Submerged Landslide with a volume of 1.5 km^3 for entire complex; note that this volume corresponds to the sum of three different landslides, or lobes, in the same complex, which have different dates. Slide failure and generated tsunami modeled with 3D multi-material mechanics model	>100,000 years; Ages for the different Goleta lobes range from 6,000-160,000 years. Location in the region offshore of the DCPP site treated parametrically; scenario slide corresponds to the combined Goleta volume placed in an offshore location that yields the 90-percentile tsunami elevation	Near SWIS: +44.8 ft / -7.2 ft (MSL) +47.7 ft / -4.3 ft (NAVD88)

As shown in Table 2, the minimum tsunami drawdown near the DCPP SWIS is due to an earthquake along the eastern half of the Aleutian Arc, while the maximum wave runup at the South Cove SWIS is associated with a large and local submarine landslide, located immediately west of the DCPP site. Computer modeling indicates that a distant landslide tsunami source, due to a hypothetical flank collapse of the Kilauea Volcano in Hawaii, for example, does not control tsunami runup levels at the DCPP site, despite producing the largest nearfield (i.e., in Hawaii) waves among all potential tsunami sources. Despite recent

occurrences in Indonesia and Japan, great tsunamis are rare events and there is large uncertainty in the estimation of their likelihood of occurrence. This is specifically true for submarine-driven landslide tsunamis.

The recurrence periods of the local submarine landslide sources studied here are judged to be 100,000 years or greater, based on our current state-of-knowledge. The maximum water surface elevations resulting from this analysis of submarine landslide sources (e.g., 44.8 ft MSL) are judged to be reasonably conservative in that they are consistent with deterministic present-day guidance and methods associated with Near Term Task Force Recommendation 2.1-flooding, and estimates of annual exceedance frequency discussed in the External Flooding Assessment Guidelines (NEI, 2016; NRC, 2016). This event produced a runup elevation that is therefore judged to have a frequency of exceedance of less than 1E-5/year based on available geologic evidence. Consequently, the authors judge that this independent analysis provides an appropriately-conservative deterministic scenario result, and it also provides a reasonable frequency-based estimate associated with application of the External Flooding Assessment Guidelines.

Upon completion of the independent tsunami hazard analysis, a comparison was performed between the potential tsunami hazard determined by PG&E, as documented in the DCPP FHRR. A summary of this comparison is provided in Table 3. All Taylor Engineering- and licensee-estimated elevations provided in the table include rare tidal levels and sea level rise.

Table 3: Comparison of the Independent (Taylor Engineering) and FHRR (the licensee).

	Taylor Engineering Tsunami Analysis Hazard Results	**Licensee Tsunami Analysis Hazard Results**
Maximum Tsunami Elevation near SWIS Location	44.8’ MSL (47.7 ft (NAVD88)); due to a local Goleta-like submarine landslide	29.9’ MSL (32.8’ (NAVD88)); due to a local Goleta-like submarine landslide
Minimum Tsunami Elevation near SWIS Location	-18.0’ MSL (-15.1’ (NAVD88)); due to a distant earthquake along the Aleutian Arc	-18.6’ MSL (-15.7’ (NAVD88)); due to a local Goleta-like submarine
Maximum Speed and Duration of Tsunami Currents	44.3 ft/sec (for thirty seconds); due to a local Goleta-like submarine landslide	82 ft/sec (for a few seconds); due to a local Goleta-like submarine landslide

The highest computed water elevations near the DCPP SWIS, for both the Taylor and FHRR sets of analyses, are associated with a hypothetical and local Goleta-like submarine landslide. Differences in the resulting elevations are due to different assumptions regarding

the slide geometry and application of different numerical models for the slide motion. As an indication of the significance of expert interpretation in tsunami generation due to geologically-rare landslides, it is the opinion of Taylor Engineering that both our independent and the FHRR analyses are technically sound, using information and methods found in peer-reviewed scientific literature. Additionally, both analyses are likely conservative, in that both use the cumulative volume of the multi-slide Goleta complex; this is a landslide larger than any known to have occurred along the local margin.

Finally, it should be noted that the results presented in this report are based on numerous simplifying assumptions and rely on limited site-specific data. The analyses are also replete with uncertainties regarding conceptual models for tsunami scenarios and consequences along the California coastline. Thus, the results and conclusions presented herein should be carefully interpreted.

Table of Contents

TECHNICAL EVALUATION REPORT - TSUNAMI

The licensee reported in its Flood Hazard Reevaluation Report (FHRR) that the reevaluated hazard, including associated effects, for site flooding due to tsunamis does not indicate any potential flooding of safety-related structures (PG&E, 2016).

Consistent with the guidance provided to all licensees when preparing their flood hazard reevaluations (NRC, 2012), Taylor Engineering, used present-day methodologies and regulatory guidance in performing the independent evaluation of the tsunami hazard at the Diablo Canyon Nuclear Power Plant (DCPP) site. For reference, key elevations for structures at the DCPP site are listed below:

- Powerblock (nominal grade) elevation: 26.8 m (NAVD88)
- Service Water Intake Structure (SWIS) pump minimum water level: -6.1 m (NAVD88)
- SWIS Snorkel Openings elevation: 14.8 to 15.9 m (NAVD88)
- SWIS Pump System Deck elevation: 6.2 m (NAVD88)

All elevations and distances provided in this technical report are provided in metric units. For reference, 1 meter = 3.28 ft.

1.0 Historical Tsunami Data

1.1 Historical Record

Information Submitted by the Licensee

The FHRR (PG&E, 2016) provides a complete review of historically-reported and instrumentally-recorded tsunamis from local and distant earthquakes as well as from local submarine landslides. The tsunami sources used and historical information provided by the licensee are similar to that presented in this independent (Taylor Engineering) evaluation.

Taylor Engineering Technical Evaluation

The Natural Hazard Interactive Map uses the data from the National Geophysical Data Center (NGDC) Tsunami Database (NGDC, 2015). An interactive map search was performed for tide-gauge measurements and eyewitness accounts for southern California (32.5°N to 35°N). For measurements, the inquiry returned 25 entries as shown in Table 1.1-1. This table provides the tide station location at which the tsunami was measured, the distance from the tide station to the tsunami source (D_s), and the measured tsunami wave height (H_s). The sedimentological record of some of these sources in discussed in Wilson et al. (2014).

In addition to tide station measurements, there are a large number of eyewitness accounts of tsunamis in California. While these eyewitness records are often less reliable, they are used to corroborate other accounts and indicate potential unknown source locations. A total of 58 eyewitness accounts exist in the database (NGDC, 2015) and are provided in Table 1.1-2. A number of the events in the tables that occurred before 1945 can be defined as local events due to either local submarine landslides or earthquakes. None of the events after 1945 were local events; they were generated by large earthquakes around the subduction zones of the Pacific Ocean. Both the largest instrumentally recorded tsunami as well as the largest eyewitness estimate are from Santa Barbara, CA.

Table 1.1-1: Tide Gauge Measurements along Southern California (NGDC, 2015).

Date	Location	Latitude	Longitude	D_s [km]	H_s [m]
12/17/1896	Santa Barbara, CA	34.48	-119.69	unknown	2.5
4/1/1946	Port Hueneme, CA	34.15	-119.18	4021	0.8
4/1/1946	Point Arguello, CA	34.58	-120.65	3893	1.1
11/4/1952	Port Hueneme, CA	34.15	-119.18	6471	0.66
3/9/1957	Los Angeles-Moorage 174, CA	33.75	-118.7	4943	0.5
3/9/1957	Port Hueneme, CA	34.15	-119.18	4850	0.53
5/22/1960	Long Beach, CA	33.75	-118.22	9239	0.88
5/22/1960	Santa Monica, CA	34.00	-118.50	9277	1.4
5/22/1960	Alamitos Bay, CA	33.75	-118.12	9234	0.61
5/22/1960	Port Hueneme, CA	34.14	-119.19	9325	1.34
5/22/1960	Santa Barbara, CA	34.48	-119.69	9382	1.37
5/22/1960	San Diego, CA	32.72	-117.17	9089	0.7
5/22/1960	Wilson Cove, CA	33	-118.55	9187	0.64
5/22/1960	Los Angeles, CA	33.72	-118.27	9239	0.76
5/22/1960	La Jolla, CA	32.87	-117.26	9107	0.52
5/22/1960	Terminal Island (Los Angeles), CA	33.75	-118.25	9240	0.95
3/28/1964	Rincon Island, CA	34.35	-119.43	3583	0.91
3/28/1964	Santa Monica, CA	34.00	-118.5	3654	1.03
3/28/1964	San Diego, CA	32.72	-117.17	3837	0.53
2/27/2010	Santa Monica, CA	34.00	-118.5	9123	0.64
2/27/2010	Santa Barbara, CA	34.48	-119.69	9230	0.91
2/27/2010	La Jolla, CA	32.87	-117.26	8953	0.6
3/11/2011	Santa Monica, CA	34.00	-118.50	8443	0.85
3/11/2011	Santa Barbara, CA	34.48	-119.69	8324	1.02
3/11/2011	San Diego, CA	32.71	-117.17	8629	0.63

Table 1.1-2: Eyewitness Accounts of Tsunamis along Southern California (NGDC, 2015).

Date	Location	Latitude	Longitude	D_s [km]	H_s [m]
12/21/1812	El Refugio (Gaviota), CA	34.47	-120.20	41	3.4
12/21/1812	Ventura, CA	34.27	-119.28	58	2
12/21/1812	Santa Barbara, CA	34.42	-119.68	32	2
5/27/1862	San Diego, CA	32.72	-117.17	3	1.2
8/13/1868	Wilmington, CA	33.78	-118.25	7681	0.76
8/13/1868	San Pedro, CA	33.71	-118.27	7677	0.76
4/16/1877	Anaheim Landing, CA	33.74	-118.10	223	1.8
5/10/1877	Wilmington, CA	33.78	-118.25	7960	1.68
5/10/1877	San Pedro, CA	33.71	-118.27	7956	2.07
5/10/1877	Gaviota, CA	34.47	-120.20	8144	1.83
5/10/1877	Anaheim, CA	33.84	-117.90	7941	1.52
11/22/1878	Wilmington, CA	33.78	-118.25	276	1
12/11/1913	Santa Barbara, CA	34.42	-119.68	unknown	4.5
11/4/1927	Surf, CA	34.67	-120.58	24	1.8
8/31/1930	Venice, CA	33.99	-118.47	16	3.05
8/31/1930	Santa Monica, CA	34.01	-118.50	13	3.05
4/1/1946	Avalon, Catalina Is., CA	33.35	-118.33	4140	1.8
4/1/1946	Catalina Harbor, Catalina Is., CA	33.43	-118.51	4122	1.5
4/1/1946	Santa Barbara, CA	34.42	-119.68	3968	0.91
5/22/1960	Santa Barbara, CA	34.42	-119.68	9376	1.2
5/22/1960	Los Angeles, CA	33.72	-118.27	9238	0.9
5/22/1960	Avalon, Catalina Is., CA	33.35	-118.33	9207	0.61
5/22/1960	Port Hueneme, CA	34.14	-119.19	9325	1.8
5/22/1960	San Diego, CA	32.72	-117.17	9089	1.2
3/28/1964	Santa Barbara, CA	34.42	-119.68	3566	0.8
3/28/1964	Santa Catalina Is., CA	33.38	-118.42	3720	1.54
3/28/1964	San Diego, CA	32.72	-117.17	3837	0.99
11/29/1975	Isthmus Harbor, Catalina Is., CA	33.44	-118.50	3931	1.4
11/29/1975	Avalon Harbor, Catalina Is., CA	33.35	-118.33	3944	1.4
2/27/2010	Mission Bay, San Diego, CA	32.76	-117.25	8943	0.6
2/27/2010	Ventura, CA	34.27	-119.28	9189	0.9
2/27/2010	Oxnard, CA	34.15	-119.18	9173	1
2/27/2010	Port Hueneme, CA	34.15	-119.18	9173	0.7
2/27/2010	Sunset, CA	33.72	-118.07	9074	0.5
2/27/2010	Newport Beach Harbor, CA	33.59	-117.92	9054	0.5
2/27/2010	Dana Point Harbor, CA	33.47	-117.70	9031	0.7
2/27/2010	Oceanside Harbor, CA	33.18	-117.37	8988	0.6
3/11/2011	Oceanside Harbor, CA	33.18	-117.37	8582	0.5

Table 1.1-2: Eyewitness Accounts of Tsunamis along Southern California (Continued)

Date	Location	Latitude	Longitude	D_s [km]	H_s [m]
3/11/2011	Marina Del Rey, CA	33.98	-118.45	8449	1
3/11/2011	Ocean Beach, CA	32.74	-117.26	8620	1
3/11/2011	Pt Loma Sub Base/Ballast Pt, CA	32.67	-117.24	8627	0.5
3/11/2011	Shelter I. Dock, San Diego, CA	32.71	-117.23	8625	0.8
3/11/2011	Encinitas/Batiquitos, San Elijo, CA	33.04	-117.29	8598	1
3/11/2011	Coronado Island Lifeguard HQ, CA	32.69	-117.18	8630	0.6
3/11/2011	Long Beach Marina, CA	33.75	-118.22	8481	0.7
3/11/2011	Ventura Harbor, CA	34.27	-119.28	8368	1.3
3/11/2011	Channel Islands Harbor, CA	34.15	-119.22	8381	1.2
3/11/2011	La Jolla, CA	32.87	-117.26	8612	0.9
3/11/2011	Port Hueneme, CA	34.15	-119.18	8384	1.4
3/11/2011	Mission Bay, San Diego, CA	32.76	-117.25	8620	0.9
3/11/2011	Dana Point Harbor, CA	33.47	-117.70	8539	0.6
3/11/2011	Huntington Harbor, CA	33.72	-118.06	8495	0.72
3/11/2011	King Harbor , Redondo Beach, CA	33.83	-118.39	8463	0.7
3/11/2011	Ballona Creek, CA	34.03	-118.35	8453	0.6
3/11/2011	Silver Strand State Beach, CA	32.63	-117.14	8637	0.6
3/11/2011	Imperial Beach, CA	32.58	-117.10	8643	0.5
3/11/2011	Oxnard, CA	34.15	-119.18	8384	1.2
3/11/2011	Carlsbad, CA	33.15	-117.33	8587	0.6

1.2 Paleo-Tsunami Record

Information Submitted by the Licensee

The FHRR does not directly discuss the paleo-tsunami record, although details are provided about submarine landslide sources with inferred ages greater than 10,000 years (PG&E, 2016).

Taylor Engineering Technical Evaluation

A search in the tsunami deposit database returned six entries, but only two contain information about actual tsunami deposits (Kuhn, 2005; Muhs and Szabo, 1982, https://www.ngdc.noaa.gov/hazard/tsudep.shtml). The other four entries reference publications about the potential of tsunami generation by submarine slides or brief presentation abstracts for which more in-depth information is unavailable. Kuhn (2005) described liquefaction features in the area of Carlsbad, CA. Liquefaction features are often formed in unconsolidated and wet sediments during earthquakes. However, some of the sandy deposits found in the area have sedimentary features that were recognized in tsunami deposits in other areas. Features that were used to ascribe a tsunamigenic formation include (Kuhn, 2005; Pratt, 2002):

- The presence of chaotic, turbid, sedimentary debris, commonly mixed with wood fragments, shells, clay balls and pods of sharp, angular pieces of terrace deposits and bedrock, and locally capped by peat.
- The initial event deposits grade from coarse to landward-fining.
- The pebbles are imbricated.
- The landward movement of sediment is "lobe form," similar to those in the Philippines Islands produced by the 1994 Mindoro earthquake (Daag et al., 1995).
- The "v-shaped" chaotic features were inferentially caused by an abrupt "hydraulic jump" when tsunami waves reach a "bedrock high" or very resistant surface feature, a phenomenon often associated with fluid-like features exposed in the overlying sediments (Morner, 1996).
- The abrupt landward termination of sand wedges has an angle similar to, but steeper than dunes (Daag et al., 1995).

These features have indeed been described in tsunami deposits. However, they also can be found in deposits generated by coastal storms or other coastal flooding events. There is a large variety of sedimentary features that can be formed during a tsunami and it is difficult to determine without background information if the described deposits can indeed be identified as tsunami deposits. Kuhn (2005) speculates that the source of the tsunami that created these deposits is seismic or related to a submarine landslide. Both tsunami sources are possible in California.

The second potential tsunami deposit is described by Muhs and Szabo (1982) at the Eel Point terrace on Clemente Island, CA. While the authors do not mention tsunami deposits directly, this entry is in the tsunami deposits database because the authors describe fossil layers whose generation is possible by tsunamis. The Eel Point terrace was formed about 127,000 years ago and contains mollusks and rounded andesite pebbles and cobbles with little matrix. The fact that pebbles and cobbles are present point to larger waves or tsunamis. However, no unequivocal evidence exists that would clearly confirm a tsunamigenic origin for these deposits.

1.3 Conclusions

There have been eight tsunami events with measurements and 15 with eyewitnesses' accounts along the Californian coast between 32.5°N and 35°N. These include the very large tsunami of 1946, 1952, 1960, 1964, and 2011, all of which caused substantial damage and loss of life at impacted coastlines along the Pacific Ocean. Of the six entries in the tsunami deposits database, careful evaluation indicated that only two—from Carlsbad and Clemente Island—contain information relevant to this evaluation. However, no conclusive evidence confirmed that tsunamis formed the deposits in those two areas.

2.0 Potential Tsunami Source Characteristics

2.1 Potential Tsunamigenic Sources

Information Submitted by the Licensee
The FHRR discusses three possible mechanisms for tsunamis: local submerged (submarine) landslides, distant (far field) earthquakes, and local earthquakes (PG&E, 2016). The examined far field sources include the Aleutian Alaska Subduction Zone, the Semidi Subduction Zone, the Kamchatka Subduction Zone and the Japan Subduction Zone. Rupture of the Hosgri Fault and Santa Lucia Bank Fault are considered significant seismic local sources. The FHRR considers two different submarine landslide sources, one in relatively shallow water and another in deep water (PG&E, 2016).

Taylor Engineering Technical Evaluation
Potential tsunami sources likely to determine the Probable Maximum Tsunami (PMT) at the Diablo Canyon Power Plant (DCPP) site include subaerial and submarine landslides, volcanos, near-field intra-plate earthquakes, and inter-plate earthquakes. The causative tsunami generator for the PMT at the DCPP site is a submarine landslide.

2.1.1 Source Generator Characteristics

In this subsection, tsunami sources used for the analysis are described in terms of their identification, characteristic, and tsunami-generation parameters. Discussed first are potential tsunamigenic sources, followed by parameters associated with the maximum credible earthquakes and submarine landslides around the site.

2.1.2 Subaerial Landslides

Information Submitted by the Licensee
The FHRR does not discuss the possibility of tsunamis generated by subaerial landslides (PG&E, 2016).

Taylor Engineering Technical Evaluation
With regard to subaerial landslides, there are no coastal cliffs of high relief in the immediate area of the site that are known to be a location of large subaerial landslides. Thus, there are no areas of subaerial coastal landslides near the reactor site that would produce tsunami-like waves exceeding the amplitude of those generated by other sources. The analysis does include investigation of large volcanic flank collapse in subsection 2.1.3.

2.1.3 Volcanogenic Sources

Information Submitted by the Licensee
The FHRR does not discuss volcanoes as a tsunami generating source (PG&E, 2016).

Taylor Engineering Technical Evaluation
Volcano-flank collapse has been studied recently as a source of significant tsunami with large far-field amplitudes. The first study was the collapse of the Cumbre Vieja in the

Canary Islands, Spain (Ward and Day, 2001; Løvholt at al., 2008). More recently, Paris et al. (2011) and Ramalho et al. (2015) found evidence that a tsunami which displaced large blocks in the Cape Verde archipelago was generated by a flank collapse. Estimated local tsunami amplitudes for this source exceed that of the 1952 Lituya Bay (Alaska) rock-slide generated tsunami. The Lituya Bay tsunami had an amplitude of 152 m (scaled up from Fritz et al., 2001, and simulated by Weiss et al., 2009) and a runup of 524 m above sea level (e.g., Tocher and Miller, 1959; Miller, 1960; Slingerland and Voight, 1979).

In the Atlantic Ocean, volcano flank collapses occur exclusively on volcanic islands that were created by mantle plumes. In the Pacific Ocean, volcano flank collapses can occur on islands whose generation mechanisms are similar to those in the Atlantic Ocean, such as the Hawaiian Islands. However, volcano flank collapse can also occur around the Ring of Fire where volcanoes are located directly at the coast. Fig. 2.1.3-1 shows the locations where volcano flank collapse is known or projected that have relevance for the site.

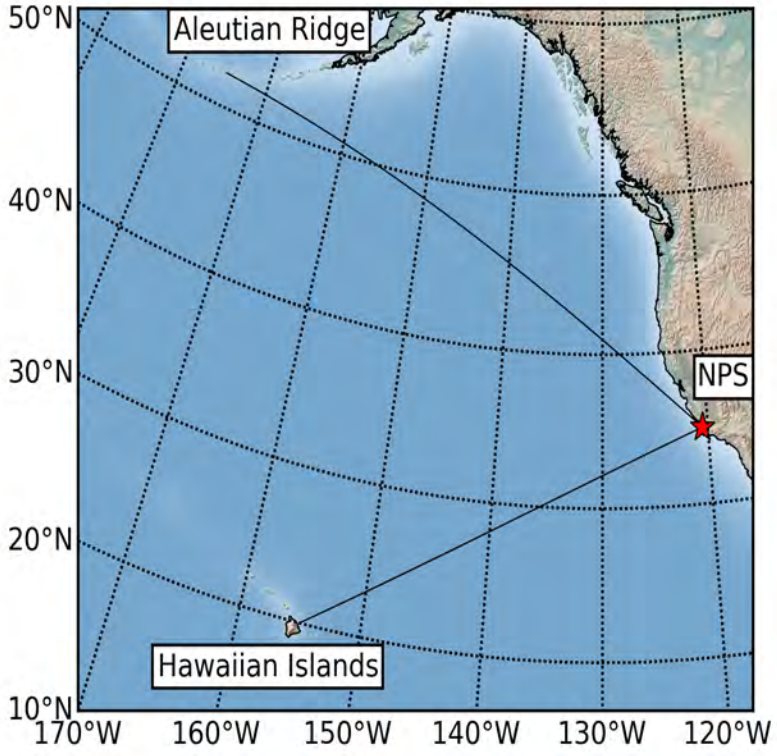

Figure 2.1.3-1: Location of the Hawaiian Island with Kilauea Volcano, the Aleutian Ridge, and the DCPP site (red star labeled NPS (Nuclear Power Station)). Background topography data from GEBCO (Becker et al., 2009).

Generally, flank collapses are common processes with volcanic island growth (i.e., Wolfe et al., 1994; Duffield et al., 1982; Lenat et al., 1989; Holcomb and Searle, 1991; Krastel et al., 2001, Moore et al., 1994; Watts and Masson, 1995). Flank collapses can be the direct result of volcanic process or indirectly triggered by earthquakes that are generated by volcanic processes. Observations and descriptions of significant flank collapses are rare

and often based solely on surficial observations (Moore et al., 1994; Watts and Masson, 1995), which makes the evaluation of their tsunamigenic potential difficult. However, modern geophysical data, such as multichannel seismic reflection data in combination with high-resolution bathymetric surveys of the submarine volcanic slopes enable the study of the internal structure of the seafloor, which gives important insights into the kinematics of the collapse motion. The kinematics of a collapse is the crucial element that is missing to link a flank collapse to the leading tsunami wave amplitude traveling away from source.

The Kilauea volcano is the most active volcano on earth, evidenced by an extensive historic record of its activity. The best studied portion of the Kilauea Volcano in terms of collapses is the area seaward of the Hilina fault system (Fig. 2.1.3-2). This system and its collapse have been studied since the 1930s (e.g., Stearns and Clark, 1930; Moore and Krivoy, 1964; Swanson et al., 1976; Lipman et al., 1985; Smith et al., 1999). Earlier estimates of the slump area (approx. 5,200 km^2) by Moore et al. (1989) were corrected by Smith et al. (1999) to approx. 2,100 km^2 with an estimated volume between 10,000 and 12,000 km^3.

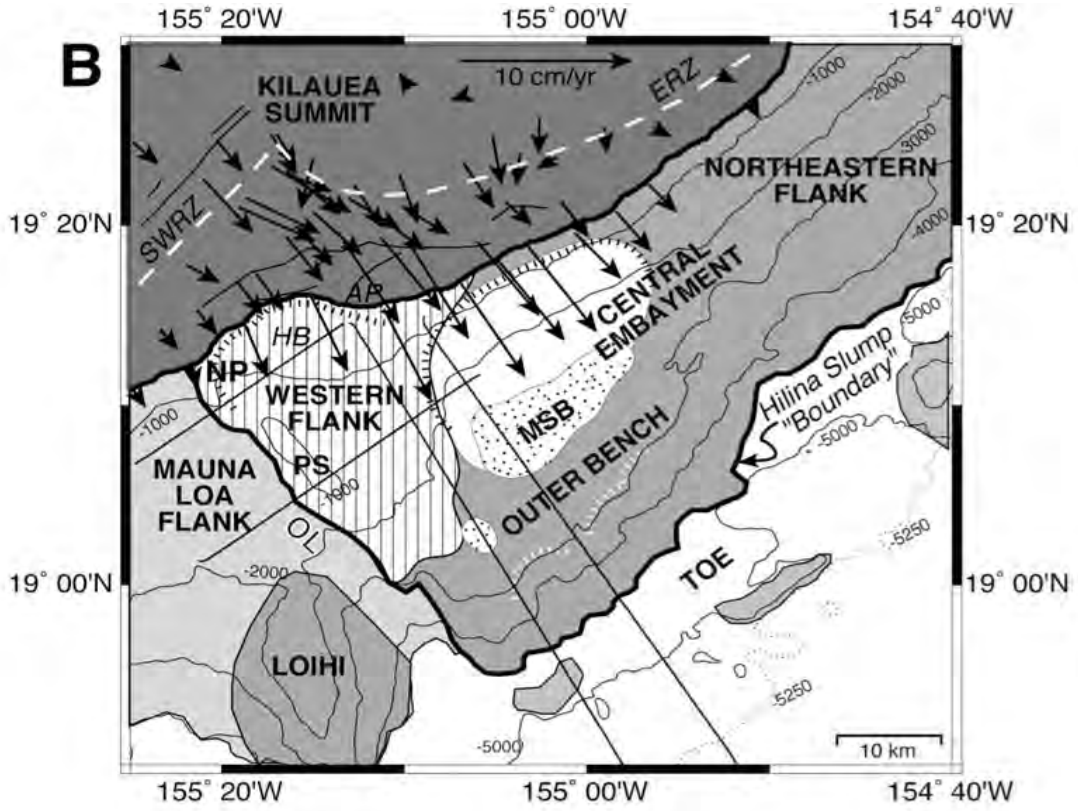

Figure 2.1.3-2: Map of the south flank of the Kilauea volcano. The Hilina slump is outlined in bold. The vectors represent GPS ground displacement vectors resolved for the time interval between 1990 and 1996 from Owen et al. (2000). Modified after Morgan et al. (2003).

The flank collapse described in these references occurred between 25,000 and 50,000 years ago. The recurrence interval as well as future collapse scenarios are difficult to predict and carry significant uncertainty. A further complicating factor is that the Kilauea volcano essentially has been growing on the flanks of Mauna Loa, which has its own collapse history. This coupling makes it theoretically possible that larger collapse masses can occur, for which no reliable geophysical method exists at this time to estimate the volume of material associated with those collapses. However, due to the fact that the Kilauea volcano is so active, the likelihood for a collapse that includes material from the underlying Mauna Loa volcano is significantly low. Therefore, we base our conservative scenario on the geophysical reality that can be constrained with geotechnical approaches (i.e., Okubo, 2004).

The Aleutian Ridge is the western part of the Aleutian Arc, which is a volcanic island-arc complex. The Aleutian Arc features 41 active volcanoes of which 17 are in the Aleutian Ridge and have erupted at least once in the past 250 years (Simkin and Siebert, 1994; Miller et al., 1998; Schaeffer and Nye, 2002) (see Fig. 2.1.3-3). The volcanic activity along the entire arc started about 46 million years ago and has experienced intermittent activity spikes (Jicha et al., 2006). The geophysical characteristic of the region is governed by the subduction of the Pacific Plate that has 90° subduction angle and an approximately 7.5 cm/year subduction rate in the eastern portion of the arc complex. In the western portion (Aleutian Ridge), the relative plate motion between the Pacific Plate and North American Plate is almost parallel and the subduction rate decreases to about 2.5 cm/year (Grow and Atwater, 1970; DeLong et al., 1978; Engebretson et al., 1985).

Figure 2.1.3-3: Volcanoes of the Aleutian Arc with Aleutian Ridge on the west and Alaska Peninsula in the east (modified after Montanaro and Beget, 2011).

Montanaro and Beget (2011) documented 17 volcano collapses along the Aleutian Ridge (Table 2.1.3-1) and estimated respective collapse volumes. Seven of the volcano collapses occurred in the Pleistocene between 11,700 years and about 2.6 million years ago, six in the last 11,700 years, and four at unknown times.

The volcano on Great Sitkin Island is an andesitic stratocone that is composed of a series of lava flows and lava domes forming an arcuate-shaped structure that is open to the northwest. This arcuate feature cuts into a series of lava flows in the northeast part of the island. The arcuate feature is a subdued headscarp that was formed during an edifice collapse (Waythomas et al., 2003a; Montanaro and Beget, 2011). The seafloor north of the island features large hummocks (some > 1km). These deposits have been interpreted as runout masses of a single flank collapse event (Waythomas et al., 2003a, Coombs et al., 2007). However, Montanaro and Beget (2011) reinterpreted this structure as two distinct collapse events. The younger deposit covers about 650 km^2 and the older one about 1000 km^2 with an estimated volume of 47 km^3 of which all is of subaerial origin. Montanaro and Beget (2011) propose that the older deposit belongs to a collapse event of the Sandy Bay shield volcano that is below the more recent one.

Table 2.1.3-1: Characteristics of the Volcano Collapses of the Aleutian Ridge (Montanaro and Beget, 2011).

Collapse	Location	Timing (Age)	Estimated Volume (km^3)
Kiska I	Kiska Island	Pleistocene	11.7
Kiska II	Kiska Island	Pleistocene	36.5
Kiska III	Kiska Island	Holocene	0.43
Segula I	Segula Island	Holocene	---
Segula II	Segula Island	Holocene	---
Little Sitkin I	Little Sitkin Island	Pleistocene	---
Little Sitkin II	Little Sitkin Island	Unknown	---
Gareloi I	Gareloi Island	Unknown	8.3
Gareloi II	Gareloi Island	Holocene	---
Gareloi III	Gareloi Island	Holocene	11
Sakaja I	Tanaga Island	Holocene	2.9
Bobrof	Bobrof Island	Unknown	8.8
Kanaga	Kanaga Island	Pleistocene	25
Adagdak	Adak Island	Pleistocene	---
Great Sitkin I	Great Sitkin Island	Pleistocene	47
Great Sitkin II	Great Sitkin Island	Pleistocene	---
Seguam	Seguam Island	Unknown	---

The Kanaga Island volcano is an andesitic stratovolcano that is bound at its south margin by the Kanaton Ridge. The Kanaton Ridge formed during a northward-directed flank collapse. This flank collapse destroyed Mount Kanaton, an ancestral volcano to the recent Kanaga volcano (Waythomas et al., 2002; Waythomas et al., 2003a-b). The mapped runout deposits cover an area of 370 km^2 that elongated in SSE-NNW direction (Montanaro and Beget, 2011) with a collapse volume estimated to be 25 km^3.

The Kiska volcano is a Holocene stratocone whose last eruption was in 1990 (Miller et al., 1998). The subaerial portion of the volcano features multiple fault lines and collapse scarps, representing evidence of multiple flank collapse events. The morphologic feature of the runout masses confirms the occurrence of at least three distinct collapses. Runout masses of the oldest collapse cover an area of about 165 km^2 with a collapse volume of approximately 11.7 km^3 (approximately 35% of aerial origin). The second oldest collapse was the largest with the runout masses covering 300 km^2. This deposit contains blocks of 250 x 200 x 50 m to 750 x 450 x 90 m. The volume of this collapse was estimated to be 36.5 km^3 of which approximately 28% is of aerial origin. The youngest collapse is small with its runout mass covering only 4 km^2. The estimated collapse volume is 0.43 km^3, all of which is of aerial origin.

All collapses point toward the Bering Sea. However, it should be noted that the south sides of the islands are also active and undergo significant changes due the active nature of the margin. It is possible that more collapses occurred in the past, but their traces could have been removed by subduction-related processes. Therefore, there is no physical reason to not place flank collapses on the Pacific side of the Aleutian Ridge. Furthermore, the internal structure of the runout masses is not available for any of these volcanoes. Collapse volumes may consist of material of submarine or subaerial origins, or a combination of both. For example, the largest estimated collapse volume for Great Sitkin is all of subaerial origin. When accelerated subaerial collapse masses hit the water surface, a significant amount of the kinetic energy of the moving slide mass is converted to open a water cavity whose collapse generates nonlinear waves that break very close to the generation area. Therefore, we argue that a sizable submarine volcano flank collapse with little subaerial contribution is a much more efficient tsunami generator in the Aleutian Ridge than the collapse with the largest volume.

2.1.4 Intra-Plate Earthquakes

Information Submitted by the Licensee

The FHRR provides details and modeling for two local, intra-plate sources, including discussion about earthquakes on the local Hosgri Fault, where the Lompoc 1927 earthquake is believed to have occurred (PG&E, 2016).

Taylor Engineering Technical Evaluation

The state of California, with the exception of the northern coastline, is not in the immediate vicinity of a major subduction zone. However, smaller faults exist that are capable of producing local tsunamis. This evaluation considered near-field tsunami sources based on information available in several California tsunami hazard studies.

Ten different faults from southern California were considered in the analysis: Anacapa-Dume, Carlsbad, Catalina Island, Coronado Bank, Lausen Knoll, San Clemente, San Mateo, Santa Monica Bay and Newport-Inglewood (Table 2.1.4-1). They are discussed in Borrero et al. (2001), Borrero et al. (2004), Barberopoulou et al. (2011) and references therein. In addition to these southern California faults, we also considered the Point Reyes Fault, which is located offshore of San Francisco Bay and the Ventura Fault multi-segment rupture scenario from the recent publication of Hubbart et al. (2014). Sources from the Cascadia Subduction Zone (CSZ) are analyzed in the far-field sources section of this report.

2.1.5 Inter-Plate Earthquakes

Information Submitted by the Licensee

The FHRR provides details for a number of potential far-field earthquakes (PG&E, 2016). The examined far-field sources include the Aleutian Alaska Subduction Zone, the Semidi Subduction Zone, the Kamchatka Subduction Zone, and the Japan Subduction Zone.

Taylor Engineering Technical Evaluation

The Pacific Marine Environmental Laboratory (PMEL) of the National Oceanic and Atmospheric Administration (NOAA), as part of its real-time tsunami forecasting system, has discretized the circum-Pacific subduction-zones into sub-faults of size 100 x 50 km (along-strike length by along-dip width). The sub-faults are prescribed a strike angle that closely follows the boundary (Bird, 2003). The dip angle and the down-dip extent of unit sources are based on the best knowledge of local fault geometry (e.g. Kirby et al., 2005), which we assume are accurately represented. Also, for the purposes of tsunami modeling, rake angle is fixed at 90^{o}, thus representing pure thrust rupture. It has been shown by Titov et al. (1999) that these parameters do not have a big effect in the far-field tsunami amplitudes.

As an example, Figure 2.1.5-1 shows the sub-faults and the NOAA labeling for the Japan subduction zone. The numbers represent the source column number which run along the subduction zone and the letters in front of the numbers represent the source row name in the down-dip direction. The rows go from shallowest to deepest in the following order: B, A, Z, Y, X, W, V. Source rows C and D represent normal faulting sources (per the McKenzie and Jackson, 2012, tsunami generation mechanism) which are not considered in this report. For details about the source location and parameters refer to Tang et al. (2010).

Table 2.1.4-1: Source Specification for Near-field Earthquake Scenarios Modeled in this Report.

Sources Number	Source Name	References	Segment	Lon (deg)	Lat (deg)	Length (km)	Width (km)	Dip (deg)	Rake (deg)	Strike (deg)	Slip (m)	Depth (km)
L1	Anacapa Dume	Uslu (2008)	1	241.13	34.03	40	18	55	90	270	2.5	5
L2	Channel Island Thrust	Borrero et al. (2001)	1	240.5	34.3	56	34	20	90	280	3.6	17
L3	Carlsbad Thrust Fault	Barberopoulou et al. (2011)	1	242.6	33	30	12	30	90	324	5	1.5
L4	Catalina Islands	Borrero et al. (2004)	1	242.14	33.03	21.9	14	89	172.9	313	4	0.5
			2	241.97	33.17	28.2	14	85	143.1	293	5	1
			3	241.69	33.26	16.1	14	70	123.7	277	2.8	1
			4	241.52	33.28	20.2	14	80	146.3	303	3.6	1
			5	241.6	33.34	8.1	14	80	149	300	6.4	1.5
			6	241.53	33.38	40.2	14	80	153.4	297	4.5	1
			7	241.14	33.54	29.7	14	89	166	315	4.1	0.5
L5	Coronado Bank Fault	Borrero et al. (2004)	1	242.93	32.2	39.56	10	80	153.4	328.3	2.4	0.5
			2	242.7	32.51	24.55	10	80	135	327.6	4.2	0.5
			3	242.55	32.7	29.66	10	80	135	337	2.8	0.5
L6	Lausen Knoll	Borrero et al. (2004)	1	242.14	33.37	8.8	12.8	70	135	290	1.5	0.5
			2	242.06	33.375	7.9	12.2	80	135	308	3	0.5
			3	241.99	33.42	10	12.2	80	135	308	5	0.5
L7	Lompoc 1927	Satake & Somerville (1992)	-	239.13	34.36	28	14	66	95	340	2.5	3
L8	Newport Inglewood Fault - 1	Barberopoulou et al. (2011)	1	241.8	33.7	30	8	70	170	335	4	10
L9	Newport Inglewood Fault - 2	Barberopoulou et al. (2011)	1	241.8	33.7	30	8	70	10	315	4	10
L10	Newport Inglewood Fault - 3	Barberopoulou et al. (2011)	1	241.8	33.7	30	8	0	10	0	4	10
L11	Newport Inglewood Fault - 4	Barberopoulou et al. (2011)	1	241.8	33.7	30	8	70	10	155	4	10
L12	Point Reyes Fault	Barberopoulou et al. (2011)	1	241.8	38.19	39.5	12	50	90	333	3.4	0.1
			2	237.16	37.95	37.5	12	50	90	300	3.4	0.05

Table 2.1.4-1: Source Specification for Near-field Earthquake Scenarios Modeled in this Report (Continued)

Sources Number	Source Name	References	Segment	Lon (deg)	Lat (deg)	Length (km)	Width (km)	Dip (deg)	Rake (deg)	Strike (deg)	Slip (m)	Depth (km)
L13	San Clemente Bend Region	Borrero (2001)	1	242.86	31.75	18.52	10	89	-161.6	330.4	1.6	0.5
			2	242.76	31.9	8.86	10	89	158.2	310.2	2.7	0.5
			3	242.48	32.08	6.96	10	80	135	307.8	7	0.5
			4	242.69	31.95	23.65	10	89	166	304.9	4.2	0.5
			5	242.41	32.11	12.92	10	85	149	314.5	5.8	0.5
			6	242.32	32.19	6.9	10	89	161.6	312.4	3.2	0.5
			7	242.26	32.24	19.5	10	70	-161.6	311.8	1.6	0.5
L14	San Clemente Fault	Borrero (2001)	1	241.4	33.1	30	8	70	162	305	8	7.6
			2	241.54	32.95	50	14	75	18	140	8	1
L15	San Mateo Thrust	Borrero et al. (2004)	1	242.42	33.22	5.5	12	45	120	290	4	0.5
			2	242.36	33.25	11.4	12	45	120	318	4	0.5
			3	242.28	33.32	10.85	12	45	120	327	4	0.5
L16	Santa Monica Thrust	Uslu (2008)	1	241.41	34.075	40	18	55	90	260	2.4	15
L17	Pitas Point-Ventura Fault	Hubbard et al. (2014)	1	240.566	34.357	45.1	9.7	50	90	275.8	6	0.5
	Lower Red Mountain Fault	Hubbard et al. (2014)	1	240.518	34.592	32.5	22	35	90	276.1	6	7.5
	Lower Red Mountain Fault	Hubbard et al. (2014)	2	240.752	34.612	29	22	35	90	249.2	6	7.5
	Upper Red Mountain Fault	Hubbard et al. (2014)	1	240.377	34.438	16.1	9.7	50	90	269.3	6	0.5
	Upper Red Mountain Fault	Hubbard et al. (2014)	2	240.573	34.411	16.7	9.7	50	90	289.2	6	0.5

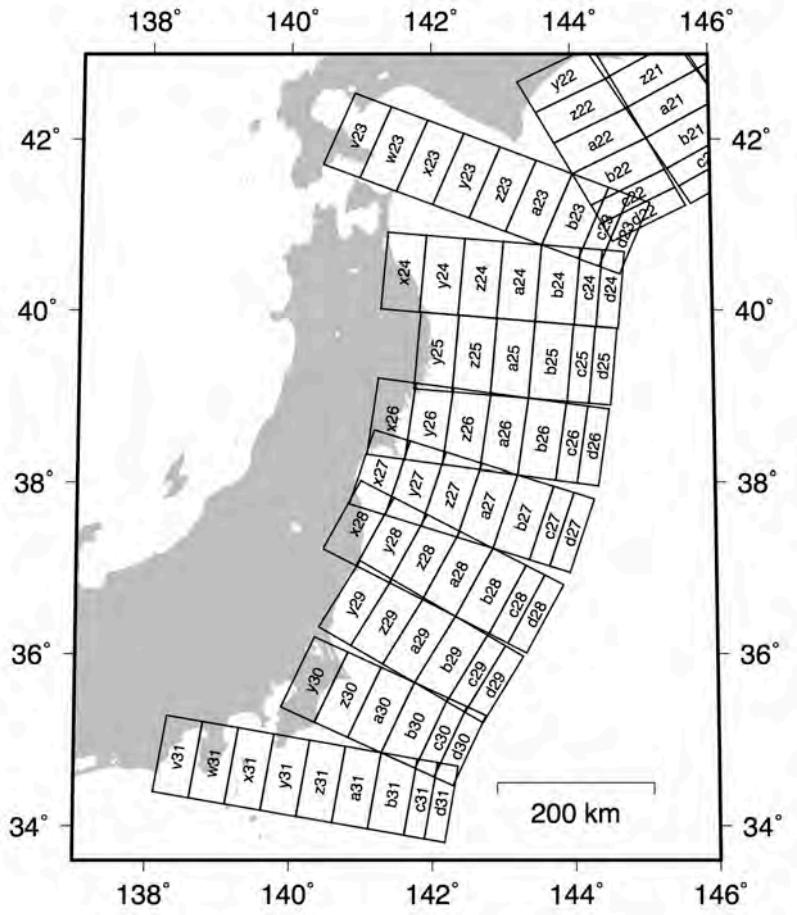

Figure 2.1.5-1: NOAA's Unit Sources and Labeling along the Japan Subduction Zone (KISZ).

The surface deformation from the rupture of each sub-fault was computed using Okada's (1985) method for a 1-m slip, thus using the term *unit sources* for the sub-faults. The tsunami amplitudes and velocities across the Pacific basin were computed using the Method Of Splitting Tsunami (MOST)hydrodynamic model (see Section 3.1) on a 4 arc-min grid and stored in an on-line database at 16 arc-min resolution. Since surface deformation and deepwater propagation are linear functions of slip magnitude, the tsunami amplitudes across the Pacific Ocean can be readily obtained for any combination of unit sources and slip magnitudes. Therefore, the variation of slip magnitude during seismic rupture can be accounted for by creating more complex faulting scenarios (Titov et al., 2011). This linear property of deepwater tsunami propagation is the basis of NOAA's tsunami source inversion procedure during real-time tsunami forecasts, which is described in more detail in Percival et al. (2009).

To identify which subduction zones direct more energy toward the DCPP site, we performed a sensitivity analysis by utilizing the NOAA/PMEL unit sources database. The tsunami amplitude time series for each unit source is available at discrete nodes with 16

arc-min spacing. We selected the closest node directly offshore from the DCPP site (see Figure 2.1.5-2) and saved the maximum (positive) amplitude from each unit source. Figure 2.1.5-3 shows the maximum amplitude in millimeters from all the row B (shallowest) unit sources considered here. Sources from the Alaska-Aleutians and Cascadia Subduction Zones produce the biggest amplitudes offshore of the DCPP site. Uslu (2008) noted that northern and central California are susceptible to tsunamis from these regions and it is also confirmed here.

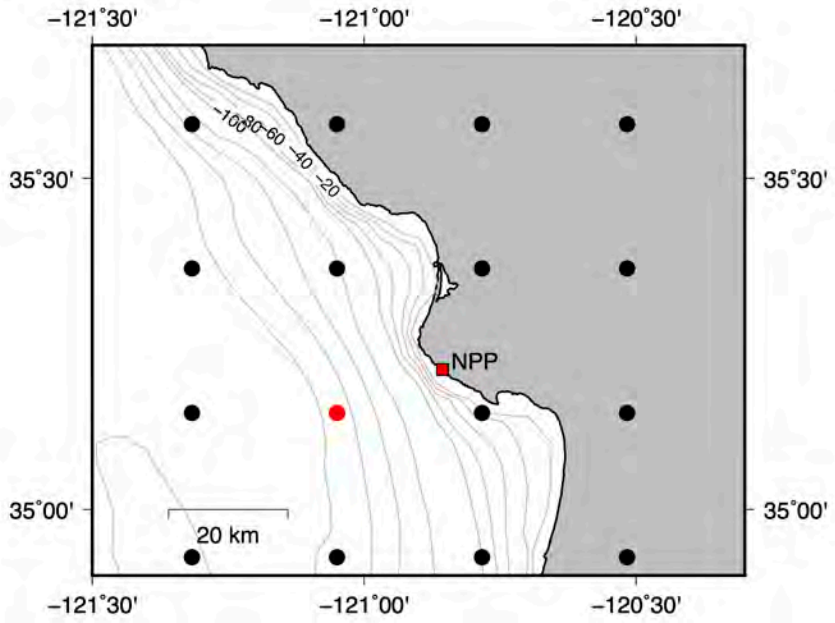

Figure 2.1.5-2: Location of numerical gauge (red dot) offshore of the DCPP site (red square) which was selected for pre-assessment of tsunami intensity. Black dots are all the propagation database grid points near the reactor site with 16 arc-min spacing.

All unit sources have the same moment magnitude (assuming earth's rigidity [μ] is constant everywhere) and, therefore, the sensitivity test does not take into account the largest possible earthquake magnitude for each subduction zone. Maximum amplitude varies between sources due to differences in the fault geometry (dip angle), the distance from source to site, and the oceanic bathymetry/topography controlling directivity. It cannot be immediately concluded, without taking maximum possible earthquake magnitudes into consideration, where the worst-case tsunami source for the DCPP site might be located.

In the following sections, we outline the general steps followed to obtain the sources that produce the maximum possible tsunamis at the DCPP site. We also provide a more detailed description of the sources used for each subduction zone in separate subsections.

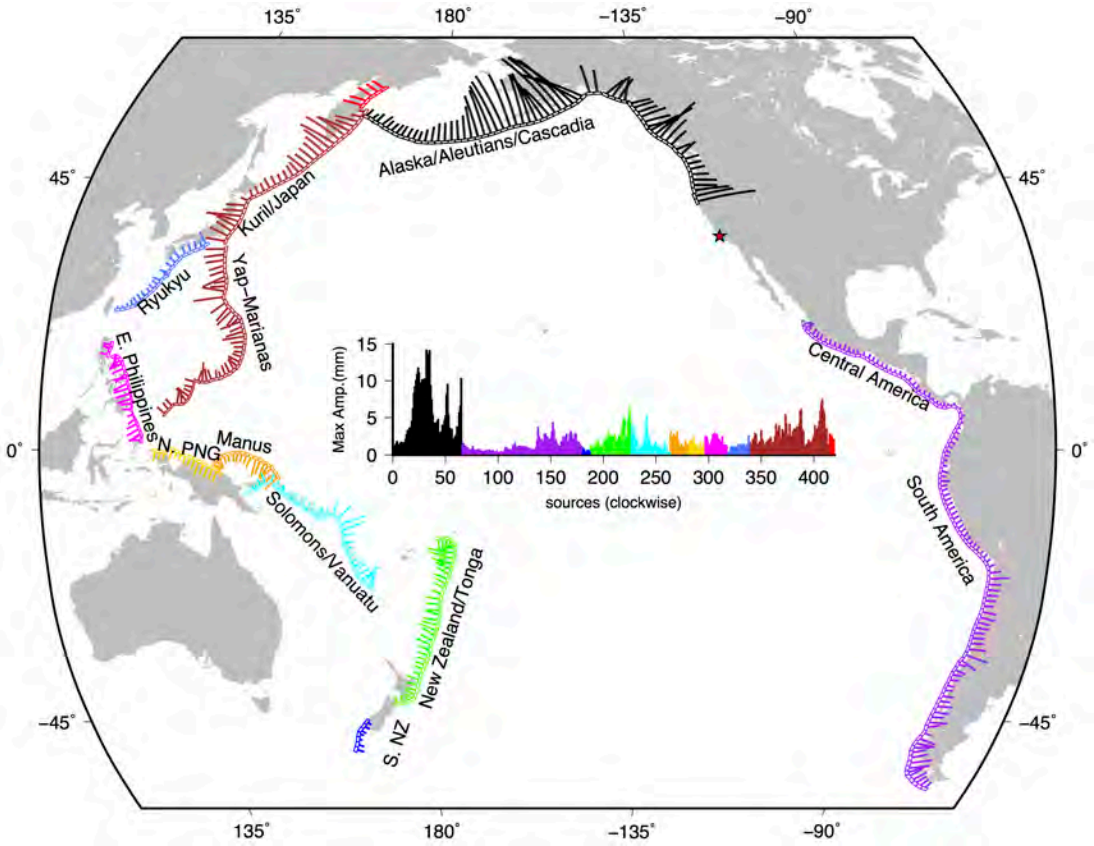

Figure 2.1.5-3: Tsunami hazard sensitivity for the DCPP site to the location of the unit sources (only shallowest [row B] unit sources shown here). The lengths of the bars show the relative maximum amplitude offshore of the DCPP site from each unit source for a 1 meter slip. The inset figure shows the maximum amplitude values in millimeters, moving clockwise around the Pacific Ocean, starting from W. Aleutians and ending at N. Kamchatka. Red star shows the location of the DCPP site; all data shown above based on Taylor Engineering analyses.

2.1.5.1 Source Magnitude

To obtain the maximum possible earthquake magnitude for each subduction zone, we refer to three relevant publications: McCaffrey (2008), Berryman et al. (2013), and Rong et al. (2014) (hereafter referred to with the initials MC08, GEM13 and RO14, respectively).

In the first two publications (MC08 and GEM13), subduction zones are divided in discrete sections and for each section a maximum possible magnitude m_x is assigned based on the length of the segment and the seismogenic layer depth considered. In MC08 and GEM13, the along-strike segment boundaries are defined based on plate kinematic information and/or from the presence of geological barriers, which are open to interpretation. For example, features thought to be barriers have been crossed during earthquake ruptures such as the Australian-Woodlark-Pacific triple plate junction, which was crossed during the 2007 $M_w8.1$ Solomon Island earthquake (Taylor et al., 2008). Also, the length-magnitude

empirical relations used in these publications are simplistic and may not be appropriate for M_w9+ earthquakes (Kalligeris et al., 2017).

In the case of implementing a frequency-magnitude relation, such as the *Tapered Gutenberg-Richter* (TGR) distribution that RO14 used, maximum magnitude is defined relative to a time frame. This allows a more realistic definition to m_x, the *maximum probable magnitude* $m_p(T)$. Even though the *TGR* distribution is truncated at the tail of the G-R distribution and is constrained by the moment rate conservation principle, it still suffers from the statistical error of the limited sample at higher earthquake magnitudes. In the case of Cascadia, RO14 utilized the 10,000-year turbidity record of Goldfinger et al. (2012), which is complete for magnitudes above M8-8.5, to extend the seismic catalog beyond the instrumental period. However, for other subduction zones very little paleoseismic information exists to constrain the tail of the *TGR* distribution. In addition, there is a debate of whether the β parameter should be global, i.e. by using global earthquakes from the seismic catalog or zone-specific (RO14 and references therein). In the case of zone-specific, it can be argued that the distribution is more fitting to a particular faulting regime and tectonic setting. However, the earthquake event sample is significantly reduced. RO14's maximum probable earthquake is expressed in terms of a return period; the authors selected the maximum m_p *(10,000 years)* from Table 2.1.5.1-1 for each subduction zone based on the annual exceedance frequency of merit discussed in the External Flooding Assessment Guidelines (see NEI, 2016; NRC, 2016).

On the other hand, the segment ruptures of MC08 and GEM13 can be assigned a return period using:

$$T = \frac{u_{av}}{f\chi v} \qquad (2.1.5\text{-}1)$$

where u_{av} is the average slip across the rupture, f is the fraction of the total seismic moment released by M9 earthquakes, v is the plate convergence rate, and χ is the seismic coupling coefficient. The recurrence time estimated by MC08 for the maximum magnitude events range from hundreds to thousands of years.

Subduction zones are delineated following Flinn and Engdahl (1965) and Flinn et al. (1974), and are so-named "F-E" zones (see Figure 2.1.5.1-1). In the absence of a definite argument on which maximum magnitude to use for each subduction zone, we selected the maximum reported for each F-E zone by the three aforementioned references (Table 2.1.5.1-1).

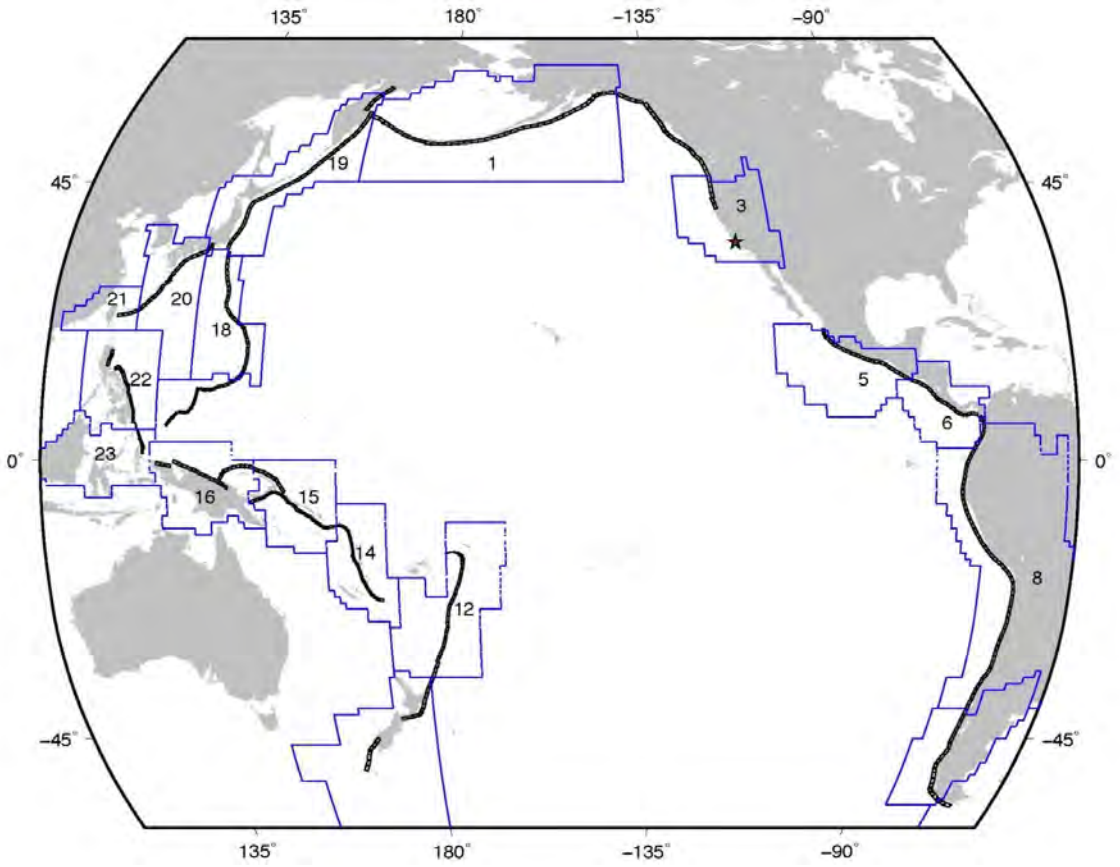

Figure 2.1.5.1-1: Subduction zones (F-E zones) around the Pacific Ocean that were considered in this report. The numbered zones are the ones analyzed by Rong et al. (2014) [RO14] to derive maximum probable magnitudes $m_p(T)$ for each zone. The zone numbers correspond to: 1, Alaska-Aleutians; 3, Cascadia; 5, Mexico-Guatemala; 6, Central America; 8, Andean South America; 12, Kermadec-Tonga-Samoa; 14, New Hebrides Islands; 15, Bismarck-Solomon Islands; 16, New Guinea; 18, Guam-Japan; 19, Japan-Kamchatka; 20, Japan-Ryukyu; 21, Taiwan; 22, Philippines. Rong et al. (2014) modified the F-E zone of Cascadia for their analysis to include the northern part. The NOAA/PMEL unit sources (row B only) are also shown. The star (*) designates the DCPP site.

Table 2.1.5.1-1: Maximum magnitudes reported for all F-E zones. The maximum for each F-E zone is shown in bold font.

Subd. zone	Location	GEM13	L (km)	W (km)	MC08	L (km)	W (km)	RO14 m_p(10000 yrs)
AASZ	Alaska	**9.63**	1963	123	9.5	1489	129	9.4
AASZ	Cascadia	9.2	1415	68	9.5	1048	256	**9.6**
CSSZ	Mexico	9.23	1710	40	**9.4**	1378	112	9.1
CSSZ	C. America	8.71	533	68	**9.4**	1506	107	9.3
CSSZ	S. America	**9.88**	2502	178	9.5	1304	178	9.7
NTSZ	Kermadec	9.42	1627	87	9.4	1450	98	**9.8**
NGSZ	N. Guinea	9.03	764	100	9.2	1030	117	**9.8**
KISZ	Guam-Japan	9.48	1822	85	9.5	1812	95	**9.6**
KISZ	Kamchatka-Japan	**9.73**	2223	134	9.3	1242	91	9.5
RNSZ	Rykukyu	9.09	1440	35	9.2	1131	95	**9.6**

2.1.5.2 Slip Magnitude

Since tsunami generation is directly linked to the co-seismic vertical surface deformation, the slip magnitude controls, to a large extent, the tsunami generation. In the near-field, slip magnitude and distribution also control the tsunami runup (Okal and Synolakis, 2004). However, far away from the source, the details of slip distribution are less important (Okal and Synolakis, 2008) and it is reasonable to assume a uniform slip model.

Given the earthquake magnitude, deciding on a reasonable source area and slip magnitude is very ambiguous. Typically, scaling laws relating earthquake magnitude and fault dimensions are used (e.g. Wells and Coppersmith, 1994). However, due to the small sample, our knowledge about the rupture processes during very large earthquakes is limited. Indicative of this statement is the disagreement of fault modes proposed for the 2011 Tohoku earthquake (MacInnes et al., 2013). In our study, we employ the formula used by MC08 and GEM13 of u_{av}=2.5 ± 1.0 x $10^{-5}L$, which is based on extrapolation of the Wells and Coppersmith (1994) scaling relations (alternative and more recent empirical relations are provided by Leonard, 2010). However, instead of taking the mean value, we used u_{av}=3.5 x $10^{-5}L$. The earth's rigidity is taken as a constant and equal to $\mu = 30\ GPa$, which is reasonable for the shallow sources considered here. Both assumptions were made to maximize the tsunami amplitude given an earthquake magnitude.

For the rupture area, we used the maximum estimated lengths and widths provided in MC08 and GEM13 as a guide. In some cases, where the length and width of the subduction zone are limited (e.g., New Guinea F-E zone), Taylor Engineering staff used a larger slip magnitude (u_{av} > 3.5 x $10^{-5}L$) to match the maximum magnitude. Finally, since the unit source size is pre-defined, the dimensions of the fault rupture areas for each earthquake scenario are multiples of 100 km along strike times and multiples of 50 km along dip.

2.1.5.3 Source Specification

The segmentation of the subduction zones suggested by MC08 and GEM13 is based on changes in the direction and rate of plate convergence and/or natural geologic breaks. Based on the argument that such boundaries have been crossed in the past, in some of the subduction zones we repositioned the maximum length segments in places where more tsunami energy is beaming towards the site.

The magnitude, rupture area, and slip magnitude of the far-field sources modeled in this report are given in Table 2.1.5.3-1. The unit sources corresponding to each source are also provided using NOAA/PMEL's labels. A more detailed description about the sources is provided in the following sections.

Table 2.1.5.3-1: Source Specification for Far-field Inter-plate Earthquake Scenarios Modeled in this Report

Source	Subduction zone*	Location	M_w	Length (km)	Width (km)	Slip (m)	Fault model specification*
AA-1	ACSZ	Alaska	9.6	1500	150	52.5	a22-a36, b22-b36, z22-z36
AA-2	ACSZ	Alaska	9.6	1700	100	59.5	a20-a36, b20-b36
CAS-1	ACSZ	Cascadia	9.6	1500	varies	52.5	a51-a65, b51-b65, z55-z62
CAS-2	ACSZ	Cascadia	9.6	1700	100	59.5	a49-a65, b49-b65
CAS-3	ACSZ	Cascadia	9.6	1400	varies	varies	50m*(a52-a56, b52-b56) + 60m*(a57-a60,b57-b60,z57-z60) + 70m*(a61-a63, b61-b63,z61-z62) + 80m*(a64-a65,b64-b65)
ME-1	CSSZ	Mexico	9.4	1100	100	38.5	a1-a11, b1-b11
CA-1	CSSZ	C. America	9.4	1100	100	38.5	a15-a25, b15-b25
SA-1	CSSZ	Peru	9.9	2500	varies	87.5	a49-a73, b49-b73, z49, z53-63, z67-73
SA-2	CSSZ	C. Chile	9.9	2500	varies	87.5	a72-a96, b72-b96, z72-73, z88-z96
SA-3	CSSZ	S. Chile	9.9	2500	varies	87.5	a83-a107, b83-b107, z88-z107
KT-1	NTSZ	Kermadec	9.8	2500	100	87.5	a12-a36, b12-b36
NG-1	NGSZ	N. Guinea	9.8	1500	100	120	a1-a15, b1-b15
NG-2	NGSZ	N. Guinea	9.8	1200	100	150	a1-a12, b1-b12
GJ-1	KISZ	Marianas	9.6	1800	100	63	a44-a61, b44-b61
GJ-2	KISZ	Marianas	9.6	1800	100	63	a34-a51, b34-b51
JK-1	KISZ	Kurils	9.7	2200	100	77	a1-a22, b1-b22
JK-2	KISZ	Kurils	9.7	1700	150	59.5	a2-a18, b2-b18, z2-z18
RN-1	RNSZ	Ryukyu	9.6	1800	100	63	a4-a21, b4-b21

*Refers to the four-lettered subduction-zone code adopted by NOAA/PMEL.

2.1.5.4 Alaska-Aleutians Subduction F-E Zone

The Alaska-Aleutian Subduction Zone (AASZ) is one of the two major tsunamigenic zones in the continental U.S. The AASZ has produced major earthquakes in the past (Figure 2.1.5.4.1-1) that resulted in trans-oceanic tsunamis. The three most notable earthquakes in the region during the instrumental period are the $8.2M_w$ 1946 Aleutian Islands (Johnson and Satake, 1997), $8.6M_w$ 1957 Andreanof Islands (Johnson et al., 1994), and $9.2M_w$ 1964 Prince William Sound (Plafker, 1969; Kanamori, 1970) earthquakes.

The $8.2M_w$ 1946 earthquake is well known for the disproportionate size of the earthquake-generated tsunami. The tsunami was destructive both in the near- and far-field. In the near-field, it destroyed the Scotch Cap Lighthouse in Unimak Island, where runup reached 42 m (Okal et al., 2003). The enhanced near-field runup of this particular tsunamigenic earthquake with the typical characteristics of *tsunami earthquakes* (Kanamori, 1972), has been attributed to the triggering of a local submarine landslide (Okal et al., 2003). In the far-field, the generated tsunami impacted coastal areas as far as the Marquesas Islands of French Polynesia and Hilo, Hawaii (Fuchs, 1982). In the Hawaiian Islands, runup heights reached over 11 m at Oahu and 16 m at Hilo (Loomis, 1976). In California, a 1 m amplitude wave was reported in Crescent City, whereas the most damaging effects were noted in Half Moon Bay where the waves shoved boats nearly 300 m inland as the water level rose 3 m above the original level (Lander et al., 1993).

The $8.6M_w$ Great Aleutian Islands earthquake occurred on March 9, 1957 in the Aleutian Island arc (Figure 2.1.5.4.1-1). The earthquake ruptured along 1200 km of the Aleutian Trench and is one of the longest ruptures ever recorded from aftershocks (Johnson et al., 1994). In the far-field, the generated tsunami reached 16 m at Kauai, 6.5 m at Oahu and 10 m at Hawaii Island (Loomis, 1976). In California, minor damage was reported in San Diego, as the waves arrived in the form of a late surge with currents reaching 30 mph (Lander et al., 1993).

The Good Friday earthquake of 1964, by the sheer size of the energy released, caused widespread destruction in the near-field and generated a trans-Pacific tsunami. The magnitude of the earthquake was evaluated at $9.2M_w$ (7.5×10^{29}dyne-cm) by Kanamori (1970) using long-period surface waves, rendering it the third largest earthquake recorded after the $9.6M_w$ 1960 Chilean and $9.3M_w$ 2004 Sumatran earthquakes. Plafker (1969, 1972) measured surface deformation in the near-field to propose a fault rupture 800 km long, 175 to 290 km wide, 9° dip, and 20+ m of slip in the eastern part of the Alaskan subduction zone. The generated tsunami waves were particularly destructive in Kenai Peninsula and the Kodiak Islands group where an initial sea withdrawal was reported and peak tsunami crest elevation reached 10 m (Grantz et al., 1964). Runup in the Gulf of Alaska reached 20 to 30 m, with the maximum elevation of 27 to 30 m above mean lower low tide near the head of Aialik Bay (Wilson and Torum, 1968). In Hawaii, waves generally reached 1.5 to 1.8 m with a maximum of 4.5 m in Oahu Island (Loomis, 1976). In California, runup was pronounced in the northern part of the coast, reaching 6 m in Crescent City, and decreased moving south to 3 m in San Francisco Bay and 3.8 m in Santa Cruz (Wilson and Torum,

1968). The decay of the tsunami wave height (north to south) along the California coast is also evident in the tide gauge records shown in Table 2.1.5.4-1.

Table 2.1.5.4-1: Maximum rise or fall (in meters) at the tide stations in California for tsunami events between 1946-1964 (Source: Spaeth and Berkman 1965).

Station	1946	1952	1957	1960	1964
Crescent City	1.8	2.1	1.3	3.3	4.0+
San Francisco	0.5	1.1	0.5	0.9	2.3
Santa Monica	No Data	1.1	0.9	2.8+	2.0
Los Angeles	0.8	0.6	0.6	1.5	1.0
La Jolla	0.4	0.2	0.6	1.0	0.7
San Diego	0.4	0.7	0.5	1.4	1.1

2.1.5.4.1 Zonation

As is evident in Figure 2.1.5.4.1-1, the biggest part of the Alaska-Aleutians Arc has ruptured in the past century. The two exceptions are the west part of the Aleutian Trench near the Komandorksi Islands (west of the 1965 rupture area), and near the Shumagin Islands (between the 1938 and 1957 rupture areas). Near Komandorksi Islands, subduction is taking place at an oblique angle and it is not clear if it is capable of producing large earthquakes (Wesson et al., 2007 and references therein). That section of the arc does not pose a big threat to the DCPP due to directivity of tsunami propagation across the ocean. For the Shumagin Islands *seismic gap*, on the other hand, it has been found that the seismic coupling is very low and most of the slip is aseismic (Feymueller and Beavan, 1999; Wesson et al., 2007). In the zonation of MC08, the Alaska-Aleutians Arc is divided into three segments: W. Aleutians, with *L=1244 km*; E. Aleutians, with $L = 1092\ km$; and Alaska, with $L = 1489\ km$ (Figure 2.1.5.4.1-2). Since MC08 does not provide more detailed information where the segments start and finish, for this analysis the three segments are distributed along the arc and the Alaskan segment is interpreted as overlapping the Shumagin seismic gap. The GEM13 zonation, which follows that of Wesson et al. (2007), considers the Shumagin gap as a separate segment, and the arc east of Shumagin is divided into three more segments (Figure 2.1.5.4.1-2). This GEM13 zonation was based on kinematic data and for the purpose of accommodating smaller magnitude ($\approx M_w 8$) events for the seismic hazard assessment study of Wesson et al. (2007). However, Wesson et al. (1999) and Wesson et al. (2007) in their analyses assumed that no large earthquake would rupture through the Shumagin segment.

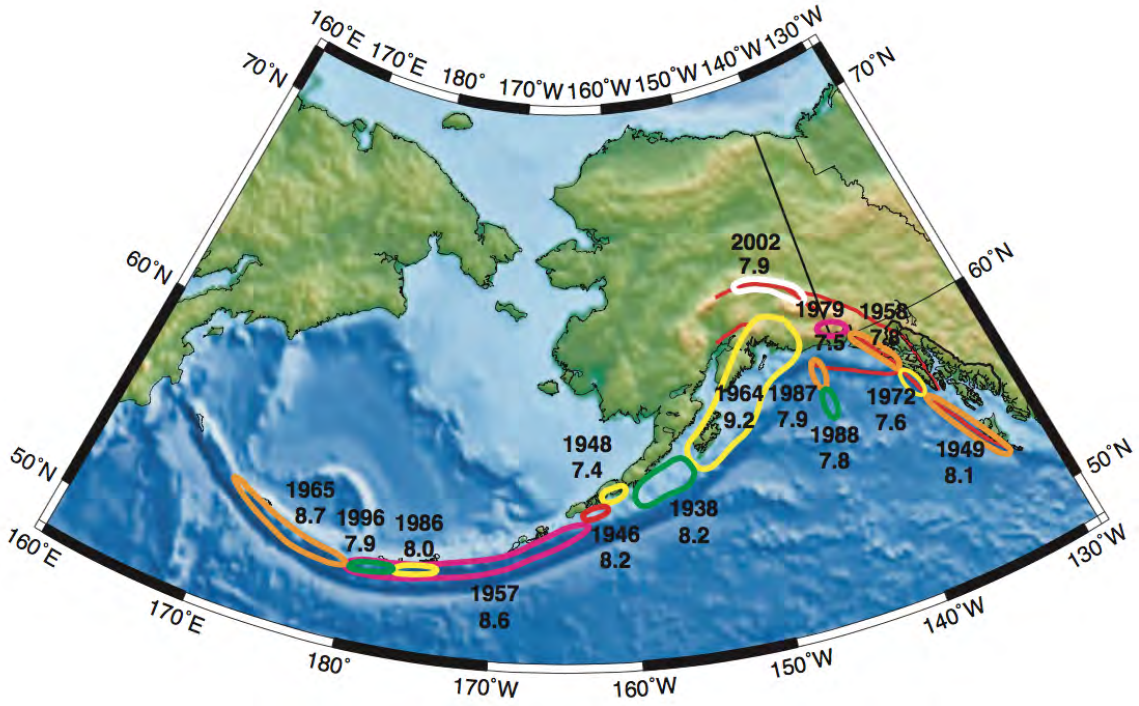

Figure 2.1.5.4.1-1: Estimated major earthquake rupture areas (1900–2004) in the Alaska-Aleutians and British Columbia subduction zones (Wesson et al. (2007).

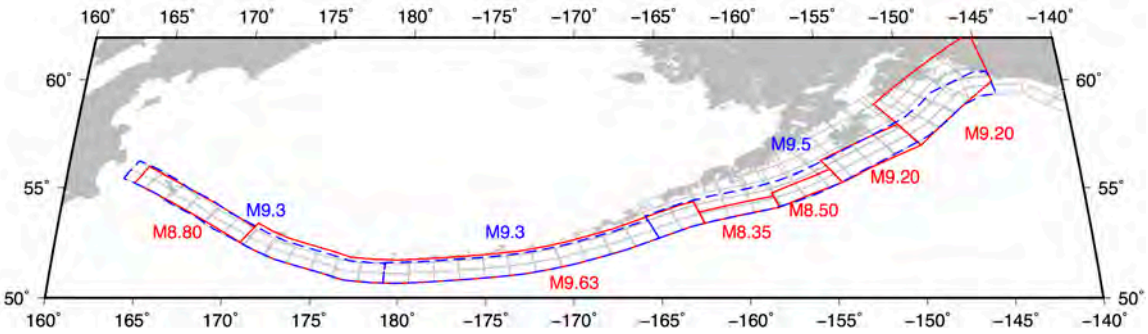

Figure 2.1.5.4.1-2: The Alaska-Aleutian Subduction Zone segments as defined by McCaffrey (2008 [MC08]; blue dashed lines and blue font) and Berryman et al. (2013 [GEM13]; red solid lines and red font). NOAA's unit sources are shown with the gray rectangles.

2.1.5.4.2 Maximum Magnitude Sources

Referring to Table 2.1.5.1-1, we selected the maximum magnitude for the AASZ, i.e. $M_w 9.63$ suggested by the GEM13 report. Based on this magnitude, we propose two sources of length, *L=1500 km* and *L=1700* km and width *W=150 km* and *W=100 km,* respectively. The width of the sources is above or below the preferred width *W=123 km* of GEM13. Along-dip, both sources are positioned in the shallowest part of the trench to maximize the vertical surface deformation, and consequently, the tsunami generation efficiency. In the

along-strike direction, both sources are placed in the part of the AASZ that beams the most tsunami energy towards the DCPP site (Figure 2.1.5.4.2-1). Both sources rupture through the Shumagin seismic gap that is believed by Wesson et al. (1999, 2007) to be a boundary for fault rupturing. We argue that when dealing with earthquake scenarios of very long return periods, such geologic boundaries could be potentially ruptured, as was the case with the 2007 Solomon Island earthquake that crossed a triple plate junction and the 2011 Tohoku earthquake that crossed multiple theoretical segment boundaries (Rong et al., 2014 and references therein). It should be noted that in the probabilistic tsunami hazard study of Tsunami Pilot Study Working Group (TPSWG) (2006) for Seaside, Oregon, and Gonzalez et al. (2009), the Shumagin gap was also overlapped by a source positioned between the eastern Aleutians and Kodiak Island (Source 2 in Gonzalez et al., 2009).

The selected unit sources (using NOAA's numbering) and slip magnitude are given in Table 2.1.5.3-1 (Sources AA-1 and AA-2). The abnormal high slip of u_{av}~*60m* for source AA-2 has been suggested to occur during the slip history of the 2011 Tohoku earthquake by Shao et al. (2011).

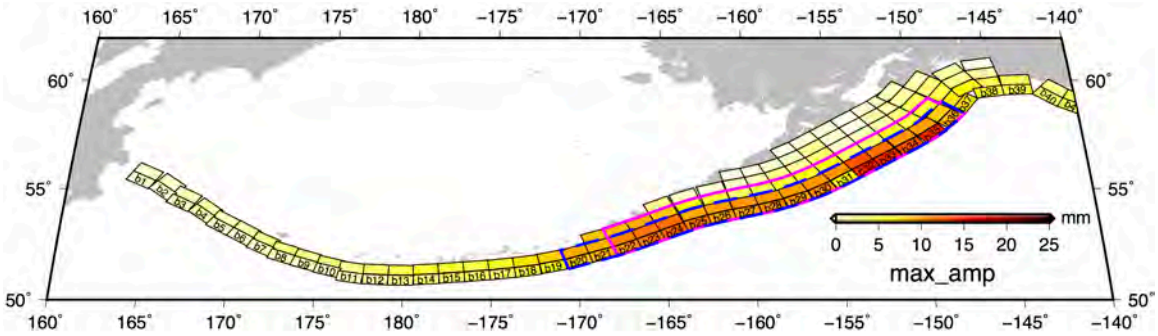

Figure 2.1.5.4.2-1: NOAA's unit sources and numbering along the Alaska-Aleutians Subduction Zone. Colors represent the maximum elevation *in millimeters at the numerical tide gauge offshore of the DCPP site, from each unit source using 1 m slip. The two sources AA-1 and AA-2, considered in this report, are shown with the blue continuous line and dashed magenta colors, respectively.*

2.1.5.5 Cascadia Subduction F-E Zone

The Cascadia Subduction Zone (CSZ) is the second largest subduction zone in the U.S. after the Alaska-Aleutians. It was thought that CSZ does not produce great magnitude earthquakes until the work of Atwater (1987) and the discovery that the origin of the 1700 orphan tsunami in Japan was a M9 earthquake in Cascadia (Satake et al., 1996). CSZ defines, to a large extent, the tsunami hazard in the states of Washington, Oregon and California due to the proximity of the subduction zone to those states and due to the paleoseismic records indicating that a great earthquake (M9) occurs in CSZ every ~500–530 years (Goldfinger et al., 2012).

In terms of slip distribution, we do not consider more complex rupture sources in the case of Cascadia, which is not a far-field source in the strict sense. The first reason for that is

because the deformation area of a M9 Cascadia rupture would not reach DCPP; therefore, various deformation patterns would not affect the vulnerability of the site. The second reason is that the main beam of tsunami energy is propagating at right angles towards the fault, southwest towards the open ocean and not towards the DCPP site (see Okal, 2008 for notes on directivity). The waves from Cascadia arrive as edge waves traveling along the continental shelf.

All the Cascadia sources were assigned a magnitude M_w=*9.6*, which corresponds to m_p*(10,000 years)* from RO14 for CSZ. The first source spans between unit sources 51–65 (*L=1500km*) and all the rows available are used, resulting in M_w=*9.58*. The second source is longer (*L=1700km*), and using the two shallowest rows (*W=100km*) results again in M_w=*9.58*, but with more slip (Figure 2.1.5.5-1). In the third source, we adopt a variable slip magnitude scheme, increasing the slip from 50 m in the northern unit sources to 80 m in the southern four unit sources. The magnitude of the third source is M_w=*9.64*.

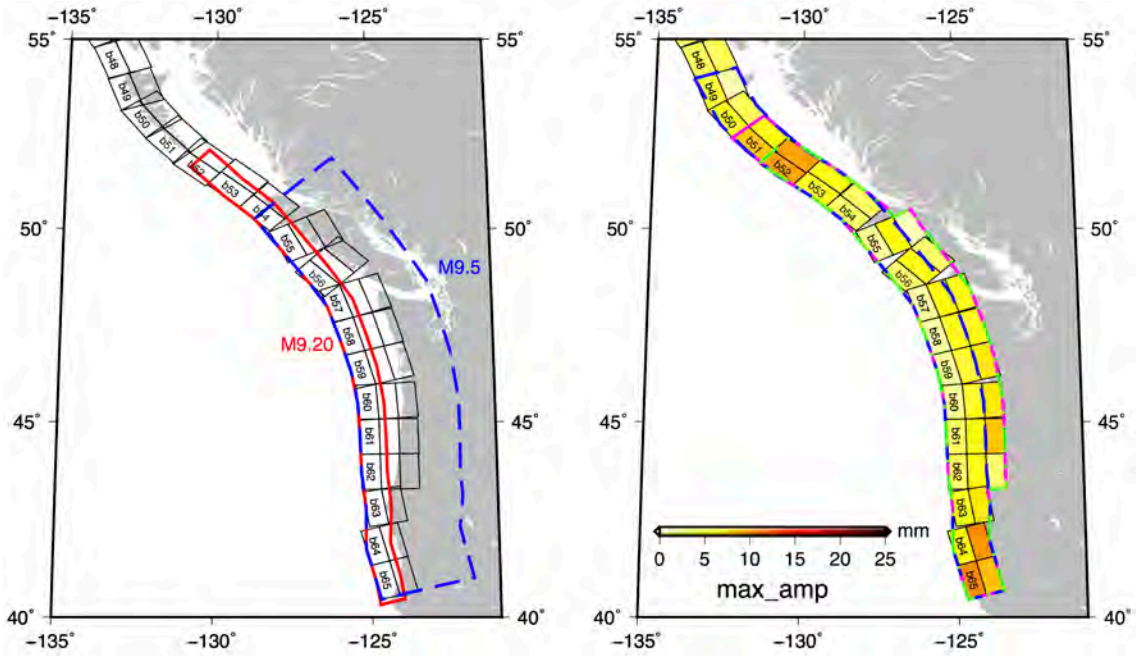

Figure 2.1.5.5-1: NOAA's unit sources along the Cascadia Subduction Zone. In the left figure, the continuous red and blue dashed polygons correspond to the segments proposed by Berryman et al. (2013) [GEM13] and McCaffrey (2008) [MC08] for Cascadia. In the right figure, the magenta, the blue dashed, and the green dash-dot polygons correspond to CAS-1, CAS-2 and CAS-3 M_w9.6 sources, respectively. The colors in the right figure represent the maximum elevation *in millimeters at the numerical tide gauge offshore of the DCPP site, from each unit source using 1 m slip.*

2.1.5.6 Mexico and Central America F-E Zones

For both the Mexico and Central America F-E zones, the maximum earthquake is M_w=*9.4*, which corresponds to the maximum magnitude proposed by MC08. The length, width, and

slip magnitude for both sources are *L=1100km*, *W=100km* and u_{av}*=38.5m,* respectively (Figure 2.1.5.6-1). The rupture length and width are taken from MC08 and GEM13, and the average slip is determined such that the specified magnitude is satisfied.

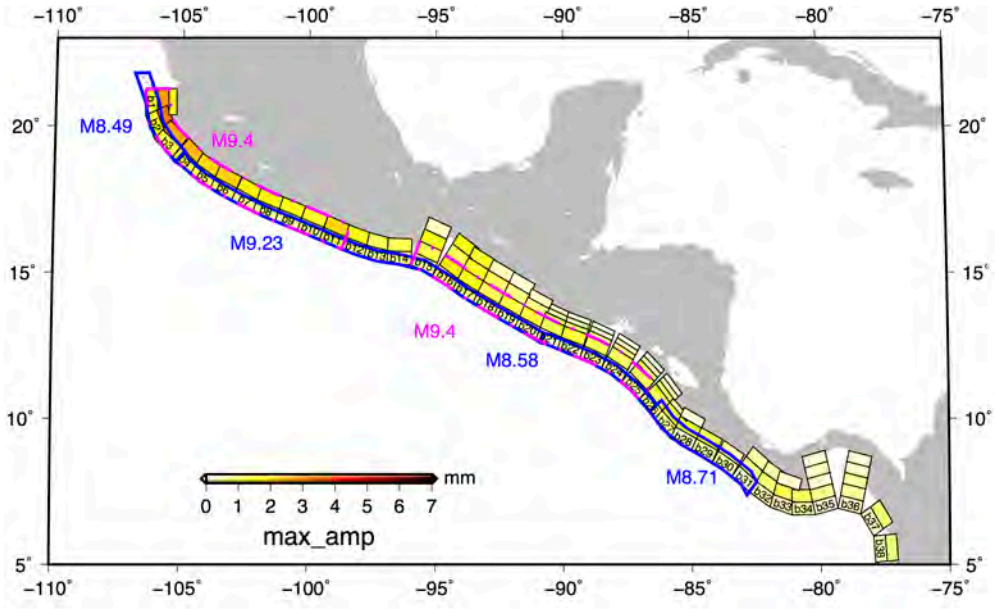

Figure 2.1.5.6-1: Berryman et al.'s (2013) [GEM13] segments (blue polygons) and the sources of this report (dashed magenta polygons) are overlaid on NOAA's unit sources in the Mexico and Central America F-E zones. Colors represent the maximum elevation *in millimeters at the numerical tide gauge offshore of the DCPP site, from each unit source using 1 m slip.*

2.1.5.7 South America F-E Zone

South America is one of the circum-Pacific subduction zones always considered in tsunami hazard studies for California. The southern Chile part of the subduction zone, along which the 1960 M_w*9.5* Chile earthquake rupture occurred, directs tsunami energy northwest in the Pacific and controls, to a large extent, tsunami hazard in southern California (Uslu, 2008).

Earthquake recordings and historical data reveal that almost the entire length of the South America subduction zone has ruptured over the past few centuries (Bilek, 2010). Along the coastal segment of Colombia, Ecuador, and northern Peru, few earthquakes greater than M_w*8* exist in the catalogs. However, the 1960 M_w*7.6* northern Peru earthquake is categorized as a *tsunami earthquake* (Bilek, 2010). Central Peru on the other hand has a long history of big and tsunamigenic earthquakes, with five earthquakes assigned magnitudes between M_w*8.8-9.3* (Okal et al., 2006). The largest known event is the 1868 earthquake, of estimated magnitude M_w*9.2-9.3*, that generated a destructive trans-oceanic tsunami (Okal et al., 2006 and references therein). The Chilean coast further south has also produced great historical earthquakes, with eight M_w*>8* earthquakes having occurred in the instrumental period alone. The most well-known event in this area is the 1960 M_w*9.5* Chilean earthquake (Plafker and Savage, 1970), which is the largest recorded earthquake

in history of seismology. Most recently, the 2010 $M_w8.8$ Maule earthquake produced a trans-oceanic tsunami (Fritz et al., 2011) that caused minor to moderate damage to ports and harbors in southern California (Wilson et al., 2013).

GEM13 discretized the South America subduction zone into six segments, with the longest segment ($L=2502km$) along the Peruvian coast being assigned $M_w9.88$ magnitude. MC08 suggests four segments, with the longest ($L=1599km$) also being along the Peruvian coast with moment magnitude $M_w9.5$. RO14 assigned a maximum probable magnitude in the South America subduction zone of $m_p(10{,}000\ years)=9.7$, using the generic β-value and associated m_c. In this report, we consider three earthquake source scenarios, all of which are assigned $L=2500km$ and $u_{av}=3.5x10^{-4}L=87.5m$, resulting in magnitudes a little over $M_w9.88$ proposed by GEM13. The position of the first is along the Peruvian coast, inside the Peru segment suggested by GEM13 (Figure 2.1.5.7-1). The other two sources are positioned along the Chilean coast, in locations that maximize the directivity toward the DCPP site (Figure 2.1.5.7-2).

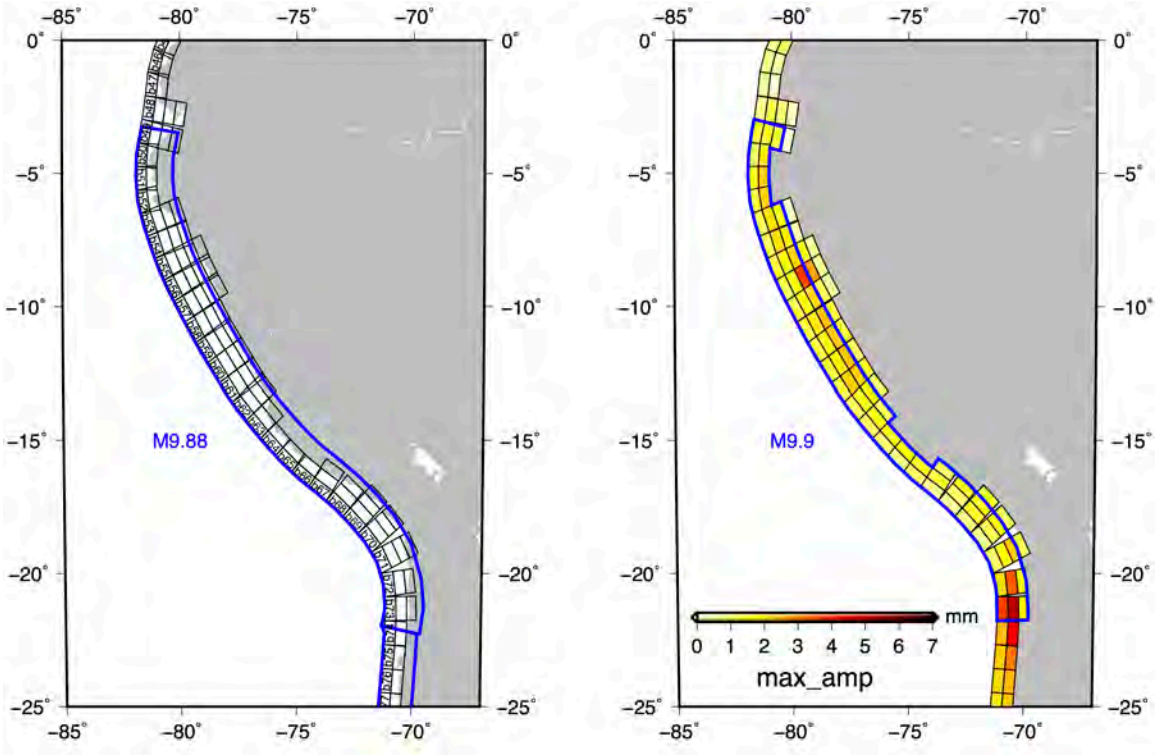

Figure 2.1.5.7-1: Left: The rupture segments of Berryman et al. (2013 [GEM13]; blue polygons) are overlaid on NOAA's unit sources in the South America F-E zone (Ecuador to Peru). Right: The source of this report is outlined with the continuous blue polygon. Colors represent the maximum elevation *in millimeters at the numerical tide gauge offshore of the DCPP site, from each unit source using 1 m slip.*

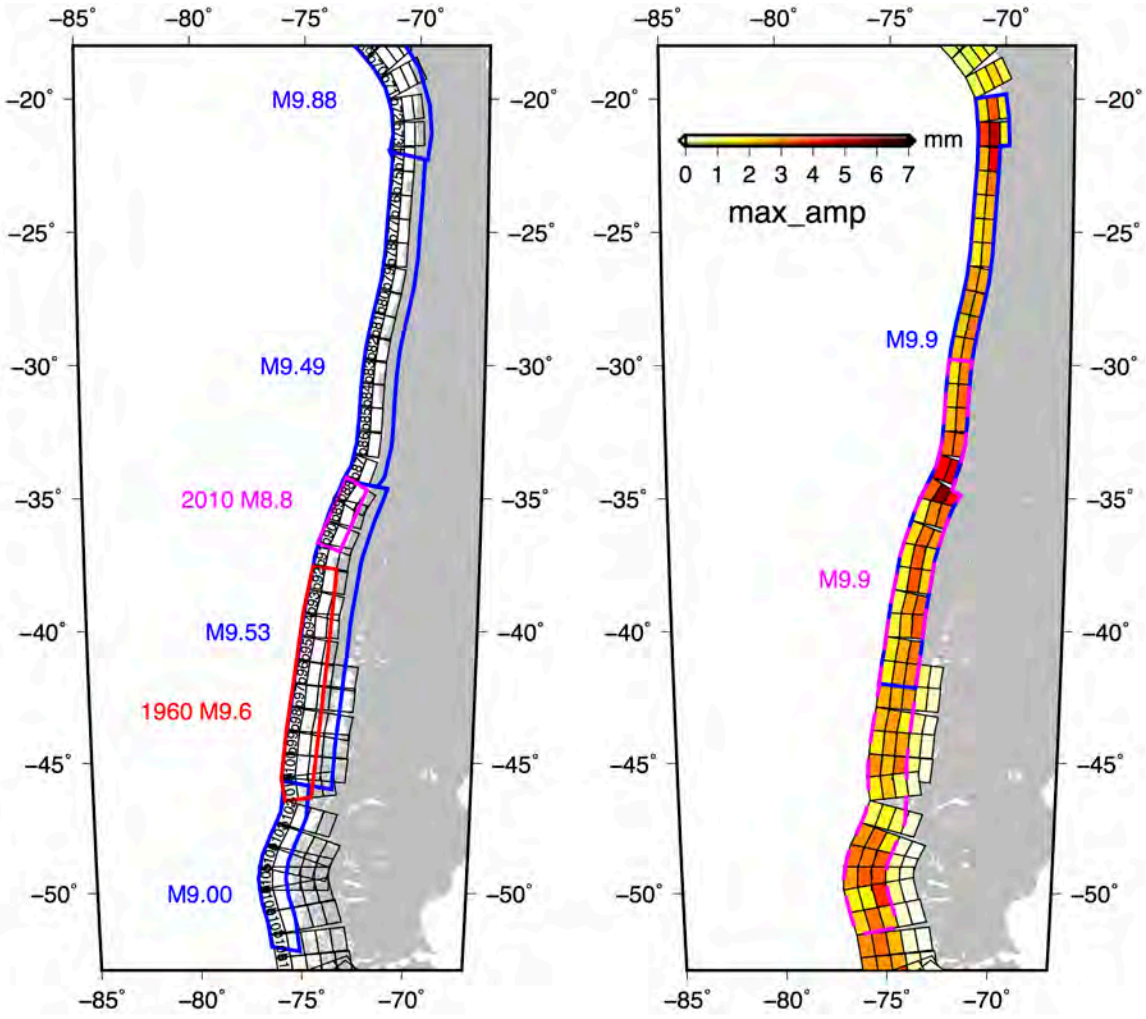

Figure 2.1.5.7-2: Left: The rupture segments of Berryman et al. (2013 [GEM13]; blue polygons) and the approximate rupture areas of the 2010 Maule and 1960 Chile earthquakes are overlaid on NOAA's unit sources in the South America F-E zone (Chile). Right: The sources of this report are outlined with continuous blue and dashed magenta polygons. Colors represent the maximum elevation *in millimeters at the numerical tide gauge offshore of the DCPP site, from each unit source using 1 m slip.*

2.1.5.8 Kermadec-Tonga-Samoa F-E Zone

For the Kermadec-Tonga-Samoa F-E zone, the proposed source has M_w=*9.8*, which corresponds to the maximum probable magnitude proposed by RO14. The length, width, and slip magnitude of the source are *L=2500km*, *W=100km,* and u_{av}=*87.5m,* respectively (Figure 2.1.5.8-1). The rupture length and width are taken from MC08 and GEM13, and the average slip is determined such that the specified magnitude is satisfied.

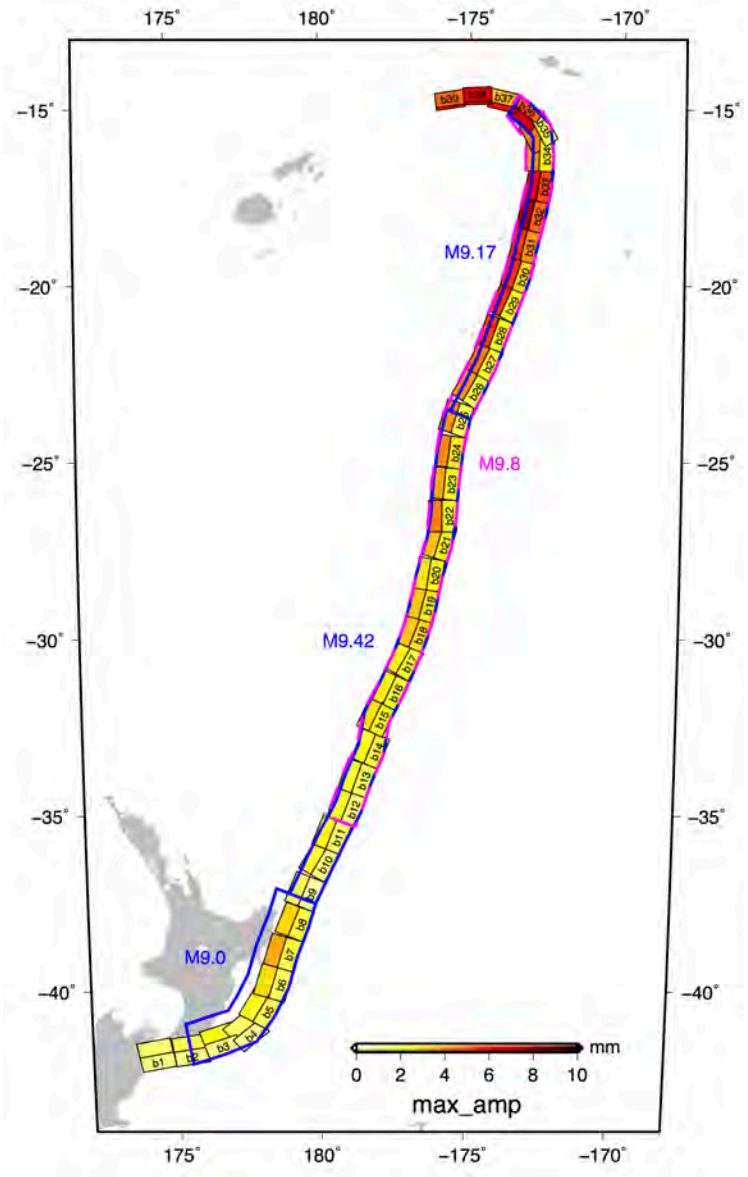

Figure 2.1.5.8-1: The rupture segments of Berryman et al. (2013 [GEM13]; blue polygons) and the KT-1 source of this report (dashed magenta polygon) overlaid on NOAA's unit sources in the Kermadec-Tonga-Samoa F-E zone. Colors represent the maximum elevation *in millimeters at the numerical tide gauge offshore of the DCPP site, from each unit source using 1 m slip.*

2.1.5.9 New Guinea F-E Zone

For the New Guinea F-E zone, RO14 proposed a maximum probable magnitude of M_w=*9.8*, which corresponds to the maximum probable magnitude proposed by RO14. The GEM13 report suggests two rupture segments with length *L=660km* and *L=600km* (Figure 2.1.5.9-1), whereas MC08 suggests a single rupture segment of length *L=1030km*. To accommodate a magnitude M_w=*9.8* earthquake, we propose two sources: the first utilizes all the New Guinea Seismic Zone (NGSZ) unit sources (1–15), including the ones along the Manokwari Trench (see Milsom et al., 1992; Okal, 1999); the second utilizes only the unit sources along the New Guinea Trench (1-12). Due to the limited rupture size of both sources, the required slip to reach M_w=*9.8* is extremely high (u_{av}=*120m* and u_{av}=*150m,* respectively).

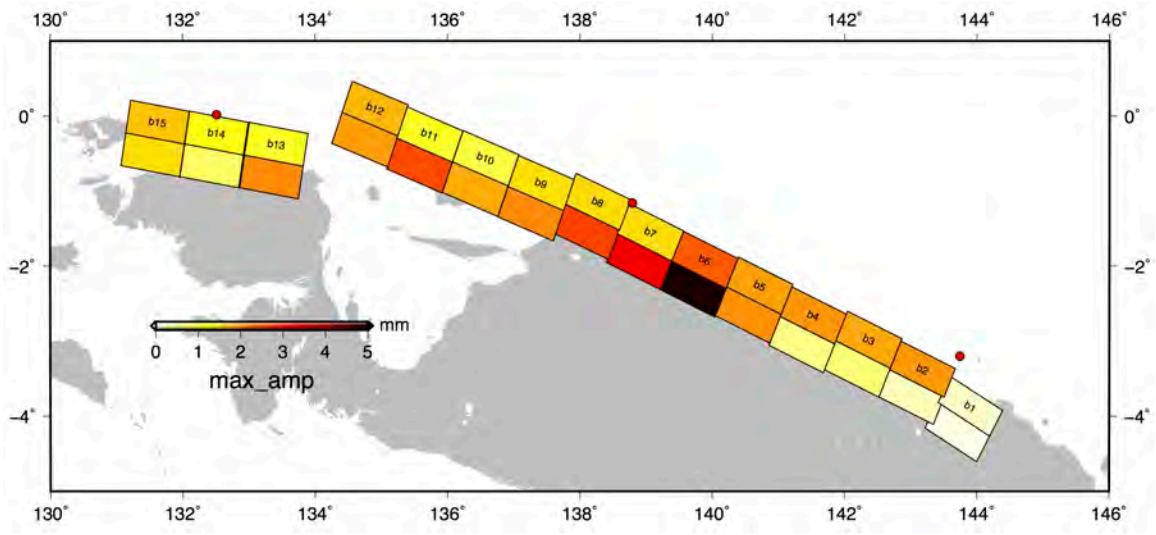

Figure 2.1.5.9-1: NOAA's unit sources in the New Guinea F-E zone; the segment endpoints of Berryman et al. (2013) [GEM13] are shown with the red dots. Colors represent the maximum elevation *in millimeters at the numerical tide gauge offshore of the DCPP site, from each unit source, using 1 m slip.*

2.1.5.10 Japan-Ryukyu F-E Zone

For the Japan-Ryukyu F-E zone, the proposed source has M_w=*9.6*, which corresponds to the maximum probable magnitude proposed by RO14. The length, width, and slip magnitude of the source are *L=1800km*, *W=100km,* and u_{av}=*63m,* respectively (Figure 2.1.5.10-1). The rupture length and width are taken from MC08 and GEM13, and the average slip is determined such that the specified magnitude is satisfied.

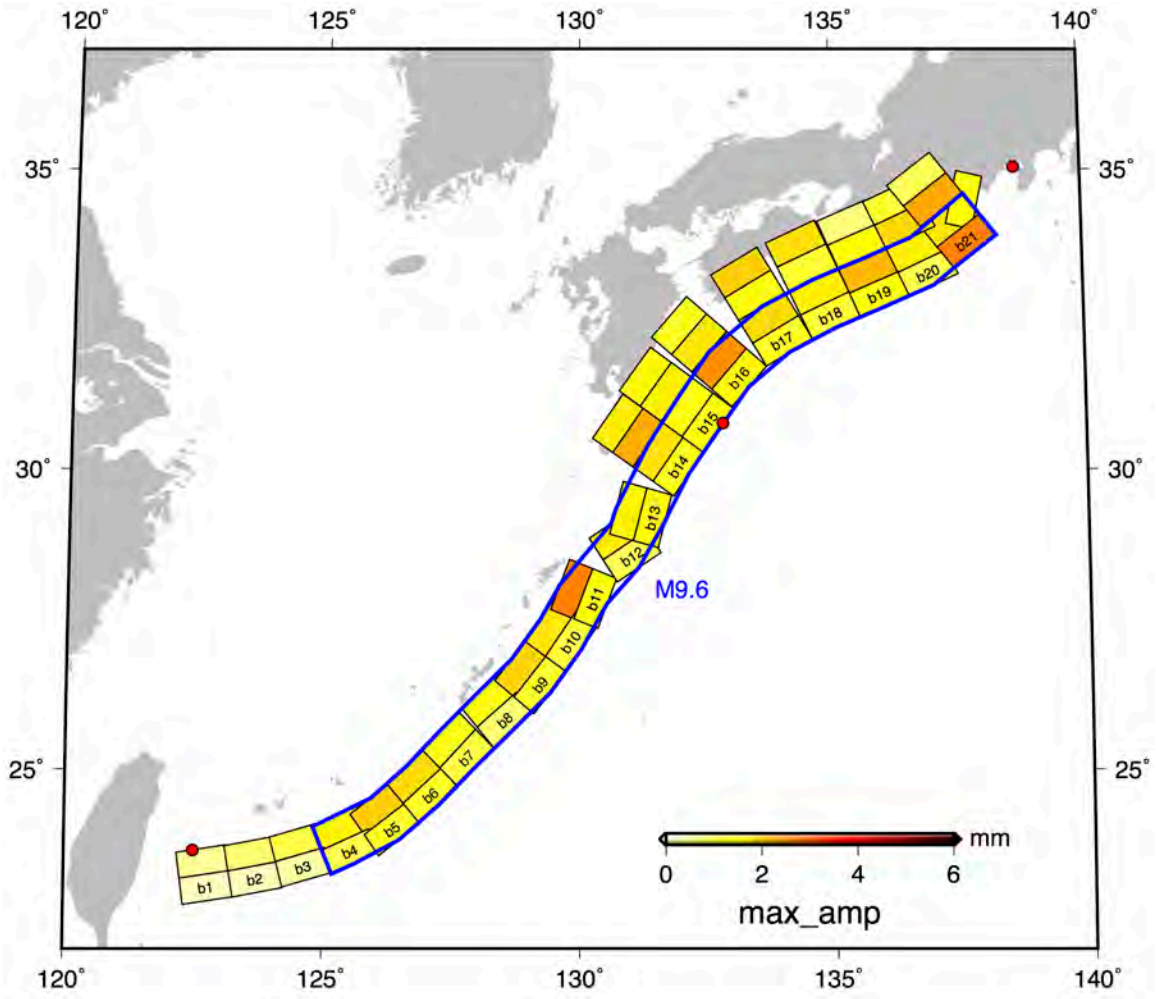

Figure 2.1.5.10-1: NOAA's unit sources in the Japan-Ryukyu F-E zone; the segment endpoints of Berryman et al. (2013) [GEM13] are shown with the red dots and the RN-1 source is outlined with the blue polygon. Colors represent the maximum elevation *in millimeters at the numerical tide gauge offshore of the DCPP site, from each unit source, using 1 m slip.*

2.1.5.11 Guam-Japan F-E Zone

For the Guam-Japan F-E zone, we develop two sources, GJ-1 and GJ-2, which characterize rupture along the southern and northern part of this F-E zone, respectively. The proposed sources have M_w=*9.6*, which corresponds to the maximum probable magnitude proposed by RO14. The length, width, and slip magnitude for both sources are *L=1800km*, *W=100km,* and u_{av}=*63m,* respectively (Figure 2.1.5.11-1). The rupture length and width are taken from MC08 and GEM13, and the average slip is determined such that the specified magnitude is satisfied.

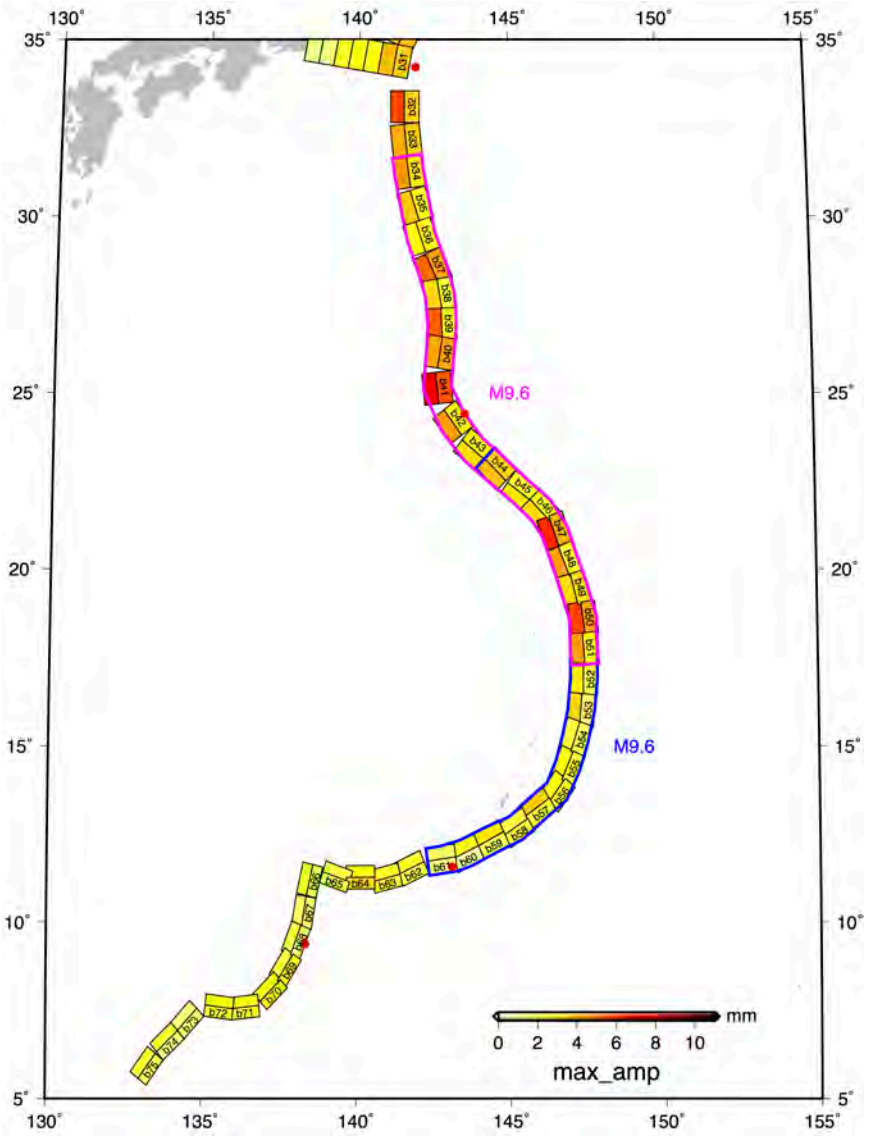

Figure 2.1.5.11-1: NOAA's unit sources in the Guam-Japan F-E zone; the segment endpoints of Berryman et al. (2013) [GEM13] are shown with the red dots and the GJ-1 and GJ-2 sources are outlined with the blue and magenta polygons. Colors represent the maximum elevation *in millimeters at the numerical tide gauge offshore of the DCPP site, from each unit source, using 1 m slip.*

2.1.5.12 Kamchatka-Japan F-E Zone

For the Kamchatka-Japan region, we develop two sources, JK-1 and JK-2, which characterize rupture along the southern and northern part of this F-E zone, respectively. The proposed sources are assigned M_w=*9.7*, which corresponds to the maximum magnitude proposed by GEM13. The length, width, and slip magnitude for the sources are *L=2200km*, *W=100km,* and u_{av}=*77m* for JK-1 and *L=1500km*, *W=150km,* and u_{av}=*59.5m* for JK-2 (Figure 2.1.5.12-1). The rupture length and width are taken from MC08 and GEM13, and the average slip is determined such that the specified magnitude is satisfied.

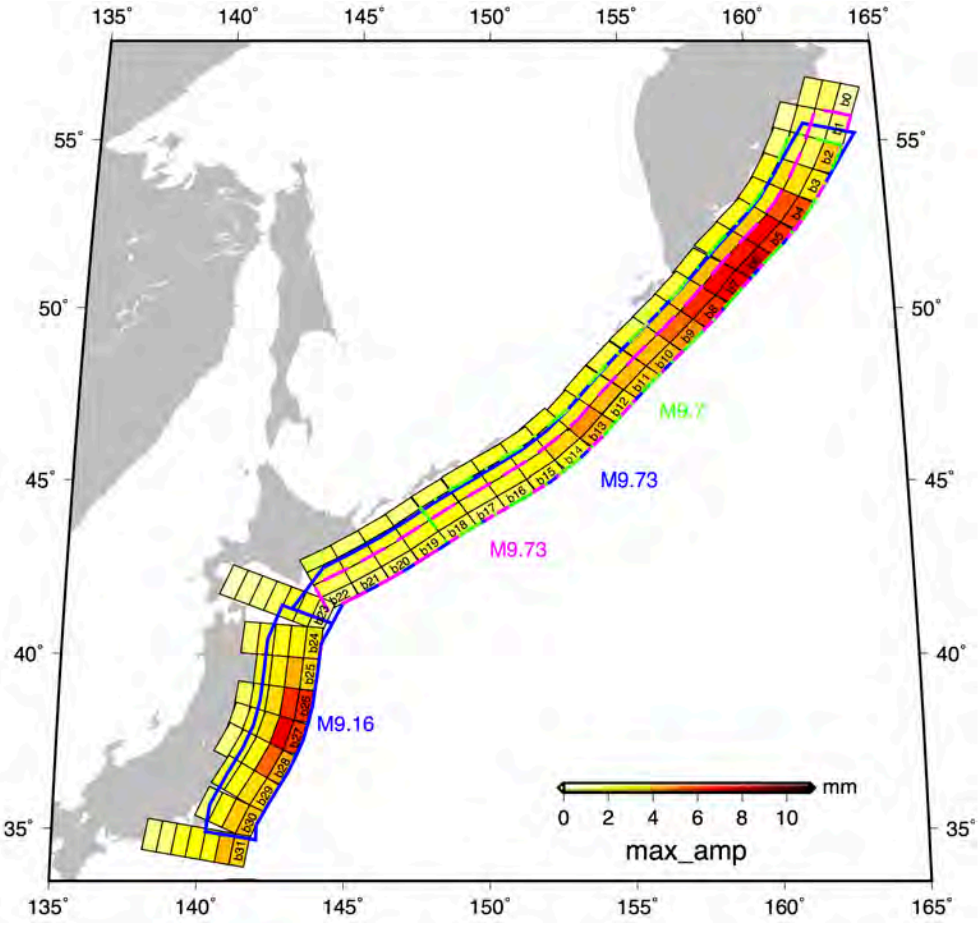

Figure 2.1.5.12-1: Berryman et al.'s (2013) [GEM13] segments (blue polygons) and the sources of this report (JK-1 with dashed magenta and JK-2 with dashed green polygons) are overlaid on NOAA's unit sources in the Kamchatka and Japan *F-E zones. Colors represent the maximum* elevation *in millimeters at the numerical tide gauge offshore of the DCPP site, from each unit source, using 1 m slip.*

2.1.6 Submarine Landslides

Information Submitted by the Licensee

The FHRR provides details for a number of local submarine landslides (PG&E, 2016). Based on that information, the FHRR identified and considered two different submarine

landslide sources, one in relatively shallow water (based on the Goleta submarine landslide) and another in deep water (based on the Big Sur submarine landslide) hypothetically placed offshore of the DCPP site. The data used to characterize these landslide sources, as well as the bathymetry and topography utilized in the FHRR modeling, are publically available. Taylor Engineering used the same information for its analyses described below.

Taylor Engineering Technical Evaluation

The coastal area offshore of California was mapped during the GLORIA mapping project (USGS, 2015a) that was part of an effort to create an Exclusive Economic Zone. This Exclusive Economic Zone effort was initiated by President Reagan in 1983 and included extensive geophysical data gathering up to 200 nautical miles offshore of all U.S. coastlines. The product of the GLORIA effort includes continuous data of the seafloor and shallow seismic structures. The resolution with which bathymetric features are imaged varies spatially due to a broadly varying quality of the return signal, but the overall horizontal resolution of the products is 250 m (Paskevich et al., 2011). The imagery gathered in the GLORIA effort is, for the vast majority of the California coast, the most detailed information that exists about the near and offshore bathymetric features, including the evidence of submarine mass failures. However, the varying resolution presents a challenge to consistently search for evidence of submarine mass failures and then quantify the extent of the runout masses, volumes, and location of headscarps.

With the above imprecision noted, slide volumes can be estimated with the GLORIA data. McAdoo et al. (2000) employed the data collected by the GLORIA mapping project the coasts of Oregon, California, Gulf of Mexico, and New Jersey/Maryland. Table 2.1.6-1 contains 25 submarine landslides considered in McAdoo et al. (2000) that are located between 40.41°N and 36.24°N; note however that this table excludes the slides in the Santa Barbara Channel in southern California.

Most of the mass failures visible in the GLORIA data are related to the submarine canyon systems that form very prominent features offshore of California. These canyons pass through large portions of the shelf and continental slope and provide very efficient pathways for sediment transport from the nearshore to the deep sea. The efficient pathways can be seen as one of the reasons why the North America west coast has relatively fewer observed submarine mass failures than the more-tectonically passive margin of the east coast. As mentioned earlier, the volume estimates by McAdoo et al. (2000) potentially carry a significant error because they are based on volume estimates of the runout masses from the GLORIA imagery with questionable resolution. It is likely that smaller slides have a large volume error estimates due to poor resolution, while the volumes for the larger slides may be overestimated due to the fact they form large aprons that are very difficult to identify in the imagery. The trigger mechanism for most of the slides is most likely small tectonic earthquakes, which are very frequent due to the geodynamic position of California in the Ring of Fire along the Pacific Rim. An alternative trigger mechanism for those mass failures on flanks of the submarine canyons could be over steepening of the slope due to canyon-bottom erosion during events of large sediment bypass and erosion in the submarine canyons.

Table 2.1.6-1: Documented Mass Failures along the California Coast (from McAdoo et al., 2000).

Longitude	Latitude	Estimated Volume [km^3]
40.41	124.89	3.2
40.01	124.93	0.6
39.96	124.92	0.2
39.73	124.66	4.3
39.73	124.97	10.0
39.71	124.58	2.4
39.66	124.21	4.5
39.69	124.47	2.6
39.68	124.77	0.3
39.67	124.86	0.7
39.26	124.26	3.2
39.25	124.37	0.9
38.89	124.17	1.0
38.89	124.13	3.0
38.88	124.09	0.7
38.69	123.89	1.4
38.00	123.77	4.6
37.75	123.55	3.7
37.70	123.54	1.2
37.33	123.32	1.2
37.14	123.32	6.2
36.99	122.76	0.1
36.71	122.85	8.0
36.52	122.44	6.2
36.24	122.45	18.2

A probabilistic model was developed by Watts (2004) to predict the tsunamis generated by submarine mass failures off the coast of southern California. The model employed simple probability distributions (Uniform or Poisson) of the parameters that control tsunami generation. The model used a simple mass failure assessment, which includes slides and slumps as two distinct end members of a continuous spectrum of submarine mass failure. The tsunami generation model used in the Watts (2004) analysis is the two-dimensional and three-dimensional boundary element model which features fully non-linear boundary conditions, complete dispersion of resolvable waves, and second order updating of free surface position (Grilli and Watts, 1999; Grilli and Watts, 2001; Grilli et al., 2002). Two and three-dimensional tsunami amplitude curve fits were used to produce rapid case studies and tsunami hazard assessments.

In order to find a complex ensemble of slope behavior and tsunami amplitudes, Watts (2004 performed many Monte Carlo simulations of random trials. Results from the model suggest

that a submarine landslide-generated tsunami with amplitude greater than 1 m can be expected off southern California every 75 years. More importantly, the potential exists to generate local tsunami amplitudes in excess of 10 m based solely on offshore morphology.

Thus, based on the aforementioned, there is potential for large submarine landslide-generated tsunamis along the California coastline. This hazard exists throughout offshore areas in the state. For the rest of this section, individual failure areas, from Monterey Bay to southern California, which might be relevant to the tsunami hazard at the DCPP site will be looked at in detail.

2.1.6.1 Monterrey Bay (Moss Landing Failure)

On October 17, 1989, an earthquake of magnitude 7.1 resulted in deep rupture along the San Andreas Fault in the Santa Cruz Mountains of California. The earthquake caused liquefaction of the sediment under a sand spit which destroyed the Moss Landing Marine Laboratories (MLML) and damaged other structures. Greene et al (1991) used data from side-scan sonograms, high-resolution seismic reflection, and bathymetric profiles to study the movement of sediment toward and into the head of the submarine canyon after the earthquake event. Several lobate features were identified, but all of them were subsequently destroyed by winter storms. A scarp was also identified along one track line west of the MLML. Along the north wall of the canyon, large slumps were identified that appeared to have failed due to a Pleistocene-age river channel that was exposed during erosion of the canyon. The south wall of the canyon had fresh slump scarps measuring 6.3 m formed by deltaic deposits from the Salinas River. At a depth of 12 m, liquefaction fronts were identified on the south side of the head of the canyon. This study indicates that liquefaction will occur along the Moss Landing Spit during any major earthquake ($> M_w 7$).

2.1.6.2 Monterrey Bay (Various Landslides)

McAdoo et al. (2000) characterized 83 submarine landslides at four different tectonic environments on the continental slopes of Oregon, central California, Texas, and New Jersey. A total of 25 failures were identified in California, four near the Monterey Canyon. The largest failures in California occurred in areas of active sedimentation and erosion, suggesting that sedimentation and erosion are more important controlling factors than slope. Failures in canyons offshore of California are most likely related to canyon incisions, where a landslide scar is left perched as the canyon floor is eroded. Fifteen of the 25 mapped failures in California occur on the sidewalls of the major canyons of sea-valleys. The Monterey Canyon example occurs at 36.24°N, -122.54°W. McAdoo et al. (2000) does not present a tsunami potential analysis, only mentioning that most of the landslides could have been triggered by earthquakes.

Lee (2005) presents an interpretation of submarine landslide features around the Pacific Ocean. The paper includes a description of turbidity-velocity-structure information from slide material within the Monterey Canyon. A maximum velocity of 2 m/s was estimated with flow durations of as much as eight hours. The author suggests, based on Greene et al (2006), that landslides have influenced the development of Monterey Canyon. The canyon walls are typically covered with mass wasting features. Landslides at this location have

caused the development of new meanders that have affected the opposite wall, therefore generating second-generation landslides.

2.1.6.3 Gaviota and Goleta Slides

The Santa Barbara Basin separates the southern California mainland from the Anacapa and San Miguel Islands and features five distinct submarine landslides (Figure 2.1.6.3-1). This area is tectonically complex with several major faults, such as Pitas Point (PPF in Figure 2.1.6.3-1), Red Mountain (RPF), Northern Channel (NCF), and Oak Ridge (ORF). Also marked in Figure 2.1.6.3-1 are seismic clusters (cross-hatched areas) and locations of main earthquakes (black squares). The biggest slide in the Santa Barbara Basin is the Goleta slide.

The Goleta slide complex measures 14.6 km in length with a width of 10.5 km (Greene et al., 2006), and can be seen in detail in Figure 2.1.6.3-2. Figure 2.1.6.3-3 shows stratigraphic sequences and structures of the Goleta slide. The eastern section is the biggest of the three sections. Seismic evidence shows that this segment was deposited on top of at least five earlier slide deposits (Fisher et al., 2005). Also, the western section shows evidence that earlier mass failure has taken place at this location (Fisher et al., 2005). The displaced volume of the entire Goleta slide complex total is estimated to be about 1.51 km^3 (Greene et al., 2006). It can also be considered as three major lobes with roughly the same displacement volume of 0.5 km^3 each. This complex contains remains of at least three past events that age 75,000, 130,000, and 164,000 years. The water depth of the head scarp is 150 m with most of the scarp located in much shallower water than the slides. Due to extensive geophysical exploration of hydrocarbon reservoirs in the Santa Barbara Basin, the basin bathymetry as well as shallow seismic features are very well resolved with a very small error.

Borrero et al (2001) modeled a small failure (0.2 km^3), similar to the Gaviota mudslide, and predicted runup height of about 2 m near the city of Santa Barbara. Also, a larger volume failure was modeled (4 km^3) that predicted runup height of up to 20 m, also near Santa Barbara. These events pose a moderate threat to this area and would only affect a small portion of the shoreline.

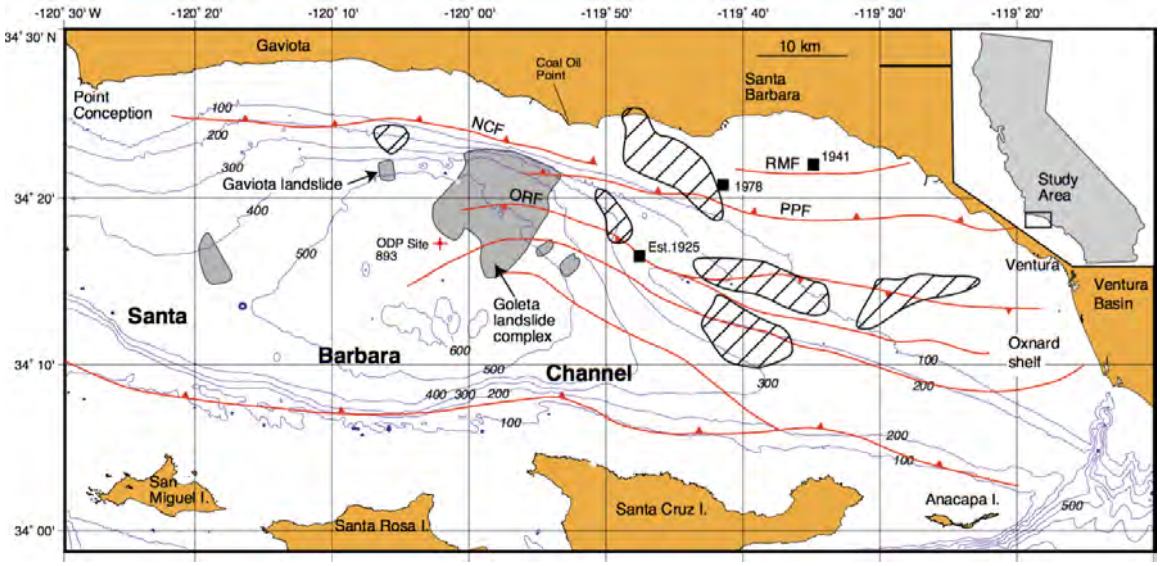

Figure 2.1.6.3-1: Map of the western Santa Barbara Basin, where submarine slides are shown as the gray shaded areas. Major fault lines are marked as red lines: RMF - Red Mountain, NCF - North Channel, and ORF - Oak Ridge. The cross-hatched areas represent seismic clusters, and the black squares are the location of main earthquakes in the Santa Barbara Basin(Fisher et al., 2005).

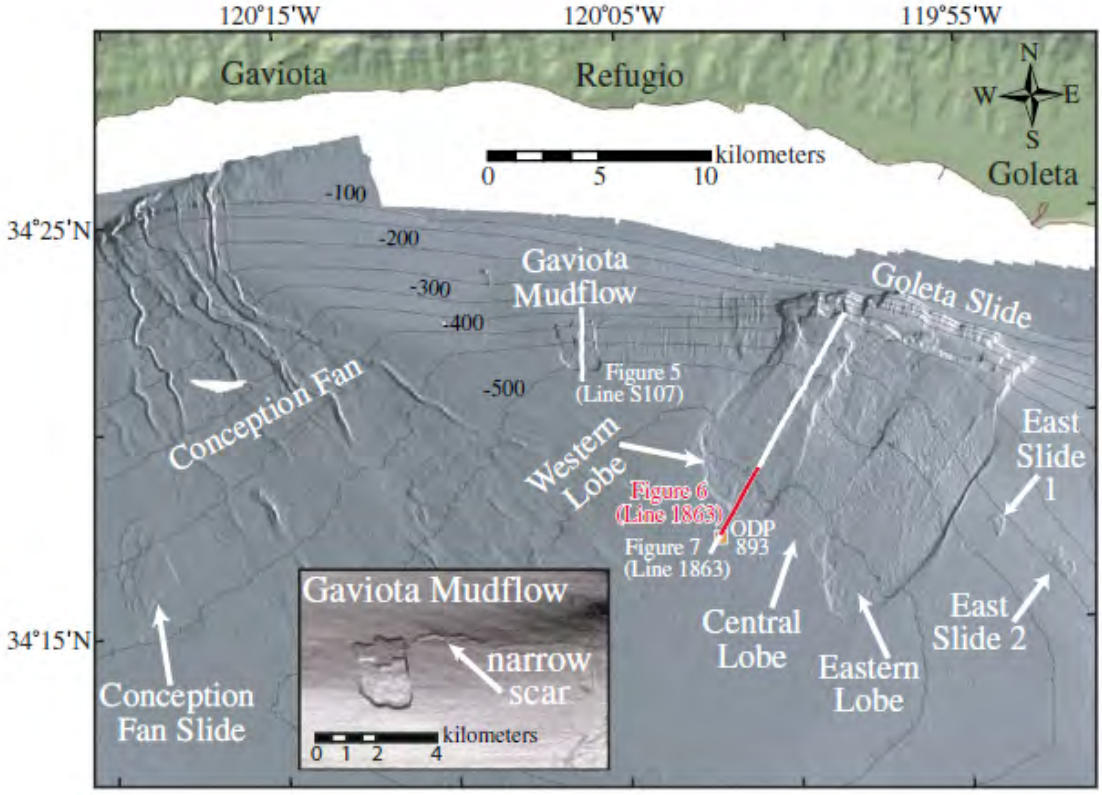

Figure 2.1.6.3-2: Multi-beam Image of Submarine Landslide Complexes in the Santa Barbara Basin (taken from Greene et al., 2006).

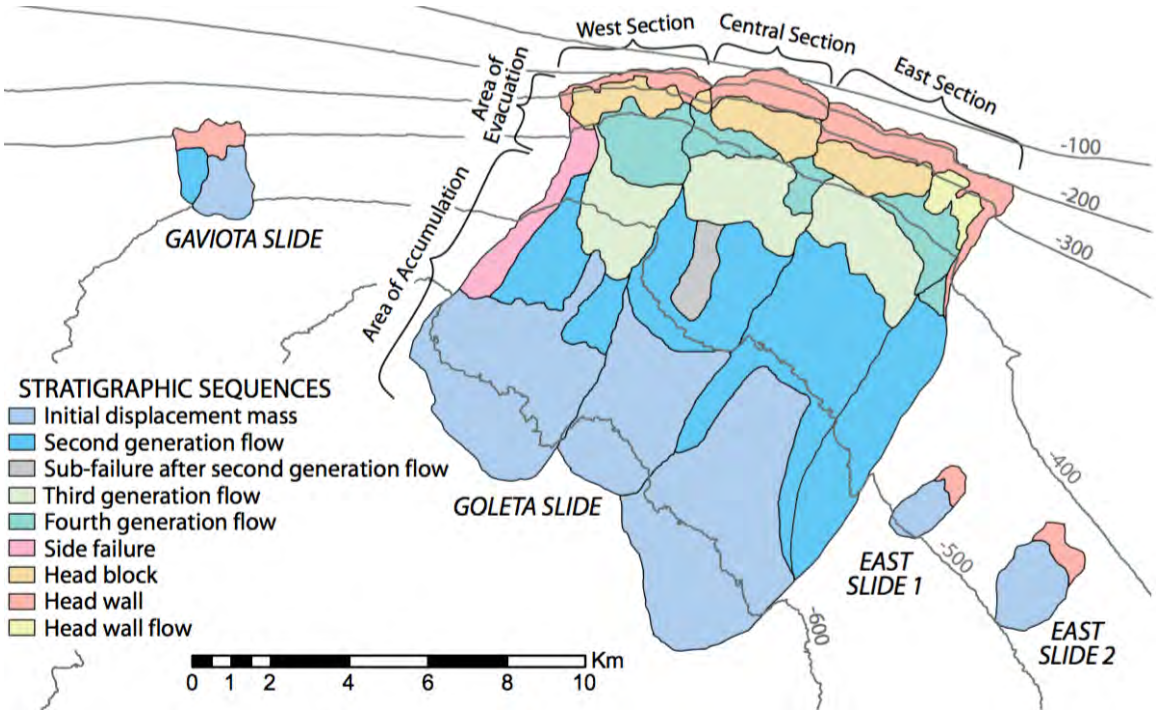

Figure 2.1.6.3-3: Identified structural components of the Goleta slide complex showing the different lobes, flows, and blocks that created the complex compound mass movement feature (Greene et al., 2006).

2.1.6.4 Santa Monica Basin

In the Santa Monica Basin, Lee et al. (2004) note two buried mass wasting deposits located near the base of the slope in the eastern part of the basin. Compared to the other failures discussed in this report, these deposits are very small. Both deposits are buried 15 to 20 m below the seafloor and have a maximum thickness of 4 m. They extend 250 to 300 m from the base of the slope to the floor of the basin. The widths are unknown since they were identified using one profile, but assuming a width of 200 m, we estimate a volume of 0.0002 km^3. The age of the slope failures are approximately 10,000 years.

2.1.6.5 San Pedro Escarpment (Palos Verdes Slide)

Bohannon and Gardner (2004) used high-resolution multi-beam sonar data with spatial resolution of 4–8 m as well as high resolution multichannel seismic data to identify submarine slope failures and active faults at the San Pedro escarpment, southwest of Long Beach, CA. The San Pedro escarpment is a 25 km-long linear basin slope located between San Pedro Sea Valley and Redondo Canyon, flanking the southwestern edge of the Palos Verdes uplift. The escarpment is oriented with slopes ranging from 11.5° to 17° between water depths of 75 to 750 m. There exists an abrupt change of slope at the base, decreasing from greater than 10 to less than 2 degrees. Bohannon and Gardner (2004) divided the

escarpment into two sections: the southeastern part or sea valley segment (SVS) and the northwestern part or Redondo segment (RS). The SVS is eroded back 0.5 km compared to RS and is considered an area with submarine landslide features (Hampton et al. 1996 and Hampton et al. 2002).

According to Bohannon and Gardner (2004), the RS segment has higher potential for future failure since most of its slope material is still in place, while the SVS is a region where a large amount of slope material has been removed by submarine landslides. For this particular area, an earthquake magnitude of M_w7 may be needed to trigger a slide (Locat et al. 2004). There are limited data presented in the study concerning the RS segment.

The Palos Verdes slide (PVS), shown in Figure 2.1.6-4, separates the two sections and is the largest individual failure scar in the area. The data noted here are taken from Bohannon and Gardner (2004). The PVS extends from the shelf break at about 70 m depth to the base of the basin slope at depth of 780 m. The area is 2-km wide at its base and 4.6-km long. The floor includes large blocks up to 4 m high and 200 m in horizontal dimension. The volume of the PVS, or material removed during the slide, is between 0.34 to 0.72 km^3. The floor of the channel is littered with debris avalanche blocks and reflects a similar volume to the PVS. The age of the PVS debris avalanche deposit was calculated to be 7,500 years old (Normak et al., 2004). It is not known if these failures resulted in a tsunami. A tsunami elevation estimate of 8 to 12 m along the Palos Verdes coastline was predicted by Bohannon and Gardner (2004) based on simplistic modeling.

Locat et al. (2004) also analyzed the failure and post-failure stages of the PVS. According to Locat et al. (2004), depths at the toe of the slope vary from 400 to 800 m and the slope angle varies from 10-17 degrees. The debris avalanche traveled and spread over a distance of 8 km leaving deposits 10-15 m thick. For the PVS failure stage analysis, Locat et al. (2004) suggest that the slide could have been triggered by an earthquake of M_w7 or more and that the geometry of the slide mass can be described by a width of 1,000 m and a thickness from 40 to 80 m.

Seismic and multibeam surveys were used for geomorphological analysis in Locat et al. (2004). The slope stability package, SlopeW, was used to assess the limit equilibrium state of the slope under ambient and seismic loading. Mohr-Coulomb failure criterion was used to predict material failure behavior and BING, a one dimensional flow dynamics model, was used for post-failure analysis of the mass. Finally, the calculation of the tsunami wave was based on a one-dimensional approximation proposed by Murty (1979). The result of the Locat et al. (2004) analysis indicates that this submarine landslide could have triggered a significant tsunami wave height of 10 to 50 m near Palos Verdes. This large range in the estimation is due to uncertainty in the initial acceleration phase; this study noted the importance of the initial acceleration for the estimation of tsunami waves generated by submarine landslides.

Borrero et al. (2004) studied and modeled several scenarios as potential tsunami sources for the Southern California Bight to estimate coastal runup. In this study, they considered

three tsunami sources, including PVS. The tsunami amplitude from Bohannon and Gardner (2004) analysis was used to initiate the simulation and the shape was derived based on empirical relations from Raichlen and Synolakis (2003) and Synolakis (2003). The numerical model MOST was used to calculate tsunami propagation and runup. Runup heights ranged from 0.6 to 5.5 m along the steep cliffs of the Palos Verdes Peninsula.

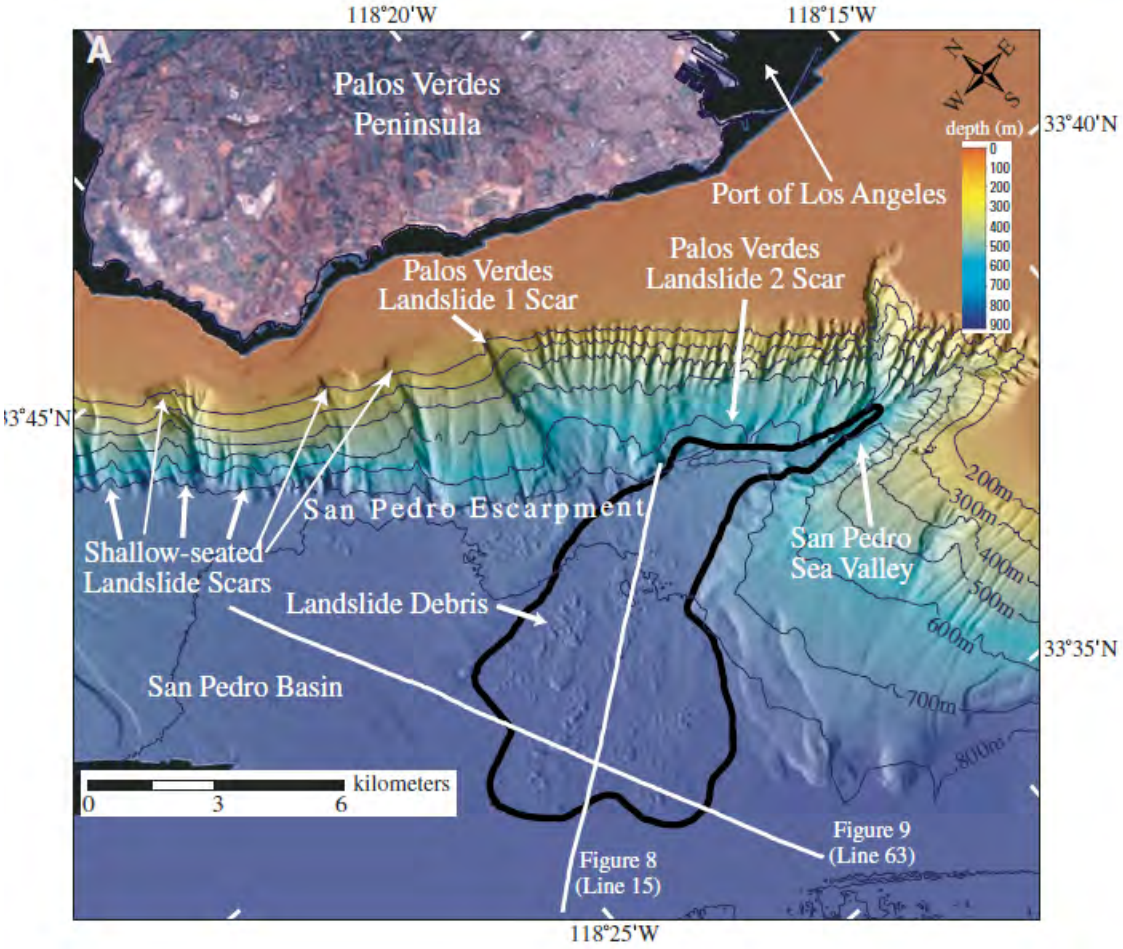

Figure 2.1.6-4. The San Pedro escarpment and the Palos Verdes debris avalanche. Taken from Borrero et al. (2004).

2.1.6.6 Thirtymile and Fortymile Banks Slides

Legg and Kamerling (2003) present a discussion of two examples of large-scale basement-involved submarine landslides offshore of southern California. Data from hydrographic soundings, multibeam swath bathymetry, and side-scan sonar systems were used to study and identify the submarine landslides. The first example is the Thirtymile Bank, which is a northwest trending ridge of Catalina Schist, mantled with Miocene volcanic and sedimentary rock. Catalina Schist and volcanic rocks provide well-defined slip surfaces for large-scale submarine landslides. The Catalina Schist basement complex is composed of rocks that are very weak and prone to failure; this statement is supported by evidence of the numerous subaerial landslides mapped around Thirtymile Bank, including the

Fisherman Cove slide (Bailey, 1941; Rowland, 1984; Cann, 1985; Francis et al. 1998). The Fisherman Cove slide on Santa Catalina Island is 1.7 km long, 0.65 km wide, with maximum thickness of 60 m and slope angle of 11 degrees (Cann, 1985). Due to the similarities in rock types, stratigraphy, and structures, areas between Thirtymile Bank and Santa Catalina Island are also likely prone to failure.

The Thirtymile Bank escarpment is six kilometers long and three kilometers wide. In cross-section there appears to be 3 to 5 individual blocks separated by normal faults. The largest block in this complex is almost equilateral with sides about 3.5 km. This block covers an area of about 3 km^2 and has a variable thickness from 350 m to 600 m. The failure mechanism for this slide appears to be composite with slumping. Also, a rock mass buried by La Jolla fan turbidities imply an age of more than 2 million years. Other slide blocks are still on the escarpment and may be 100,000 years old.

Another large potential submarine landslide was identified between the Fortymile Bank and the North San Clemente Basin. At this location, north-northwest trending blocks of 7-8 km long by 4-5 km wide material appear to be displaced laterally about 5 km from the steep arcuate-shape escarpment near the crest of the bank. The Fortymile Bank slide block is about 5-10 km^3 and is of similar scale to the slump that generated the 1998 Papua New Guinea tsunami. Seafloor samples from the Fortymile Bank are comparable to the ones from the Thirtymile Bank. Based on the data, Legg and Kamerling (2003) suggest that both slumping and sliding may have occurred at this location. An estimated vertical drop of 500-600 m was calculated. Using the late Quaternary hemipelagic sedimentation rate for this area, the submarine landslide age was calculated to be less than 1 million years old.

Estimates of the maximum tsunami wave height from these slides are presented by modeling the Fortymile submarine landslide as both rotational and translational landslides (Von Huene et al., 2004). The Fortymile submarine landslide was considered in Von Huene et al. (2004), to the west of San Diego. Dimensions used were 7 km wide, 5 km initial length, 650 m initial water depth, and 200 m initial failure thickness. For the rotational slump model, Von Huene et al. (2004) calculated an initial offshore tsunami wave height of 7 to 9 m, considerably lower than the 50 m offshore wave height found with the transitional slide model.

2.1.7 Seismic Seiches

Information Submitted by the Licensee
The FHRR does not discuss seismic seiches (PG&E, 2016).

Taylor Engineering Technical Evaluation
Seismic seiches are fundamentally a different type of wave than tsunamis. Rather than being impulsively generated by displacement of the seafloor, seismic seiches occur from resonance of seismic surface waves (continental Rayleigh and Love waves) within enclosed or semi-enclosed bodies of water. The harmonic periods of the oscillation are dependent on the dimensions and geometry of the body of water. In 1964, seiches were set up from seismic surface waves emanating from the M_w9.2 Gulf of Alaska earthquake. The

efficiency at which the seiches occurred at great distance from the earthquake is primarily explained by amplification of surface wave motion from the thick sedimentary sections (McGarr, 1965). As the magnitude of the 1964 earthquake is close to the maximum possible for that subduction zone (Bird and Kagan, 2004), it is likely that the historical observations of 1964 seiche wave heights, as high as 1.8 m, are the maximum possible. Such heights are much less than the PMT elevations at the DCPP site.

2.1.8 Conclusions

In summary, we list the following findings of our analysis of potential tsunami source characteristics for the DCPP site.

- There is sufficient evidence to consider submarine landslides offshore of the site as a present-day tsunami hazard for the purpose of defining the PMT at the DCPP site.
- Parameters for maximum earthquakes and maximum submarine landslides were determined for each of the areas discussed in this section using known or inferred regional information.
- Distant landslide (flank collapse) sources from Hawaii and Alaska, seismogenic sources throughout the Pacific Rim, and local seismogenic sources may also produce tsunamis of sufficient magnitude to affect definition of the PMT.

3.0 Tsunami Analysis – Technical Approach

3.1 Tsunami Propagation Models

Information Submitted by the Licensee
The FHRR employs the Fully Nonlinear Boussinesq Model with total variation diminishing limiters (FUNWAVE-TVD) for tsunami propagation modeling (PG&E, 2016). This model was developed at the University of Delaware and is accurate for nonlinear and weakly dispersive water waves. The numerical scheme and equations solved are similar to those in the COULWAVE model used in the Taylor Engineering analysis.

Taylor Engineering Technical Evaluation
Numerical simulations of tsunami propagation have made great progress in the last 30 years, building off initial tsunami hazard mapping efforts (e.g. Houston and Garcia, 1978; Houston, 1980). The National Tsunami Hazard Mitigation Program (NTHMP) currently uses several tsunami computational models. These efforts by the NTHMP are sponsored by NOAA and aim to produce tsunami inundation and evacuation maps for the states of Alaska, California, Hawaii, Oregon, and Washington. The computational models include MOST, developed originally by researchers at the University of Southern California (Titov and Synolakis, 1998); Cornell Multi-grid Coupled Tsunami Model (COMCOT), developed at Cornell University (Liu et al., 1995); and TSUNAMI2, developed at Tohoku University in Japan (Imamura, 1996). All three models solve the same depth-integrated and 2D horizontal (2HD) nonlinear shallow-water (NSW) equations with different finite-difference algorithms. There are a number of other tsunami models as well, including the finite element model ADvanced CIRCulation Model For Oceanic, Coastal And Estuarine

Waters (ADCIRC) (e.g., Myers and Baptista, 1995). For a given source region condition, existing models can simulate propagation of a tsunami over a long distance with sufficient accuracy, provided that accurate bathymetry data exist. Figure 3.1-1 shows the snapshots of free surface elevations (FSE) at one hour and 44 minutes after the 2004 Sumatra earthquake occurred.

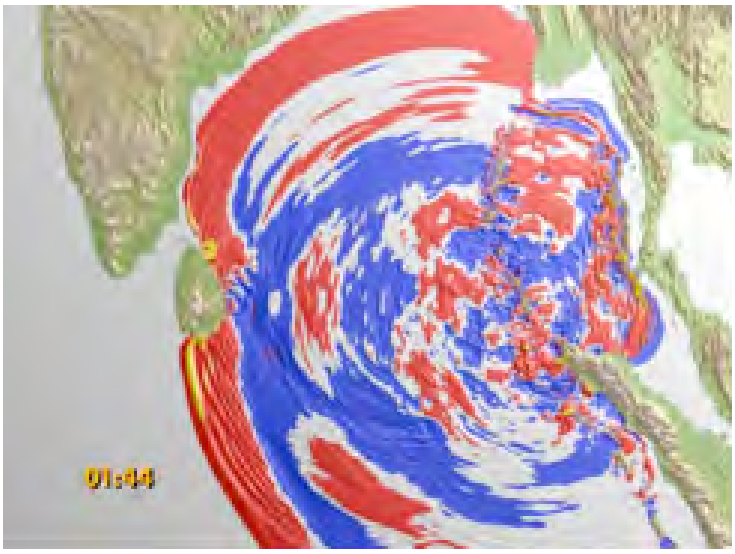

Figure 3.1-1: Snapshots of free surface elevations at one hour and forty-four minutes after the 2004 Sumatra earthquake occurred. Yellow and red colors denote positive elevation while blue denotes negative depression (numerical results based on Cornell Multi-grid Coupled tsunami (COMCOT) model, adapted from Wang and Liu, 2007).

The shallow-water equation models lack the capability of simulating dispersive waves, which could be the dominating features in submarine landslide-generated tsunamis and for tsunamis traveling a long distance. Several high-order depth-integrated wave hydrodynamics models (Boussinesq models) are now available for simulating nonlinear and weakly dispersive waves, such as Cornell University Long and Intermediate Wave Modeling Package (COULWAVE) (Lynett and Liu, 2002) and Fully Nonlinear Boussinesq Wave Model (FUNWAVE) (Kennedy et al., 2000). The major difference between the two is their treatment of moving shoreline boundaries. Lynett et al. (2003) applied COULWAVE to the 1998 Papua New Guinea tsunami with the submarine landslide source. The results agreed well with field survey data. Recently, several finite element models also have been developed based on Boussinesq-type equations (e.g., Woo and Liu, 2004). Boussinesq models require higher spatial and temporal resolutions and, therefore, are more computationally intensive. Moreover, most of model validation work was performed for open-ocean or open-coast problems. In other words, researchers have not carefully tested the models for wave propagation and oscillations in semi-enclosed regions – such as a harbor or bay – especially under resonant conditions.

Being depth-integrated and 2HD, NSW and Boussinesq models lack the capability of simulating the details of many coastal effects, such as wave overturning and the interaction between tsunamis and coastal structures, which could be either stationary or movable. At

present, these models often parameterize stationary coastal structures as bottom roughness or bottom friction. Although by adjusting the roughness and friction parameter, satisfactory results can be achieved for estimating the maximum wave runup and delineation of the inundation zone (e.g., Liu et al., 1995), these models cannot provide adequate information concerning wave forces acting on coastal structures, nor can they estimate bottom stress, which is essential in determining sediment erosion and deposition.

As a tsunami propagates into the nearshore region, the wave front undergoes a nonlinear transformation while it steepens through shoaling. If the tsunami amplitude is sufficiently large, it can break at some offshore depth and approach land as a bore – the white wall of water commonly referenced by survivors of the 2004 Indian Ocean tsunami. Wave breaking in traditional NSW tsunami models has not been handled in a satisfactory manner. Numerical dissipation is commonly used to mimic breaking, and thus results become grid dependent. Numerical dissipative approaches most notably include shock-capturing schemes. In these schemes, the local smoothness of the solution drives the numerical energy dissipation. This smoothness is strongly associated with the grid length near the shock. With shock-capturing methods, the numerical results tend to be smooth. However, the dissipation is entirely numerical, and although the general form of the dissipative terms may be of the proper physical form, the grid length and time step will inevitably affect the dissipation. In Boussinesq models, breaking must be modeled in an approximate manner owing to the fact that the depth-integrated derivation does not allow for an overturning wave. However, these breaking schemes have been validated for a wide range of nearshore conditions (e.g., Lynett, 2006).

Researchers generally use a fixed grid, finite difference or finite element method to solve these depth-integrated equations. Using a fixed grid numerical model to solve a moving boundary problem can lead to difficulties related to the loss of mass conservation and instabilities in the computations (Leendertse, 1987) as a result of imposing discrete fixed increments to the extent of wetting and drying areas (Balzano, 1998). To eliminate the difficulties related to shoreline location being locked onto a grid, Zelt (1991) used a Lagrangian model to simulate shoreline movement due to solitary wave runup. This model produced maximum runup values that compared well with experimental values, but the shape of the wave as it traveled up the slope did not compare as favorably. A handful of others have utilized Lagrangian techniques with depth-integrated equation models to simulate a moving shoreline (e.g., Gopalakrishnan, 1989; Petera and Nassehi, 1996). Another treatment of the moving boundary problem is employing a slot or permeable-seabed technique (Tao, 1983, 1984). The first application of the permeable slot with a Boussinesq-type model (Madsen et al., 1997) yielded runup errors on the order of 10% of the maximum. Modifications have been made to this permeable slot technique (Kennedy et al., 2000), increasing the accuracy, but it was also shown that the empirical coefficients that govern the technique cannot be universally determined owing to numerical stability problems (Chen et al., 2000). Lynett et al. (2002) developed an extrapolation method runup scheme, allowing for the shoreline to exist at any arbitrary location in-between grid points and negating the major drawback of using fixed grids. This method is shown to be accurate for a wide range of 1HD and 2HD problems, including the shoreline motion due to breaking and non-breaking waves (e.g., Pedrozo-Acuña et al., 2006).

Earthquake-generated tsunamis, with their long wavelengths, are ideally matched with NSW for transoceanic propagation. As described in the previous paragraphs, models such as those by Titov and Synolakis (1995) and Liu et al. (1995) have been shown to be reasonably accurate throughout the evolution of a tsunami and are in widespread use today. The numerical modeling for the earthquake sources of this report was carried out using the COMmunity Model Interface for Tsunami (ComMIT) developed by NOAA/PMEL (Titov et al. 2011). ComMIT provides a Graphic Unit Interface (GUI) which allows for the selection of model input data (initial conditions, nested bathymetric grids, and settings for the numerical computations) as well as a platform to display model output.

The base of the ComMIT system is a precomputed deep water propagation database for tsunamis generated by unit displacement on fault plane segments positioned along known and potential earthquake areas around the world's subduction zones (described in more detail in the next section). The transoceanic tsunami data of the selected and scaled sources are used as boundary conditions for a series of nested nearshore grids of increasing spatial resolution covering the coastline stretch of interest. Through the nested grids, the model propagates the tsunami waves to shore, computing wave amplitude, velocity, and overland inundation and resolving the non-linearity of the waves as they reach shallower water.

At present, the *Method Of Splitting Tsunami* (MOST) hydrodynamic model is implemented to work with the ComMIT interface. *MOST* was introduced by Titov and Synolakis (1995 and 1998). This model has been extensively validated and used for tsunami hazard assessments in the U.S. and is currently maintained and in operational use at NOAA/PMEL. Variants of the *MOST* model have been in constant use for tsunami hazard assessments in California since the mid-1990s.

MOST solves the 2+1 Nonlinear Shallow Water equations:

$$h_t + (uh)_x + (vh)_y = 0 \qquad (3.1\text{-}1)$$

$$u_t + uu_x + vu_y + gh_x = gd_x \qquad (3.1\text{-}2)$$

$$v_t + uv_x + vv_y + gh_y = gd_y \qquad (3.1\text{-}3))$$

where $h = \eta(x,y,t) + d(x,y,t)$; $\eta(x,y,t)$= *ocean surface elevation*; $d(x,y,t) =$ *undisturbed water depth* $u(x,y,t)$ and $v(x,y,t)$ are the depth averaged velocities in onshore x and long-shore y directions respectively (Titov and Synolakis, 1998).

Computations are stopped at 5 m depth in grids A and B, at which depth waves are reflected back (solid wall boundary condition is imposed). Runup and inundation computations are only performed in grid C, in which a bottom friction term is included in the momentum equations.

When examining dispersive tsunamis generated by submarine mass failures, the NSW can lead to errors (Lynett et al., 2003). The length scale of a submarine failure tends to be much less than that of an earthquake, and thus the wavelength of the created tsunami is shorter.

To correctly simulate the shorter wave phenomenon, one needs equations with excellent shallow to intermediate water properties, such as the Boussinesq equations. While Boussinesq-based models also have accuracy limitations on how deep (or short) the submarine landslide can be (Lynett and Liu, 2002), they are able to simulate the majority of tsunami-generating landslides. Thus, for the submarine landslide-generated tsunami modeling presented here, the Boussinesq-based numerical model COULWAVE (Lynett and Liu, 2002) is used. This model solves the fully nonlinear extended Boussinesq equations on a Cartesian grid. A particular advantage of the model is the use of fully nonlinear equations for both deep and shallow water. This avoids the common problem of "splitting" the analysis when the wave reaches shallow water. Applications for which COULWAVE has proven accurate include wave evolution from intermediate depths to the shoreline, including parameterized models for wave breaking and bottom friction.

COULWAVE is based on the Boussinesq-type equations, which are known to be accurate for inviscid wave propagation from fairly deep water (wavelength/depth ~2) all the way to the shoreline (Wei et al., 1995). The equation model consists of a complex set of partial differential equations that are integrated in time to solve for the FSE and the horizontal velocity vector. A fourth order Adams-Bashforth-Moulton predictor-corrector time integration scheme is required, and fourth order, centered finite differences approximate spatial derivatives. The high order scheme is required owing to the inclusion of first to third order derivatives in the model equations.

Fundamentally, the Boussinesq equations are inviscid. To accommodate frictional effects, COULWAVE includes a number of viscous submodels. The quadratic friction equation approximates bottom friction:

$$R_{BottomFriction} = f \frac{\mathbf{u}_b |\mathbf{u}_b|}{H}$$

where $\mathbf{u}_b$ is the horizontal velocity vector evaluated at the seafloor, H is the total water depth including wave elevation, and f is a bottom friction coefficient, typically in the range of 0.001 to 0.01. As noted in Lynett et al. (2002), maximum runup is sensitive to the value of f, particularly for large, breaking waves.

3.2 Source Generation and Tsunami Initial Condition Model

Information Submitted by the Licensee
The FHRR uses the Non-Hydrostatic Wave Model (NHWAVE) v.1.1 model to estimate the waves generated by submarine landslides (PG&E, 2016). This is a non-hydrostatic multi-layer model, which has been previously employed in studies of landslide-generated tsunamis. It serves a modeling purpose similar to the iSALE (Impact Simplified Arbitrary Lagrangian Eulerian hydrocode) model used in the Taylor Engineering analysis.

Taylor Engineering Technical Evaluation
There are two general categories of initial tsunami conditions in numerical models: hot-start and cold-start. In a hot-start model, there is some profile of the FSE (and/or velocity) forced at the starting time of the simulation. This profile must be taken from some other model. Alternatively, during a cold-start, all values of surface elevation and velocity are

zero and any waves must be generated by either a lateral, bottom (e.g. moving bottom due to landslide), or free surface (e.g. atmospheric pressure gradient) boundary condition. Earthquake-generated tsunami studies often use hot-start conditions. These studies assume that the seafloor deformation is impulsive (occurring over a time scale much shorter that the wave period) such that the initial free surface profile matches this deformation profile exactly, and the velocity everywhere is zero.

In order to use hot-start conditions in the propagation models, some information from a detailed model or an experimental analysis must be available. Here, for the submarine landslide-generated tsunamis, the iSALE model is used for the source region. iSALE originated from the SALE code that was developed to simulate flows of hydrodynamic materials at all speeds (Amsden et al., 1980). However, iSALE only inherited the numerical solver from the original SALE code. iSALE is successfully validated against experimental studies of hypervelocity impacts and also other hydrocodes (Pierazzo et al., 2007). iSALE solves the compressible Navier-Stokes equations and contains complex constitutive models for geophysically realistic materials.

With the hydrocode iSALE, tsunami generation during oceanic meteorite impacts has been explored (e.g., Wuennemann and Lange, 2002; Weiss et al., 2006; Weiss and Wuennemann, 2007; Wuennemann et al., 2007). Furthermore, iSALE was also used to simulate the generation of tsunami waves during submarine landslides (Weiss et al., 2009). For landslide-generated tsunami waves, laboratory experiments of the 1958 Lituya Bay rockslide and tsunami, carried out by Fritz et al. (2001), were compared with respective simulations, exhibiting an excellent match of arrival time, amplitude, and phase (Weiss et al., 2009). Model results for the Lituya Bay study are provided in Figure 3.2-1. The quality of the match provides the confidence that iSALE captures all necessary physics of the non-linear waves generated in the experiments of the 1958 Lituya Bay tsunami and is an appropriate tool for submarine landslide models presented in this study.

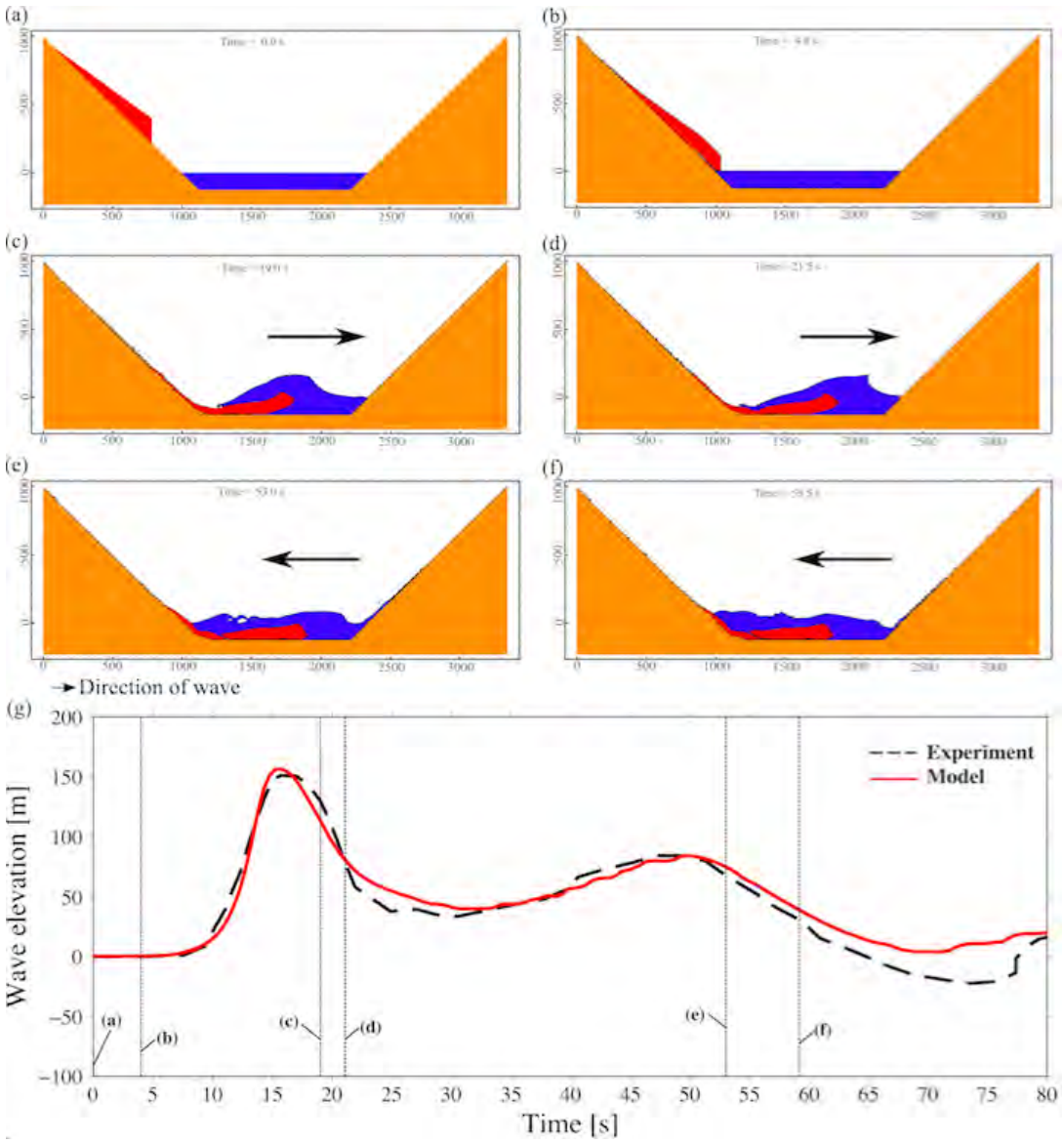

Figure 3.2-1: (a-f) Snapshots illustrating the direction of water movement associated with the maxima in the time series for the Lituya Bay study. *(g) Tsunami wave gauge record at location x=885 m. Dashed vertical lines indicate instances in (a-f). Modified from Weiss et al. (2009).*

One of the reasons that time series shown in Figure 3.2-1 match so well is the fact that the material parameters are well known because of the experiments carried out by Fritz et al. (2001). The material parameters are usually unknown. If the material parameters of the slide body are unknown, the generated tsunami wave is unconstrained. To overcome the problem of unconstrained tsunami waves, Weiss et al. (2013) suggested employing mapped runout masses of submarine landslides and choosing the material parameters of the slide body in the model in such a way that the simulated extent of the runout masses match with the observations (see Figure 3.2-2). Figure 3.2-2a depicts the bathymetry with the reconstructed pre-slide condition (slide body in red), and post-slide run out masses (in violet).

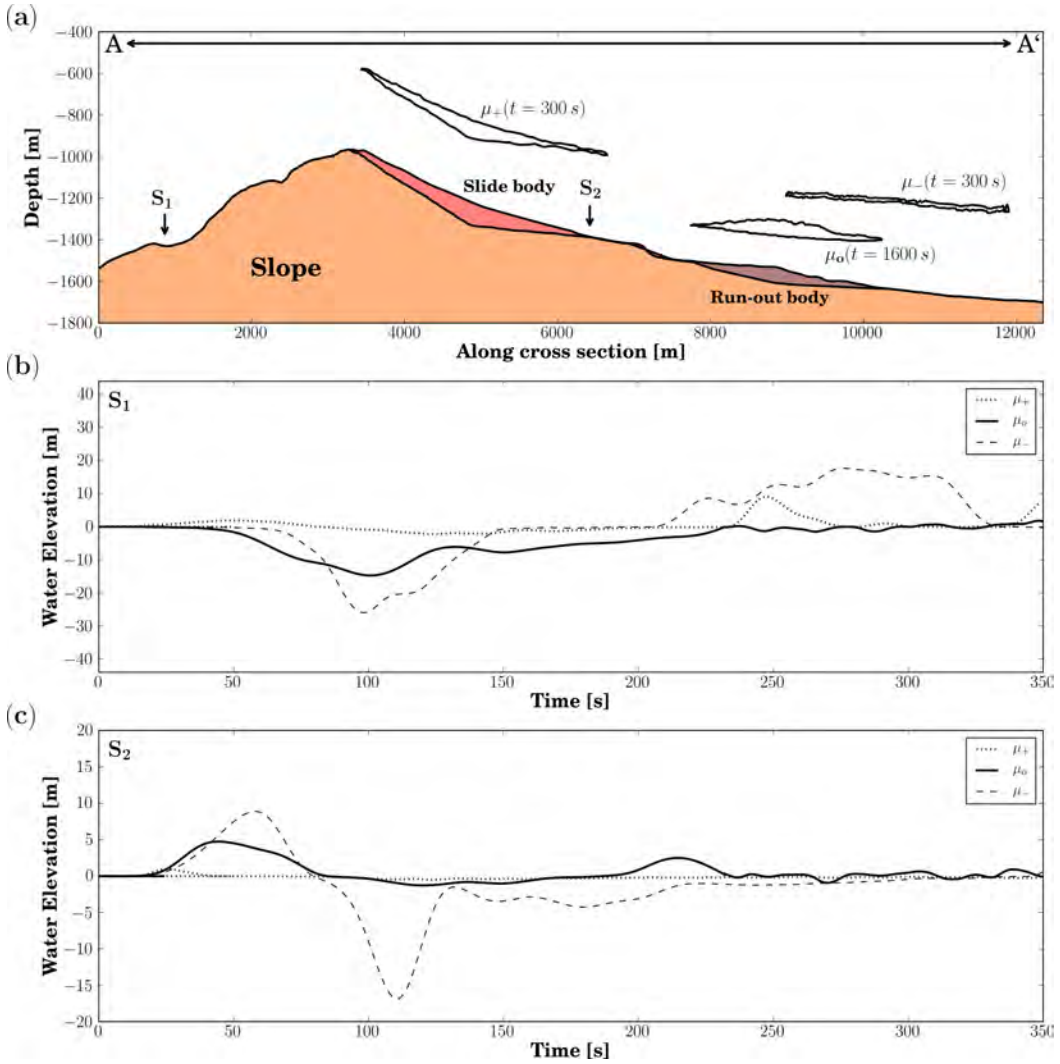

Figure 3.2-2: (a) Cross-section from A to A' from Figure (1b) (Weiss et al. [2013]) with the initial position of the slide and the location of run-out masses. Also shown are the simulated locations of slide bodies for a viscosity μ+, μ−, and μo. Simulated time series for all three slides in figure (a) are depicted for gauge location S1 in (b) and for S2 in (c). From Weiss et al. (2013).

The locations S1 and S2 correspond to the locations where the time series are shown in Figure 3.2-2b for S1 and in Figure 3.2-2c for S2. In case the viscosity of the slide body is too high (μ+), the slide body moves very little, and it moves as solid block. In Figures 3.2-2b and c, the time series for μ+ are indicated by the dotted line. If the viscosity of the slide body is too small (μ−), the slide body travels way beyond the run out masses and flows apart. The dashed line in Figures 3.2-2b and c represent the case for μ−. While the constitutive model employed in our study and in Weiss et al. (2013) can be considered as simplified, the results assuming different material parameters highlight how important the correct material parameters for the slide body are. In this study, we use the same constitutive model as in Weiss et al. (2013).

3.3. Numerical Model Error and Uncertainty

Information Submitted by the Licensee

The FHRR does not directly address error and uncertainty. However, similar to the Taylor Engineering approach, conservative estimates for various source parameters are used in the FHRR modeling studies (PG&E, 2016).

Taylor Engineering Technical Evaluation

Two main factors control model errors and uncertainties: errors in the model equations and errors in the input data. With the use of the nonlinear and dispersive Boussinesq model, we reduced model errors to a very low level while maintaining the ability to simulate the processes in a practical amount of time. Errors in the input data include bathymetry and topography errors as well as the bottom type and its associated friction. The analysis presented in this report will deal with these errors in a conservative manner. *The largest source of uncertainty in the simulation is in the representation of the tsunami initial condition, particularly for landslide sources*. For example, the specific failure behavior of the landslide governs the height of the generated wave. A fast and coherent slide may generate a very large tsunami while a slow and segmented failure may generate no detectable tsunami at all. Again, this analysis will deal with these uncertainties in a conservative manner.

3.4 Numerical Model Grid Development and Data Sources

Information Submitted by the Licensee

The FHRR describes the data sources used to generate the model grids for the tsunami hydrodynamic model (PG&E, 2016). The Taylor Engineering team relied on the same model grids for its technical evaluation.

Taylor Engineering Technical Evaluation

The bathymetry/topography grid required by the hydrodynamic model is created via two main sources: a) the GEBCO 1-minute global elevation database (Becker et al., 2009) for open ocean simulations, and b) relatively fine scale nearshore bathymetry and topography data near DCPP taken from various NOAA sources as detailed below. The shoaling effects of wave evolution over the continental shelf and slope necessitates the decrease of the spatial size of the numerical grid to accurately resolve the steepening wave profiles (non-linearity). In the finite-difference scheme employed in MOST/*ComMIT*, the shoaling effect is accounted for by using three nested grids of increasing spatial resolution. The coarsest grid (grid A) which covers the largest area has 12 arc sec resolution (≈350m), whereas the intermediate (grid B) and finest grid (grid C) have 3 arc sec (≈90m) and 1/3 arc sec (≈10m) spatial resolution, respectively (see Figure 3.4-1). The high resolution Digital Elevation Model (DEM) (grid C) for this study was obtained from the freely available database of NOAA's National Centers for Environmental Research's (NCEI) Tsunami Inundation DEMs (Friday et al., 2011). This 1/3 arc sec grid includes accurate shallow water bathymetry as well as resolution of coastal features, including the South Cove jetties, and is a standard bathymetry source for tsunami modeling applications. The intermediate grid (B) was gathered from the NOAA Coastal Relief Model (CRM), available in the NCEI

database. The 3 arc-second CRM provides the first comprehensive view of the U.S. coastal zone, integrating offshore bathymetry with land topography into a seamless representation of the coast. The coarsest grid (A) employed in this study is constructed with GEBCO data and had been used by Barberopoulou et al. (2009, 2011) to produce the tsunami inundation maps of the state of California. All the DEMs are referenced to the Mean High Water (MHW) vertical tidal datum and the World Geodetic System of 1984 (WGS 84) horizontal datum, in spherical coordinates.

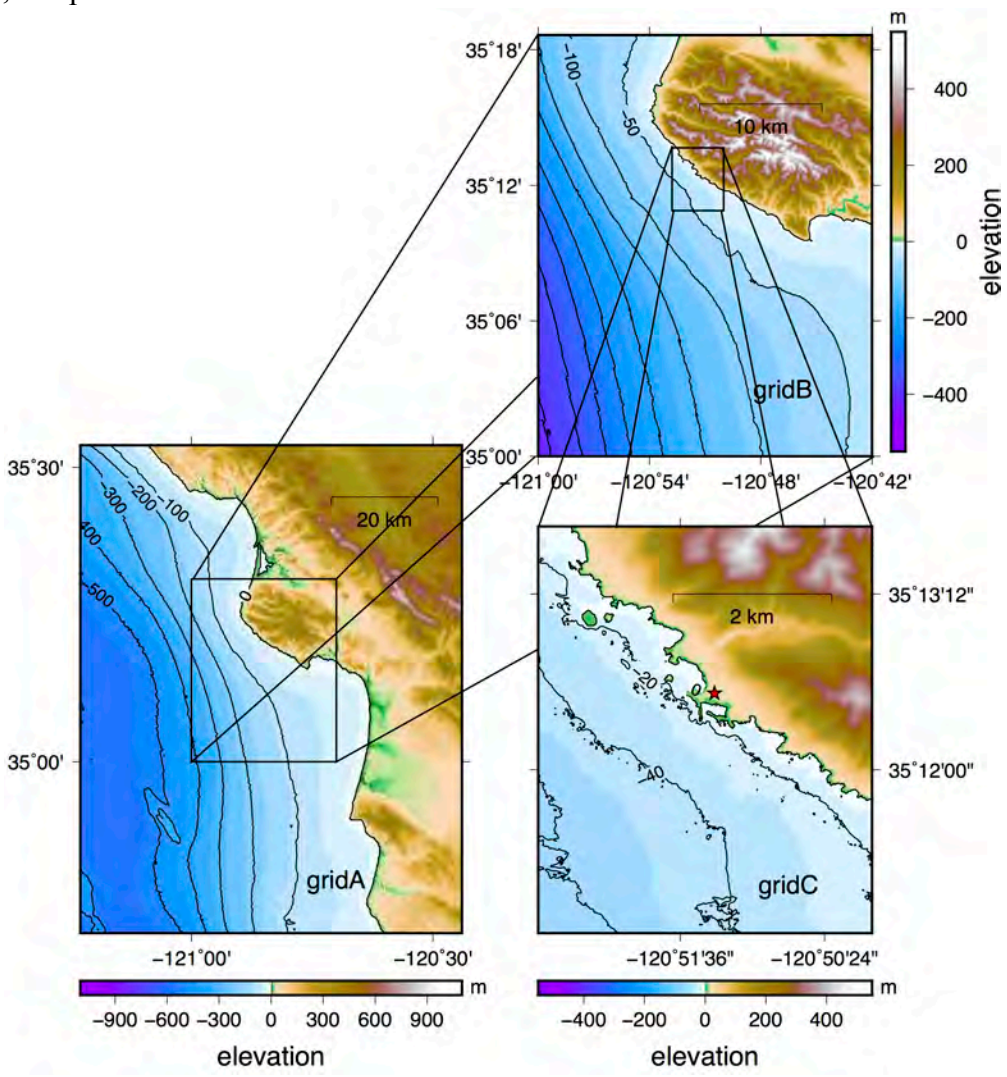

Figure 3.4-1: Nested grids of increasing resolution (grid A: 12 arc sec; grid B: 3 arc sec; grid C: 1/3 arc sec) used for the numerical computations. Location of the DCPP site is shown with red star.

3.5 Antecedent Water Levels

Information Submitted by the Licensee

The FHRR presents an antecedent water level calculated following the guidelines in NUREG/CR-6966 (NRC, 2009). The FHRR antecedent high water level is 2.13 m

(NAVD88) and the antecedent low water level is -0.58 m (NAVD88). The FHRR also presents an "Alternative High Antecedent Water Level" which uses estimates of future sea level rise instead of historical averages. This alternative high water level is 2.65 m (NAVD88). Data sources used in the FHRR are the same as those used in the Taylor Engineering water level analysis.

Taylor Engineering Technical Evaluation
Analysis of the 10% exceedance high tide was conducted for 18 years of NOAA NOS CO-OPS data at the Port San Luis, CA, tide gauge station (years 1983-2001). The 10% exceedance water level was determined to be +2.29 m (NAVD88) for these years. The long-term historical sea level rise at this station is 0.79±0.48 mm/yr according to NOAA NOS-CO-OPS data. Therefore, our estimated antecedent water level for high water predictions is 2.29 m (10% exceedance water level) + 0.05 m (40-year sea level rise accounting for design life rise) = 2.34 m (NAVD88). The 10% exceedance low tide, from analysis of the same NOAA tide data, is -0.63 m (NAVD88), and this is taken as the antecedent water level for low water predictions. Finally, it is noted that in this area, there is a difference of 0.88 m between the (NAVD88) datum and Mean Sea Level ((NAVD88) is lower).

3.6 Numerical Model Validation

Information Submitted by the Licensee
The FHRR employs the NHWAVE and FUNWAVE-TVD models for tsunami generation and propagation modeling, respectively. Scientists and engineers have used computer codes such as FUNWAVE-TVD and NHWAVE in a wide variety of tsunami studies. Appropriate references for these applications are provided in the FHRR.

Taylor Engineering Technical Evaluation
In addition to the computer codes cited in the FHRR, scientists and engineers have also used other computer codes such as iSALE, MOST, and COULWAVE in a wide variety of tsunami studies. Some of these studies include ones previously sponsored by the NRC (NUREG/CR-7222). The Taylor Engineering analysis employs the iSALE, MOST, and COULWAVE models. The following two subsections describe the primary model validation exercises.

3.6.1 Wave Breaking

In MOST, breaking is handled through a shock-capturing numerical scheme. The MOST model is able to approximately capture the evolution of a breaking bore and predicts correctly the maximum runup of broken waves (Titov and Synolakis, 1995). The COULWAVE wave breaking model utilizes the "eddy-viscosity" scheme, where an energy dissipation submodel in the momentum equation activates when the wave slope exceeds some threshold value, and continues to dissipate until the wave slope reaches some minimum value. Figure 3.6-1 shows one set of comparisons for a number of regular waves breaking and running up a slope. As can be seen, COULWAVE captures the mean values of height and water level to a high degree of accuracy.

Whereas these comparisons show that the model is capable of capturing a simplified, laboratory setup, it is also necessary to gauge the accuracy against field conditions. Researchers have compared COULWAVE with a number of field datasets; Figure 3.6-2 provides one such comparison. Here, the model captures the spectral transformation of random waves through the surf zone. Note that the breaking model uses a single set of turbulence dissipation parameters (eddy viscosity, and similar) for all trials, so there is no individual case optimization.

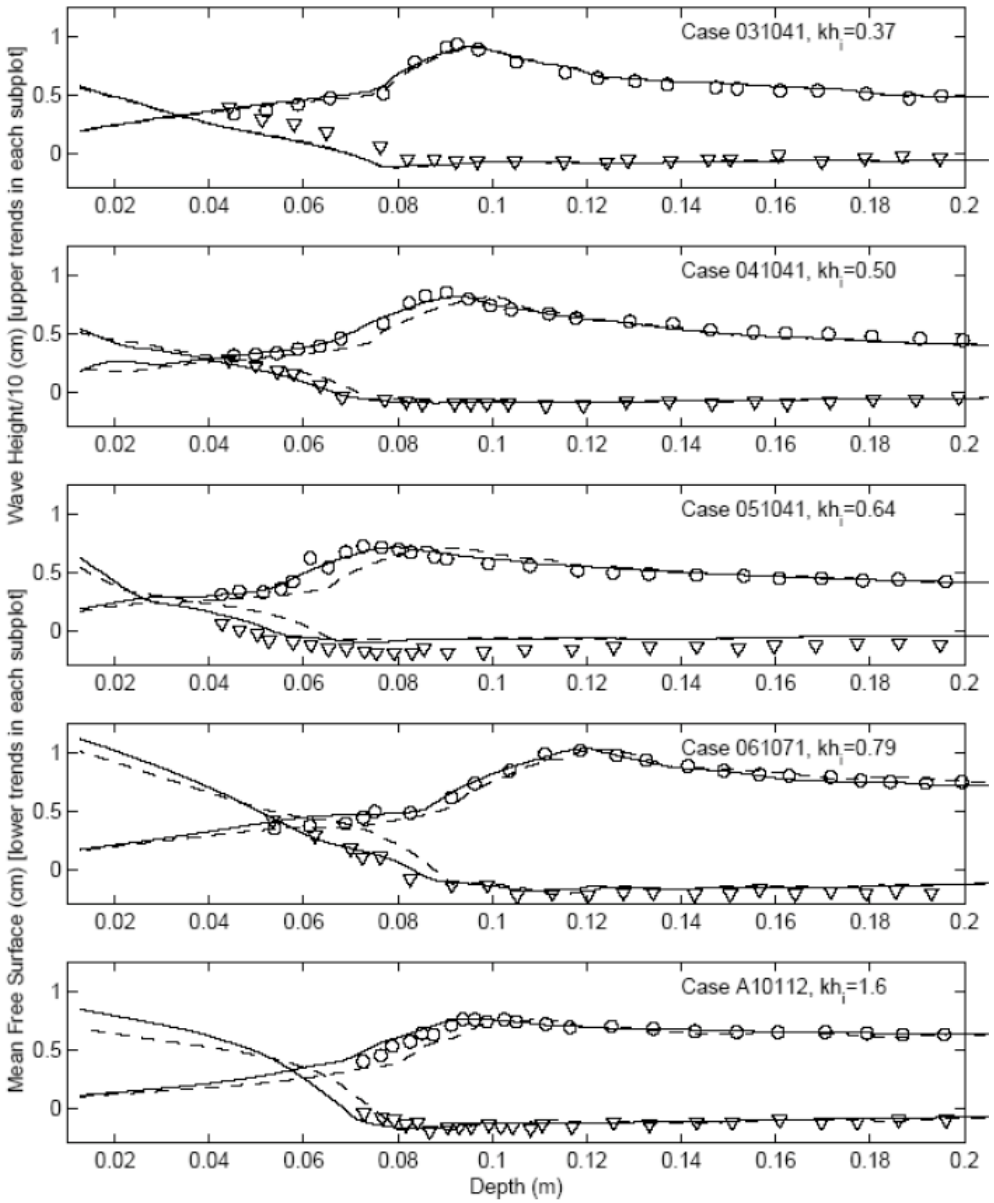

Figure 3.6-1: Wave height and mean free surface measurements from the experiments of Hansen and Svenson (1979) (symbols), the traditional Boussinesq model (dashed-line), and COULWAVE (solid line). Trials are for monochromatic waves breaking on a planar 1/20 slope.

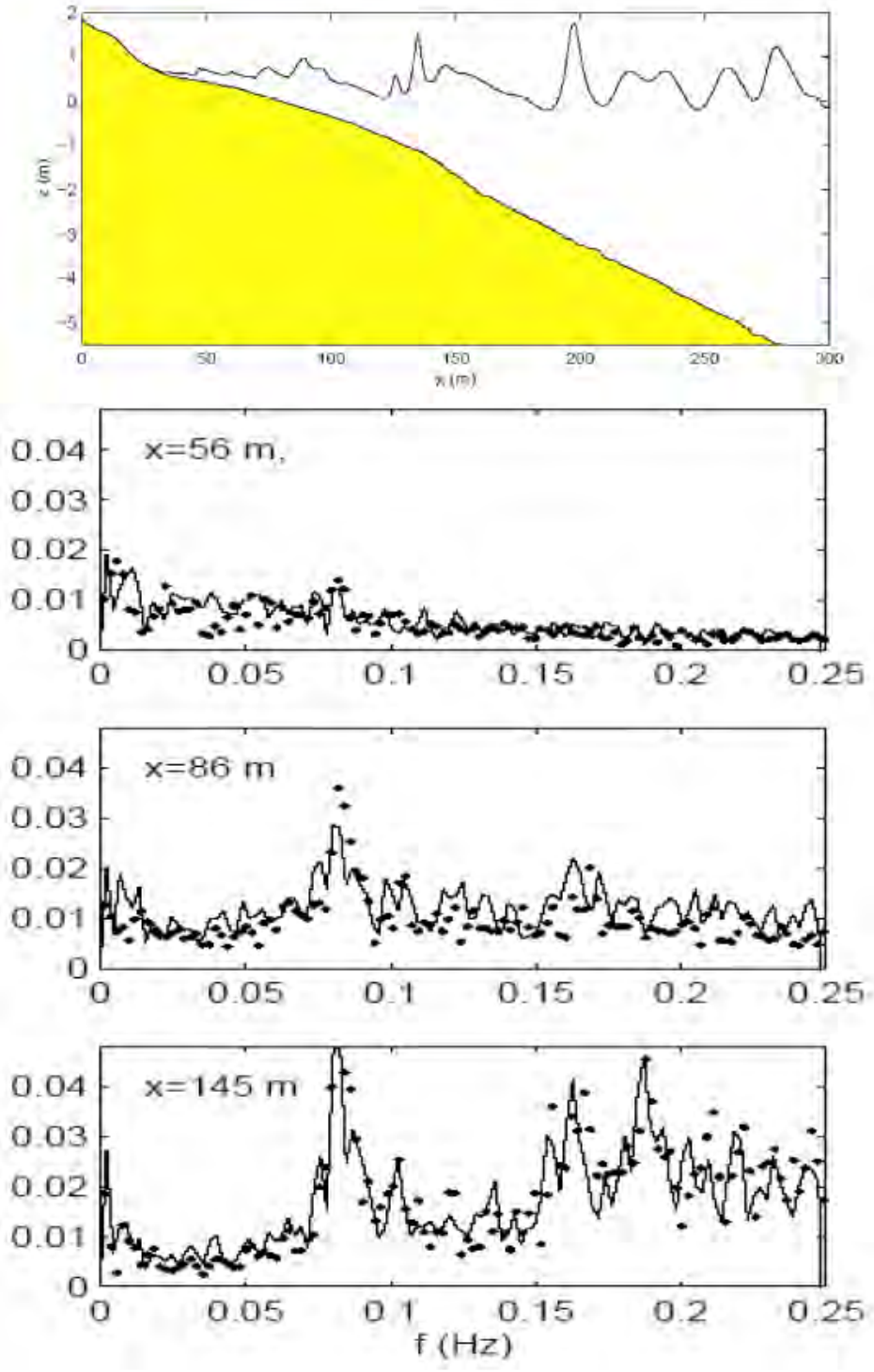

Figure 3.6-2: COULWAVE random wave comparison with field data. The lower subplots show the spectrum comparisons at three different locations. Dots are the field data from Raubenheimer (2002); solid lines are the COULWAVE results.

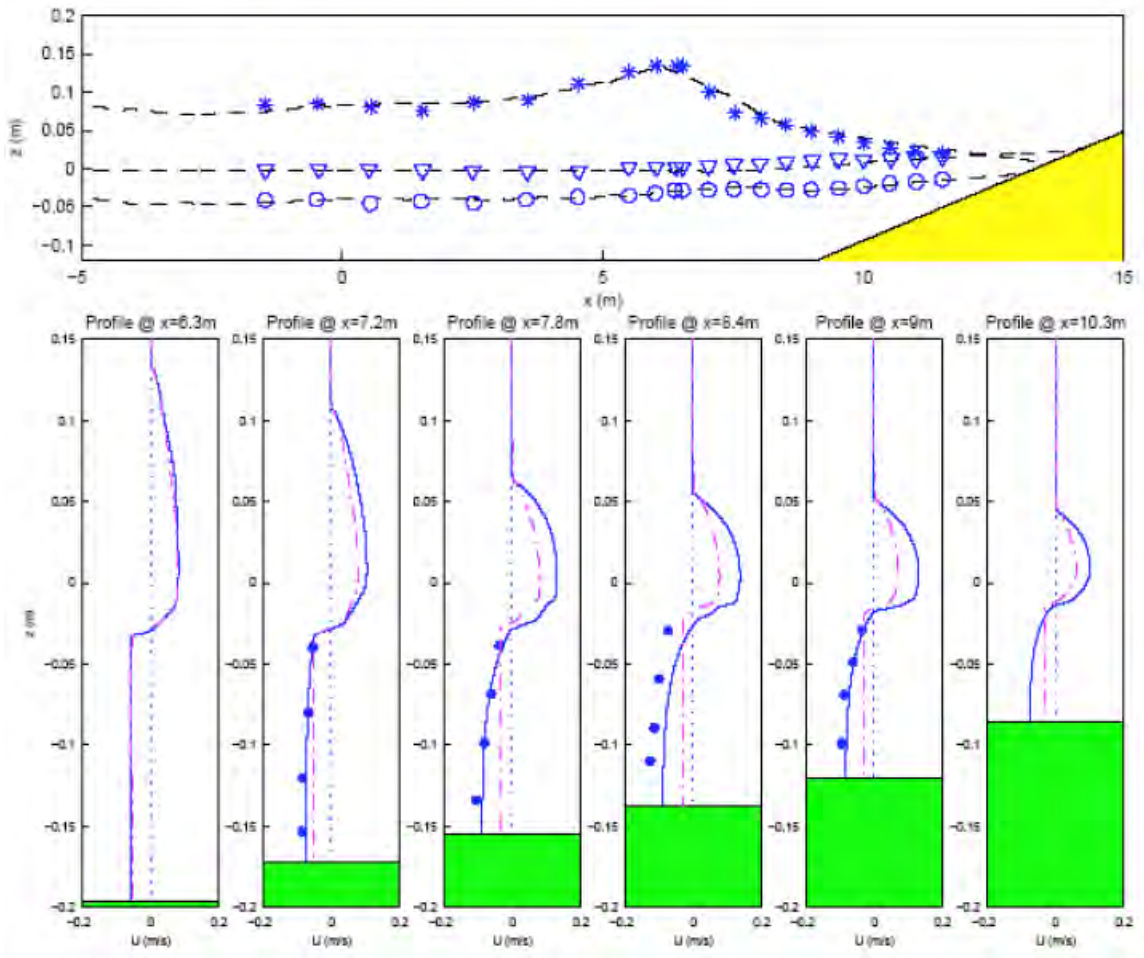

Figure 3.6-3: Comparison of numerical simulation with data of Ting and Kirby (1995) spilling breaker. The top plot shows the mean crest level (stars), mean water level (triangles), and mean trough level (circles) for the experiment, as well as the numerical simulation. The lower subplots are the time-averaged horizontal velocities, with experimental values (filled circles), COULWAVE results (solid line), and standard Boussinesq results (dashed-dotted line).

The horizontal velocity profile under breaking waves is an important component for transport-related physics in the surf zone. Using a process of superposition of velocity profiles (Lynett, 2006), instantaneous and mean profiles under breaking waves is predicted well (see Figure 3.6-3).

Studies that specifically use COULWAVE to simulate wave breaking include Lynett and Liu (2002), Lynett et al. (2003), Korycansky and Lynett (2005), Cheung et al. (2003), Lynett and Liu (2006), Lynett (2006), Lynett (2007), and Korycansky and Lynett (2007).

3.6.2 Wave Runup, Inundation, and Drawdown

The moving shoreline condition captures shoreline motion due to a wide range of wave frequencies, wave heights, and beach slopes. In COULWAVE, the shoreline algorithm was originally developed to simulate the important motion of tsunami runup (Lynett et al., 2002) and uses a variation of the so-called "extrapolation" technique. The extrapolation method has its roots in Sielecki and Wurtele (1970), with extensions by Hibberd and Peregrine (1979), Kowalik and Murty (1993), and Lynett et al. (2002). The basic idea behind this method is that the shoreline location can be extrapolated using the nearest wet points, such that its position is not required to be locked onto a fixed grid point; it can move freely to any location. The time integration uses the numerical results evaluated at the extrapolated waterline to update the solution for the next time step. This moving-boundary technique is numerically stable and does not require any artificial dissipation mechanisms.

Extensive comparisons have been made with empirical runup laws and existing experimental data for runup due to regular waves (Korycansky and Lynett, 2005). Figure 3.6-4 shows how COULWAVE compares with the so-called "Irribaren scaling for runup," an established coastal engineering relation based on deep water properties of the waves. Publications which specifically use COULWAVE for runup or the moving shoreline algorithm developed by Lynett include Lynett et al (2002), Lynett et al. (2003), Korycansky and Lynett (2005), Cheung et al (2003), Pedrozo-Acuña et al. (2006), Lynett and Liu (2006), Lynett (2006), Lynett (2007), and Korycansky and Lynett (2007).

One important aspect of runup simulation is the representation of overtopping of structures. However, quality, time-dependent data for wave overtopping of levees and dikes is sparse. Thus, as with existing published numerical models (e.g., Dodd, 1998), the large majority of comparisons provided here will use time-averaged experimental data. First, a comparison is made with the data of Saville (1955). This data set is one of the standard comparisons found in the literature (e.g., Kobayashi and Wurjanto, 1989; Dodd, 1998; Hu et al., 2000). Figure 3.6-5 is an example of the physical setup for these trials, showing a spatial snapshot from a numerical simulation. A range of freeboard and wave conditions was tested. Table 3.6-1 provides a summary of the comparisons.

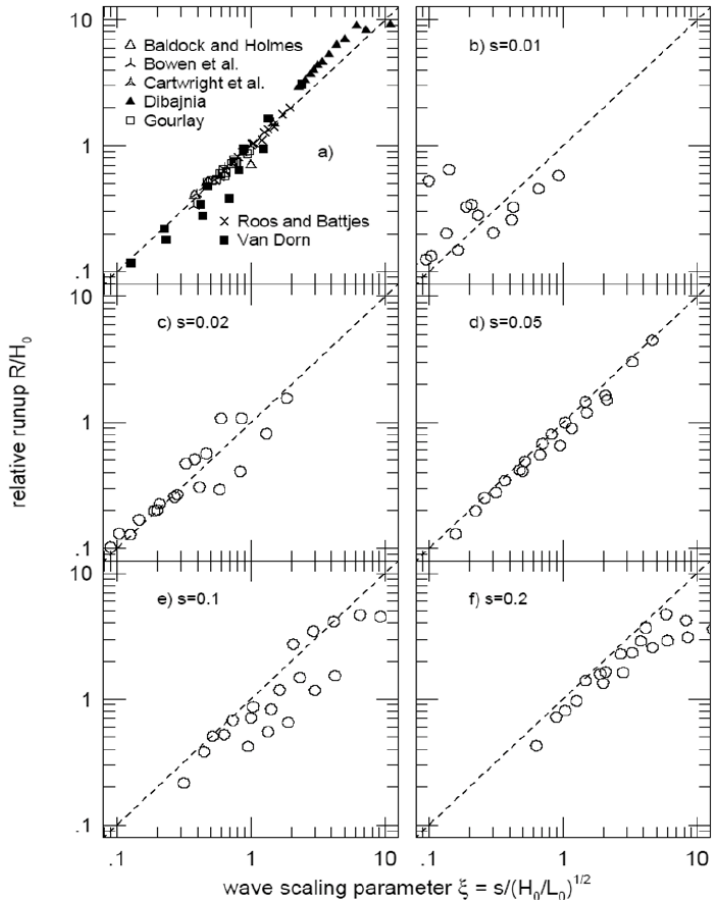

Figure 3.6-4: Wavetank experimental measurements of runup from the literature and COULWAVE runup results (open circles); adapted from Korycansky and Lynett (2005).

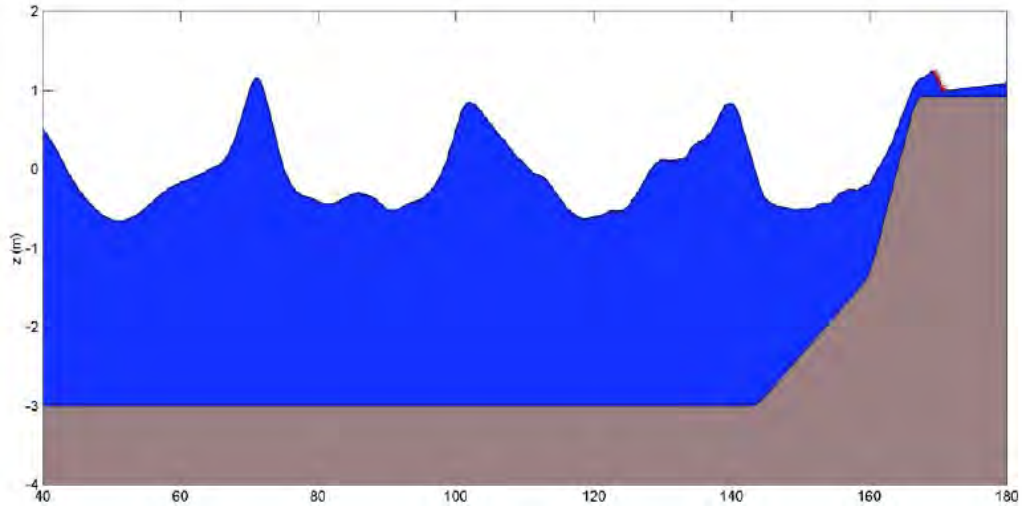

Figure 3.6-5: COULWAVE snapshot from a recreation of the Saville (1955) experiments. The general setup is a wave maker depth ~3 m, a flat portion leading up to a 1/10 slope, which connects to the "structure." In these experiments, the structure has either a 1/3 or 1/1.5 slope.

Table 3.6-1: Numerical comparisons with data from the Saville (1955) experiments. Ho is the wave height at the wave maker, T is the wave period, Htoe is the wave height at the toe of the structure, R is the distance between the structure crest and the still water level, d_toe is the water depth at the toe, slope is the 1/slope of the structure, Q_meas is the measured overtopping flux, Q_K&W is the simulated overtopping by Kobayashi and Wurjanto (1989), and Q_Bous is the COULWAVE simulated flux.

Run	Ho (m)	T (s)	Htoe (m)	R (m)	d_toe (m)	slope	Q'_meas (m2/s)	Q'_K&W (m2/s)	Q'_Bous (m2/s)
1	1.83	6.39	1.74	0.91	1.37	3	0.51	0.21	0.35
2	1.83	6.39	1.74	1.83	1.37	3	0.32	0.02	0.21
3	1.83	6.39	1.74	0.91	2.74	3	0.50	0.41	0.49
4	1.83	6.39	1.74	1.83	2.74	3	0.28	0.11	0.16
5	1.37	7.67	1.36	0.92	2.74	3	0.45	0.41	0.44
6	1.83	10.8	1.94	0.91	1.37	3	0.47	0.42	0.42
7	1.83	10.8	1.9	1.83	1.37	3	0.13	0.12	0.12
8	1.83	10.8	1.94	2.74	1.37	3	0.31	0.02	0.04
9	1.83	10.8	1.94	0.91	2.74	3	0.73	0.71	0.68
10	1.83	10.8	1.94	1.83	2.74	3	0.31	0.35	0.35
11	1.83	10.8	1.94	2.74	2.74	3	0.06	0.12	0.11
12	1.37	14.97	1.62	0.92	1.37	3	0.46	0.49	0.46
13	1.37	14.97	1.62	0.92	2.74	3	0.65	0.57	0.63
14	1.37	14.97	1.62	1.82	2.74	3	0.39	0.26	0.33
15	1.37	14.97	1.62	2.74	2.74	3	0.13	0.08	0.09
16	1.37	14.97	1.62	3.66	2.74	3	0.06	0.08	0.03
17	1.83	10.8	1.88	0.91	1.37	3	0.38	0.51	0.44
18	1.83	10.8	1.88	2.74	1.37	1.5	0.10	0.06	0.09
19	1.83	10.8	1.88	0.91	0	1.5	0.30	0.31	0.31
20	1.83	10.8	1.88	1.83	0	1.5	0.16	0.05	0.09

Overall, the agreement between the Boussinesq simulations and the experiments is quite good. Where the two diverge, the Boussinesq results tend to agree with the published numerical results of Kobayashi and Wurjanto (1989).

The Boussinesq model results must also exhibit agreement with well-established empirical formulas such as those given by Owen (1980) and van der Meer and Janssen (1995). Here, we compare the COULWAVE overtopping predictions with the formula of van der Meer and Janssen (1995). For this comparison, we test a wide range of wave and levee configurations with COULWAVE. Ranges of parameters are: levee slope from 1/3–1/8, freeboard from 0.3 to 1.2 m (1' to 4'), wave height at the structure toe from 0.6 to 2.4 m (2 to 8 ft), and wave period from 8 to16 s. The incident wave condition is a shallow water TMA spectrum using a gamma value of 3.0. Approximately 500 Boussinesq simulations were performed with COULWAVE, and the comparisons with the formula of van der Meer and Janssen (1995) are shown in Figure 3.6-6. Agreement is good.

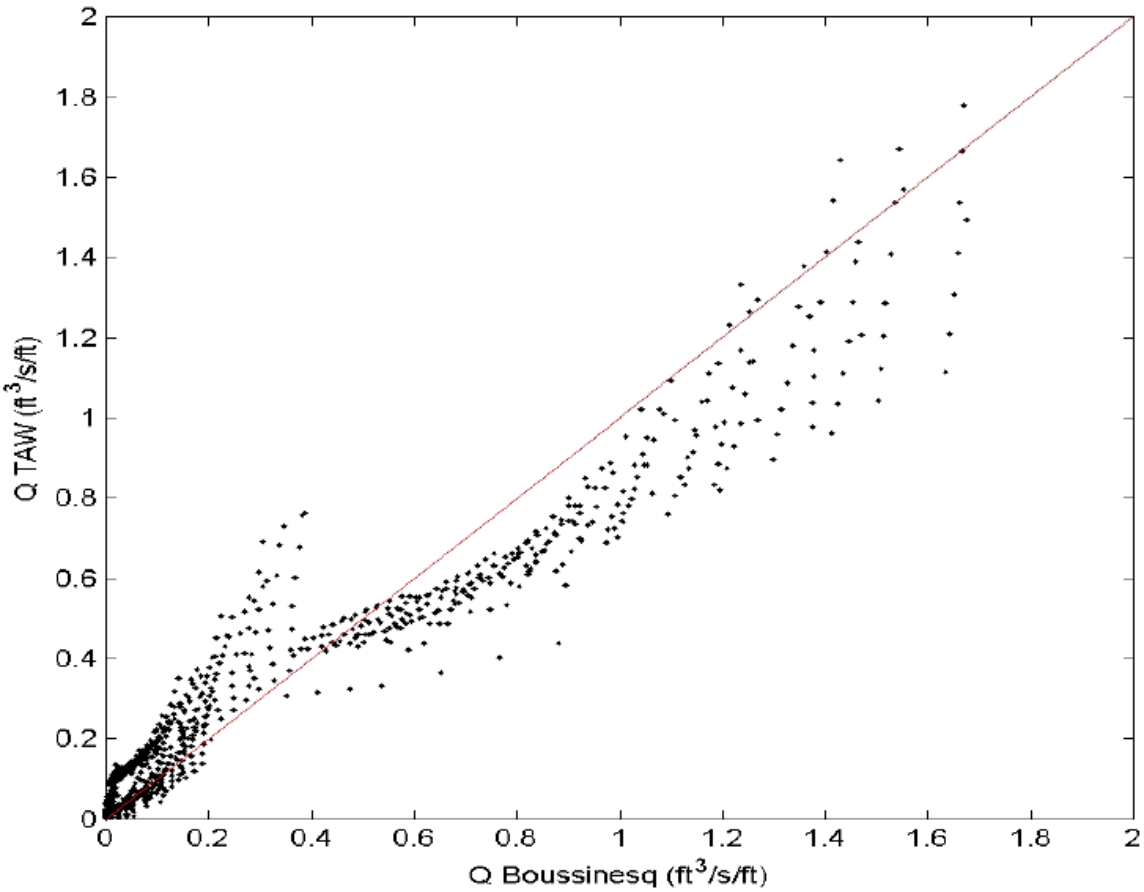

Figure 3.6-6: Comparison of Boussinesq overtopping rates (dots) with the formula given in the TAW design guidance (van der Meer and Janssen, 1995) (line).

3.7 Conclusions

The COULWAVE model is a good predictive model for use in estimating tsunami levels and runup.

4.0 Tsunami Water Levels

Information Submitted by the Licensee

The FHRR contains tsunami water level modeling for seismic sources, both local and distant, as well as for landslide sources.

Taylor Engineering Technical Evaluation

Four general types of tsunami sources were modeled to determine their impact on the DCPP site. First, modeling for large distant earthquakes estimates the effects of tsunamis near the reactor site from subduction zone earthquakes throughout the Pacific Rim. Simulation of local earthquake sources follows. While there are no large subduction zones near the reactor complex, relatively small, local earthquakes may lead to large local wave heights. The final two types of sources are both landslide sources, from either distant or local failures. For all conditions, the presented analysis employs conservative source

parameters, even when arguably unphysical, to provide an upper limit on the possible tsunami effects at the DCPP site.

4.1 Tsunamis from Distant Earthquake Sources

Information Submitted by the Licensee

The FHRR uses the FUNWAVE-TVD model to simulate four different distant tsunami sources. The magnitudes of the earthquakes fall between M_w9.1-9.2. The maximum flow elevation found near the DCPP SWIS is 5.3 m (NAVD88), and the minimum flow elevation in this area is -2.8 m (NAVD88).

Taylor Engineering Technical Evaluation

In this section, we present and discuss the results of 18 distant tsunami scenarios considered from various subduction zones around the Pacific Rim. The products of the simulations are first summarized in Table 4.1-1. For reference Figure 4.1-1 provides the bathymetry and topography in the area of the site.

Table 4.1-1 recaps the resulting maximum tsunami elevations at discharge and SWIS locations as well as the arrival times following the earthquake from different scenarios. It shows that the tsunamis from AASZ sources not only create the highest elevations, but also arrive earlier than tsunamis from other far field sources. In this context, we will discuss the outcomes of the two scenarios that create the highest water elevations at the DCPP site, scenarios AA-1 and AA-2, in more detail.

Figures illustrating each scenario include maximum (e.g. Figure 4.1.1-1) and minimum tsunami elevations (e.g. Figure 4.1.1-2) reached at each grid point for the duration of the computation and evolution of FSEs. To facilitate viewing of the results and a comparison of the tsunami elevations produced by the different earthquake scenarios, the contour plots for each of the 10 subsections in Section 4.1 apply a consistent contour colorbar range for the maximum elevation plots and a consistent range for the minimum elevation plots. Maximum tsunami elevations are important since they are directly related to coastal inundation, while minimum elevations determine the drawdown limit which is important for the continuing operation of the cooling water intake and discharge structures. Taylor Engineering computed FSE at a grid point located at the nearshore region near the site after occurrence of the earthquake (e.g. Figure 4.1.1-3), to provide detailed information on the local arrival time and the characteristics of the water level fluctuations. The FSE time series plots show the FSE relative to the antecedent water level applied in the models; however, the plots contain a text box to detail the maximum water level relative to the (NAVD88) datum. For example, within Figure 4.1.1-3, the maximum FSE equals 9.2 m relative to the antecedent water level of 2.3 m, which corresponds to a (total) maximum FSE of 11.5 m (NAVD88) (as called out in the figure's text box).

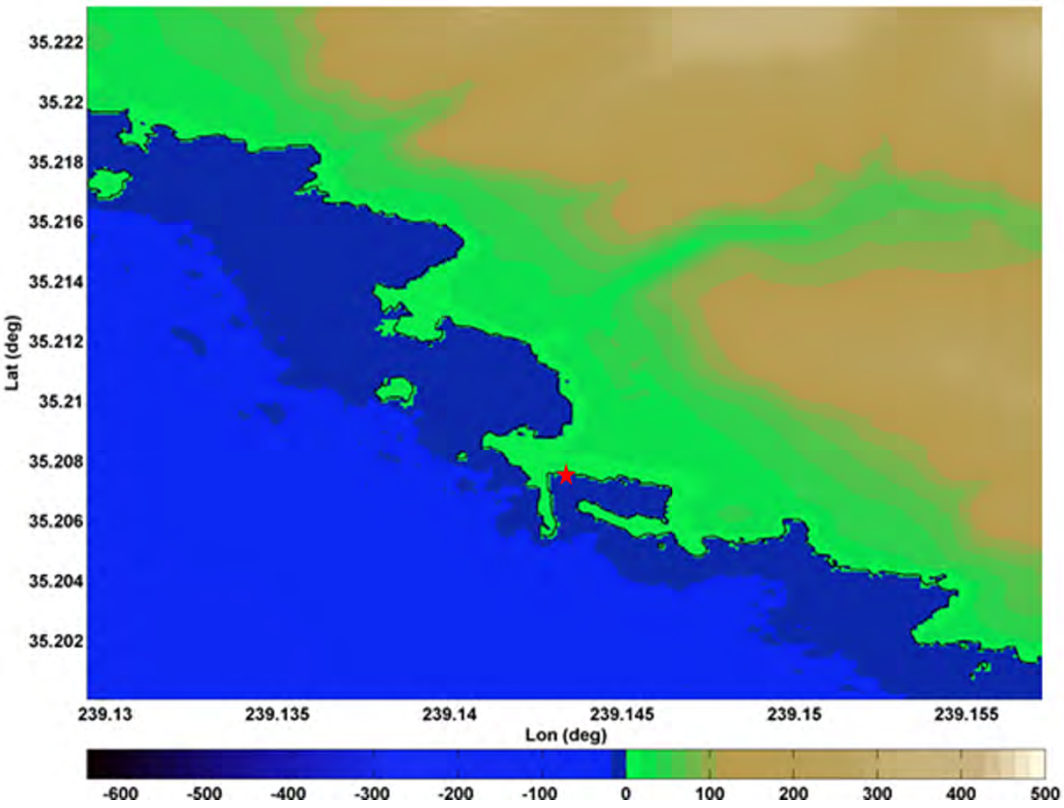

Figure 4.1-1: Digital elevation model (DEM) of the study area with elevations given in meters following the color scale. The SWIS location is given by the star.

Table 4.1-1: Tsunami arrival times of first and maximum wave and maximum tsunami elevations *near the DCPP discharge and South Cove SWIS location from all scenarios. All elevations are in (NAVD88) and include antecedent water level.*

	Arrival Time		Max. Wave Elevation (m, (NAVD88))	
Scenario	**First Wave**	**Max. Wave**	**Discharge**	**South Cove SWIS**
AA-1	5 hrs	6 hrs 25 mins	12.2	11.5
AA-2	5 hrs	5 hrs	11.3	11.2
CA-1	6 hrs	6 hrs 16 mins	2.6	2.5
CAS-1	10 hrs	19 hrs 31 mins	3.1	3.2
CAS-2	10 hrs	10 hrs	3.0	3.1
CAS-3	10 hrs	19 hrs 30 mins	3.2	3.2
GJ-1	11 hrs	13 hrs 32 mins	6.3	6.2
GJ-2	11 hrs	13 hrs 20 mins	6.5	6.6
JK-1	8 hrs 20 mins	9 hrs 45 mins	5.6	6.5
JK-2	8 hrs 20 mins	9 hrs 47 mins	5.6	6.1
KT-1	10 hrs 30 mins	12 hrs 43 mins	7.3	7.5
ME-1	5 hrs 53 mins	5 hrs 53 mins	2.8	2.8
NG-1	14 hrs 20 mins	18 hrs 17 mins	5.6	6.0
NG-2	14 hrs 20 mins	16 hrs 42 mins	6.0	6.1
RN-1	11 hrs 40 mins	17 hrs 19 mins	4.0	4.2
SA-1	10 hrs	19 hrs 28 mins	3.9	3.9
SA-2	13 hrs	19 hrs 28 mins	4.1	4.2
SA-3	13 hrs 25 mins	16 hrs 40 mins	5.5	5.8

4.1.1 Scenarios AA-1 & AA-2

Simulation results for scenario AA-1 are presented in Figures 4.1.1-1 through 4.1.1-3. The maximum tsunami elevations shown in Figure 4.1.1-1 indicate significant overland flooding and coastal inundation with this scenario. The run-up heights predicted near the DCPP site vary from 7 to 20 m. The highest run-up elevations were calculated along the steep slope immediately behind the SWIS. At the SWIS location, the maximum tsunami elevation is found to be 11.5 m. Note that in this and following sections, all elevations are in (NAVD88) and include antecedent water level.

Figure 4.1.1-2 shows the estimated minimum water elevations due to AA-1 scenario as between -1 to -7 m near the SWIS and discharge locations. Note that near the discharge location, the shoreline retracts 250 m offshore and the discharge pipes would be exposed. However, in the South Cove, the shoreline does not retract as substantially, and the minimum elevations range from -2 to -5 m. At the SWIS, the minimum elevation is -4.6 m (NAVD88), which is calculated using the antecedent low water level. Finally, Figure 4.1.1-4 displays the time series of water levels approximately at the 5 m water depth offshore of the discharge area. The tsunami for scenario AA-1 reaches the DCPP site within five hours and the maximum wave arrives 6.5 hours after the earthquake.

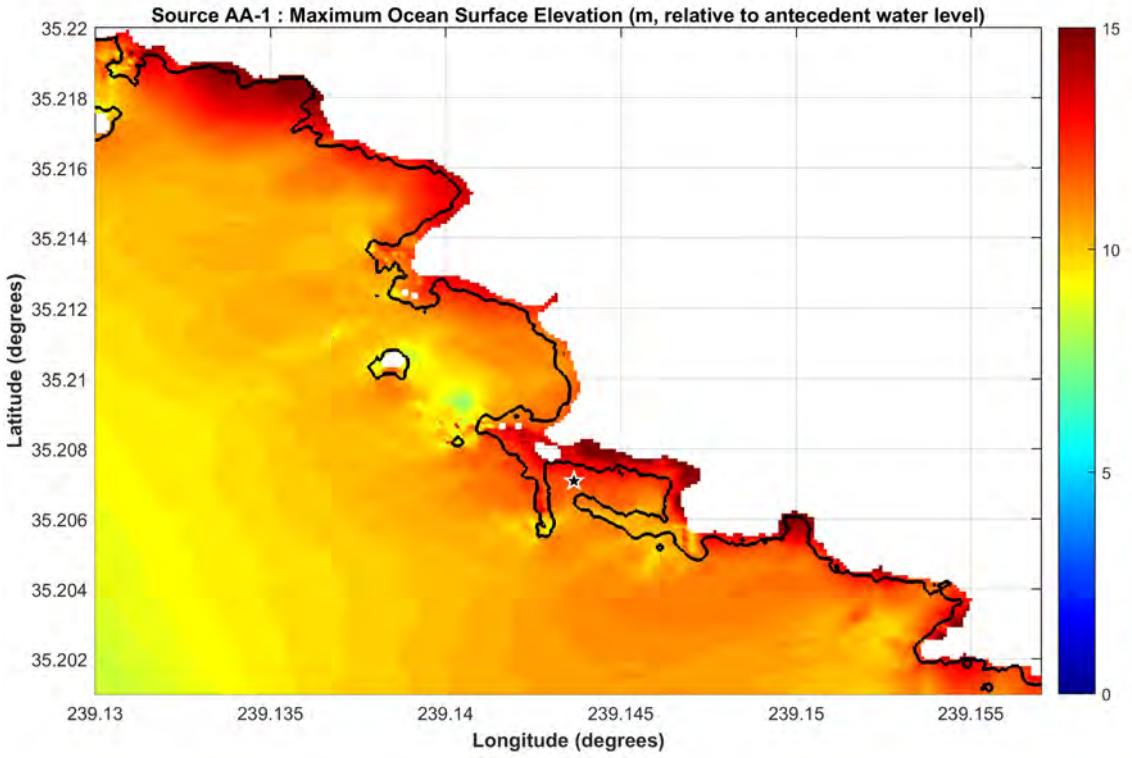

Figure 4.1.1-1: Maximum tsunami elevations (m, relative to antecedent water level) due to AA-1 scenario; the star marks the South Cove SWIS location.

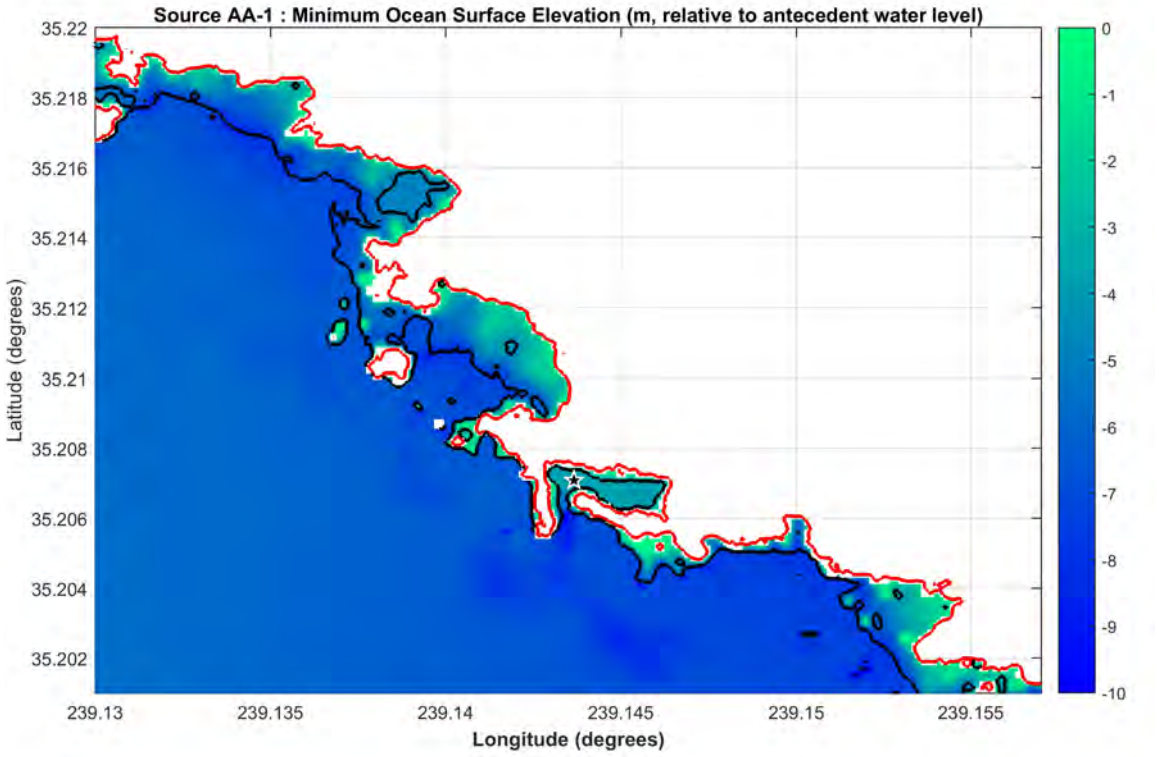

Figure 4.1.1-2: Minimum tsunami elevations (m, relative to antecedent water level) due to AA-1 scenario near the DCPP site. Red line shows the original shoreline; black line shows the estimated drawdown limit. The black star marks the South Cove SWIS location.

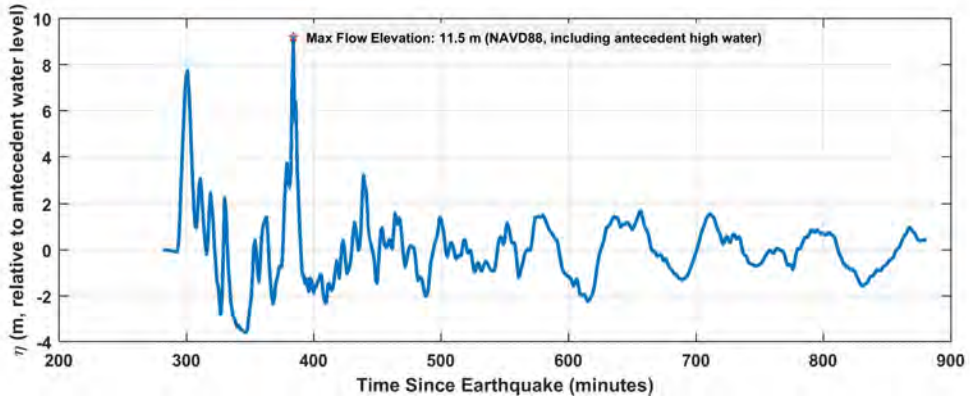

Figure 4.1.1-3: Evolution of ocean surface elevation (η) near South Cove SWIS location due to scenario AA-1, recorded approximately at 5 m water depth near the DCPP site. Vertical axis shows elevations in meters with respect to the antecedent water level, and the maximum flow elevation given in (NAVD88) including antecedent high water is noted.

Next, we turn our attention to the scenario AA-2. The oceanic propagation of this source is given in Figure 4.1.1-4. Similar to scenario AA-1, substantial flooding and inundation also occur with scenario AA-2. Coastal inundation is predicted around the area of the DCPP discharge and SWIS with run-up elevations ranging from 7 to 15 m (NAVD88) (Figure 4.1.1-5).

Figure 4.1.1-6 shows the estimated minimum water levels due to AA-2 scenario; these are in general very similar to scenario AA-1. As in scenario AA-1, the model predicts that the shoreline at the discharge site can be retracted up to 250 m; however, drawdown near the DCPP SWIS is not significant for this scenario. According to Figure 4.1.1-7 which pictures the evolution of the tsunami near the discharge in approximately 5 m water depth, the first and maximum tsunami wave for scenario AA-2 will reach the reactor site within five hours of the earthquake. Thus, considering both of these scenarios, it can be inferred that tsunami waves generated from AASZ begin to affect the southern California coast near the DCPP approximately five hours after the event, with the largest wave occurring within the first hour and a half of the tsunami event.

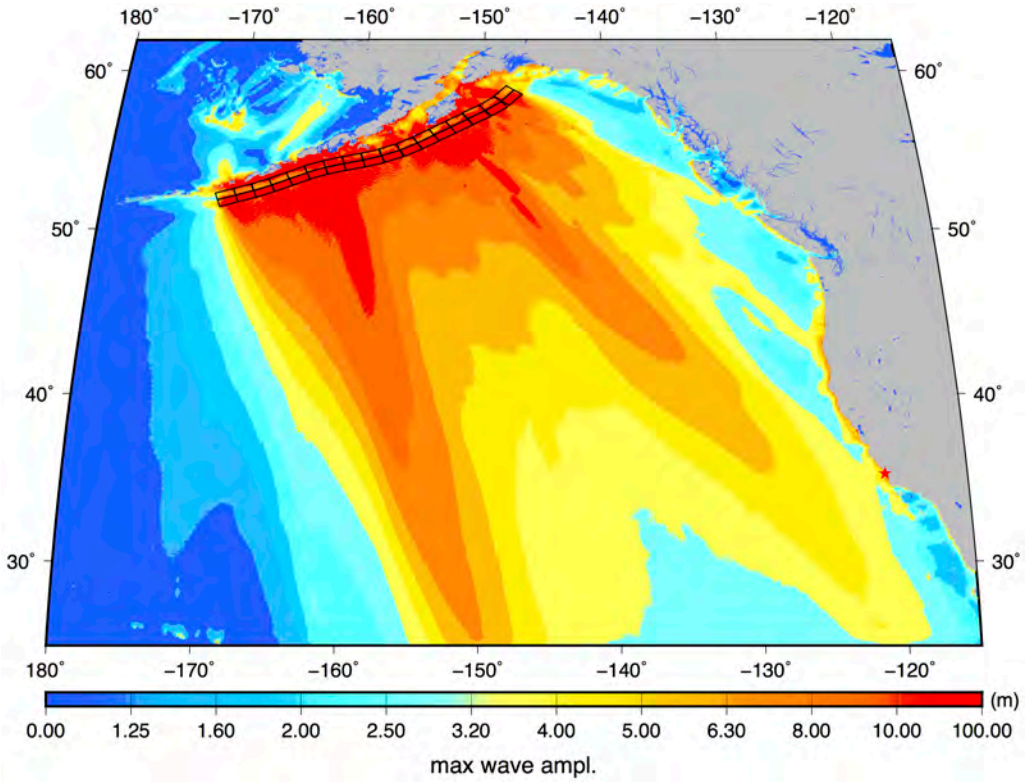

Figure 4.1.1-4: Maximum tsunami elevation from the AA-2 scenario. The unit sources considered for the scenario are shown with the black rectangles. The DCPP site is shown with the red star.

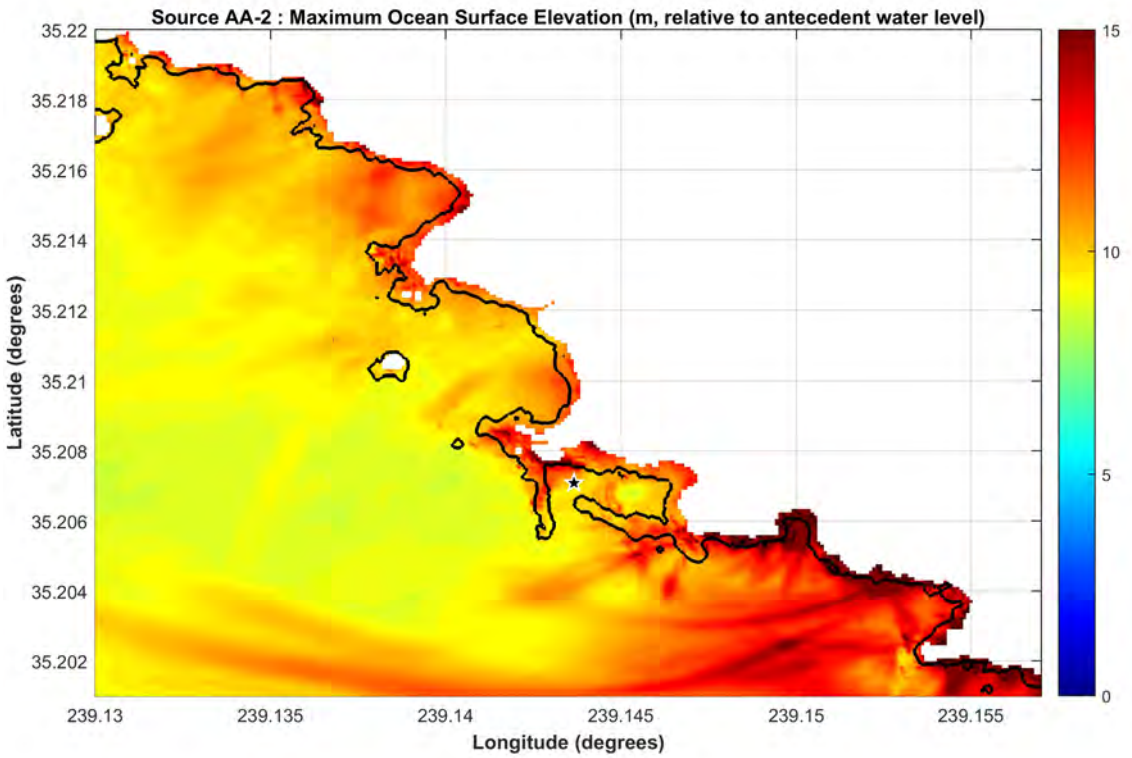

Figure 4.1.1-5: Maximum tsunami elevations (m, relative to antecedent water level) due to AA-2 scenario, where the star marks the South Cove SWIS location.

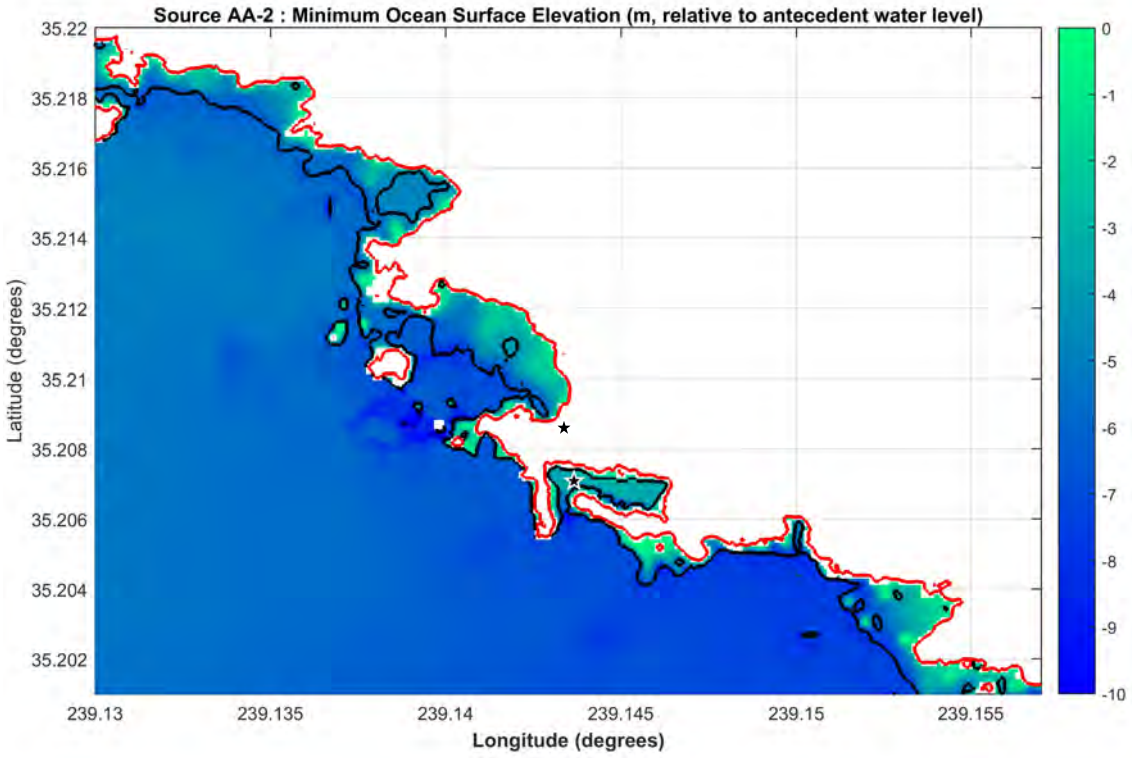

Figure 4.1.1-6: Minimum tsunami elevations (m, relative to antecedent water level) due to AA-2 scenario near the DCPP site. Red line shows the original shoreline, where black line is the estimated drawdown limit and the star marks the South Cove SWIS location.

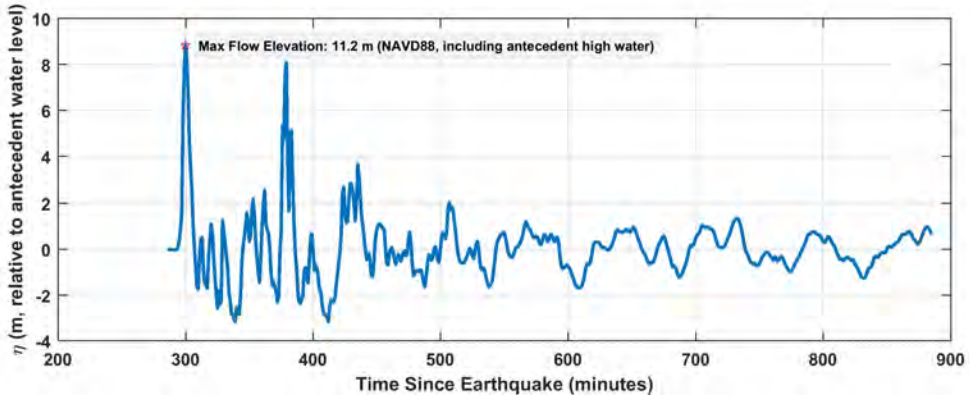

Figure 4.1.1-7: Evolution of ocean surface elevation (η) near South Cove SWIS location due to scenario AA-2 near the DCPP site. Vertical axis shows elevations in meters with respect to the antecedent water level, and the maximum flow elevation given in (NAVD88) including antecedent high water is noted.

4.1.2 Scenario CA-1

For the Central America subduction zone, only one scenario is considered. The results of the CA-1 scenario are given in Figures 4.1.2-1, 4.1.2-2, and 4.1.2-3. For the CA-1 tsunami scenario, the source model is based on uniform slip of 52.5 m. At both the DCPP SWIS and discharge locations, the computed maximum tsunami elevation is 2.5 m (NAVD88). This scenario does not cause any inundation near the DCPP site.

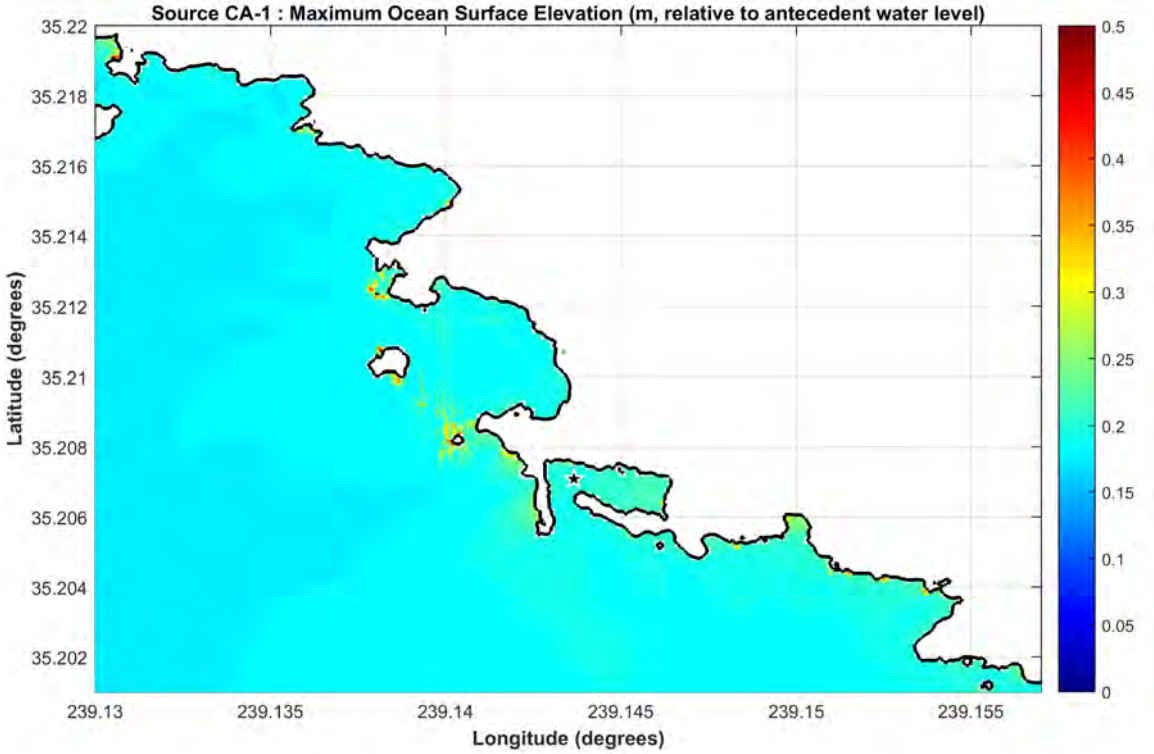

Figure 4.1.2-1: Maximum tsunami elevations (m, relative to antecedent water level) due to CA-1 scenario, where the star marks the South Cove SWIS location.

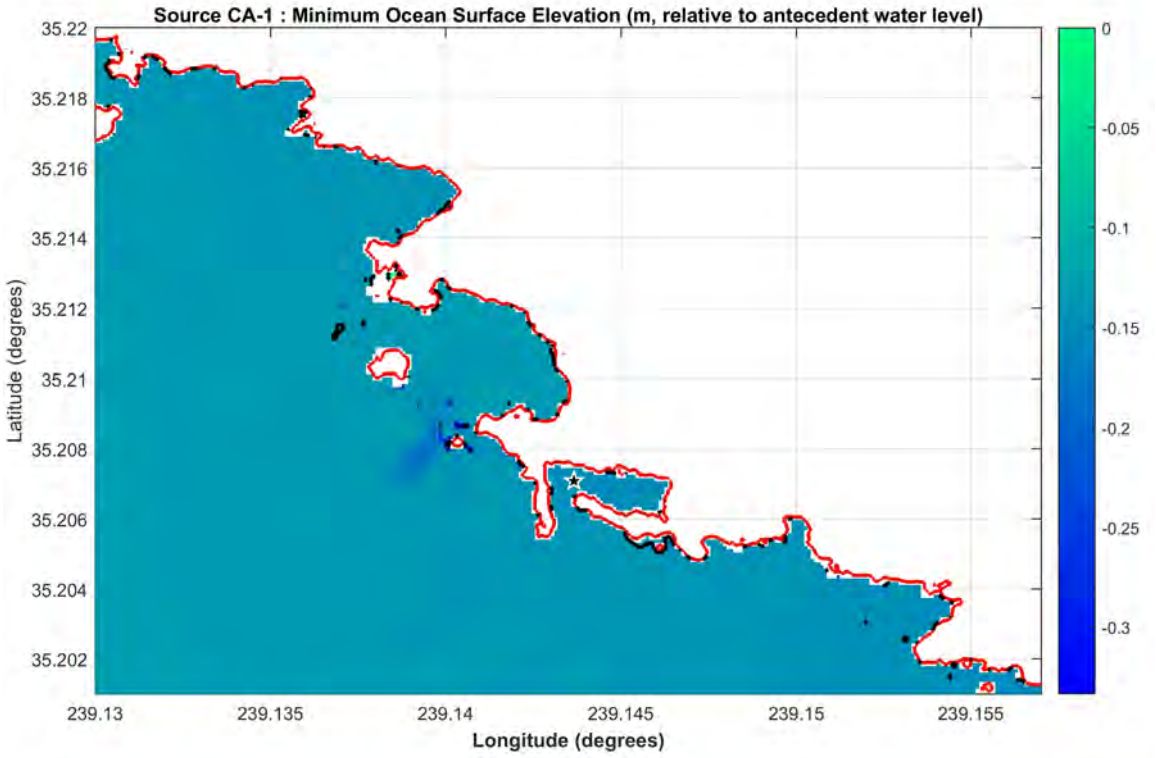

Figure 4.1.2-2: Minimum tsunami elevations (m, relative to antecedent water level) due to CA-1 scenario near the DCPP site. Red line shows the original shoreline, where black line is the estimated drawdown limit and the star marks the South Cove SWIS location.

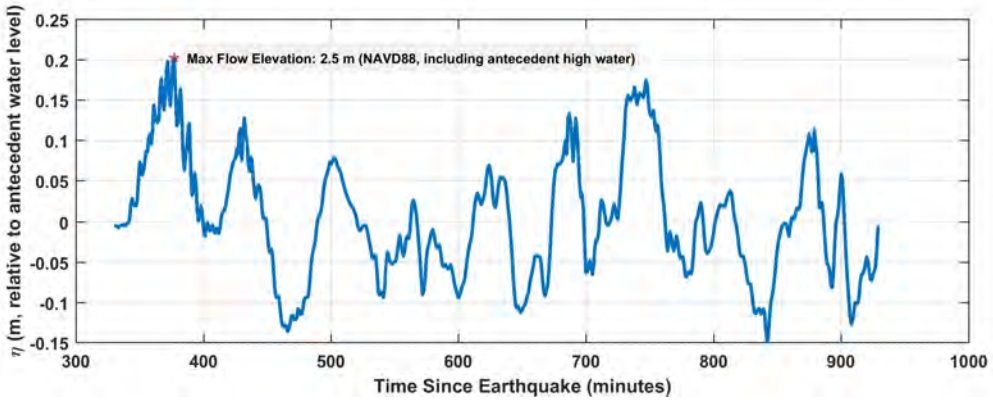

Figure 4.1.2-3: Evolution of ocean surface elevation (η) near South Cove SWIS location due to scenario CA-1 near the DCPP site. Vertical axis shows elevations in meters with respect to the antecedent water level, and the maximum flow elevation given in (NAVD88) including antecedent high water is noted.

4.1.3 Scenarios CAS-1, CAS-2 & CAS-3

For the Cascadia subduction zone, three different scenarios and two different slip models are considered: uniform slip model on scenarios CAS-1 and CAS-2, and variable slip model on scenario CAS-3. The results of CAS-1 scenario are given in Figures 4.1.3-1, 4.1.3-2, and 4.1.3-3. For the CAS-1 tsunami scenario, the source model is based on uniform slip of 52.5 m. The computed maximum tsunami elevations at the DCPP SWIS and discharge locations are 3.2 and 3.1 m (NAVD88), respectively. This scenario does not cause any significant inundation near the DCPP site, with maximum runup elevations near 1 m above antecedent water level.

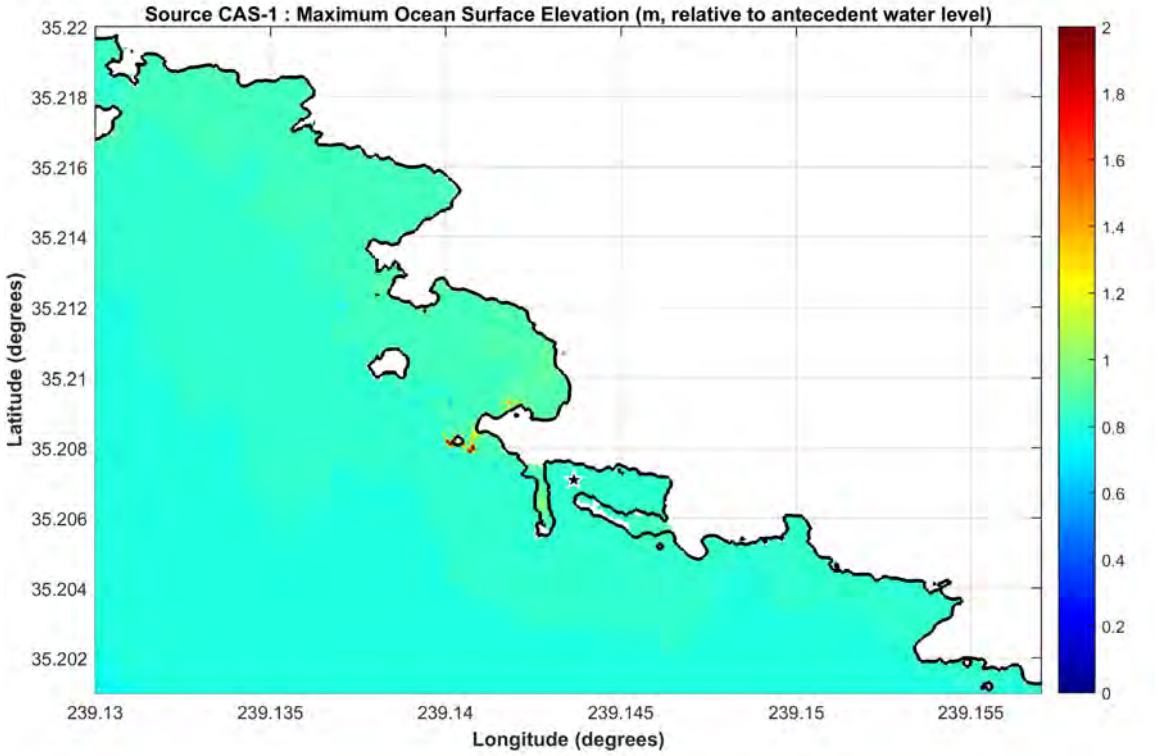

Figure 4.1.3-1: Maximum tsunami elevations (m, relative to antecedent water level) due to CAS-1 scenario, where the star marks the South Cove SWIS location.

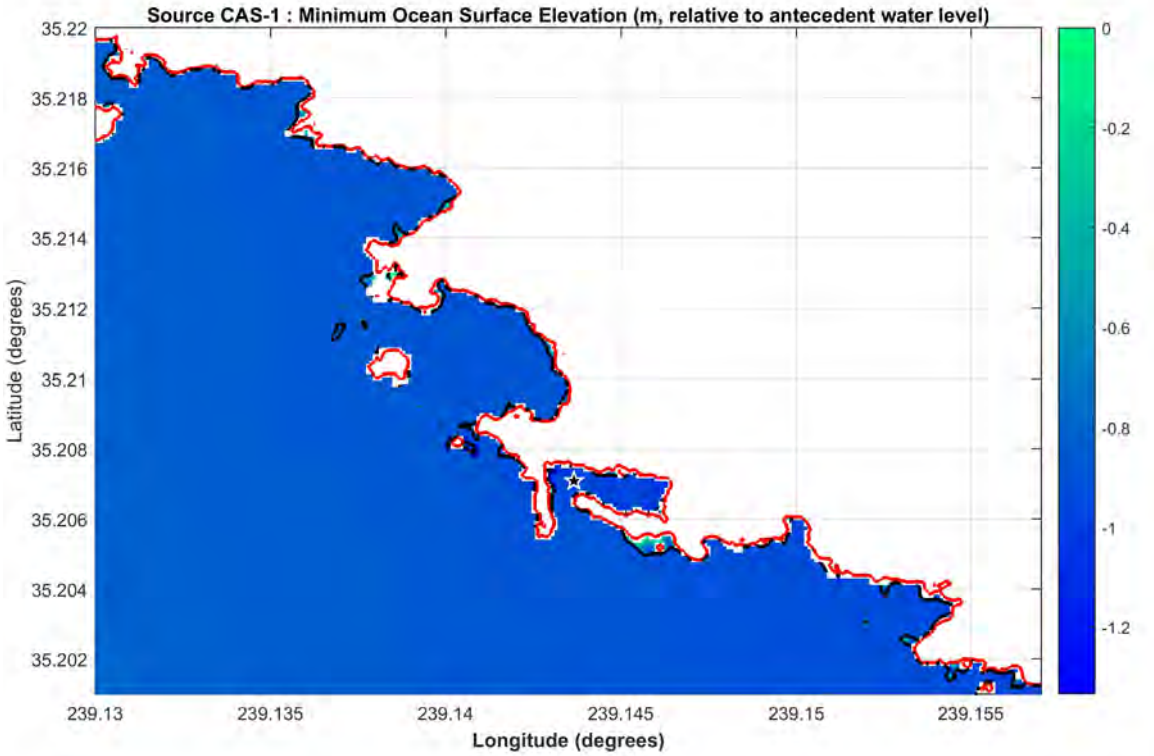

Figure 4.1.3-2: Minimum tsunami elevations (m, relative to antecedent water level) due to CAS-1 scenario near the DCPP site. Red line shows the original shoreline, where black line is the estimated drawdown limit and the star marks the South Cove SWIS location.

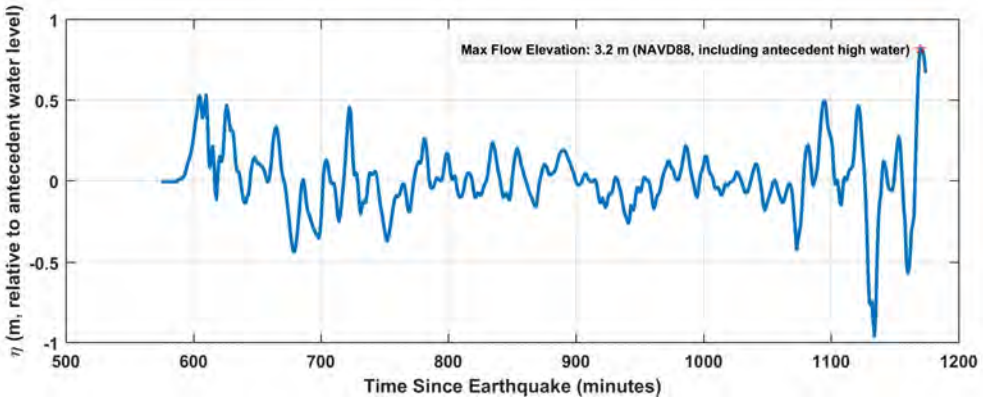

Figure 4.1.3-3: Evolution of ocean surface elevation (η) near South Cove SWIS location due to scenario CAS-1 near the DCPP site. Vertical axis shows elevations in meters with respect to the antecedent water level, and the maximum flow elevation given in (NAVD88) including antecedent high water is noted.

The results of the CAS-2 scenario are given in Figures 4.1.3-4, 4.1.3-5, and 4.1.3-6. For the CAS-2 tsunami scenario, the source model is based on uniform slip of 59.5 m. The computed maximum tsunami elevations at the DCPP SWIS and discharge locations are 3.1 m and 3.0 m (NAVD88), respectively. This scenario does not cause any significant inundation near the DCPP site, with maximum runup elevations near 0.8 m above antecedent water level.

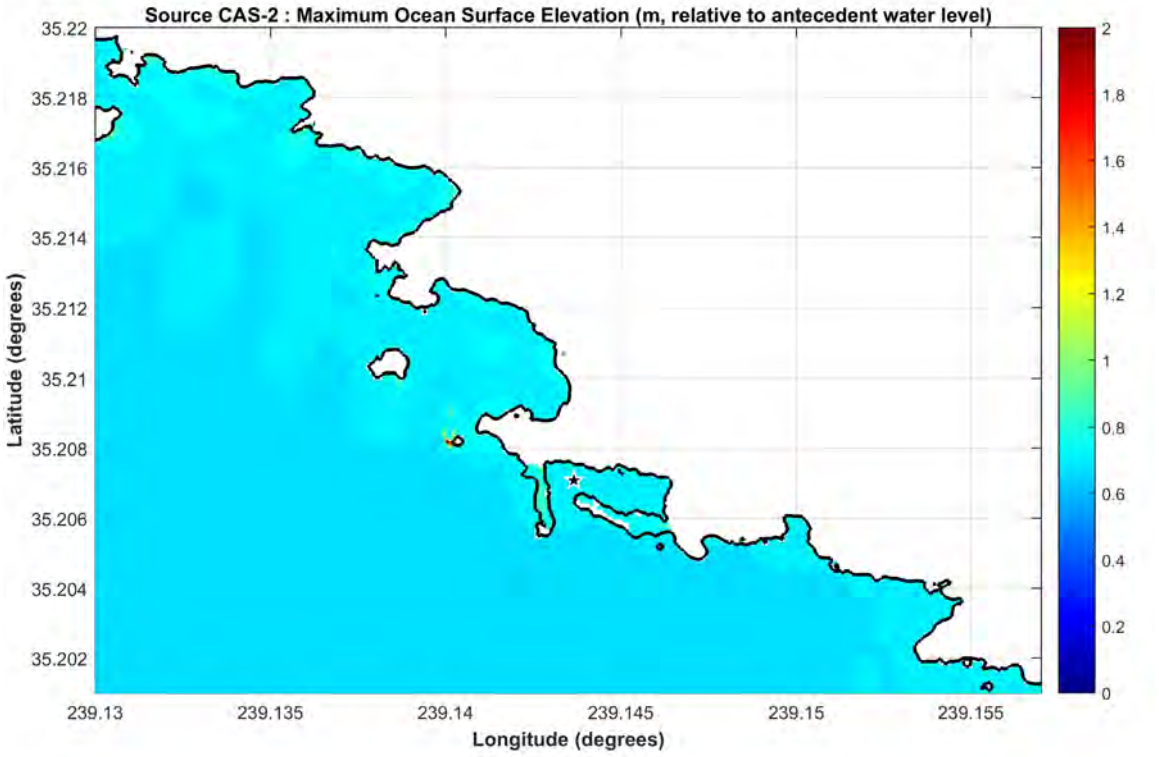

Figure 4.1.3-4: Maximum tsunami elevations (m, relative to antecedent water level) due to CAS-2 scenario, where the star marks the South Cove SWIS location.

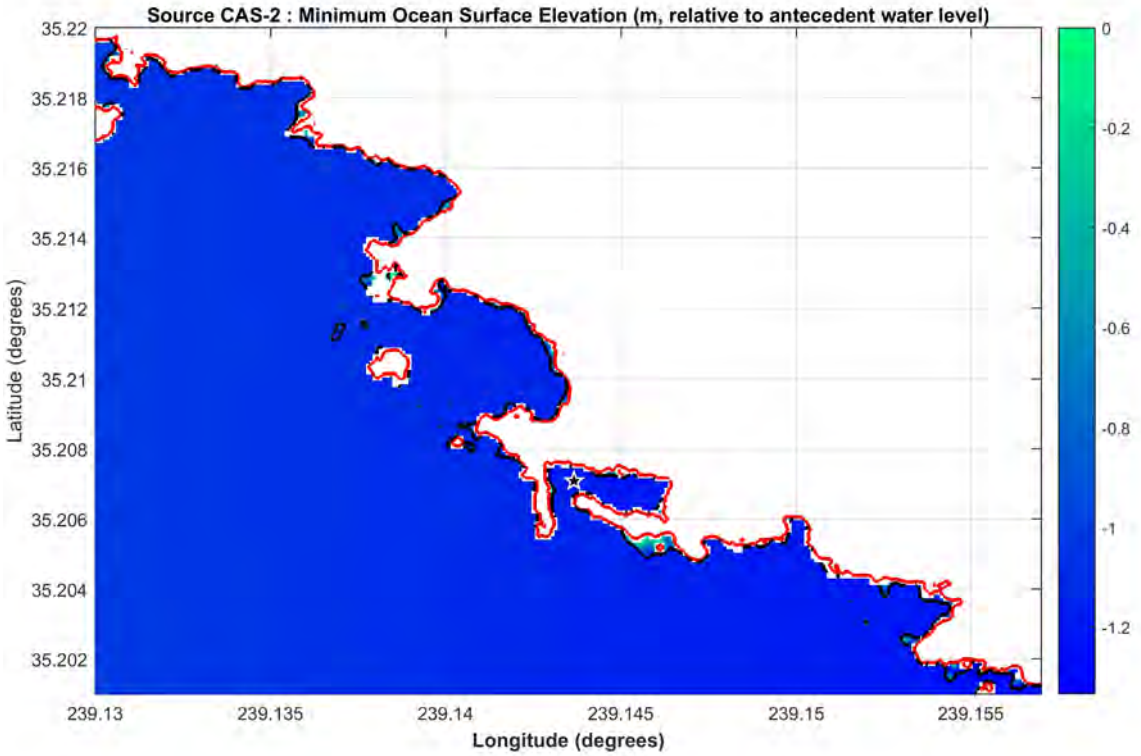

Figure 4.1.3-5: Minimum tsunami elevations (m, relative to antecedent water level) due to CAS-2 scenario near the DCPP site. Red line shows the original shoreline, where black line is the estimated drawdown limit and the star marks the South Cove SWIS location.

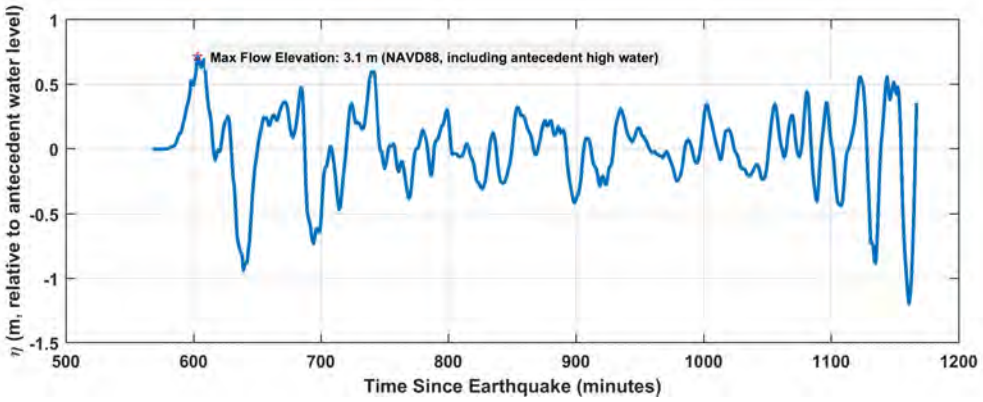

Figure 4.1.3-6: Evolution of ocean surface elevation (η) near South Cove SWIS location due to scenario CAS-2 near the DCPP site. Vertical axis shows elevations in meters with respect to the antecedent water level, and the maximum flow elevation given in (NAVD88) including antecedent high water is noted.

The results of the CAS-3 scenario are given in Figures 4.1.3-7, 4.1.3-8, and 4.1.3-9. For the CAS-3 tsunami scenario, the source model is based on variable slip, which has a spatially varying displacement on the fault plane and a peak displacement of 80 m. The computed maximum tsunami elevation at the DCPP SWIS location is 3.2 m (NAVD88). This scenario does not cause any significant inundation near the DCPP site, with maximum runup elevations near 1 m above antecedent water level.

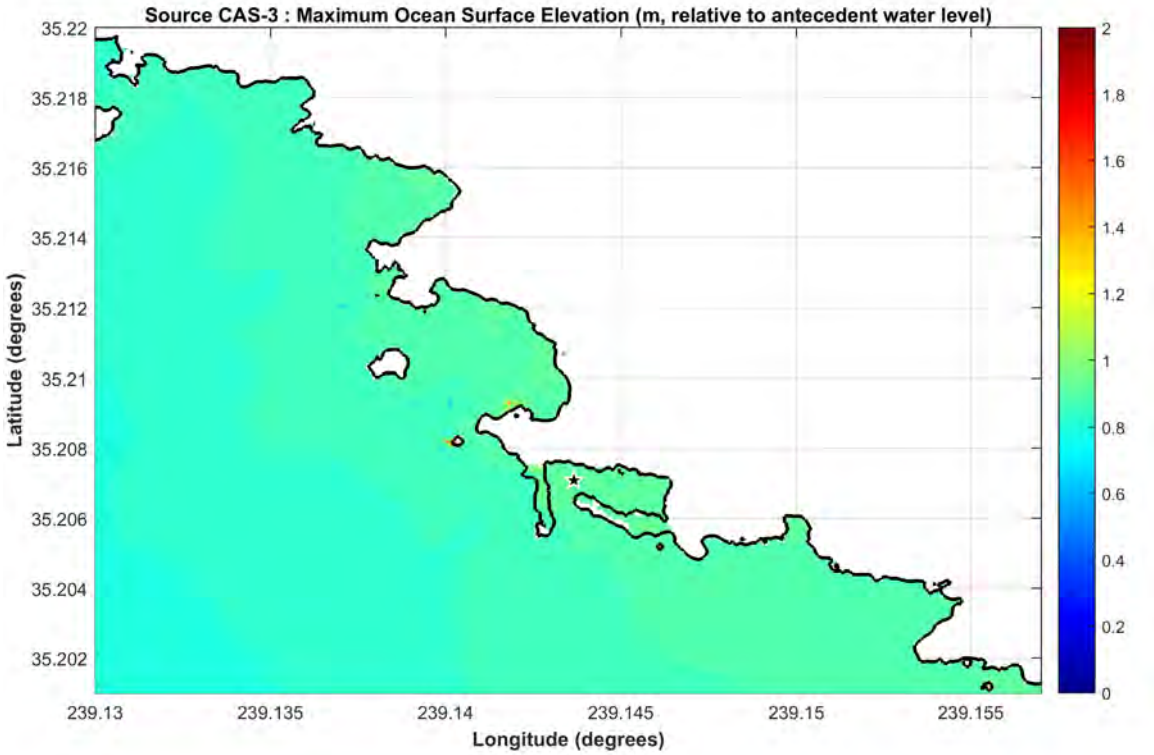

Figure 4.1.3-7: Maximum tsunami elevations (m, relative to antecedent water level) due to CAS-3 scenario, where the star marks the South Cove SWIS location.

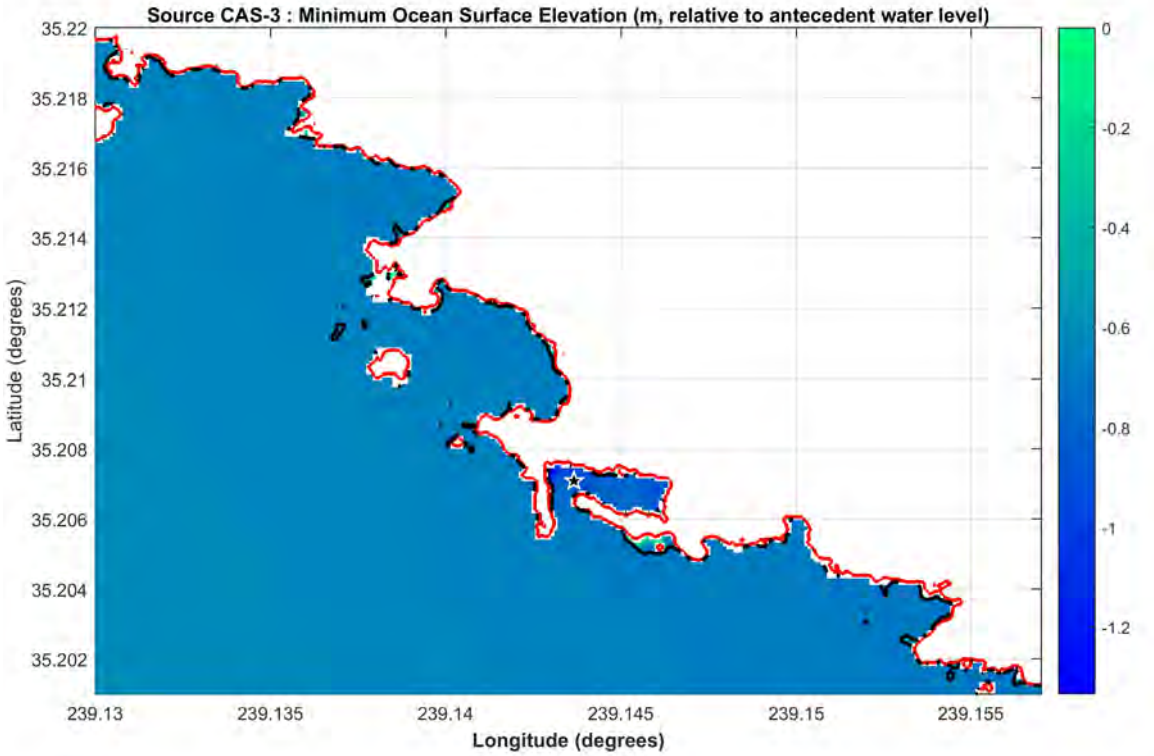

Figure 4.1.3-8: Minimum tsunami elevations (m, relative to antecedent water level) due to CAS-3 scenario near the DCPP site. Red line shows the original shoreline, where black line is the estimated drawdown limit and the star marks the South Cove SWIS location.

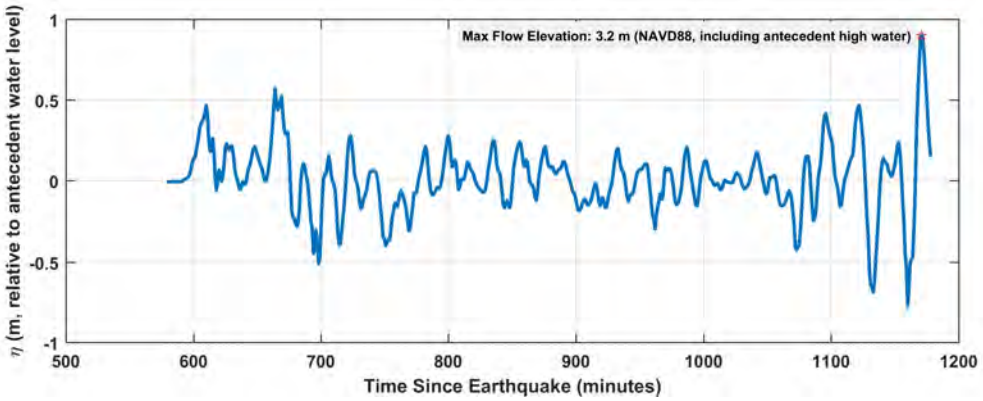

Figure 4.1.3-9: Evolution of ocean surface elevation (η) near South Cove SWIS location due to scenario CAS-3 near the DCPP site. Vertical axis shows elevations in meters with respect to the antecedent water level, and the maximum flow elevation given in (NAVD88) including antecedent high water is noted.

4.1.4 Scenarios GJ-1 & GJ-2

For the Guam-Japan subduction zone, two scenarios are modeled. Although, both scenarios employ a uniform slip of 63 m, different unit source combinations are taken into consideration. The results of GJ-1 scenario are given in Figures 4.1.4-1, 4.1.4-2, and 4.1.4-3 . For the GJ-1 tsunami scenario, the computed maximum tsunami elevations at the DCPP SWIS and discharge locations are 6.2 m and 6.3 m (NAVD88), respectively. The result indicates modest inundation of the South Cove SWIS location, with maximum runup elevations near 4 m above antecedent water level.

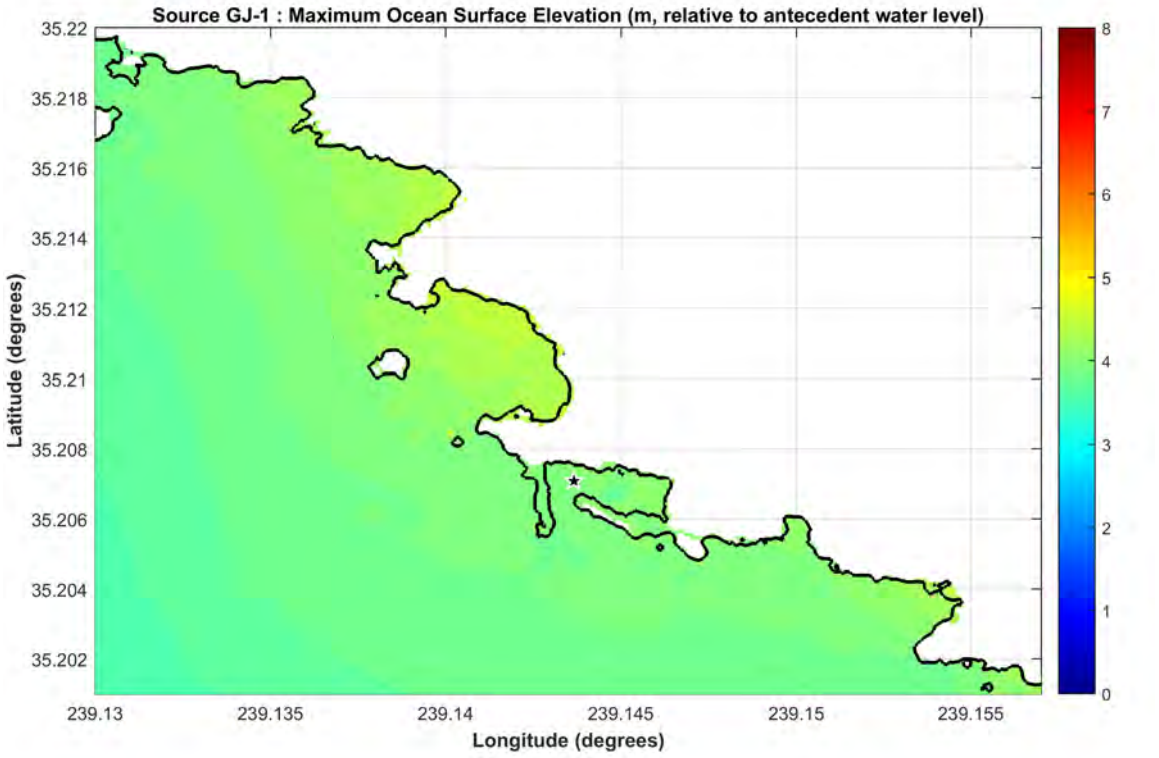

Figure 4.1.4-1: Maximum tsunami elevations (m, relative to antecedent water level) due to GJ-1 scenario, where the star marks the South Cove SWIS location.

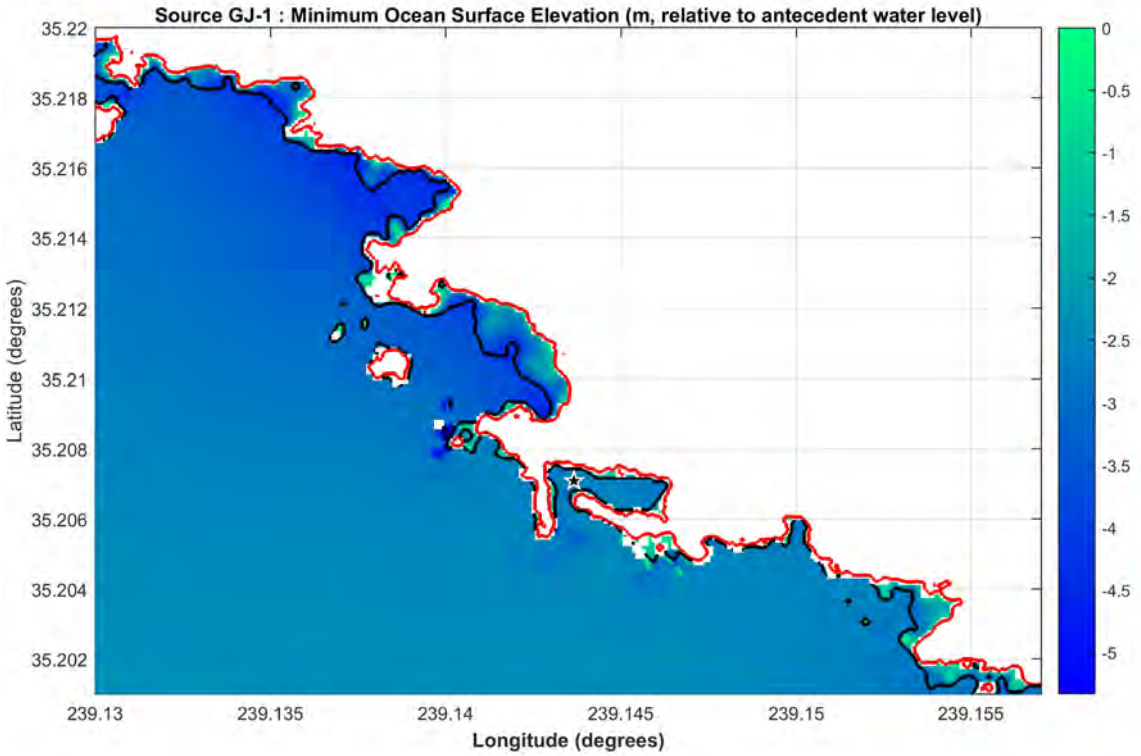

Figure 4.1.4-2: Minimum tsunami elevations (m, relative to antecedent water level) due to GJ-1 scenario near the DCPP site. Red line shows the original shoreline, where black line is the estimated drawdown limit and the star marks the South Cove SWIS location.

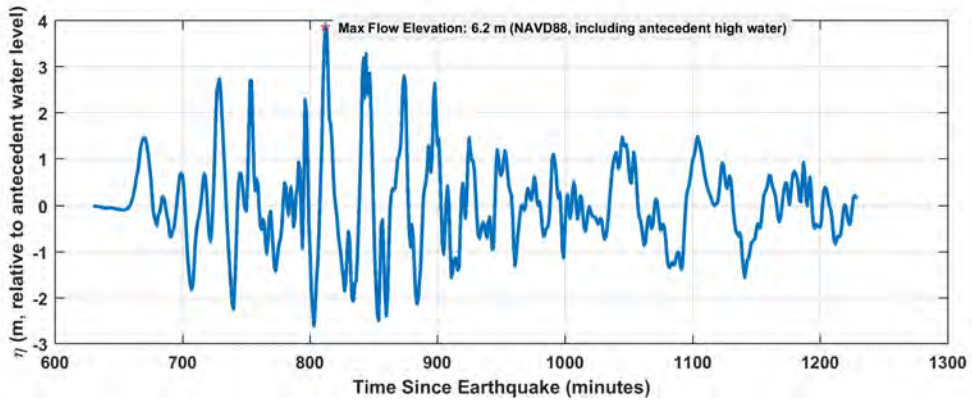

Figure 4.1.4-3: Evolution of ocean surface elevation (η) near South Cove SWIS location due to scenario GJ-1 near the DCPP site. Vertical axis shows elevations in meters with respect to the antecedent water level, and the maximum flow elevation given in (NAVD88) including antecedent high water is noted.

The results of GJ-2 scenario are given in Figures 4.1.4-4, 4.1.4-5, and 4.1.4-6. The computed maximum tsunami elevations at the DCPP SWIS and discharge sites are 6.6 m and 6.5 m (NAVD88), respectively. The result indicates modest inundation of the South Cove SWIS location, with maximum runup elevations near 5 m above antecedent water level.

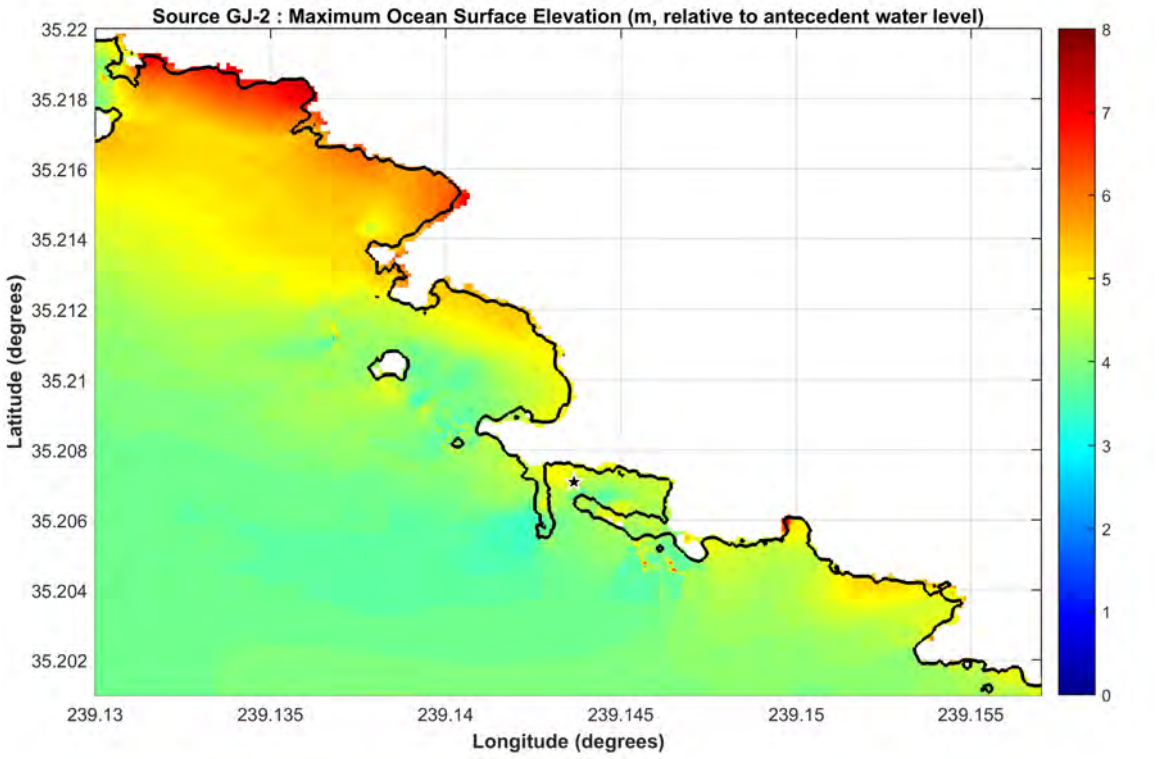

Figure 4.1.4-4: Maximum tsunami elevations (m, relative to antecedent water level) due to GJ-2 scenario, where the star marks the South Cove SWIS location.

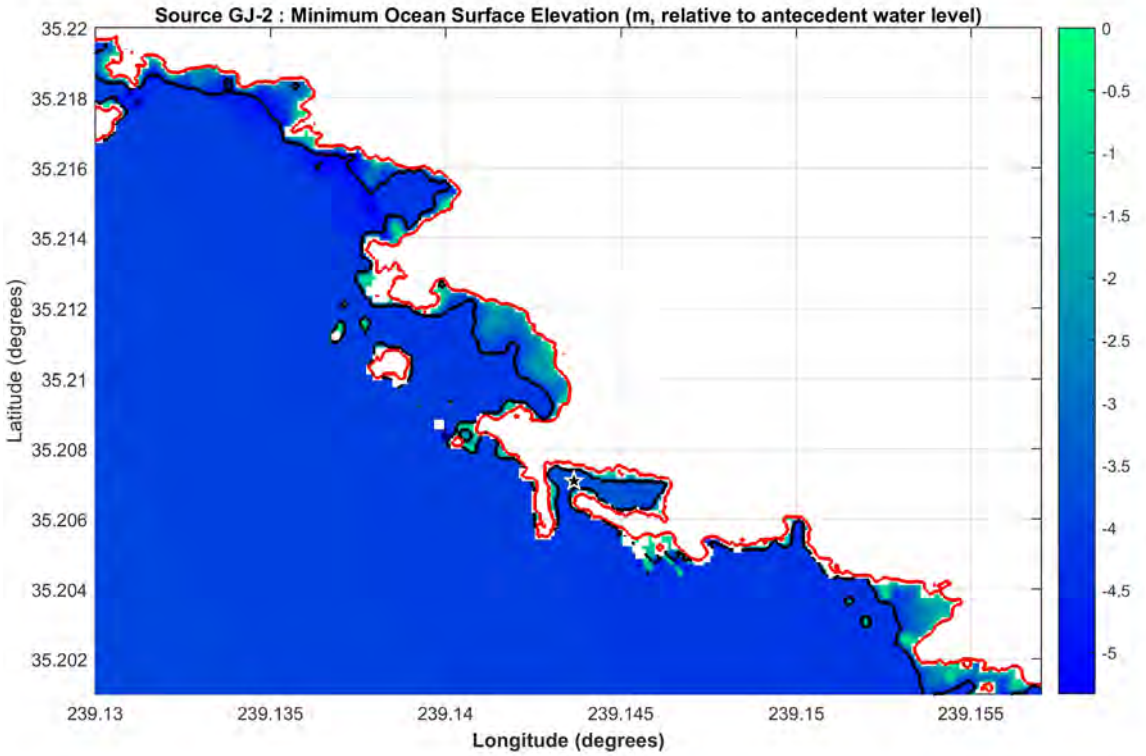

Figure 4.1.4-5: Minimum tsunami elevations (m, relative to antecedent water level) due to GJ-2 scenario near the DCPP site. Red line shows the original shoreline, where black line is the estimated drawdown limit and the star marks the South Cove SWIS location.

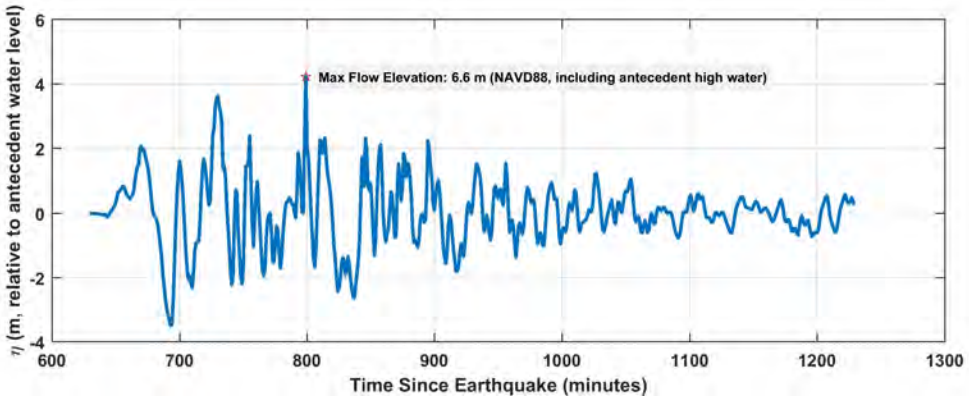

Figure 4.1.4-6: Evolution of ocean surface elevation (η) near South Cove SWIS location due to scenario GJ-2 near the DCPP site. Vertical axis shows elevations in meters with respect to the antecedent water level, and the maximum flow elevation given in (NAVD88) including antecedent high water is noted.

4.1.5 Scenarios JK-1 & JK-2

For the Japan-Kamchatka subduction zone, two different scenarios considered uniform slip distributions. The results of JK-1 scenario are given in Figures 4.1.5-1, 4.1.5-2, and 4.1.5-3. For the JK-1 tsunami scenario, the source model is based on uniform slip of 77 m. The computed maximum tsunami elevations at the DCPP SWIS and discharge locations are 6.5 m and 5.6 m (NAVD88), respectively. The result indicates modest inundation of the South Cove SWIS location, with maximum runup elevations near 4 m above antecedent water level.

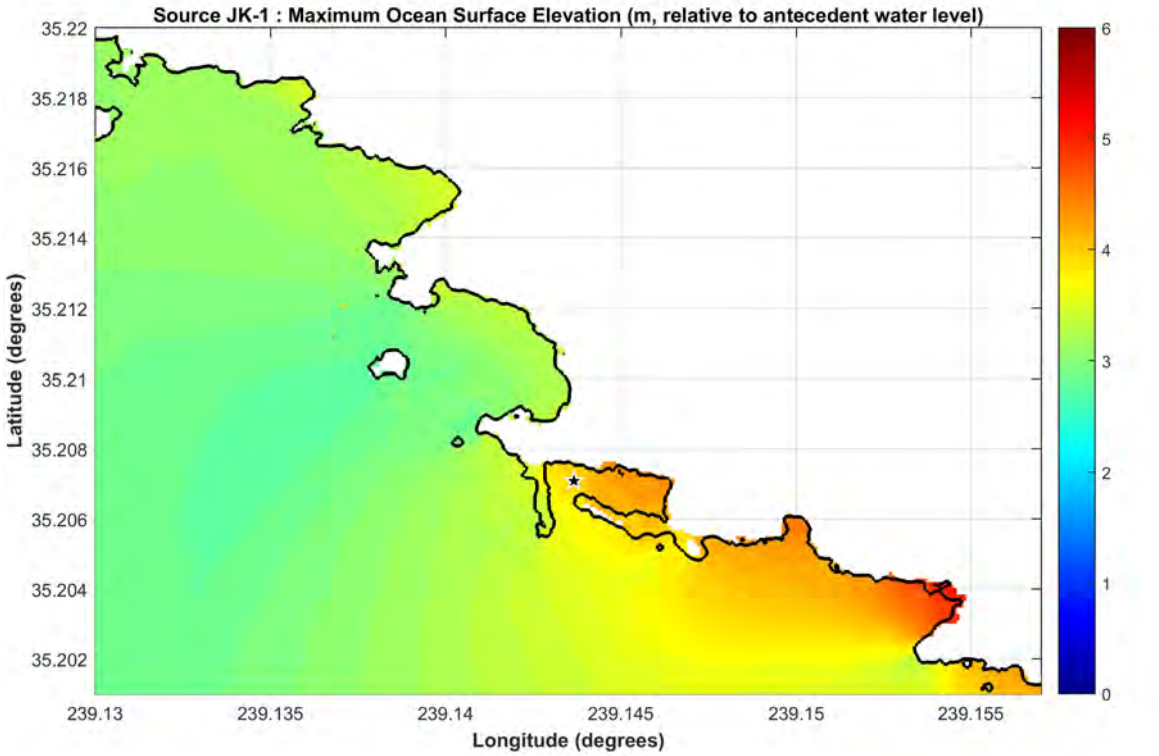

Figure 4.1.5-1: Maximum tsunami elevations (m, relative to antecedent water level) due to JK-1 scenario, where the star marks the South Cove SWIS location.

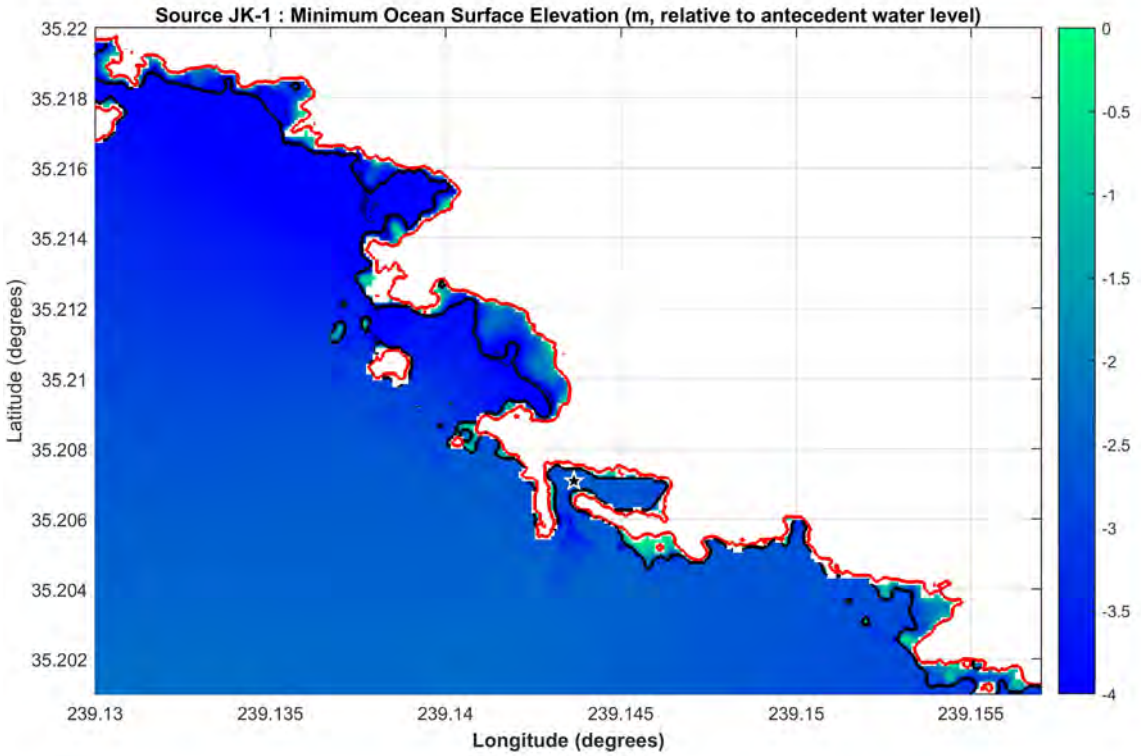

Figure 4.1.5-2: Minimum tsunami elevations (m, relative to antecedent water level) due to JK-1 scenario near the DCPP site. Red line shows the original shoreline, where black line is the estimated drawdown limit and the star marks the South Cove SWIS location.

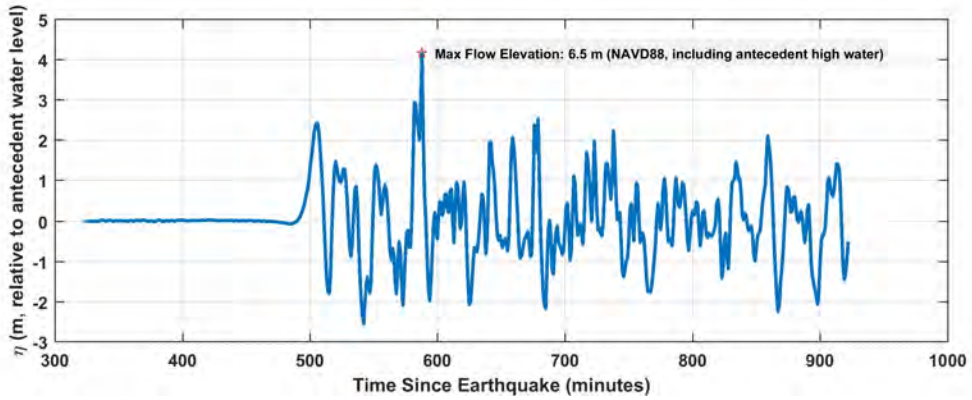

Figure 4.1.5-3: Evolution of ocean surface elevation (η) near South Cove SWIS location due to scenario JK-1 near the DCPP site. Vertical axis shows elevations in meters with respect to the antecedent water level, and the maximum flow elevation given in (NAVD88) including antecedent high water is noted.

The results of the JK-2 scenario are given in Figures 4.1.5-4, 4.1.5-5, and 4.1.5-6. For the JK-2 tsunami scenario, the source model is based on uniform slip of 59.5 m. The computed maximum tsunami elevations at the DCPP SWIS and discharge locations are 6.1 m and 5.6 m (NAVD88), respectively. The result indicates modest inundation of the South Cove SWIS location, with maximum runup elevations near 3.5 m above antecedent water level.

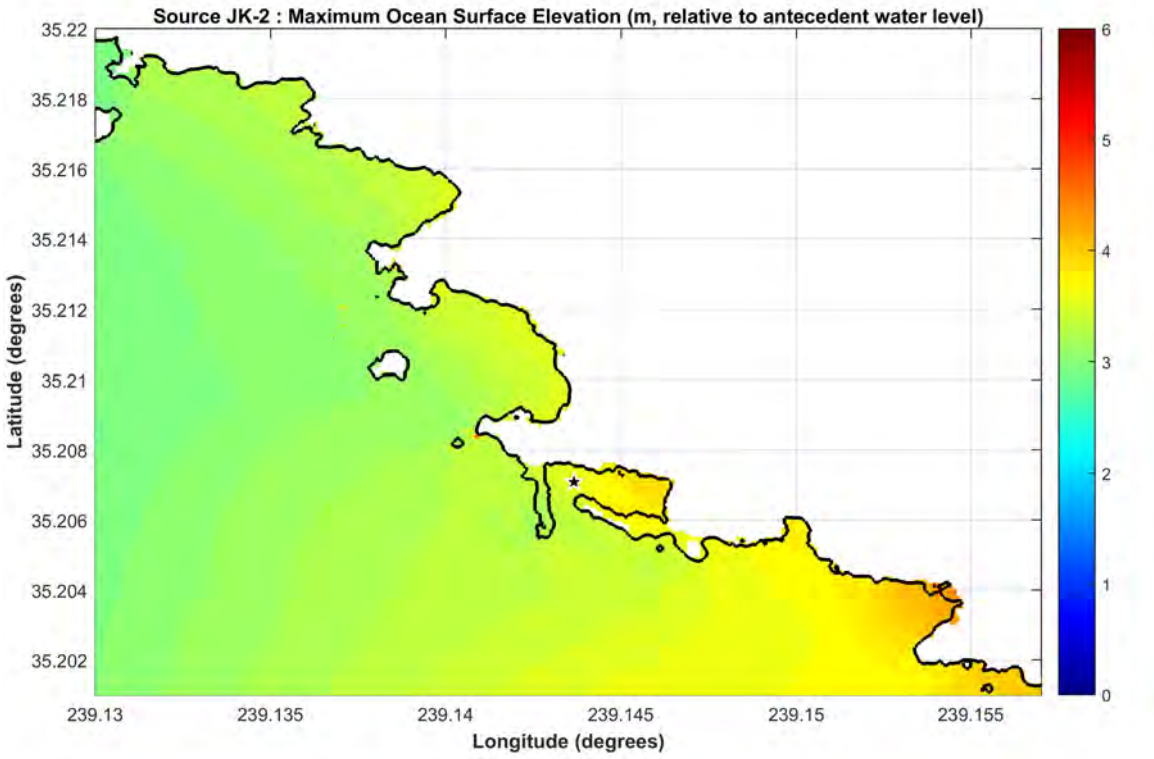

Figure 4.1.5-4: Maximum tsunami elevations (m, relative to antecedent water level) due to JK-2 scenario, where the star marks the South Cove SWIS location.

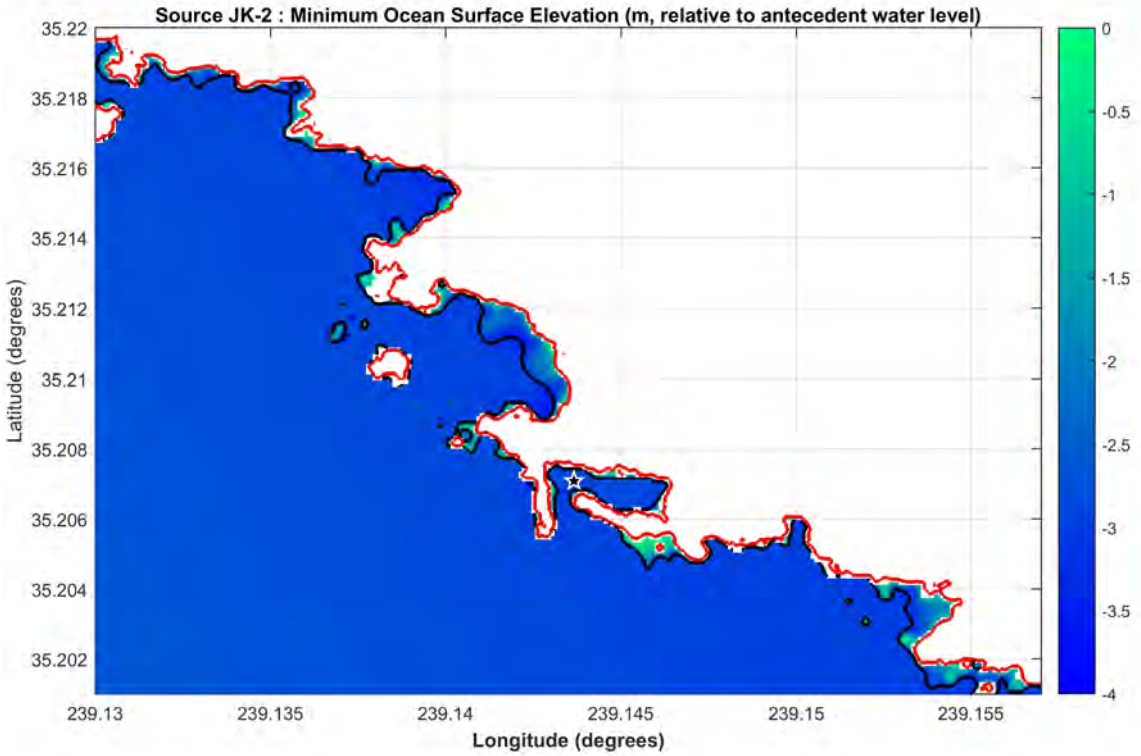

Figure 4.1.5-5: Minimum tsunami elevations (m, relative to antecedent water level) due to JK-2 scenario near the DCPP site. Red line shows the original shoreline, where black line is the estimated drawdown limit and the star marks the South Cove SWIS location.

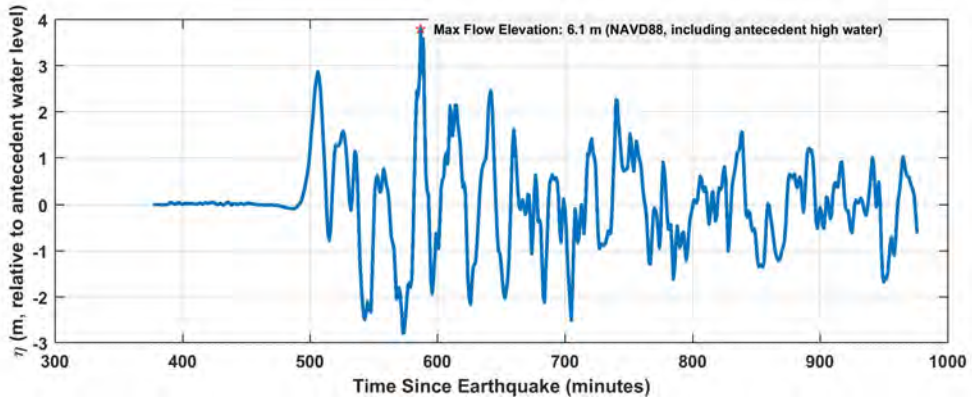

Figure 4.1.5-6: Evolution of ocean surface elevation (η) near South Cove SWIS location due to scenario JK-2 near the DCPP site. Vertical axis shows elevations in meters with respect to the antecedent water level, and the maximum flow elevation given in (NAVD88) including antecedent high water is noted.

4.1.6 Scenario KT-1

For the Kermadec-Tonga subduction zone, only one scenario with a uniform slip of 87.5 m is considered. The results of the KT-1 scenario are given in Figures 4.1.6-1, 4.1.6-2, and 4.1.6-3. The computed maximum tsunami elevations at the DCPP SWIS and discharge locations are 7.5 m and 7.3 m (NAVD88), respectively. The result indicates modest inundation of the South Cove SWIS location, with maximum runup elevations near 6 m above antecedent water level.

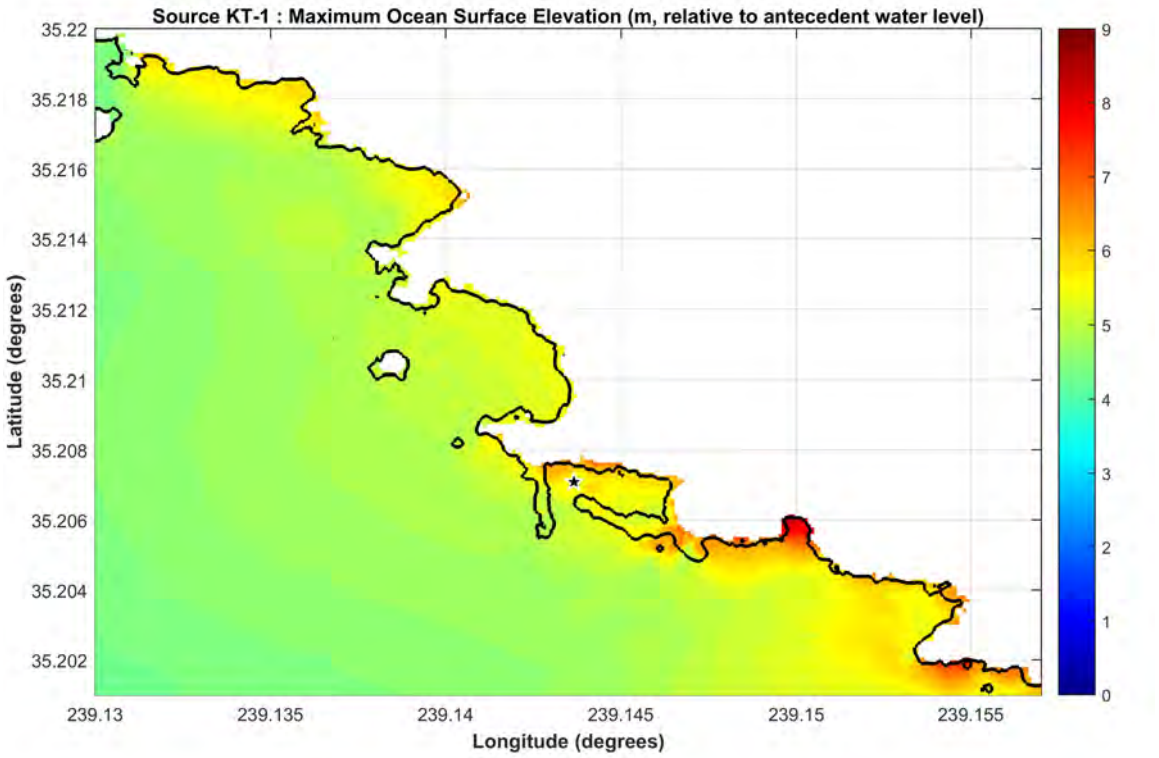

Figure 4.1.6-1: Maximum tsunami elevations (m, relative to antecedent water level) due to KT-1 scenario, where the star marks the South Cove SWIS location.

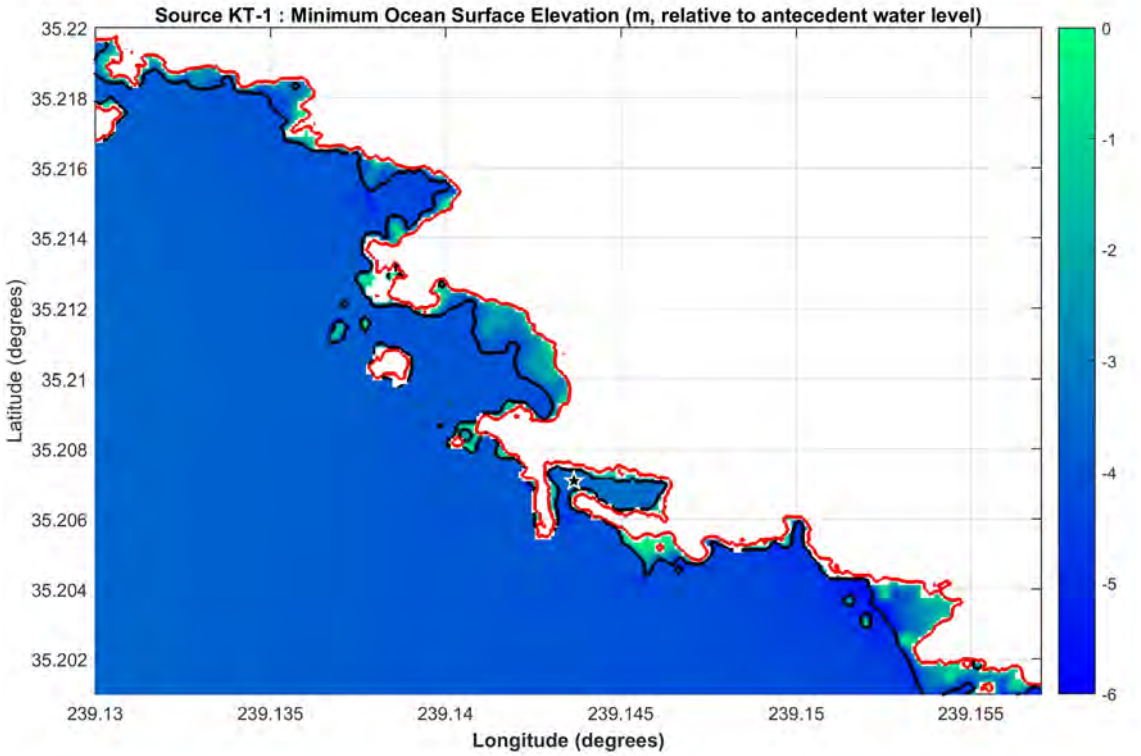

Figure 4.1.6-2: Minimum tsunami elevations (m, relative to antecedent water level) due to KT-1 scenario the DCPP site. Red line shows the original shoreline, where black line is the estimated drawdown limit and the star marks the South Cove SWIS location.

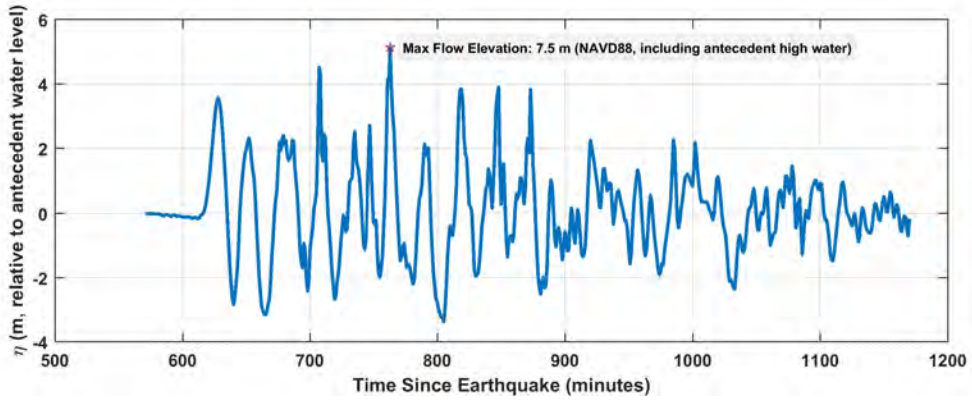

Figure 4.1.6-3: Evolution of ocean surface elevation (η) near South Cove SWIS location due to scenario KT-1 near the DCPP site. Vertical axis shows elevations in meters with respect to the antecedent water level, and the maximum flow elevation given in (NAVD88) including antecedent high water is noted.

4.1.7 Scenario ME-1

The results of the ME-1 scenario are given in Figures 4.1.7-1, .1.7-2, and 4.1.7-3. For the ME-1 tsunami scenario, the source model is based on uniform slip of 52.5 m. The computed maximum and minimum tsunami elevations at both the DCPP SWIS and discharge locations is 2.8 m (NAVD88). This scenario does not cause any significant inundation near the DCPP site, with maximum runup elevations near 0.7 m above antecedent water level.

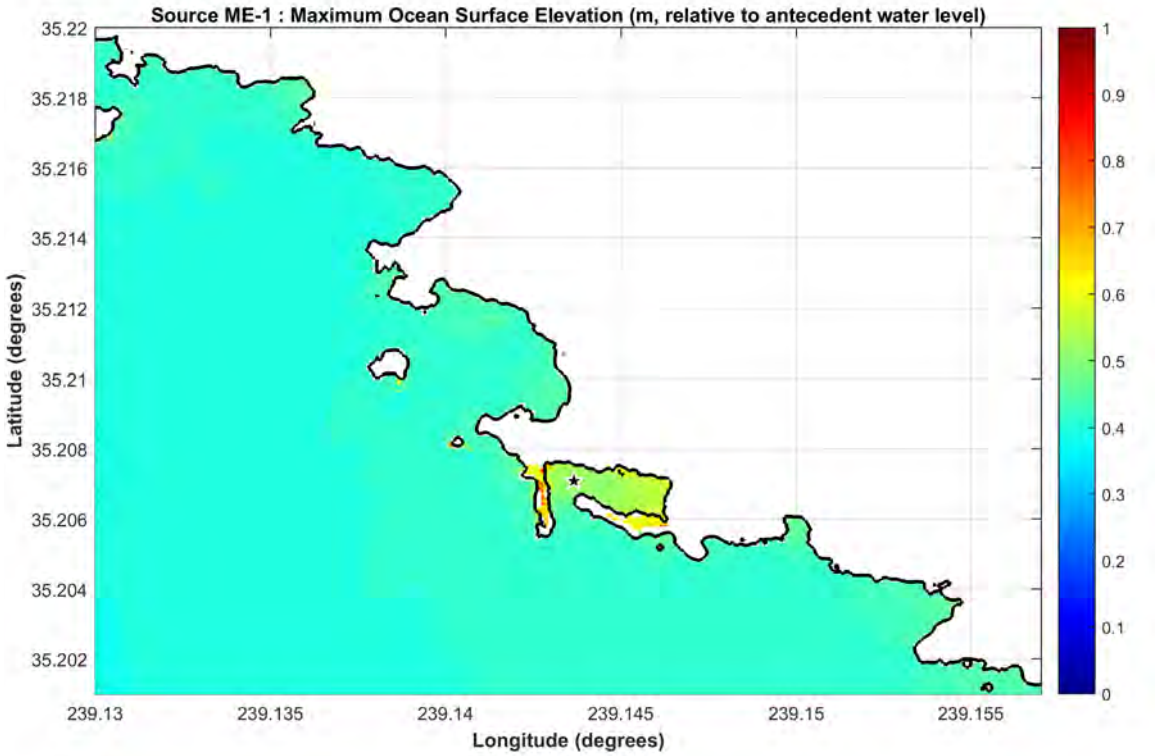

Figure 4.1.7-1: Maximum tsunami elevations (m, relative to antecedent water level) due to ME-1 scenario, where the star marks the South Cove SWIS location.

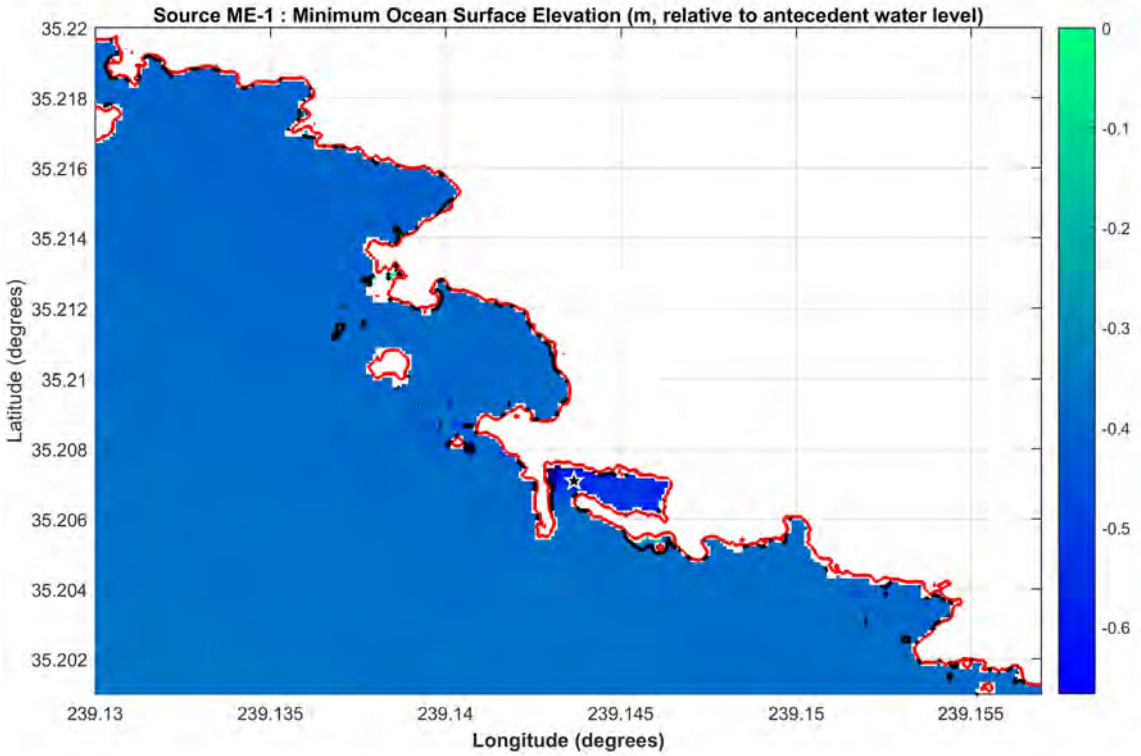

Figure 4.1.7-2: Minimum tsunami elevations (m, relative to antecedent water level) due to ME-1 scenario near the DCPP site. Red line shows the original shoreline, where black line is the estimated drawdown limit and the star marks the South Cove SWIS location.

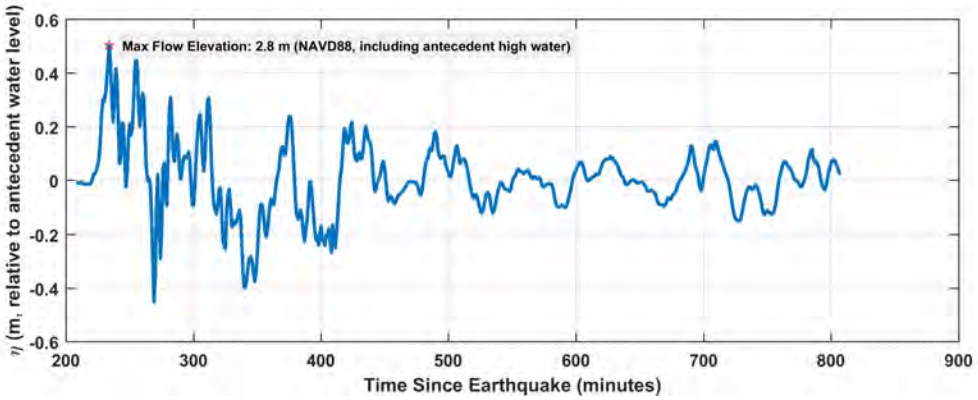

Figure 4.1.7-3: Evolution of ocean surface elevation (η) near South Cove SWIS location due to scenario ME-1 near the DCPP site. Vertical axis shows elevations in meters with respect to the antecedent water level, and the maximum flow elevation given in (NAVD88) including antecedent high water is noted.

4.1.8 Scenarios NG-1 & NG-2

For the New Guinea subduction zone, two distinct scenarios are considered, both with uniform slip distributions. The slip values are 120 m and 150 m for NG-1 and NG-2, respectively. The results of the NG-1 scenario are given in Figures 4.1.8-1, 4.1.8-2, and 4.1.8-3. The computed maximum tsunami elevations at the DCPP SWIS and discharge locations are 6.0 m and 5.6 m (NAVD88), respectively These results indicate small-scale inundation of both the discharge and SWIS locations with run-up heights in the order of 3.5 m above antecedent water level.

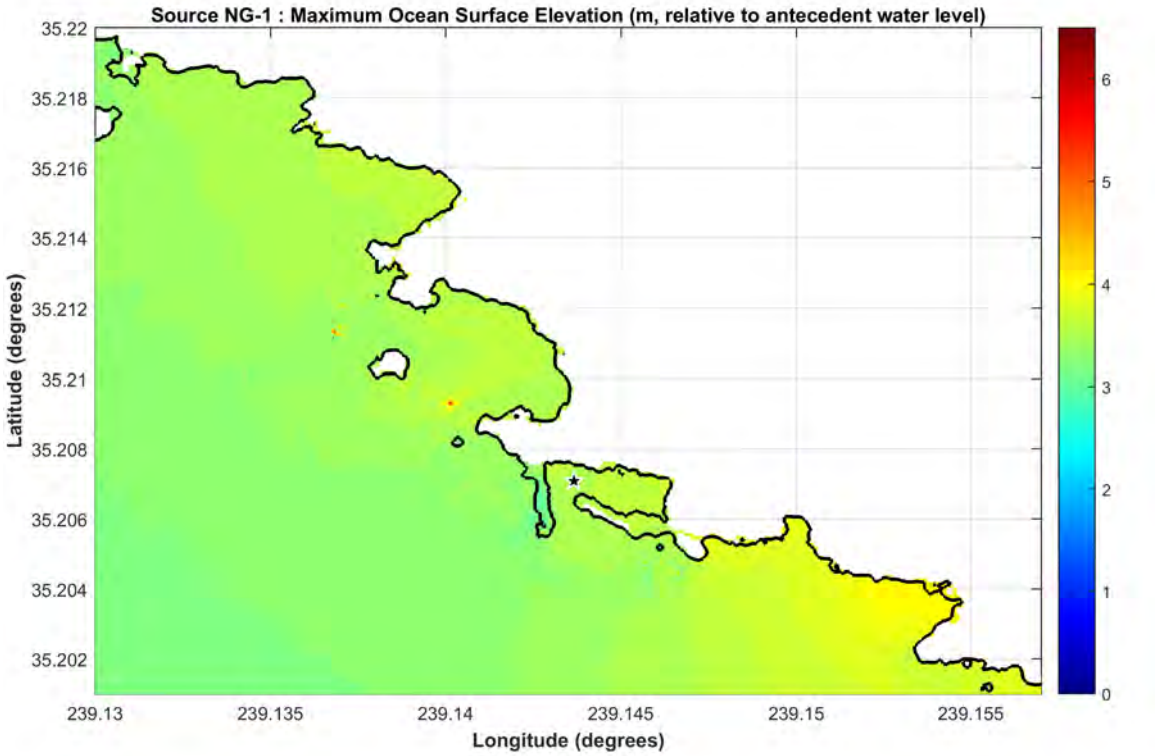

Figure 4.1.8-1: Maximum tsunami elevations (m, relative to antecedent water level) due to NG-1 scenario, where the star marks the South Cove SWIS location.

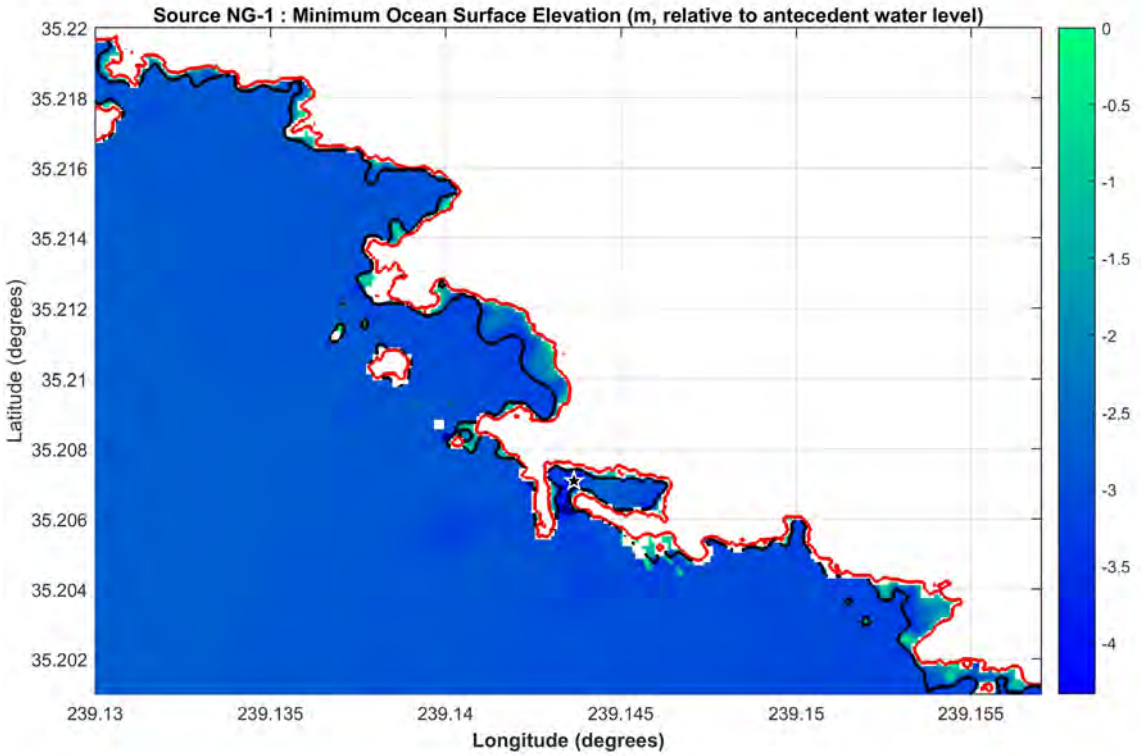

Figure 4.1.8-2: Minimum tsunami elevations (m, relative to antecedent water level) due to NG-1 scenario near the DCPP site. Red line shows the original shoreline, where black line is the estimated drawdown limit and the star marks the South Cove SWIS location.

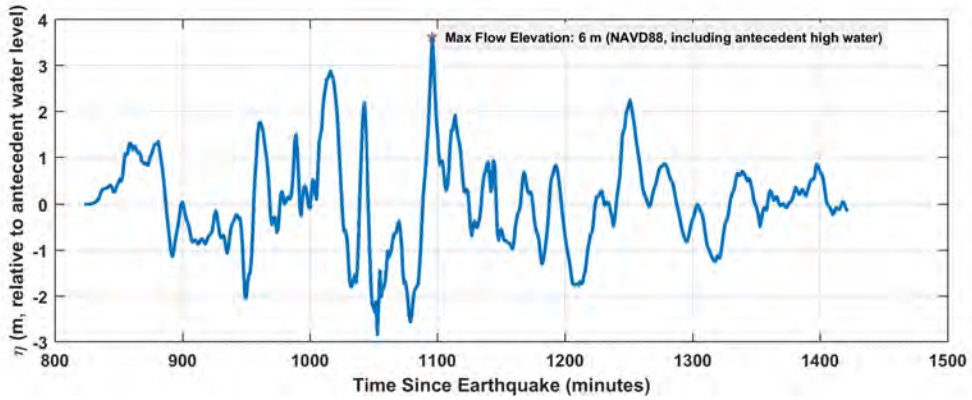

Figure 4.1.8-3: Evolution of ocean surface elevation (η) near South Cove SWIS location due to scenario NG-1 near the DCPP site. Vertical axis shows elevations in meters with respect to the antecedent water level, and the maximum flow elevation given in (NAVD88) including antecedent high water is noted.

The results of the NG-2 scenario are given in Figures 4.1.8-4, 4.1.8-5, and 4.1.8-6. The computed maximum tsunami elevations at the DCPP SWIS and discharge locations are 6.1 m and 6.0 m (NAVD88), respectively . These results indicate some small-scale inundation of both discharge and SWIS sites with run-up heights in the order of 3.5 m above antecedent water level.

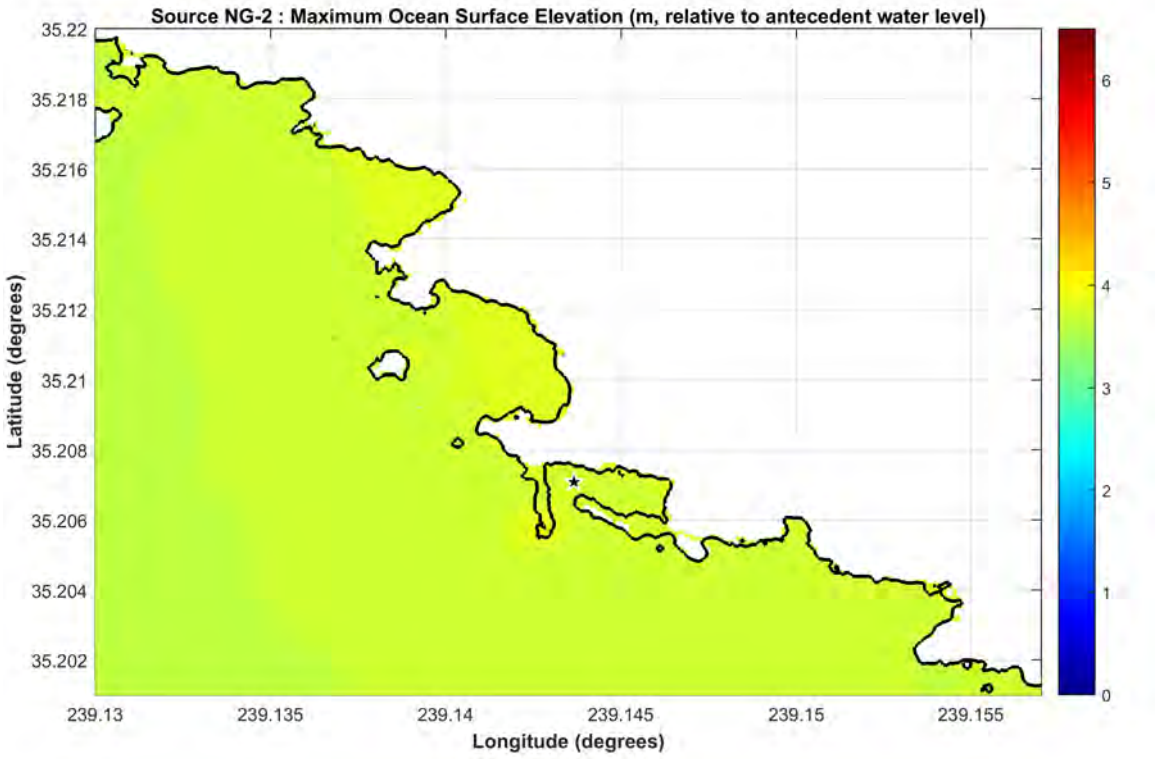

Figure 4.1.8-4: Maximum tsunami elevations (m, relative to antecedent water level) near due to NG-2 scenario, where the star marks the South Cove SWIS location.

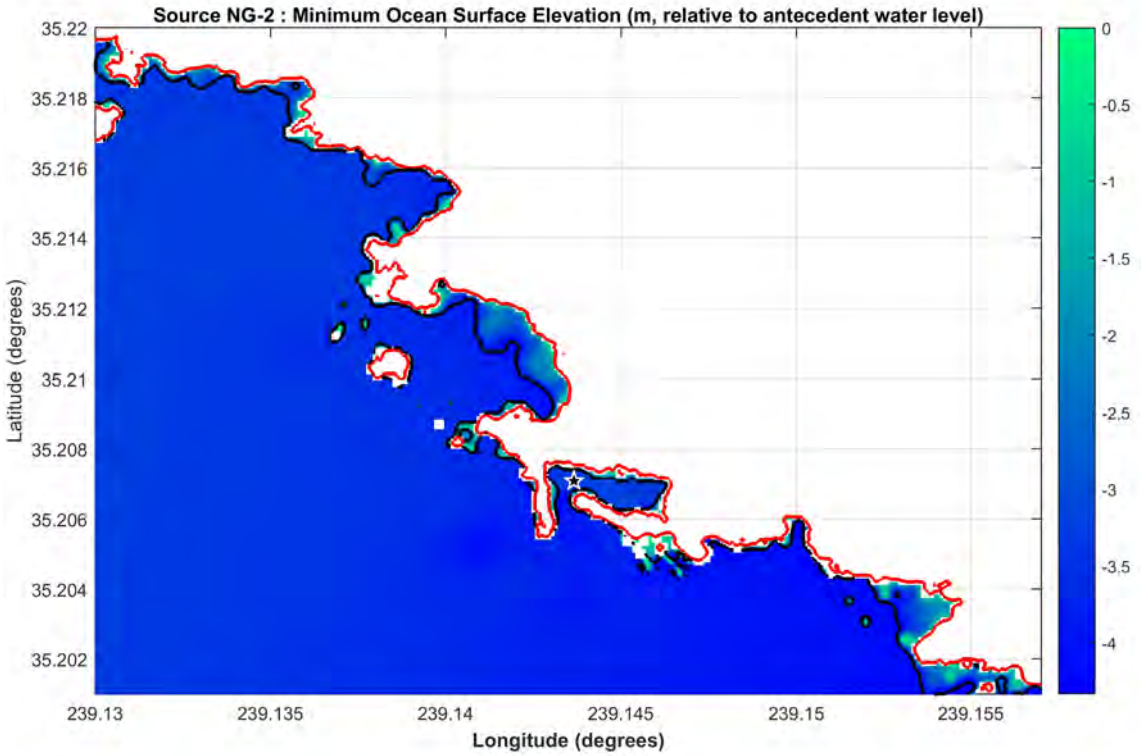

Figure 4.1.8-5: Minimum tsunami elevations (m, relative to antecedent water level) due to NG-2 scenario near the DCPP site. Red line shows the original shoreline, where black line is the estimated drawdown limit and the star marks the South Cove SWIS location.

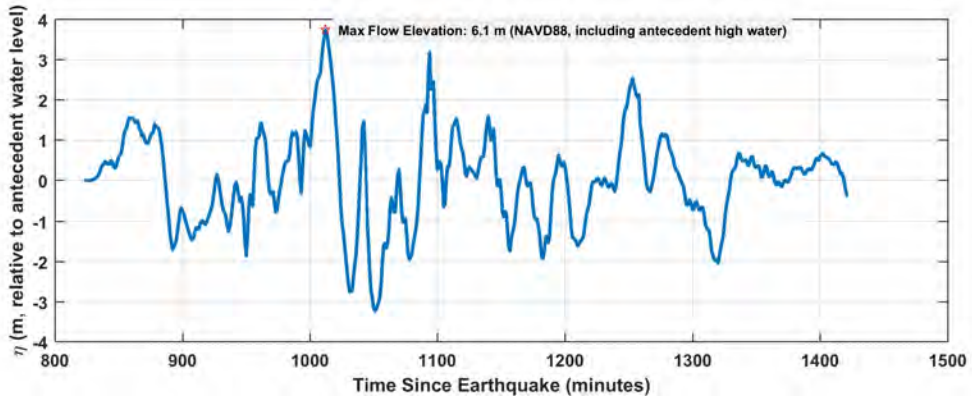

Figure 4.1.8-6: Evolution of ocean surface elevation (η) near South Cove SWIS location due to scenario NG-2 near the DCPP site. Vertical axis shows elevations in meters with respect to the antecedent water level, and the maximum flow elevation given in (NAVD88) including antecedent high water is noted.

4.1.9 Scenario RN-1

The results of the RN-1 scenario are given in Figures 4.1.8-9, 4.1.8-10, and 4.1.8-11. The computed maximum tsunami elevations at the DCPP SWIS and discharge locations are 4.2 m and 4.0 m (NAVD88), respectively. This scenario does not cause any significant inundation near the DCPP site, with maximum runup elevations near 2.0 m above antecedent water level.

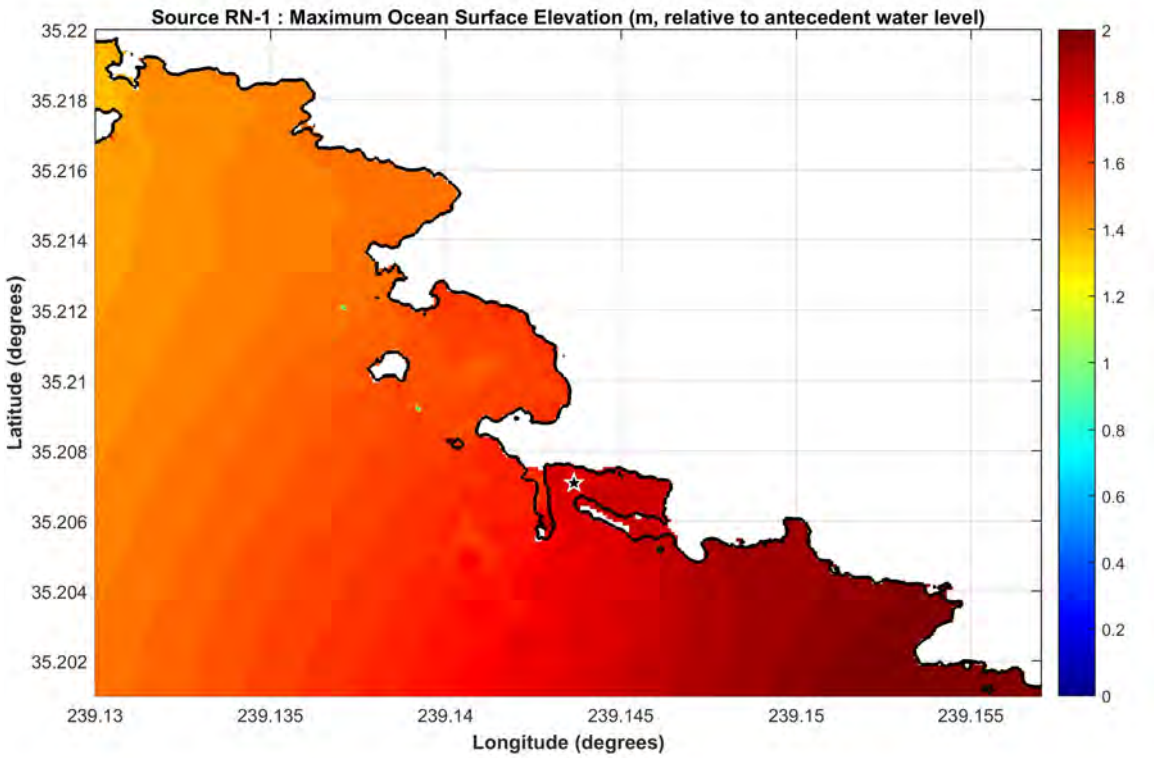

Figure 4.1.9-1: Maximum tsunami elevations (m, relative to antecedent water level) due to RN-1 scenario, where the star marks the South Cove SWIS location.

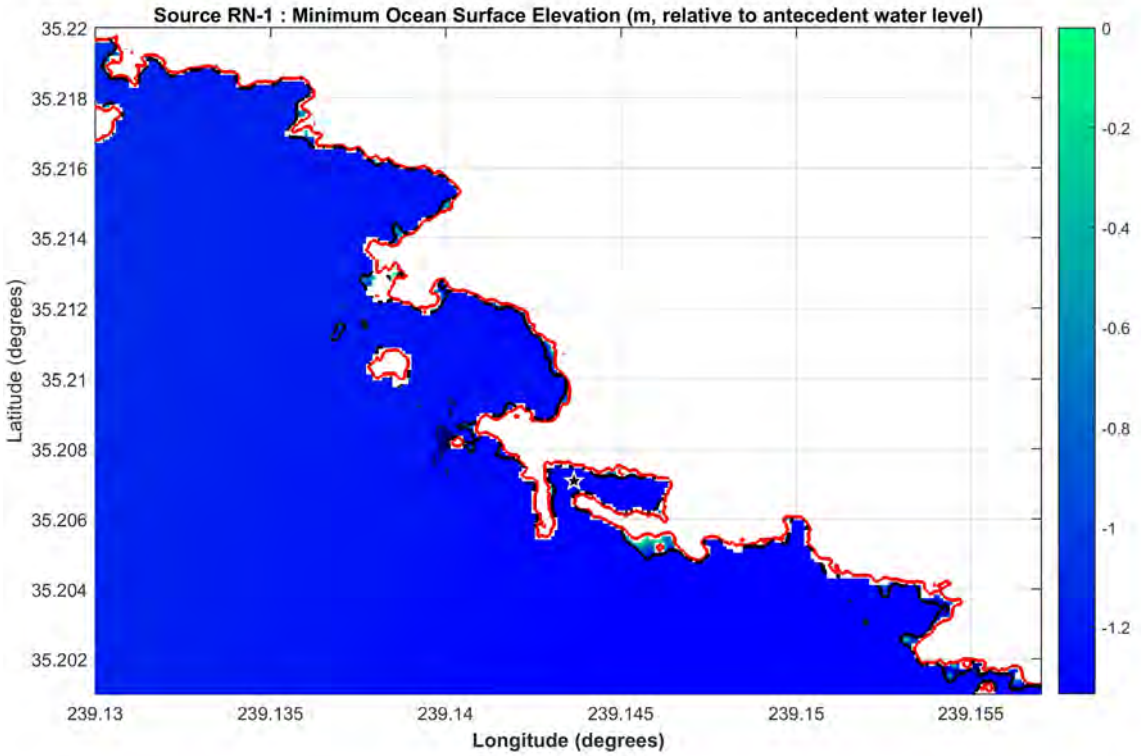

Figure 4.1.9-2: Minimum tsunami elevations (m, relative to antecedent water level) due to RN-1 scenario near the DCPP site. Red line shows the original shoreline, where black line is the estimated drawdown limit and the star marks the South Cove SWIS location.

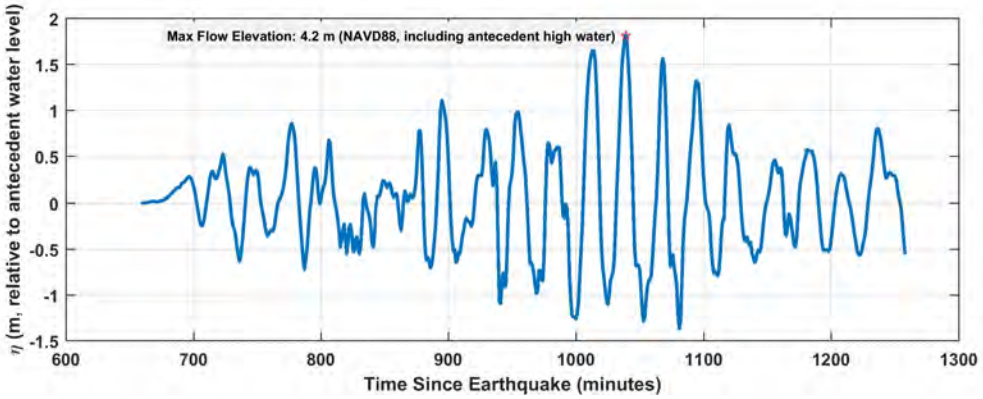

Figure 4.1.9-3: Evolution of ocean surface elevation (η) near South Cove SWIS location due to scenario RN-1 near the DCPP site. Vertical axis shows elevations in meters with respect to the antecedent water level, and the maximum flow elevation given in (NAVD88) including antecedent high water is noted.

4.1.10 Scenarios SA-1, SA-2, & SA-3

For the South America subduction zone, three different scenarios arising from different locations are considered. SA-1 is located offshore Peru, whereas SA-2 and SA-3 are located in northern and southern Chile, respectively. The results of SA-1 scenario are given in Figures 4.1.10-1, 4.1.10-2, and 4.1.10-3. For the SA-1 tsunami scenario, the source model is based on uniform slip of 87.5 m. The computed maximum tsunami elevations at both the DCPP SWIS and discharge locations is 3.9 m (NAVD88). This scenario does not cause any significant inundation near the DCPP site, with maximum runup elevations near 1.5 m above antecedent water level.

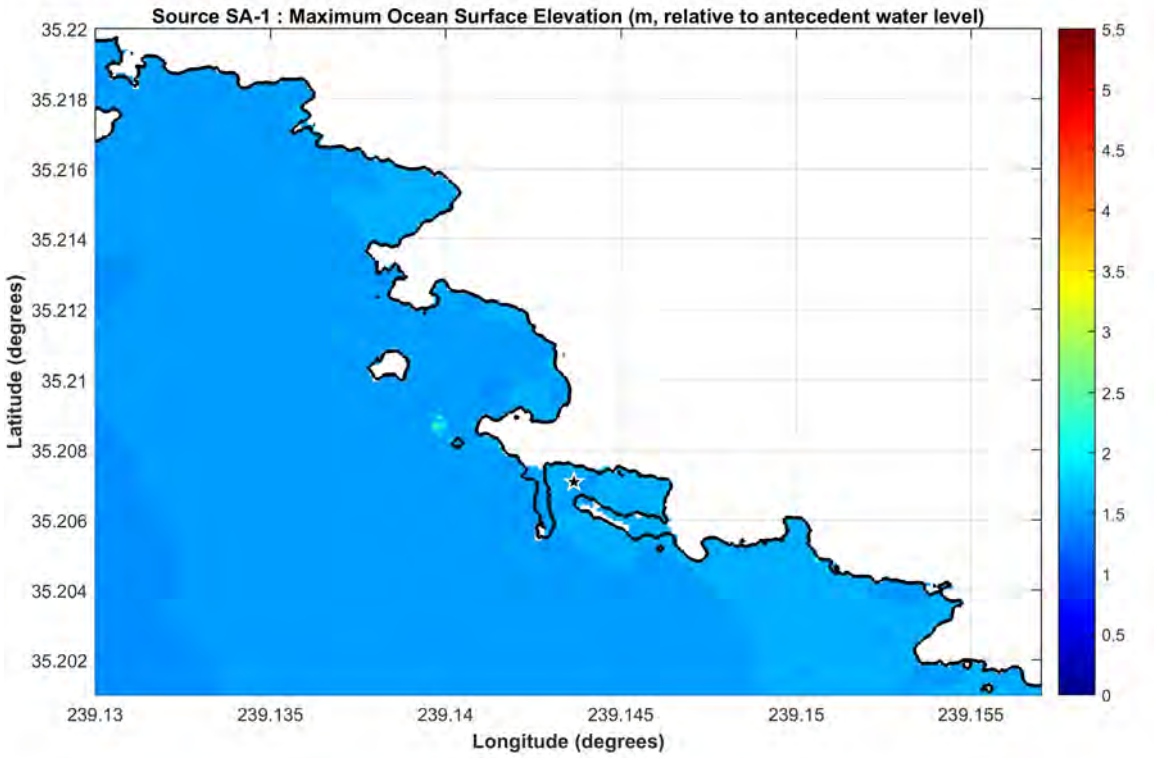

Figure 4.1.10-1: Maximum tsunami elevations (m, relative to antecedent water level) due to SA-1 scenario, where the star marks the South Cove SWIS location.

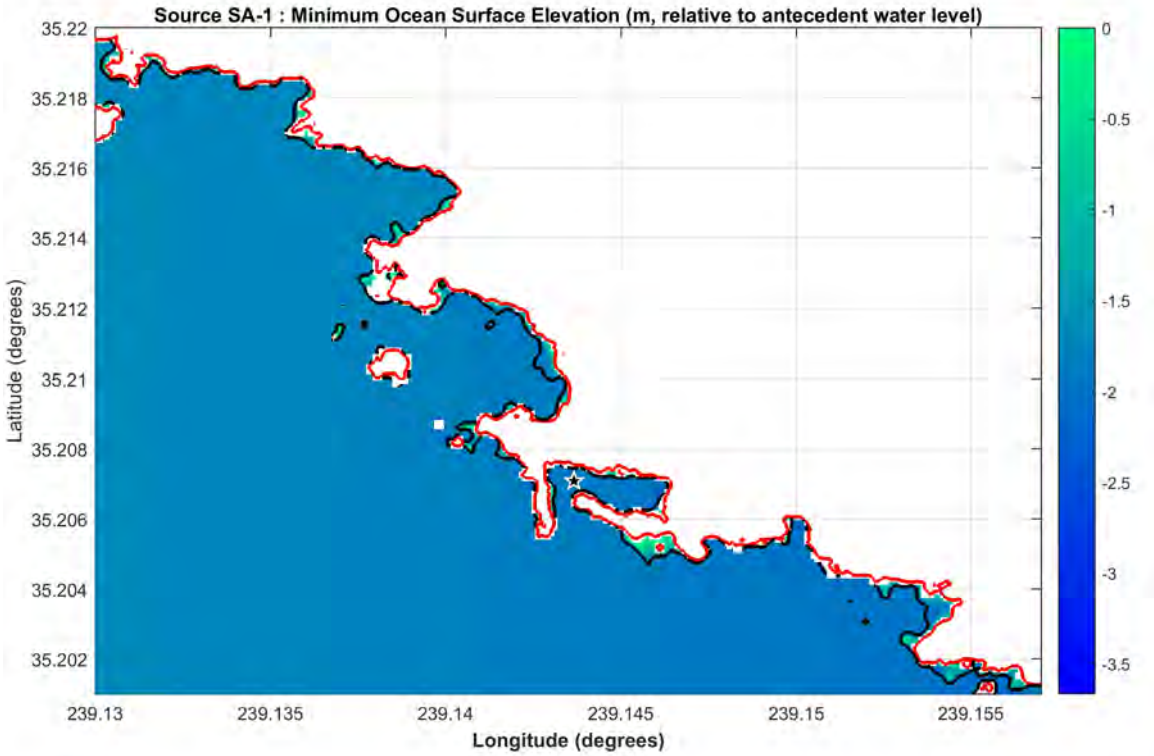

Figure 4.1.10-2: Minimum tsunami elevations (m, relative to antecedent water level) due to SA-1 scenario near the DCPP site. Red line shows the original shoreline, where black line is the estimated drawdown limit and the star marks the South Cove SWIS location.

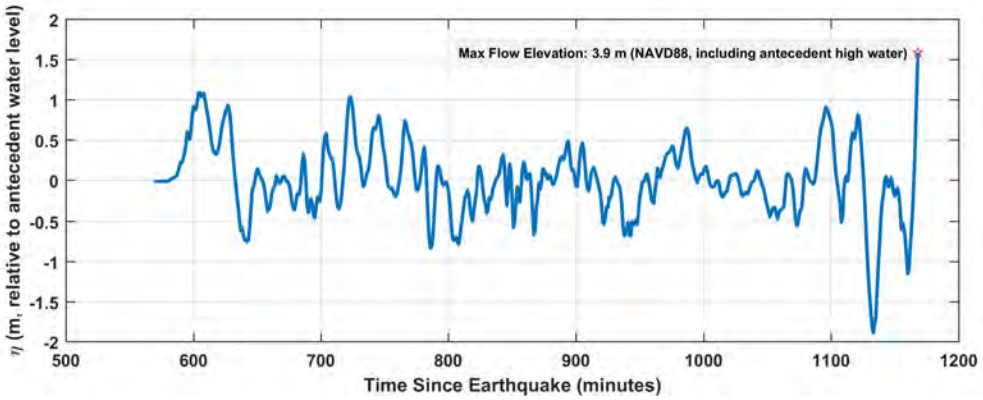

Figure 4.1.10-3: Evolution of ocean surface elevation (η) near South Cove SWIS location due to scenario SA-1 near the DCPP site. Vertical axis shows elevations in meters with respect to the antecedent water level, and the maximum flow elevation given in (NAVD88) including antecedent high water is noted.

The results of the SA-2 scenario are given in Figures 4.1.10-4, 4.1.10-5, and 4.1.10-6 . For the SA-2 tsunami scenario, the source model is based on uniform slip of 87.5 m. The computed maximum tsunami elevations at the DCPP SWIS and discharge locations are 4.2 m and 4.1 m (NAVD88), respectively. This scenario does not cause any significant inundation near the DCPP site, with maximum runup elevations near 2 m above antecedent water level.

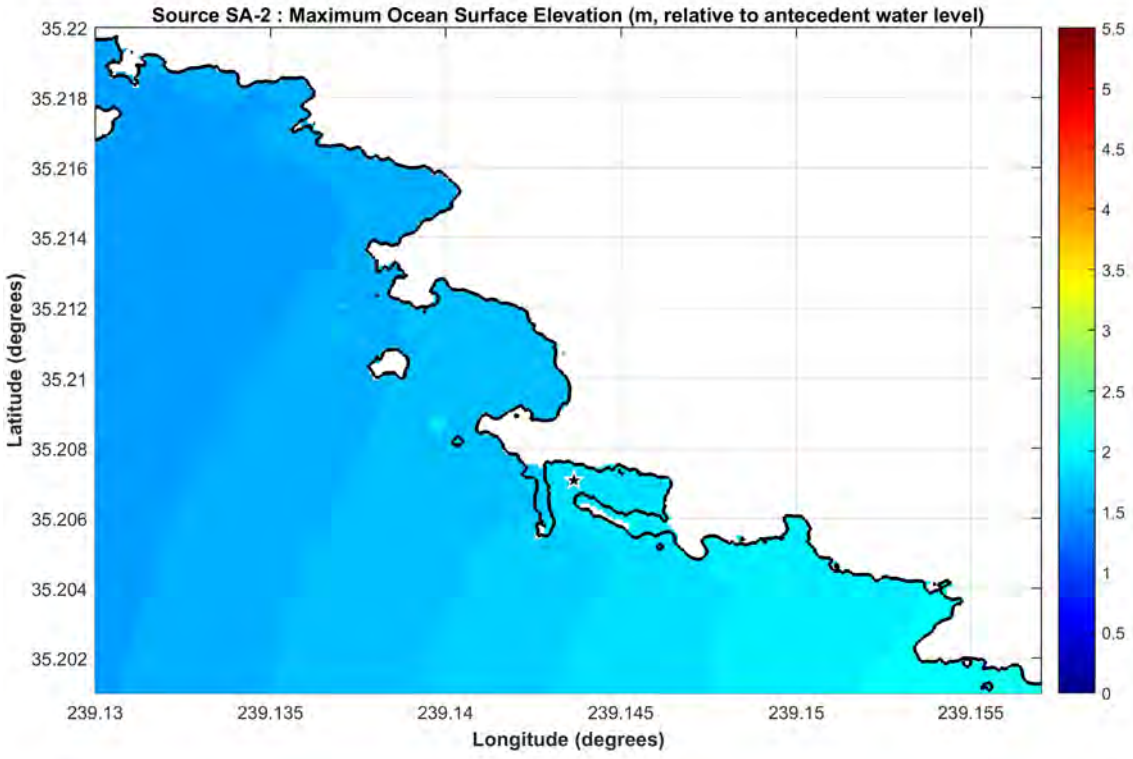

Figure 4.1.10-4: Maximum tsunami elevations (m, relative to antecedent water level) due to SA-2 scenario, where the star marks the South Cove SWIS location.

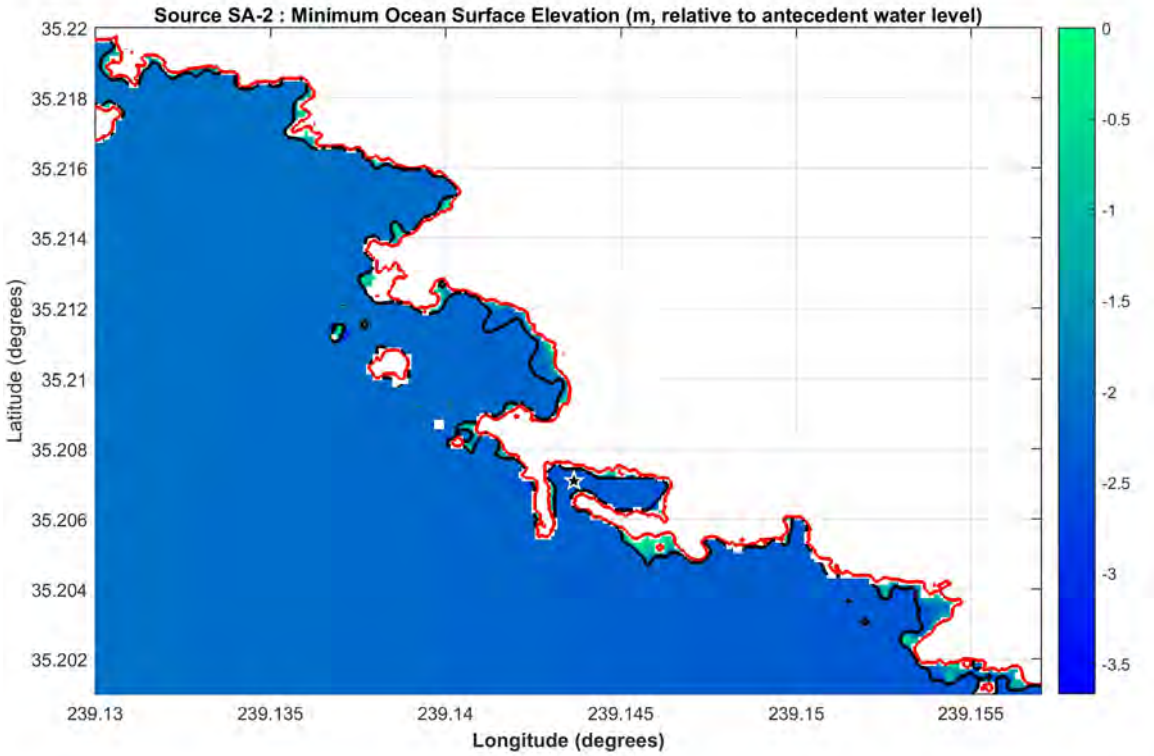

Figure 4.1.10-5: Minimum tsunami elevations (m, relative to antecedent water level) due to SA-2 scenario near the DCPP site. Red line shows the original shoreline, where black line is the estimated drawdown limit and the star marks the South Cove SWIS location.

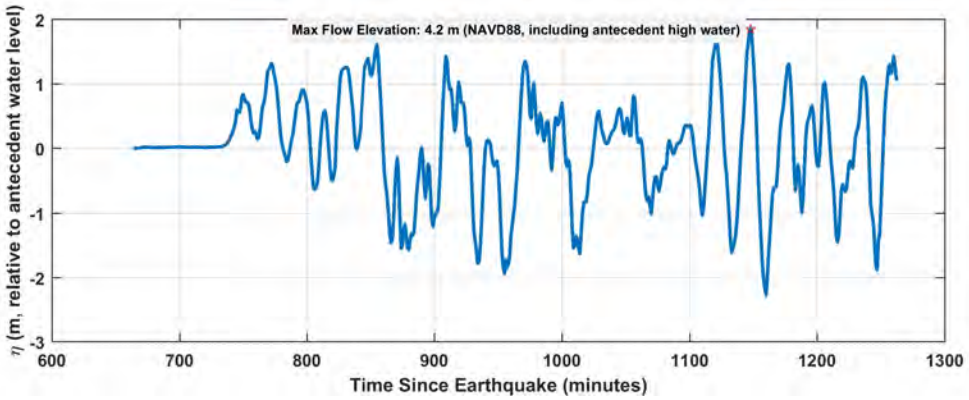

Figure 4.1.10-6: Evolution of ocean surface elevation (η) near South Cove SWIS location due to scenario SA-2 near the DCPP site. Vertical axis shows elevations in meters with respect to the antecedent water level, and the maximum flow elevation given in (NAVD88) including antecedent high water is noted.

The results of the SA-3 scenario are given in Figures 4.1.10-7, 4.1.10-8, and 4.1.10-9. For the SA-3 tsunami scenario, the source model is based on uniform slip of 87.5 m. The computed maximum tsunami elevations at the DCPP SWIS and discharge locations are 5.8 m and 5.5 m (NAVD88), respectively. The result indicates modest inundation of the South Cove SWIS location, with maximum runup elevations near 4 m above antecedent water level.

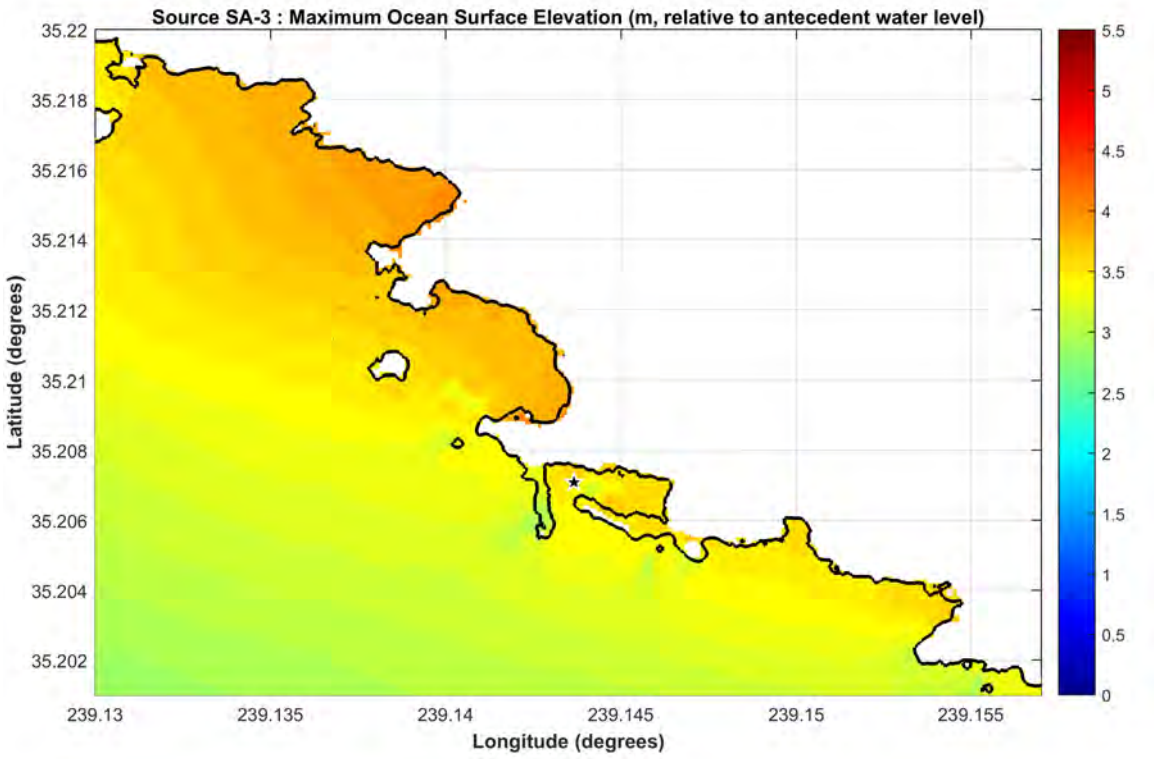

Figure 4.1.10-7: Maximum tsunami elevations (m, relative to antecedent water level) due to SA-3 scenario, where the star marks the South Cove SWIS location.

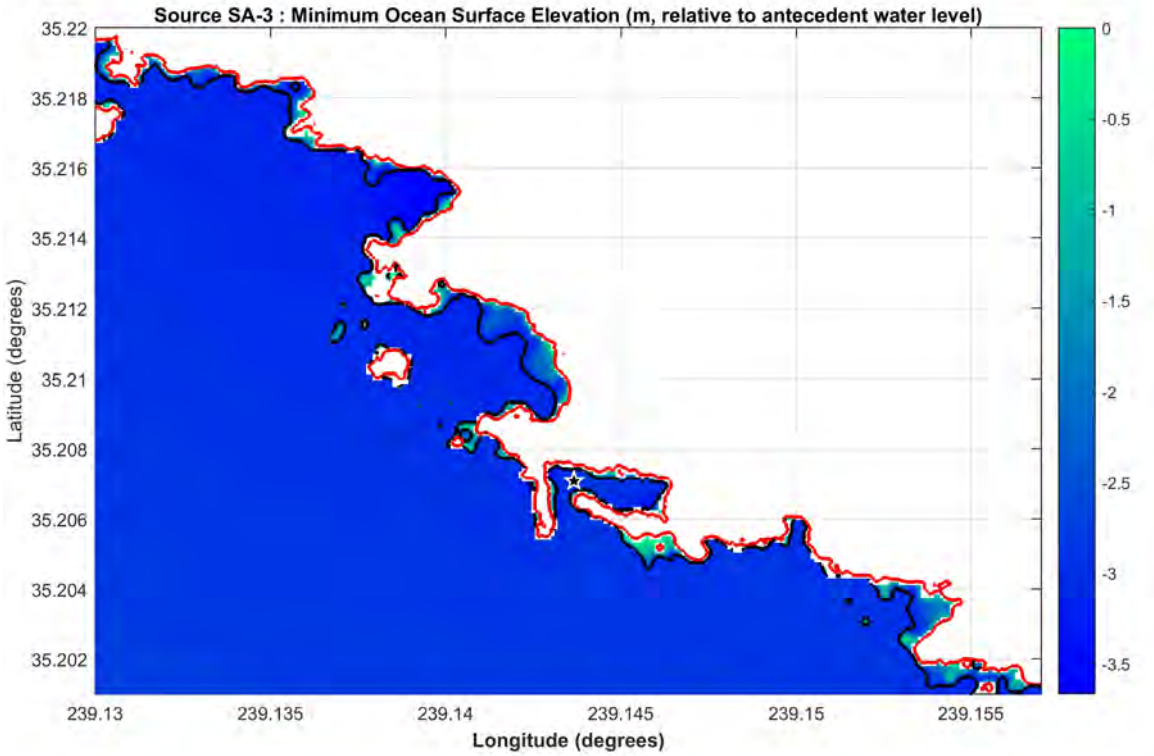

Figure 4.1.10-8: Minimum tsunami elevations (m, relative to antecedent water level) due to SA-3 scenario near the DCPP site. Red line shows the original shoreline, where black line is the estimated drawdown limit and the star marks the South Cove SWIS location.

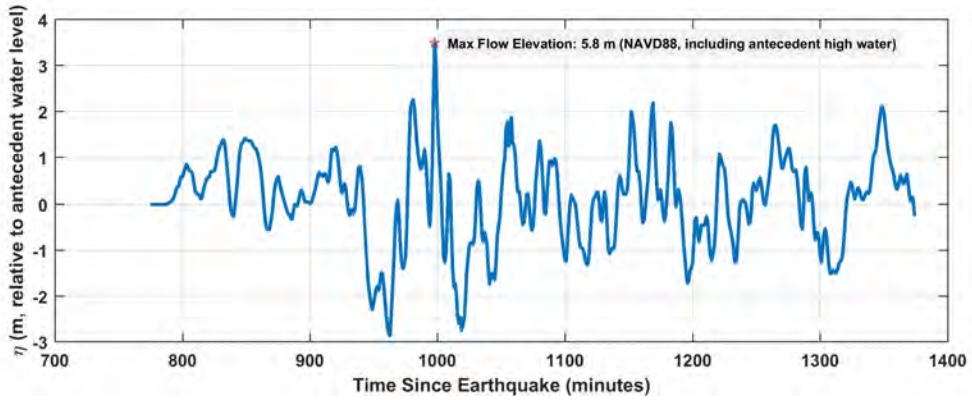

Figure 4.1.10-9: Evolution of ocean surface elevation (η) near South Cove SWIS location due to scenario SA-3 near the DCPP site. Vertical axis shows elevations in meters with respect to the antecedent water level, and the maximum flow elevation given in (NAVD88) including antecedent high water is noted.

4.2 Tsunamis from Regional Earthquake Sources

Information Submitted by the Licensee

The FHRR uses the FUNWAVE-TVD model to simulate two different local seismic tsunami sources. The magnitudes of the earthquakes fall between M_w7.5-7.7. The maximum flow elevation found near the DCPP SWIS is 0.4 m (NAVD88); the minimum flow elevation does not drop measurably below the stillwater elevation datum.

Taylor Engineering Technical Evaluation

In this section we present the results of 18 local California tsunami sources discussed in subsection 2.1.4. Regional tsunami propagation patterns in California have been computed on a computational grid using the MOST model to get the offshore tsunami water levels for each regional earthquake scenario as previously described for the distant earthquake sources. The evolution of tsunamis from all sources are gathered in Figure 4.2-1 which illustrates the sea surface elevation offshore the DCPP site for 10 hours following the simulated earthquake event. We reiterate that the time series shown in Figure 4.2-1 are from relatively coarse resolution simulations which do not resolve site-specific bathymetry and topography features, such as the South Cove jetties. These results are used to estimate the tsunami heights offshore of the DCPP site. However, due to the coarse resolution, near-DCPP runup elevations are likely an order of magnitude (i.e. ten times) larger than the maximum crest elevations shown in Figure 4.2-1. From the time series, it becomes apparent that the local California sources generate smaller tsunami waves at the DCPP site as compared to the M_w9+ far-field sources considered here. The local faults are not big enough to accommodate M_w9+ earthquakes and therefore, are deficient in terms of tsunami generation capability (compared to the M_w9+ far-field sources).

Based on the time series and taking into consideration the likely underestimation of maximum crest elevations, we conclude that the probable maximum tsunami runup is not affected by the local sources discussed in 2.1.4. The maximum tsunami runup heights for local sources described in 2.1.4 produce computed water heights of 0.5 m or less at the South Cove SWIS.

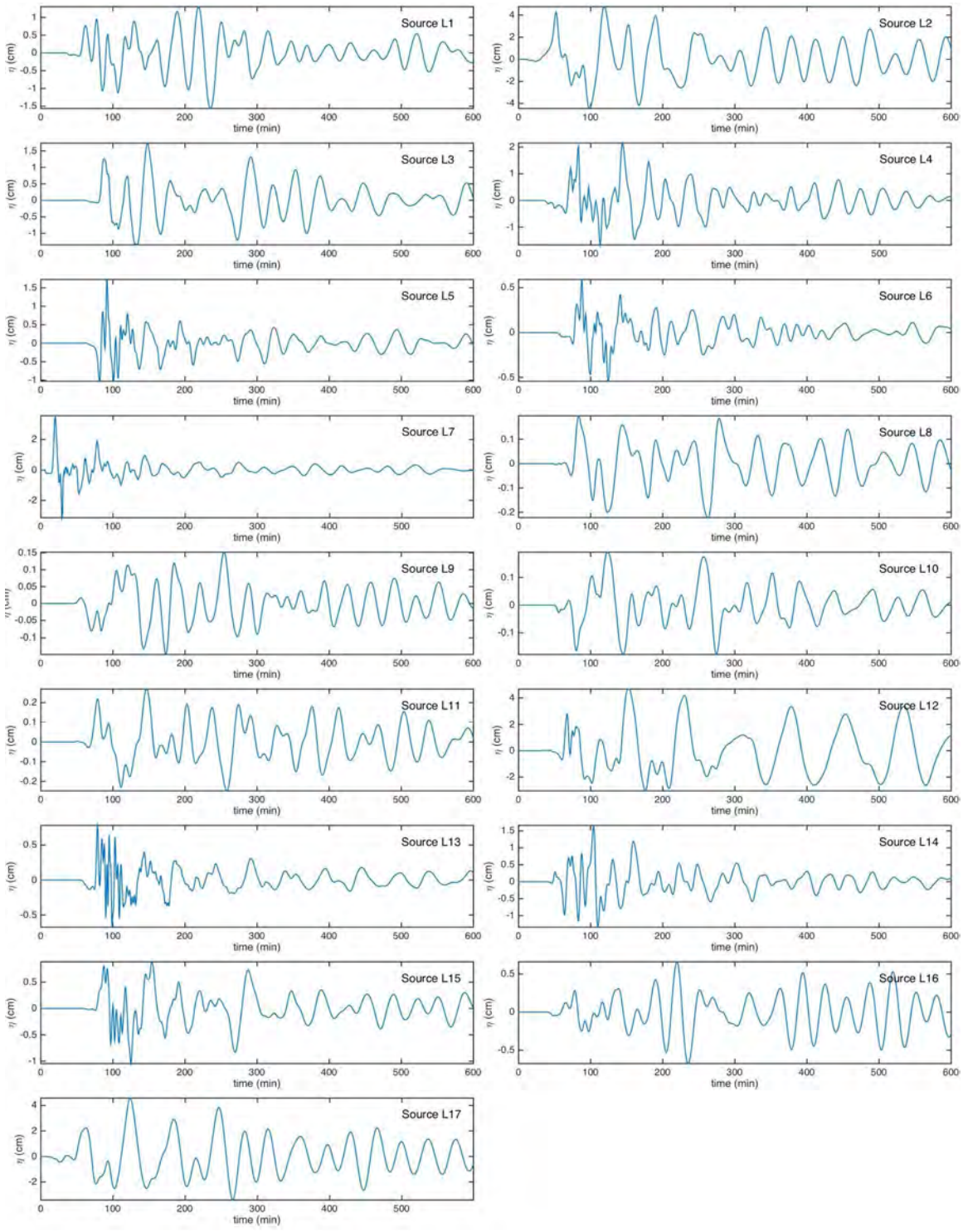

Figure 4.2-1 Offshore tsunami heights due to regional sources created near the DCPP site; note that the elevations plotted here are with respect to the antecedent water level. Sources are described in Section 2.1.4.

4.2.1 Lompoc 1927 Earthquake

The earthquake that occurred just offshore of Lompoc in 1927 along the Hosgri fault was a M_w=7.0 earthquake as discussed by Satake and Somerville (1992). Based on their analysis of tsunami records, they formed a source model for tsunami analysis with a uniform slip of 2.5 m. We use the same earthquake source model as Satake and Somerville (1992) but perform the tsunami simulation with improved bathymetric resolution (e.g., accounting for the South Cove jetties) to simulate the Lompoc 1927 earthquake-generated tsunami. Figures 4.2.1-1 and 4.2.1-2 illustrate the simulation results. The computed maximum tsunami elevations at the DCPP SWIS and discharge locations are 3.4 m and 3.5 m (NAVD88), respectively. The arrival time of the maximum tsunami elevation is estimated as one hour. This scenario does not cause any significant inundation near the DCPP site, with maximum runup elevations near 1 m above antecedent water level.

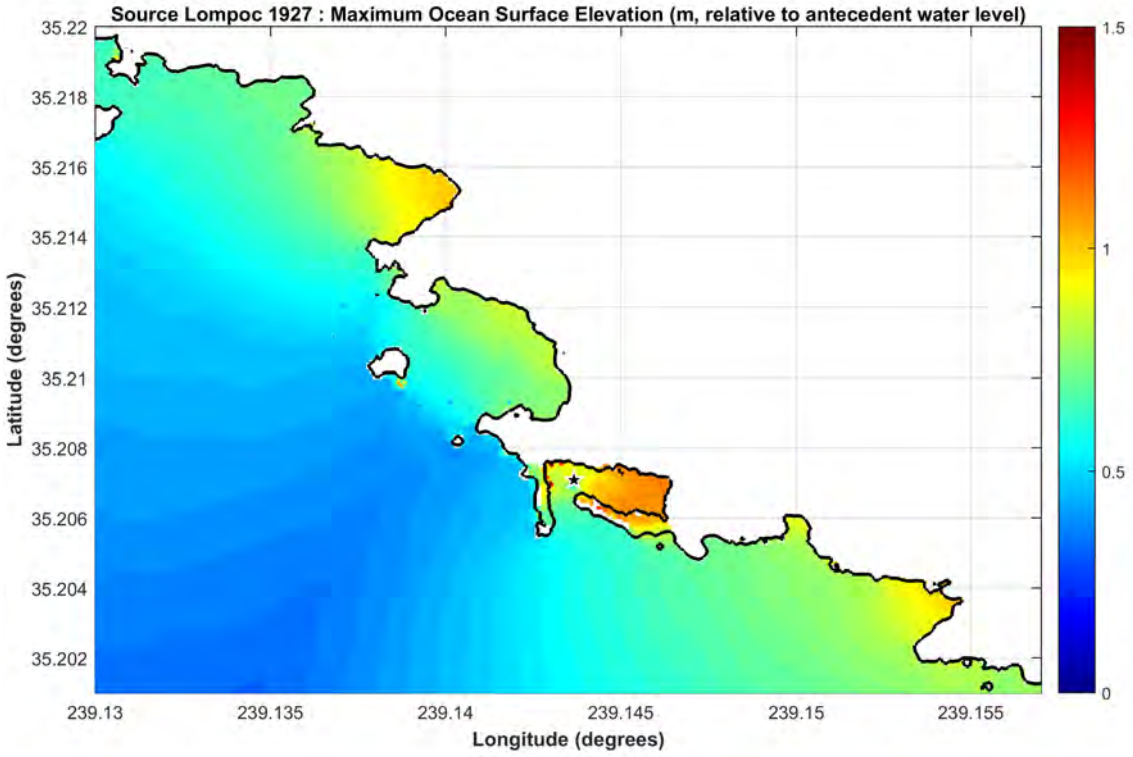

Figure 4.2.1-1 Maximum tsunami elevations (m, relative to antecedent water level) due to Lompoc 1927 earthquake scenario, where the star marks the South Cove SWIS location.

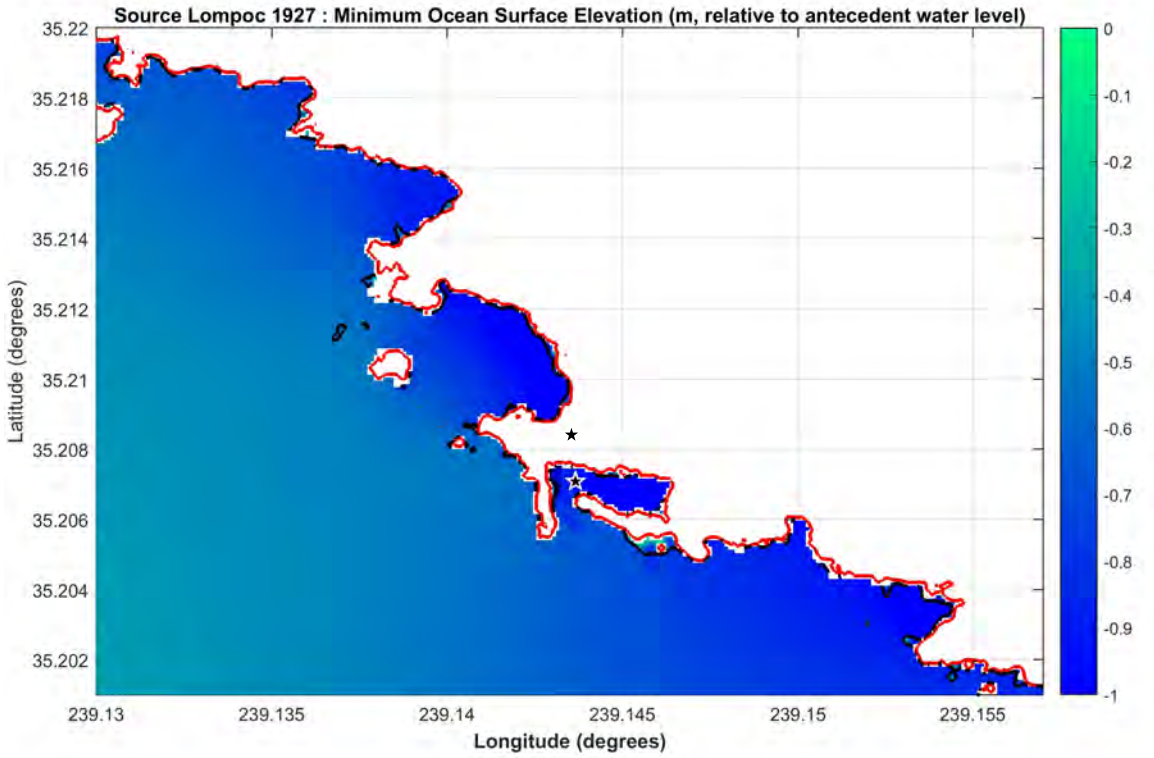

Figure 4.2.1-2 Minimum tsunami elevations (m, relative to antecedent water level) due to Lompoc 1927 earthquake near the DCPP site. Red line shows the original shoreline, where black line is the estimated drawdown limit and the star marks the South Cove SWIS location.

4.3 Tsunamis from Distant Landslide Sources

Information Submitted by the Licensee

The FHRR does not consider any distant landslide sources.

Taylor Engineering Technical Evaluation

In this section, the tsunami generated from two distant subaerial flank collapses are investigated. Due to the distant nature of the sources and the expectation that radial spreading is an important process, one-horizontal-dimension simulations of these slide sources are not undertaken. The general analysis employed here is to first understand the near-source tsunami properties with a detailed slide mechanics model, and then couple those results to an oceanic propagation model accurate for dispersive waves.

4.3.1 Kilauea Flank Collapse

The initial generation of the tsunami from this flank collapse seaward of the Hilina fault uses the geophysical information provided in subsection 2.1.3 with the numerical model iSALE. For more information about the iSALE model, see Section 3.2. Figure 4.3.1-1a shows simplified models of the pre-Hilina slump topology for different uniform friction

distributions (from Okubo, 2004), and Figure 4.3.1-1b depicts the geometric model used for collapse simulations with iSALE. The material properties of the collapsing mass are chosen to maximize the generated wave characteristics; the sparse data from the runout masses do not allow for constraining the material parameters for the collapse body with a method described in Weiss, et al. (2013). Thus, this is a conservative source mechanism.

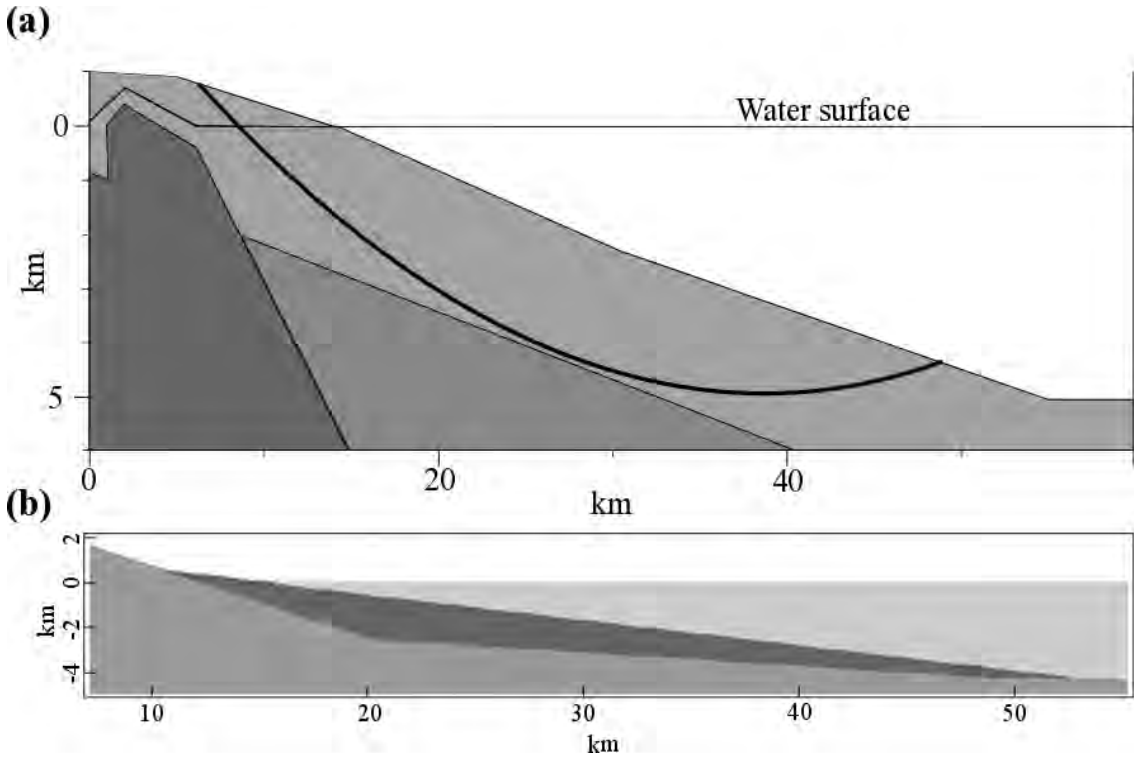

Figure 4.3.1-1: (a) Geotechnical model used from Okubo (2004). The solid line represents the surface along which the flank collapse will take place. (b) Simplified geometric model for iSALE derived from (a).

To couple the near field model (iSALE) with the oceanic propagation model (COULWAVE), wave information near the source from iSALE is integrated into COULWAVE. This leads to an initial condition for COULWAVE as shown in Figure 4.3.1-2. Furthermore, note that the location of the slide is rotated to the north, such that the generated tsunami has the optimum directionality towards the California coastline. This is an ad-hoc modification, meant to increase the conservatism of the potential source. The remaining subplots in Figure 4.3.1-2 show the radial spreading of the waves and the associated rapid decay in maximum wave amplitude. By 40 minutes after the landslide, the waves have traveled 1000 km and the maximum crest elevation has decreased to 30 m.

Away from the source region, the amplitude continues to decrease due to radial spreading, but at a much slower rate. Figure 4.3.1-3 provides a set of snapshots of the tsunami as it travels across the Pacific towards the California coastline. Halfway through its journey to California, the maximum crest elevation has decreased to less than 10 m. Note, however, that the effects of directionality are clear and significant, as the amplitude directed towards

California is larger than that directed towards Alaska or South America. By 240 minutes after the slide, the leading wave begins to enter the shallower waters offshore of California, and the wave height begins to grow through shoaling.

Figure 4.3.1-4 gives another set of snapshots of the tsunami, here zoomed-in on the California coastline. The tsunami arrives at the DCPP site 270 minutes after initiation of the slide. This simulation indicates a runup elevation of 7 m (NAVD88) at the DCPP site. While this elevation is large, this source produces a wave height less than that produced by the local landslide scenario. Therefore, this report does not examine further refinement of the potential for a tsunami wave generated by a Hawaiian flank collapse to impact the DCPP site.

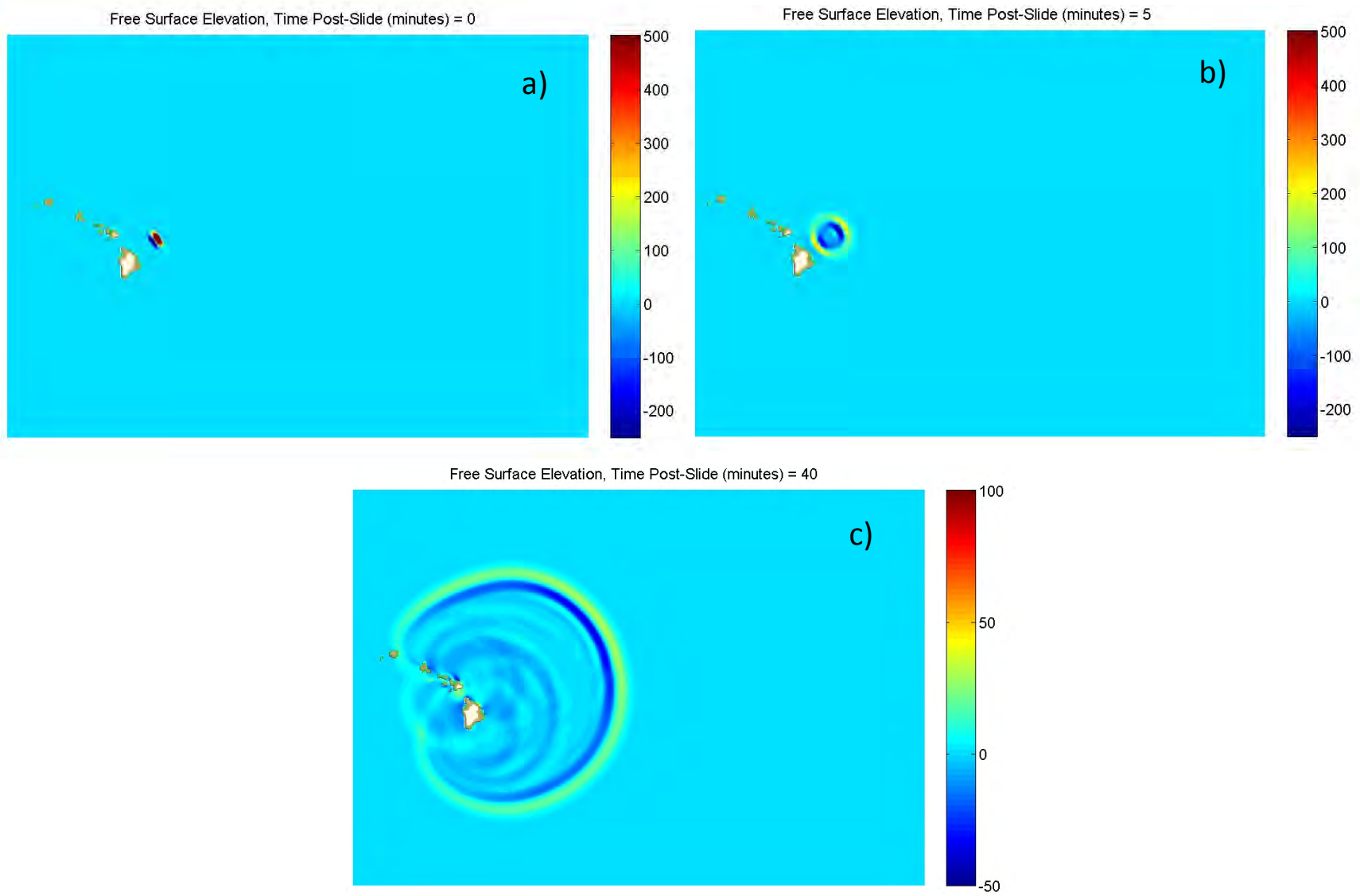

Figure 4.3.1-2: Snapshots of the ocean surface elevation in the near field for the Kilauea flank collapse; the time of the image is given in the title for each subplot, and the elevations in meters follow the colorbars to the right of each image.

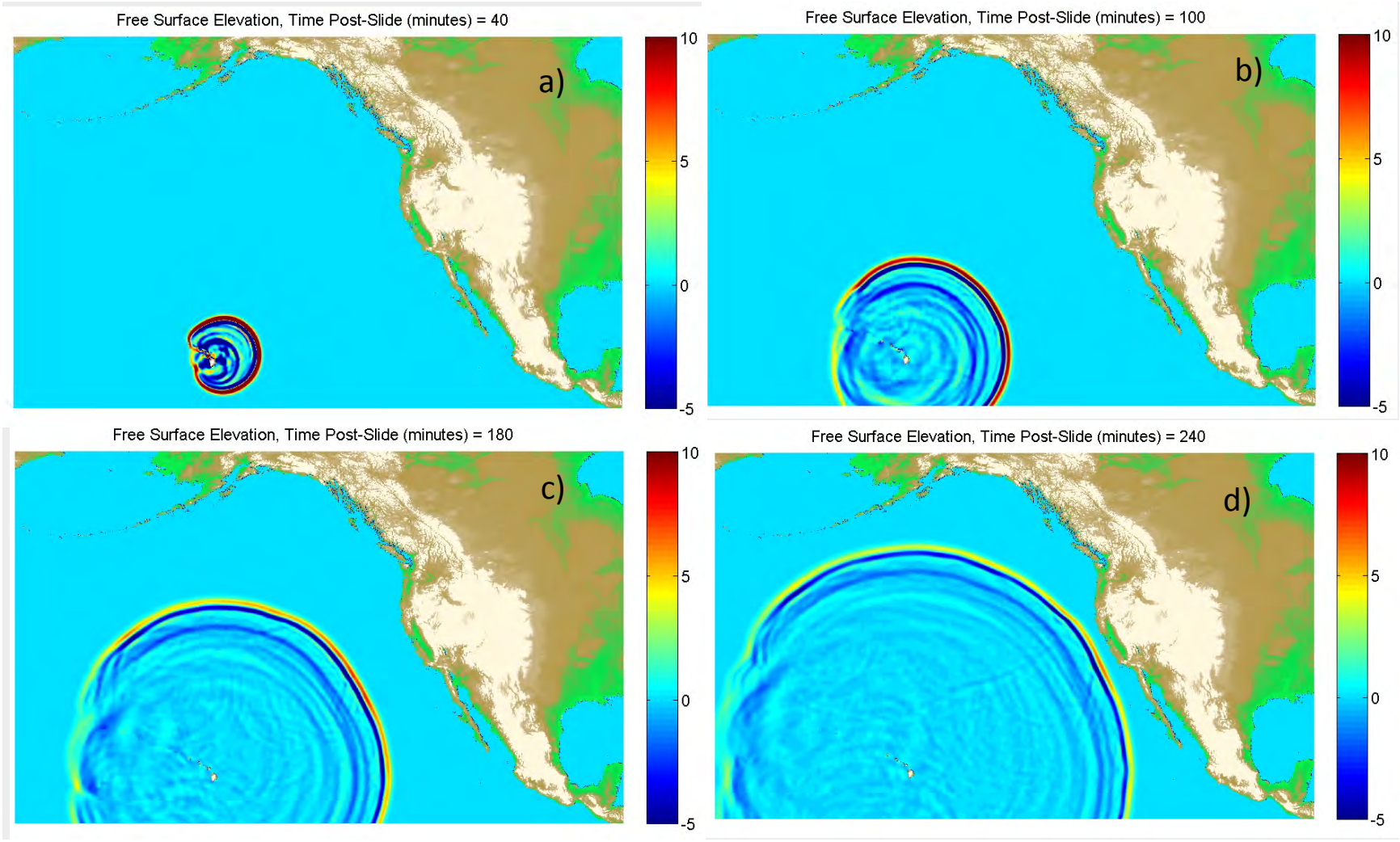

Figure 4.3.1-3: Snapshots of the ocean surface elevation for the oceanic propagation for the Kilauea flank collapse; the time of the image is given in the title for each subplot, and the elevations in meters follow the colorbars to the right of each image.

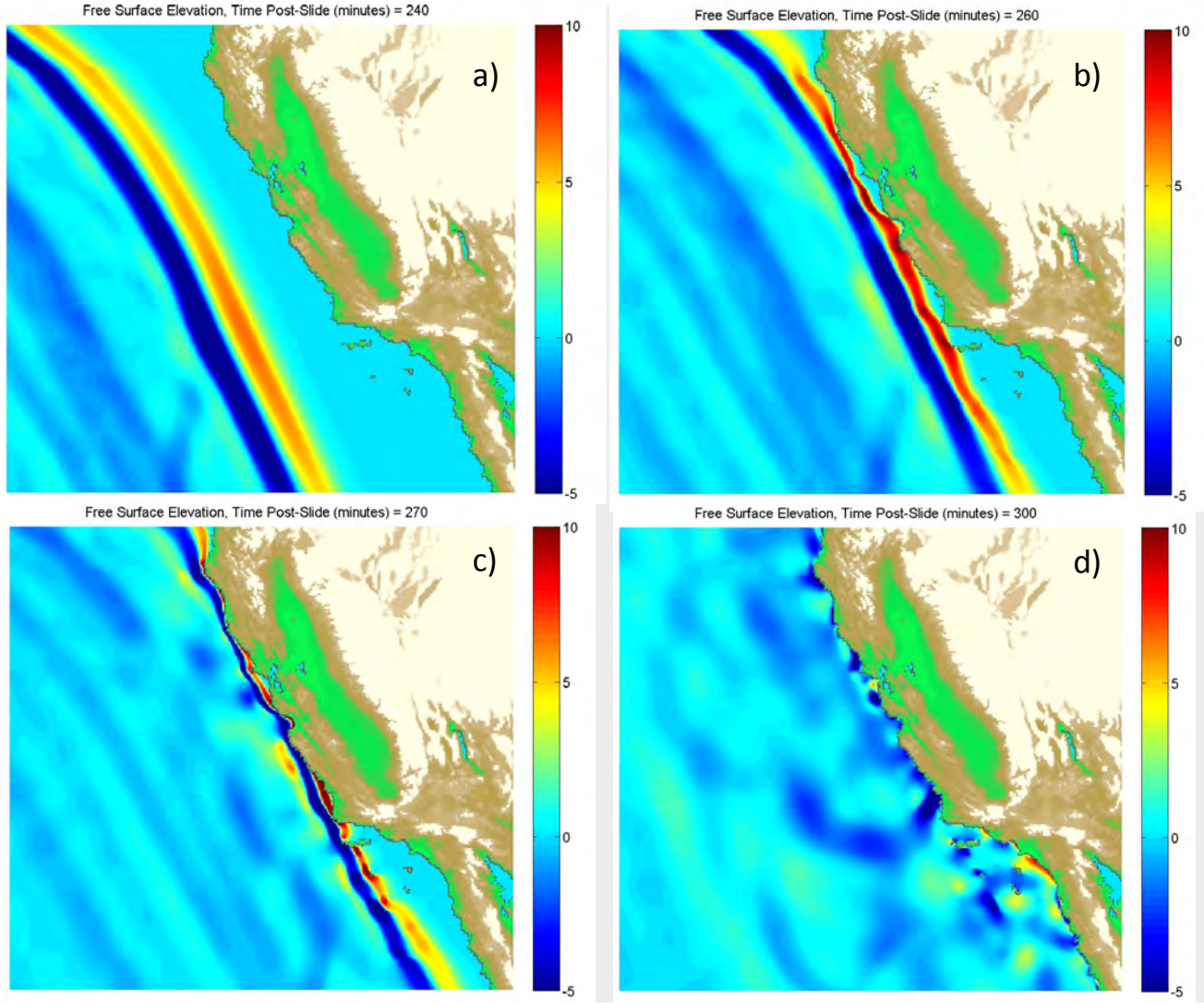

Figure 4.3.1-4: Snapshots of the ocean surface elevation near the California coast for the Kilauea flank collapse; the time of the image is given in the title for each subplot, and the elevations in meters follow the colorbars to the right of each image.

4.3.2 Aleutian Ridge Flank Collapse

The initial generation of the tsunami from this flank collapse uses the geophysical information provided in subsection 2.1.3 to set up the numerical model iSALE. Section 3.2 provides information about the iSALE model. To generate a conservative tsunami-generation scenario, we follow the same method as for the Kilauea flank collapse. Figure 4.3.2-1 depicts the geometry employed for the iSALE simulations. It is striking how similar the figures Figure 4.3.1-1(b) and Figure 4.3.2-1 are. However, it is not surprising because the slopes are controlled by the angle of repose, which is the same for the materials and conditions involved in the formation of the volcano flanks.

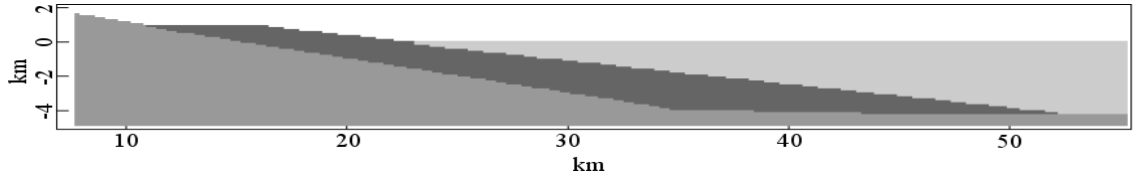

Figure 4.3.2-1. Simplified geometric model of the Aleutian volcano flank collapse for the iSALE modeling.

Due to the similar geophysical character of the Aleutian flank collapse to the Hawaiian flank collapse, the generated tsunamis are likewise similar. Again, the reader is reminded that this scenario represents a conservative source volume with a conservative source mechanism, producing a wave that is likely close to the upper limit of what is physically possible in this area.

To couple the near field model (iSALE) with the oceanic propagation model (COULWAVE), wave information near the source from iSALE is integrated into COULWAVE. This leads to an initial condition for COULWAVE as shown in Figure 4.3.1-2(a). The remaining subplots in Figure 4.3.2-2 show the radial spreading of the waves, and the associated rapid decay in maximum wave amplitude. By 40 minutes after the submarine landslide, the waves have traveled 1000 km, and the maximum crest elevation has decreased to 30 m. Away from the source region, the amplitude continues to decrease due to radial spreading, but at a much slower rate. Figure 4.3.2-3 provides a set of snapshots of the tsunami as it travels across the Pacific towards California. Halfway through its journey to California, the maximum crest elevation has decreased to less than 10 m. By 300 minutes after the slide, the leading wave begins to enter the shallower waters offshore of California and the wave height begins to grow through shoaling.

Figure 4.3.2-4 gives another set of snapshots of the tsunami, here zoomed-in on the California coastline. The tsunami arrives at the site 345 minutes after the slide. This simulation indicates a runup elevation of 5 m in the vicinity of the DCPP site. While this elevation is large, this source produces a wave height considerably less than that produced by the local submarine landslide, as well as the tsunami from the similar Hawaiian flank collapse. Therefore, this report does not examine further refinement of the potential for a tsunami wave generated by a Hawaiian flank collapse to impact the DCPP

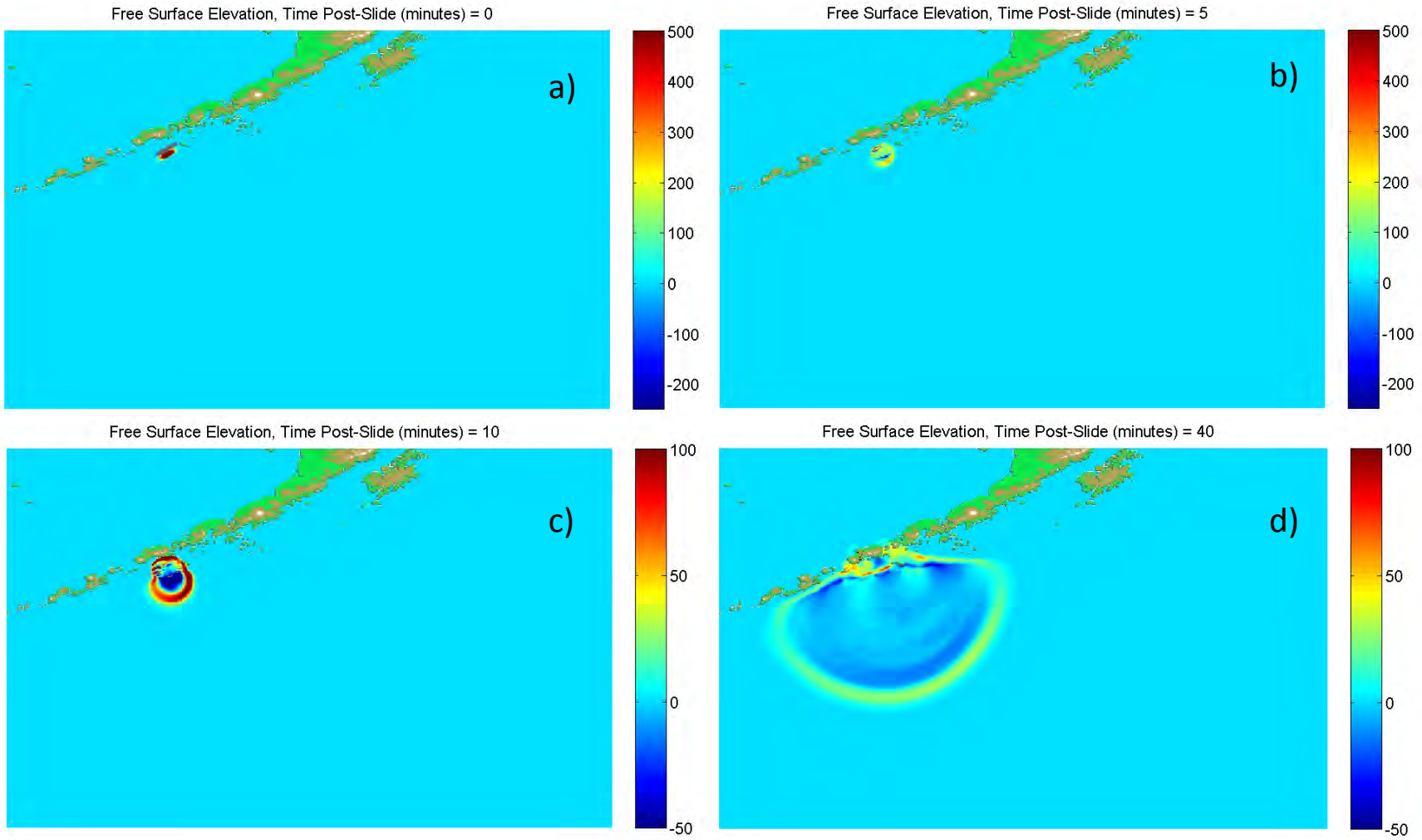

Figure 4.3.2-2: Snapshots of the ocean surface elevation in the near field for the Aleutian flank collapse; the time of the image is given in the title for each subplot, and the elevations in meters follow the colorbars to the right of each image.

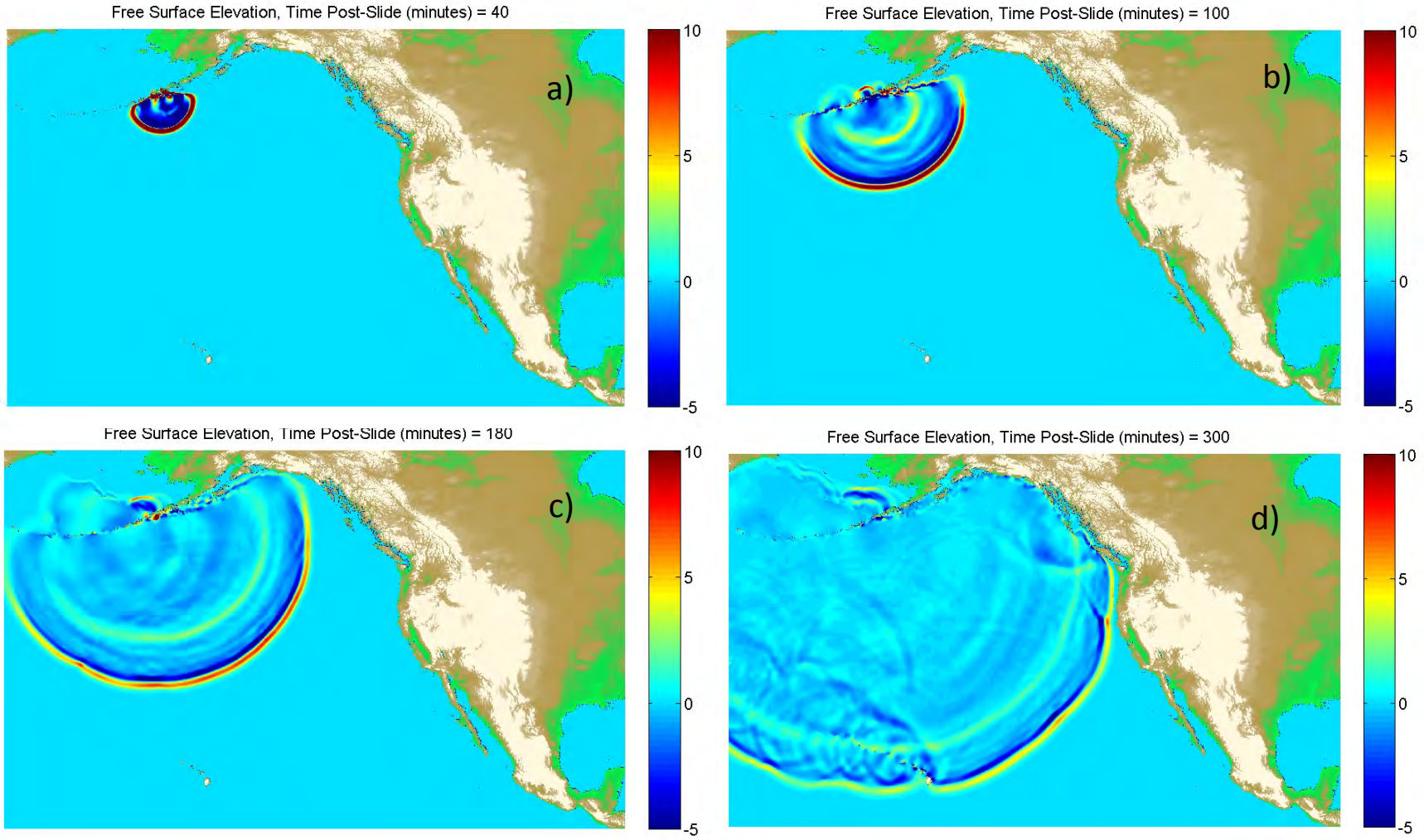

Figure 4.3.2-3: Snapshots of the ocean surface elevation for the oceanic propagation for the Aleutian flank collapse; the time of the image is given in the title for each subplot, and the elevations in meters follow the colorbars to the right of each image.

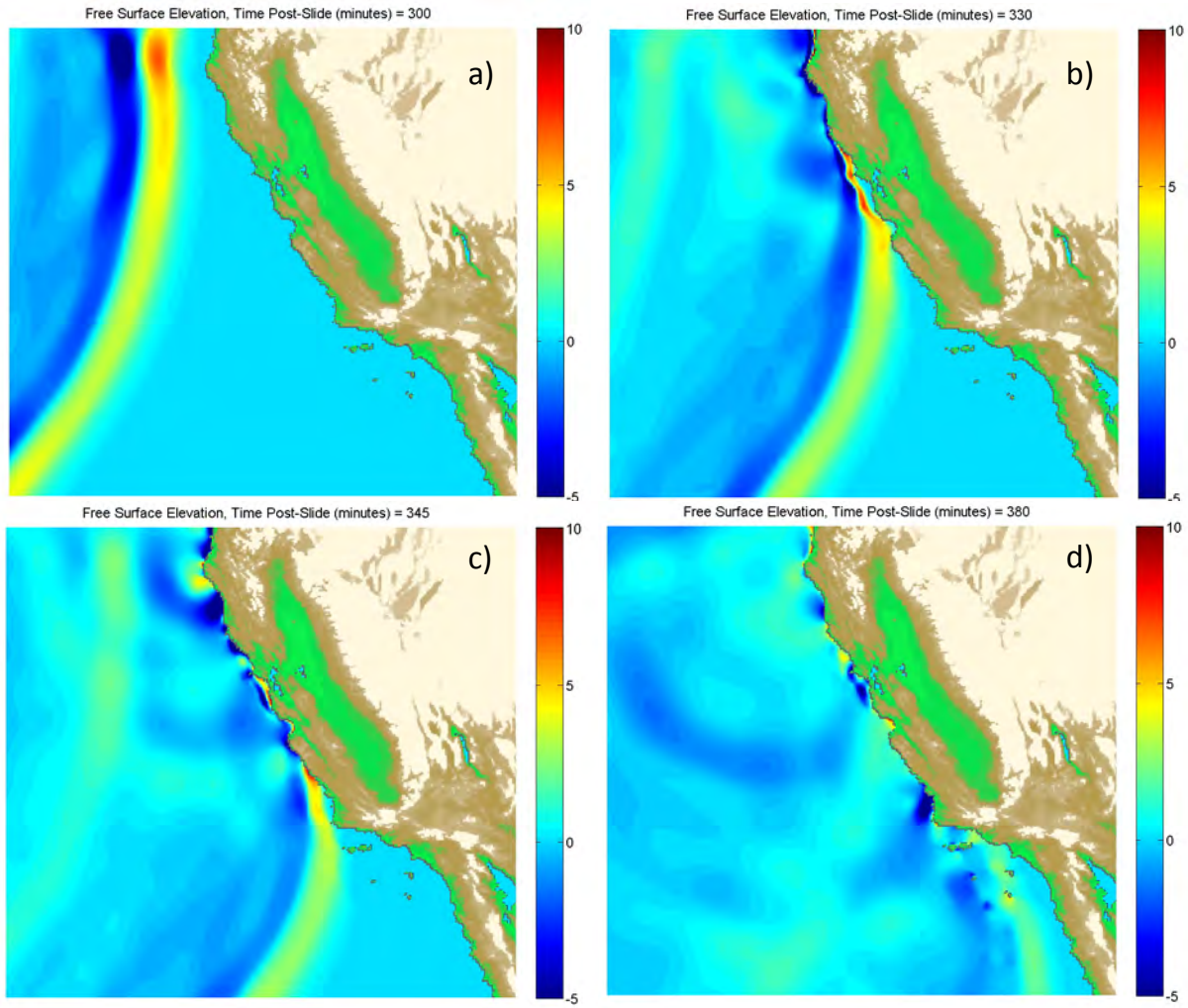

Figure 4.3.2-4: Snapshots of the ocean surface elevation near the California coast for the Aleutian flank collapse; the time of the image is given in the title for each subplot, and the elevations in meters follow the colorbars to the right of each image.

4.4 Tsunamis from Local Landslide Sources

Information Submitted by the Licensee

The FHRR uses the FUNWAVE-TVD model with near-field wave information from NHWAVE to simulate two different local submarine landslide tsunami sources. While the two tested submarine landslides originate away from the site, the licensee placed both immediately offshore of the site as a conservative approach for the purposes of the FHRR analysis. The maximum flow elevation found near the DCPP SWIS is 10.0 m (NAVD88), and the minimum flow elevation in this area is -4.8 m (NAVD88). The FHRR also mentions that the maximum runup elevation behind the SWIS is 19.0 m (NAVD88). These controlling flow elevations are due to the Goleta proxy slide.

Taylor Engineering Technical Evaluation

In this section, the potential impacts from a local submarine landslide are presented. First, in subsection 4.4.1, the geophysical properties of the "design" landslide are provided and the initial waves modeled with the iSALE tool. A deterministic approach, placing the slide in the worst-case offshore location, yields runup elevations in the vicinity of the site. To quantify a large source of uncertainty in this submarine landslide source, the offshore location of the slide is then varied. This approach, termed a "parametric sensitivity scenario," permits a simple statistical analysis to interpret the modeled output.

4.4.1 Submarine Landslide Scenario Development

As discussed in subsection 2.1.6, there is a substantial record of submarine landslides along the California margin. Due in part to a lack of high-resolution bathymetry (e.g. multi-beam sonar with spatial resolution of 10's of meters or less) bathymetry offshore of the DCPP site, there is no clear evidence for or against the occurrence of submarine landslides in this area. Figure 4.4.1-1 outlines this area of low-resolution bathymetry, termed here the "low-resolution zone." In this low-resolution zone, most of the bathymetry data offshore of the 100-200 m depth contour consists of National Oceanographic Service sounding data. With the sounding data points separated by many kilometers slide scarp identification is difficult. However, we note that immediately north and south of this zone there is evidence for submarine landslides. With the lack of high resolution data which might provide information on the existence (or absence) of historical submarine landslides in the area, the authors decided to duplicate the largest known slide in the areas immediately to the north and south of the low-resolution zone and to assume a similar slide could occur within the low-resolution zone offshore of the DCPP site. We will call such slide the "submarine landslide scenario slide" or SLS slide. Such an approach dismisses the possibility of a landslide with properties larger than the SLS slide. While the approach represents the application of all known slide information in the area, it may not be conservative. If for example, yet-to-be identified larger slides exist in the low-resolution zone, we could underestimate the maximum submarine landslide impact.

Examining areas to the north and south of the low-resolution zone, it is evident that the Goleta Slide Complex is the largest landslide in the area. The Goleta submarine landslide is discussed in detail in subsection 2.1.6, and is illustrated in Figure 4.4.1-2. As mentioned in subsection 2.1.6, the complex is composed of three clear, separate lobes, which apparently did not occur concurrently. Figure 4.4.1-3 gives approximate pre-slide and post-slide bathymetry transects for

each of these three lobes. The slide thickness varies from 90 to 155 m across the three lobes. For conservatism, here, the SLS slide will be the volume corresponding to the entire complex (i.e., the sum of the three lobes), with a maximum slide thickness of 125 m. The employed design slide thickness of 125 m is calculated from the average of the three slide thicknesses shown in Figure 4.4.1-3.

To estimate the near source wave elevation, the iSALE model is employed. A cross-section of the conservative representative near-field slide is given in Figures 4.4.1-4a and 4.4.1-4b. Figure 4.4.1-4a contains the entire computational domain, and Figure 4.4.1-4b shows the inset of the slide at the beginning of a simulation. Figure 4.4.1-4c depicts the slide body after 60 seconds. The red arrow marks the location at which the time series shown in Figure 4.4.1-4d is taken. We see that the offshore propagating wave crest is about 30 m in amplitude and about 70 seconds long, while the subsequent trough is about 42 m in amplitude and more than 250 seconds long. It should be noted that for the tsunami source, the viscosity of the slide was changed so the runout masses in the numerical model match the observations. Weiss et al., (2013) employed this method to constrain the tsunami wave generated by the Valdes Slide offshore of Chile. Thus, the analysis uses the post-slide bathymetry to constrain the slide material, which then provides a data-constrained estimate of the tsunami properties.

From the iSALE simulations, a leading depression with amplitude of 30 m and a following crest with amplitude of 25 m, as measured just landward of the headwall, characterize the shoreward propagating wave. The wave has a period of approximately four minutes. To couple the near source model (iSALE) with the wave propagation model (COULWAVE), wave information near the source from iSALE is integrated into COULWAVE.

As discussed above, the SLS slide is placed offshore of the DCPP site. Using COULWAVE, a two-horizontal-dimension simulation is run, using a grid resolution of 20 m. Reasonable bottom friction is included; a Manning's "n" coefficient of 0.025 is used throughout the domain. Note that the inclusion of bottom friction offshore of the DCPP site does not play a major role in the wave propagation, as the shelf is neither as long nor as shallow as found at other locations such as those that might be encountered on the east coast of the United States.

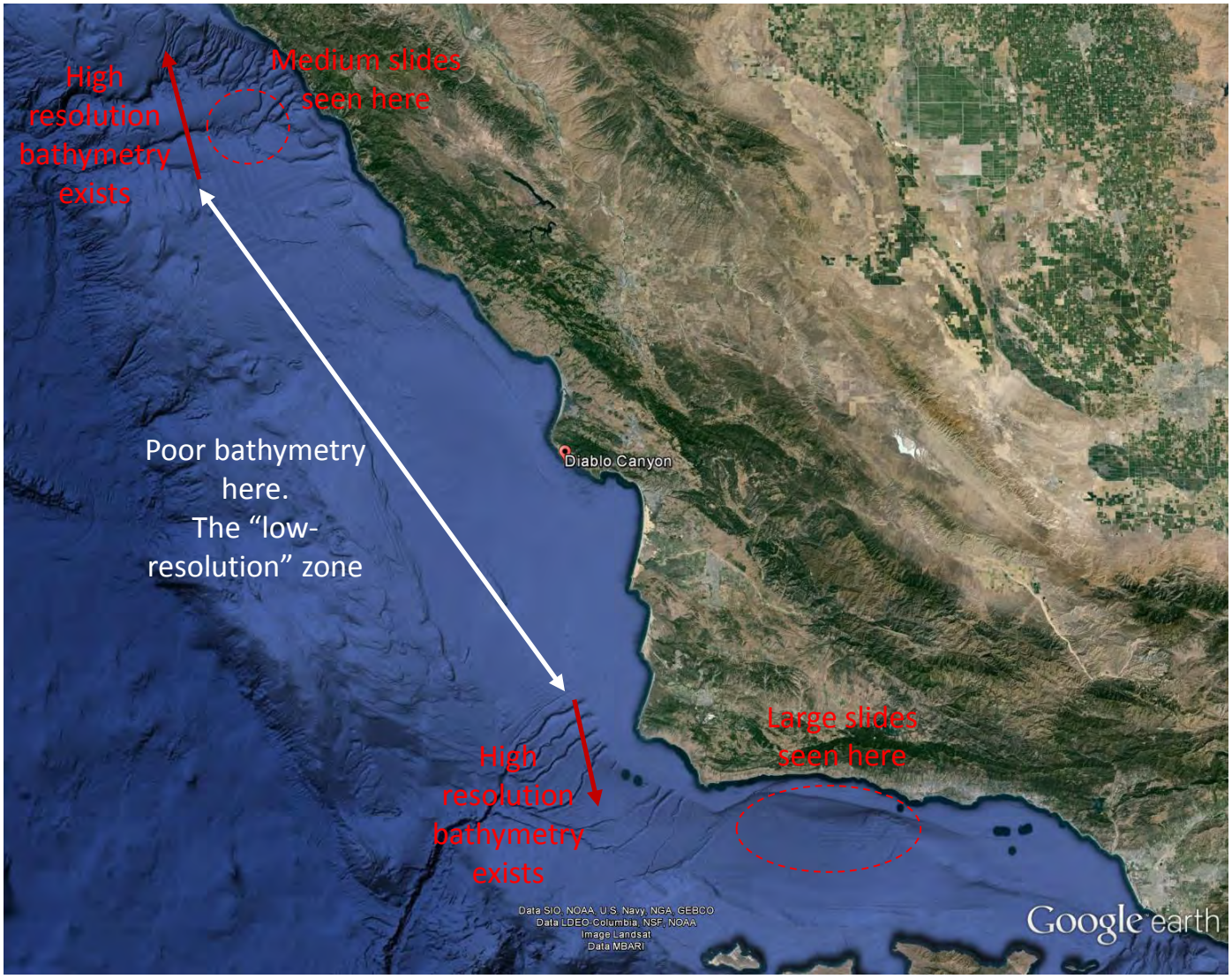

Figure 4.4.1-1: Google Earth image of the region around the site; note the location of the DCPP site provided by the red dot.

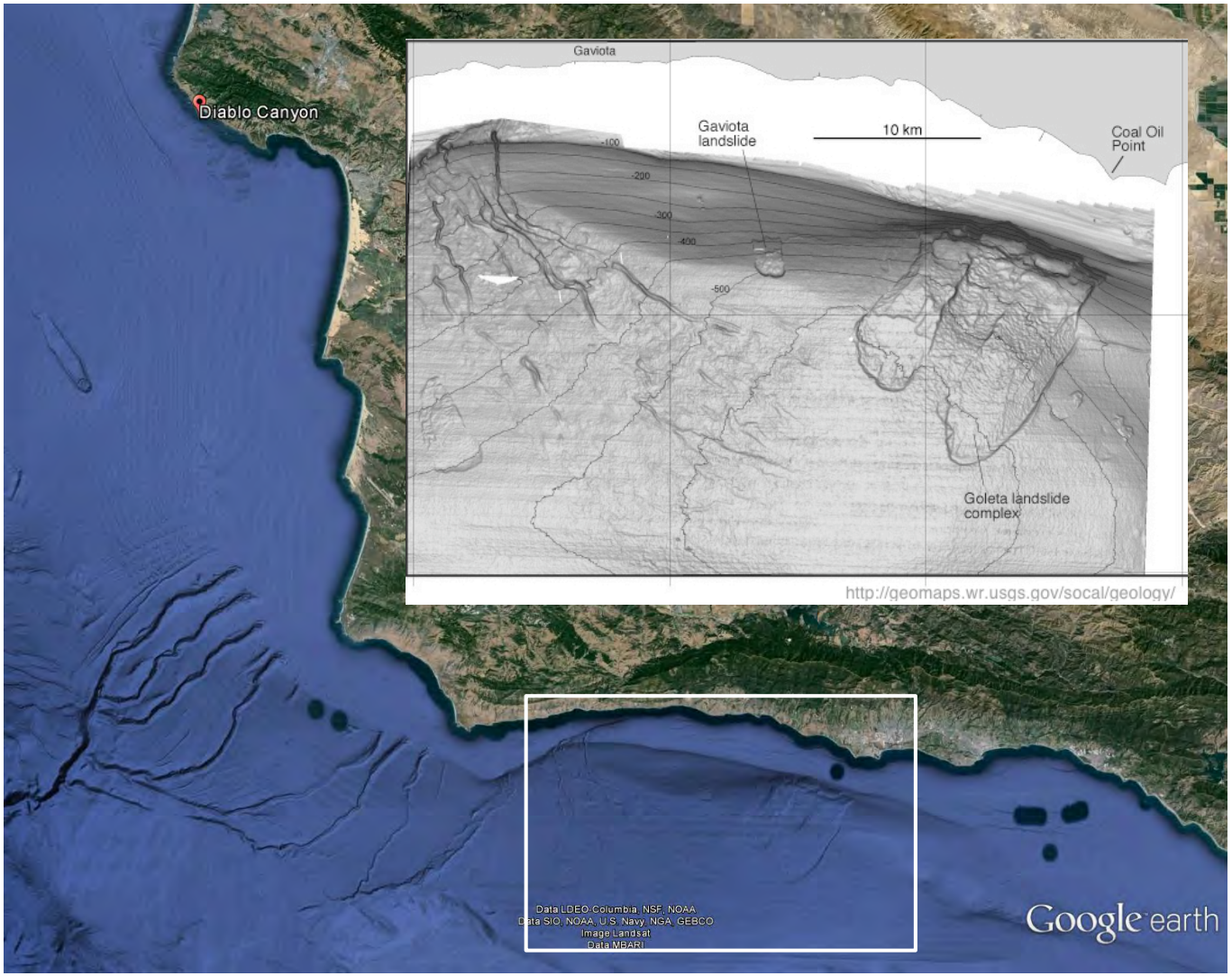

Figure 4.4.1-2: Google Earth image of the region around the DCPP site (upper left on coastline); the white box indicates the area covered in the slide image panel, which shows the various submarine landslides in this area.

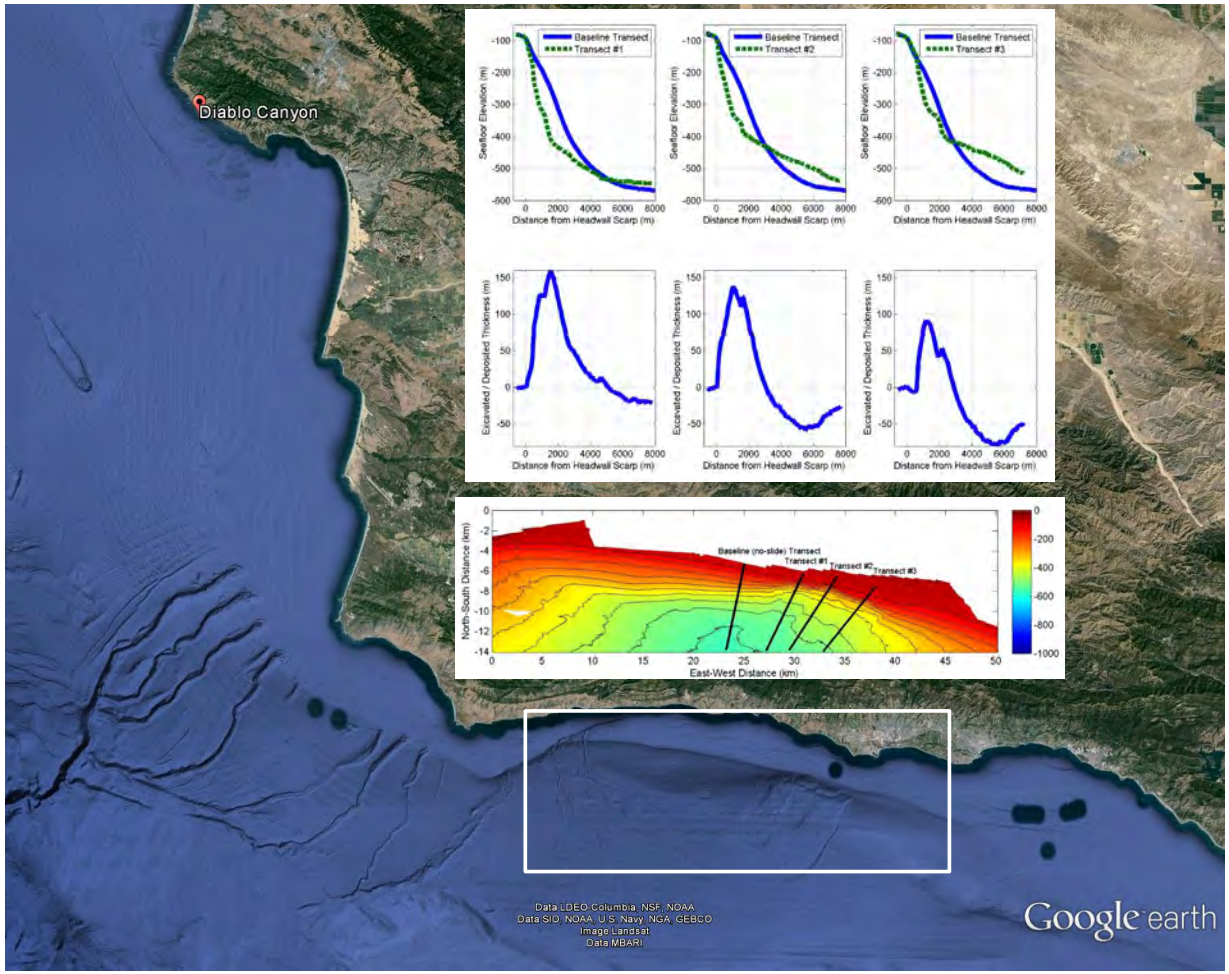

Figure 4.4.1-3: Google Earth image of the region around the site of the Goleta slide; the white box indicates the area covered in the slide image panel. The lower panel shows the bathymetry with seafloor elevation in meters, with four transects given by the black lines: a baseline (pre-slide like) transect, and a transect through each of the three slide lobes. The top panel shows the three lobe transects, and the difference between each transect and the baseline transect. This difference provides a rough estimate of the bathymetry change post-slide. Location of the DCPP site (upper left) is shown for reference.

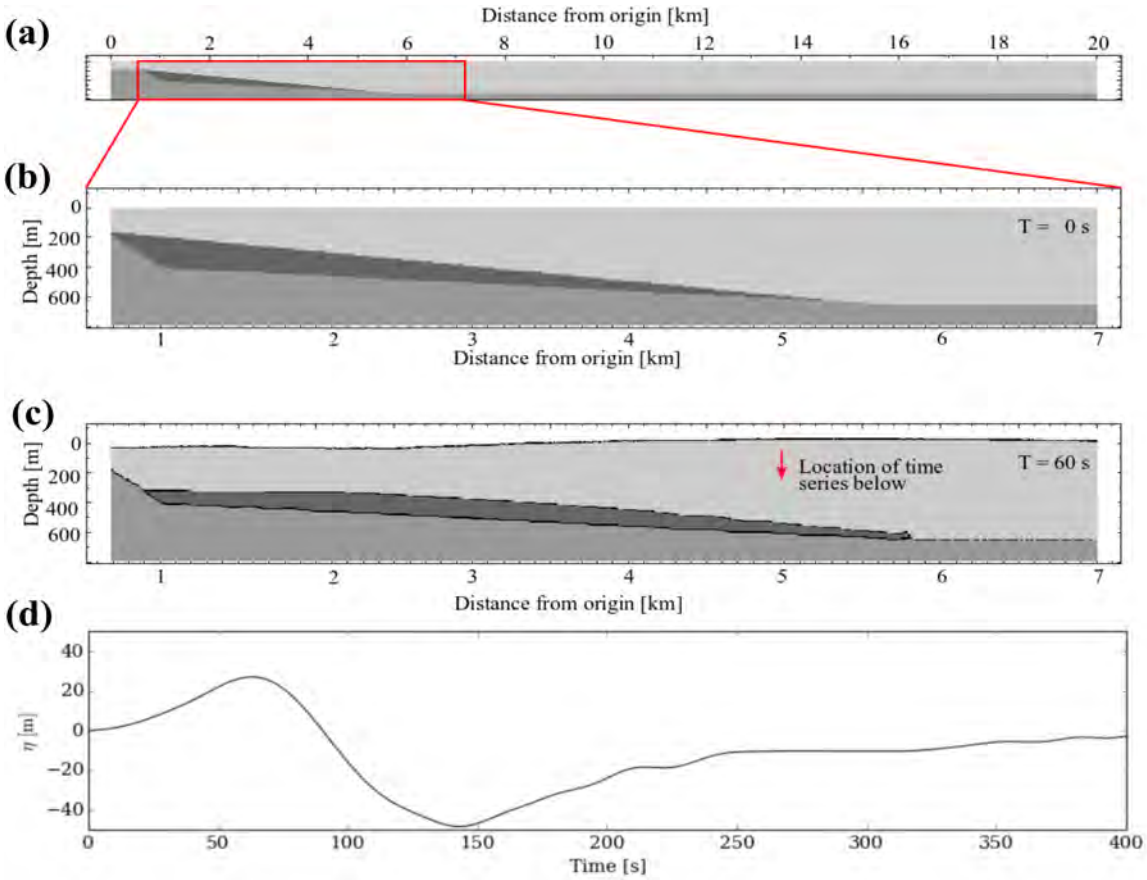

Figure 4.4.1-4: (a) Simplified geometry derived from the bathymetry transects shown in Figure 4.4.1-3. This shows the entire computational domain. (b) Close up of the slide body at the beginning of the simulations (T = 0s), (c) The slide body after 60 s. One can see the waves generated at the water surface. (d) Time series taken at the red arrow in (c). The amplitude of the crest is about 30 m with a duration of about 60 s, while the subsequent trough is 42 m in amplitude and more than 250 s long.

4.4.2 Parametric Sensitivity Analysis of Goleta Submarine Landslide Scenario (SLS) Slide

Here we characterize the tsunami hazard at DCPP using a systematic approach in which a single SLS slide is chosen and certain parameters of the event are varied as part of a parametric sensitivity analysis. The SLS slide is a conservatively-defined landslide with a volume equal to that of the entire Goleta Complex, with a maximum slide thickness of 125 m. The following assumptions and procedures are made as part of the study:

- The SLS slide can occur anywhere within the low-resolution zone, and there is no offshore location in this zone where the SLS is either more or less likely to occur in the future
- The geophysical characteristics of the seafloor with regard to submarine landslide potential in the low-resolution zone are similar to those near the Goleta Slide Complex. Therefore, the geometry and approximate recurrence of the Goleta Slide Complex can be used as a proxy for a potential submarine landslide in the low-resolution zone.
- The SLS slide is expected to have an approximate recurrence period in the low-resolution zone of at least 10,000 years, meaning that throughout the entire length of the low-resolution zone, a slide with a volume equal to or greater than the SLS slide occurs, on average, no more than once every 10,000 years. This is likely a significantly conservative estimate of the return period for a slide with the combined volume of the Goleta Complex.
- The initial amplitude of the generated waves for the SLS slide is simulated using the iSALE model based on available physical constraints, and thus is presented as a best-estimate.
- Parametric sensitivity in the iSALE generation model is not investigated, as there are limited data on which to base possible parameter variability. Thus, there is a single set of initial amplitudes associated with the SLS slide – effectively the SLS slide leads to a unique "scenario initial condition."
- Simulation of the propagation of the generated waves uses best-estimate values of bottom friction and other model parameters.
- Sensitivity or uncertainty analysis in the propagation modeling is not investigated.

The approach used here considers a deterministic initial tsunami condition and places it at different locations throughout the low-resolution zone to assess the effect of the SLS slide location on wave runup height. Specifically, a cohort of 50 simulations was performed in which the slide mass was placed at different proxy locations longitudinally along the low-resolution zone, as shown in Figure 4.4.2-1. The 50 different locations are spread with equal north-south spacing along the low-resolution zone. All slides are placed with a landward limit (headwall) at the 150 m depth contour, and the slides are each oriented to be orthogonal to the local bathymetry contours. As the slides are all placed at the same offshore depth contour, the offshore distance of each slide, or the distance between the slide and the nearest shoreline, varies from slide to slide. From the 50 different locations, runup values are calculated at the reactor site. It is noted that each of the simulations uses the identical propagation grid and model parameters, and utilizes the COULWAVE model for dispersive and nonlinear water wave transformation. Specifically, the grid size used for the 50 simulations is 100 m, and thus these simulations cannot be used to provide detailed site-specific runup predictions at the DCPP site such as the South Cove jetties or the harbor channel. A finer grid resolution is needed for "site-specific" modeling and this will be addressed later in this section. These simulations can only provide approximate runup values in the vicinity of the site and should

not be used directly to estimate the site-specific tsunami hazard at the DCPP site, including the flow elevation at the SWIS. They aid in the definition of the boundary condition to be used for the more-detailed, site-specific simulation at the South Cove location. For this reason, runup elevations discussed in this section are termed "coarse-grid-runup." Note that all elevations discussed in this section are with respect to (NAVD88).

With the database of 50 different SLS scenarios, our objective in this section is to select just one of these 50 scenarios for site-specific hazard assessment. Thus, this one *target scenario* should represent a relatively rare realization of the SLS slide. For the purposes of this analysis, we target a coarse-grid-runup value that results in an elevation greater than the simulation results for 90% of the potential locations evaluated. Effectively, with the 50 different slide scenarios simulated, we target the scenario that produces a coarse-grid-runup that is only exceed by 10% (or, here, 5) of the simulations. Combining this "target level" with the expected minimum recurrence period of the SLS slide in the low resolution zone, the resulting coarse-grid-runup elevation is judged to have a recurrence period of at least 100,000 years based on available geologic evidence. Put in different terms, our assumption is that the next SLS slide has an equal likelihood of occurring at each of the 50 scenario locations. Our target scenario, to be used for detailed site-specific analysis, produces a coarse-grid-runup near the site that equals or exceeds 45 of the scenario locations. Thus, there is only a 10% chance that the next 1-in-10,000 year slide will produce a runup greater than the target scenario. Thus, in light of this judgement and other assumptions considered in the development of the scenario landslide, the resulting runup elevation is judged to be appropriately conservative.

As an example of the parametric sensitivity simulation results, Figure 4.4.2-2 provides a time series of snapshots for the SLS slide (proxy location labeled #28 in Figure 4.4.2-1). Immediately after the onset of the submarine slide, shown in Figure 4.4.2-2(a), both a large depression and elevation wave are generated, with the depression wave on the landward side of the slide. Just after two minutes from the slide onset, waves are propagating away from the generating source area, with a leading depression wave approaching the DCPP site, and a leading elevation wave moving offshore. Owing to the steepness of the landward-traveling crest, the wave begins to break about 5 km meters offshore, as seen in Figure 4.4.2-2(c). The crest travels at a greater speed than the trough, as expected from nonlinear long wave theory, and the crest has largely overrun the trough when reaching the coastline. Also evident from these images is that the waves generated by a local submarine landslide, while producing large waves along the coast immediately onshore of the slide, attenuate quickly due to radial spreading. Simulations similar to that shown in Figure 4.4.2-2 for slide location #28 are also performed for the other 49 locations.

To understand the nature of potential wave runup near the DCPP site from the set of 50 simulations, it is useful to prepare a coarse-grid-runup distribution as a function of the location of the initiating submarine slide. Figure 4.4.2-3 summarizes the distribution of those simulations results. In the top right-hand subplot, the coarse-grid-runup distributions for all 50 computer simulations near the reactor site are plotted; each black line represents a single coarse-grid-runup distribution for each of the 50 simulations. As indicted by the figure, there is a strong concentration of these coarse-grid-runup curves at elevations less than 10 m. Next, we gather the maximum coarse-grid-runup values within 1 km of the DCPP SWIS location, from all 50 simulations. These points are outlined in red in the upper right subplot in Figure 4.4.2-3. At this point, we have collected peak values

representing the maximum coarse-grid-runup for each of the 50 different-location simulations near the DCPP site. From these 50 data points, the lower subplot Figure 4.4.2-3 plots the fraction of computer simulations that exceed each runup value for the tsunami scenario considered. This distribution exhibits the nature of many extreme natural hazards: a long flat tail. Half of the simulations generate a coarse-grid-runup elevation in excess of about 7m. About 10% of the simulations generate coarse-grid-runup values on the order of 20m near the reactor site. Runup values beyond a simulation-fraction-exceedance of 0.1 are plotted with a dashed line in Figure 4.4.2-3. At these low exceedance fractions, the uncertainty in the estimation is high due to the small number of simulated scenarios that make up this component of the trend. Thus, the dashed line implies that the relationship between an estimated runup elevation and exceedance fraction has relatively high uncertainty, and would require additional analysis to discuss with precision. Such an analysis is beyond the scope of this study. Again, we note that these simulations in the parametric sensitivity analysis can only provide approximate runup values in the vicinity of the site, and should not be used directly to estimate the tsunami hazard at the DCPP site.

With the quantification of the 90% target coarse-grid-runup elevation (or the 0.1 exceedance-fraction runup elevation, or the 10% exceedance runup elevation), it is possible to identify the target source location for the more-detailed, site-specific simulation. Figure 4.4.2-4 provides this information. From inspection of this figure, it is evident that the proxy slide #28 location produces the maximum coarse-grid-runup closest to the 90% target runup criterion, with a maximum near-site coarse-grid runup elevation of 20.2 m (NAVD88). As a result, subsequent assessment of tsunami hazard at the site was based on consideration of the deterministic event in which the SLS slide placed at this slide location. Note that slide #28 is also the slide shown in Figure 4.4.2-2. We reiterated that the simulations completed for this statistical analysis use a resolution too coarse to provide site-specific flow properties; at this point in the analysis, only proxy slide #28 is selected for additional, high-resolution simulation where various features of the site, such as the breakwaters and topography, are adequately resolved.

As noted above, this target event (the SLS at location #28) is expected to result in a runup elevation that is judged to have a frequency of exceedance of less than 1E-5/year based on available geologic evidence and the parametric study performed in this section. Consequently, the authors judge that selection of this independent analysis provides an appropriately-conservative deterministic scenario result. Furthermore, the estimated frequency of exceedance of the target event is consistent with the application of the External Flooding Assessment Guidelines (see NEI, 2016; NRC, 2016).

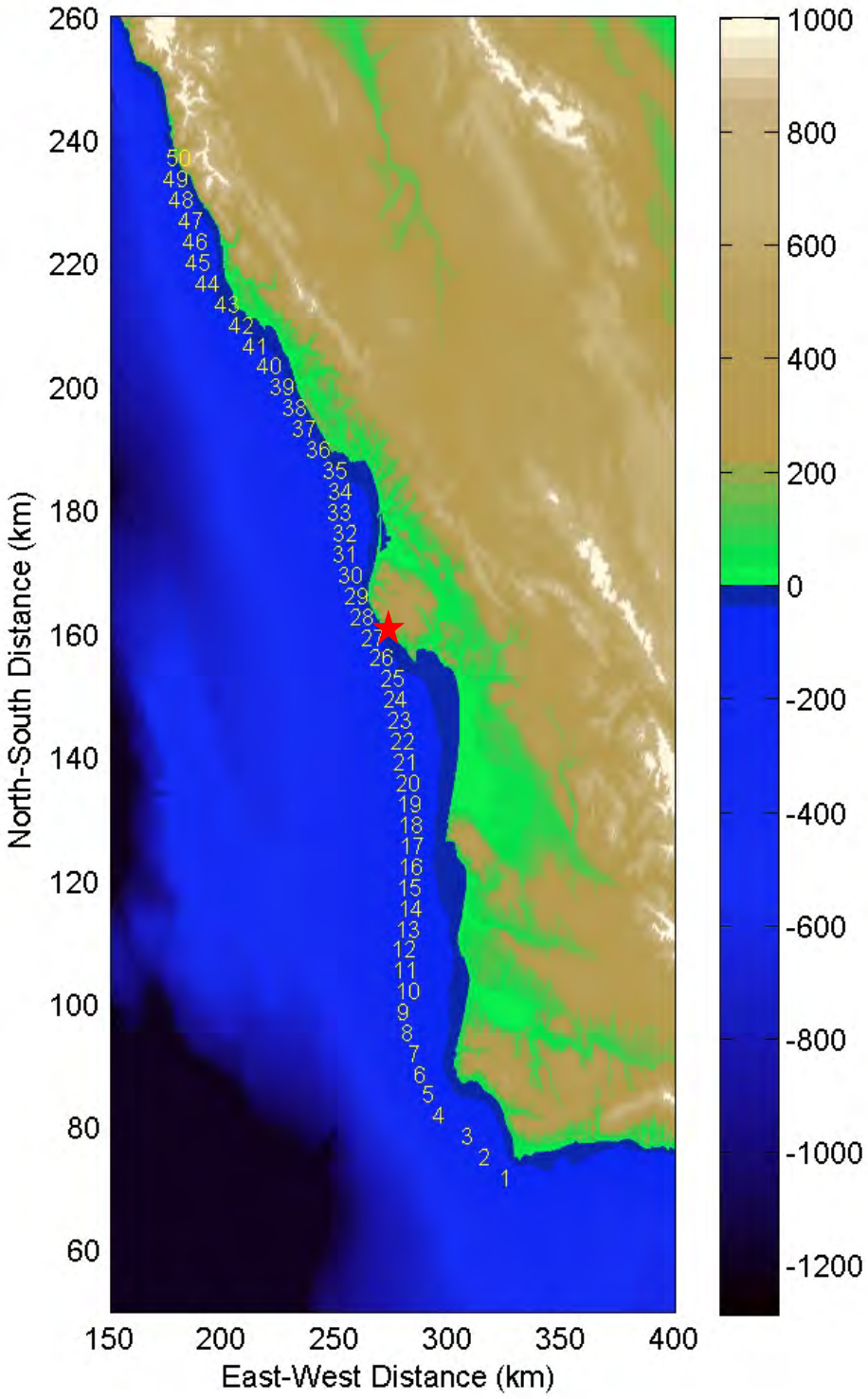

Figure 4.4.2-1: Locations of the 50 proxy slide locations simulated in the "parametric sensitivity scenario" approach near the DCPP site; the DCPP site location is given by the red star.

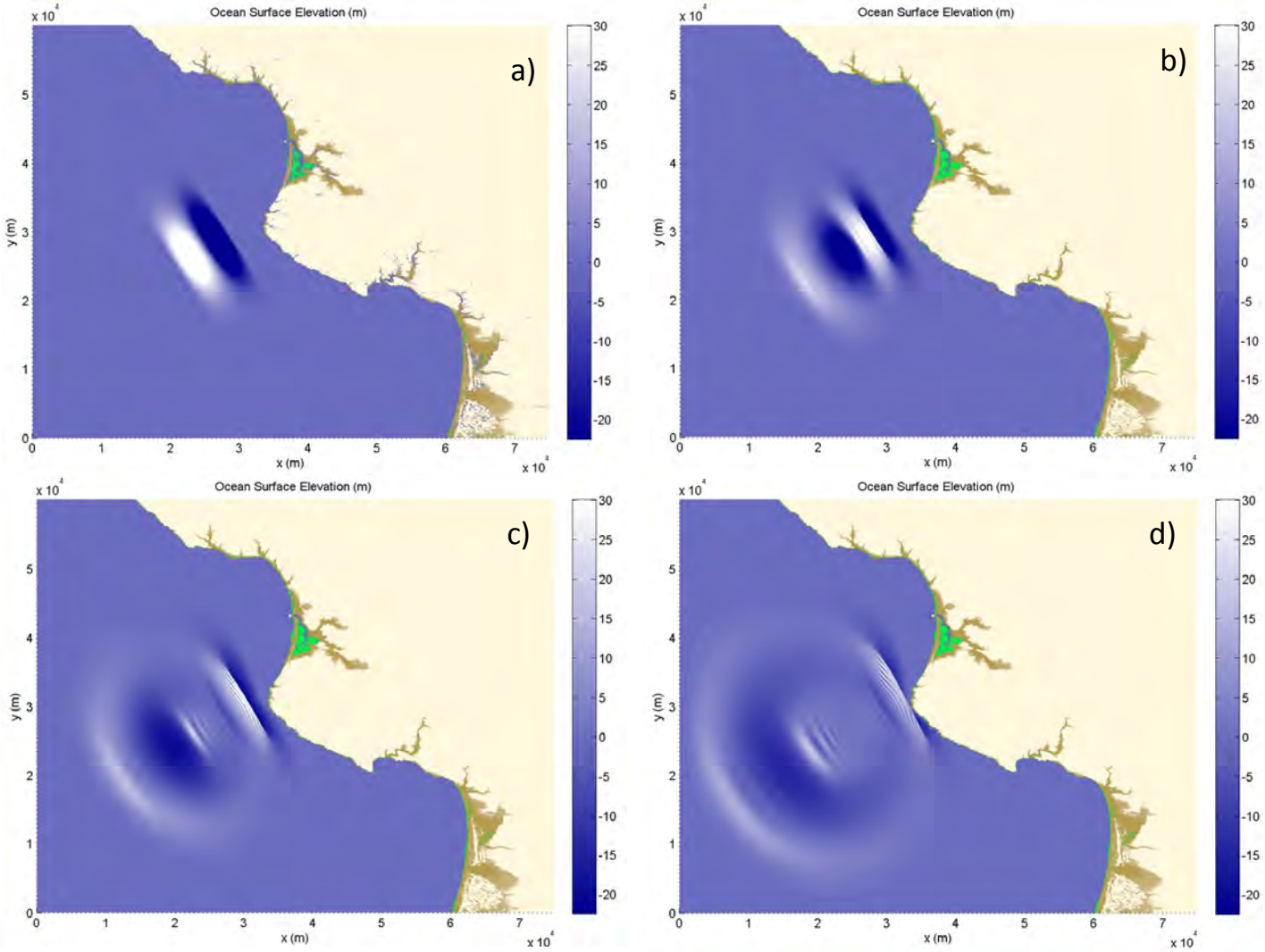

Figure 4.4.2-2: Snapshots of the ocean surface elevation for the scenario landslide (proxy slide location #28 as given in Figure 4.4.2-1) near the DCPP site: a) Time =0 minutes, b) Time = 1.7 min, c) Time = 3.3 min, and d) Time=4.8 min.

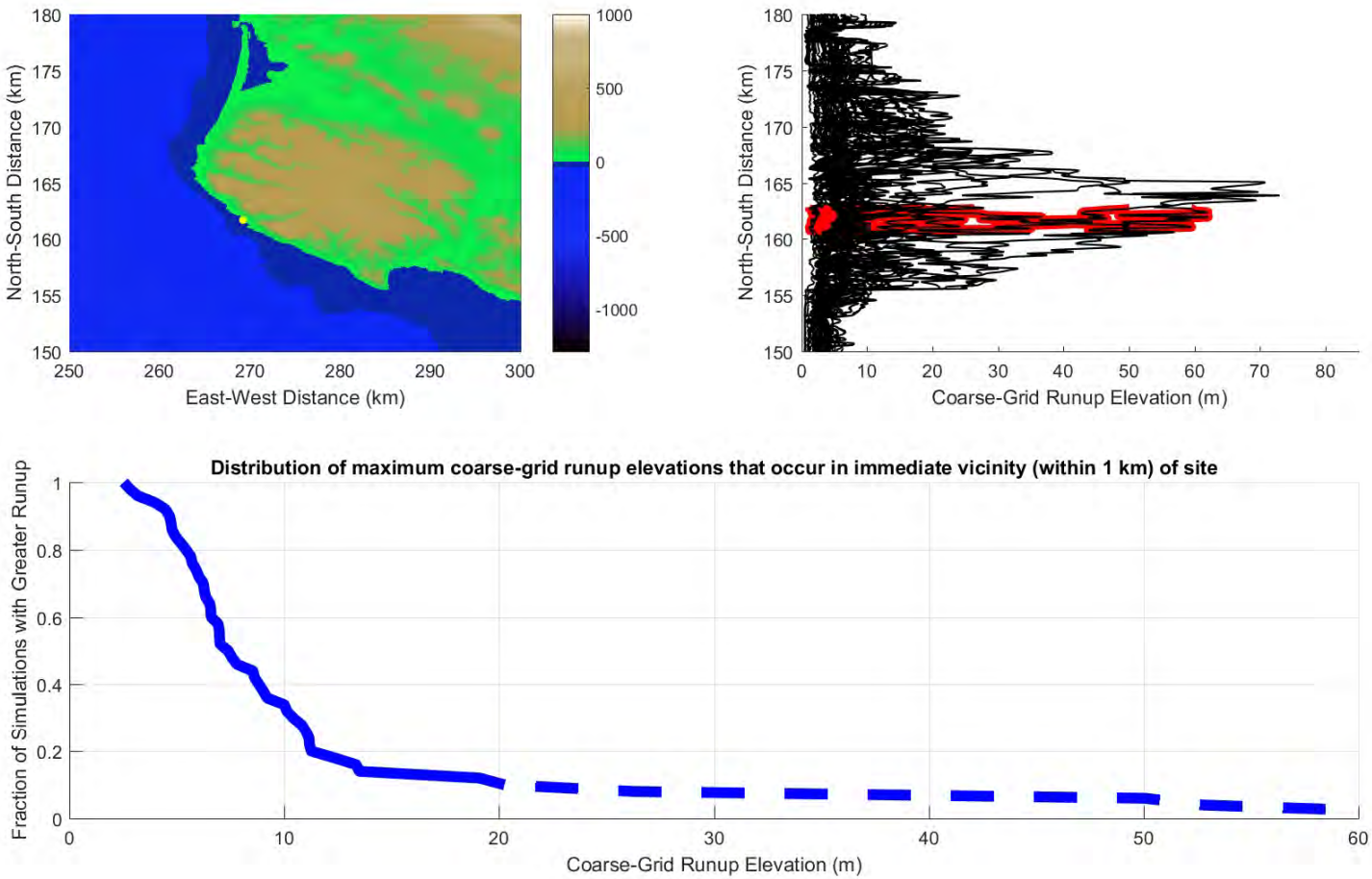

Figure 4.4.2-3: The figure at the upper left-hand corner is a topographic map near the reactor site ; the DCPP site is shown by the yellow dot. The figure in the upper right-hand corner shows the coarse-grid-runup near the DCPP site from the 50 proxy computer simulations; red shaded points are within 1km of DCPP. Note that the vertical axes of these two plots are the same. The bottom plot shows the exceedance curve of all the red-highlighted water elevation points in the upper right-hand plot. It should be noted that the tsunami results presented in this figure are based on the numerical simulation of a geologically-rare event. As such, the models relied on numerous simplifying assumptions and are based on limited site-specific data. The analysis is also replete with uncertainties regarding conceptual models for tsunami consequences and scenarios along this section of the California coastline. Thus, the results and conclusions presented in this figure should be carefully interpreted.

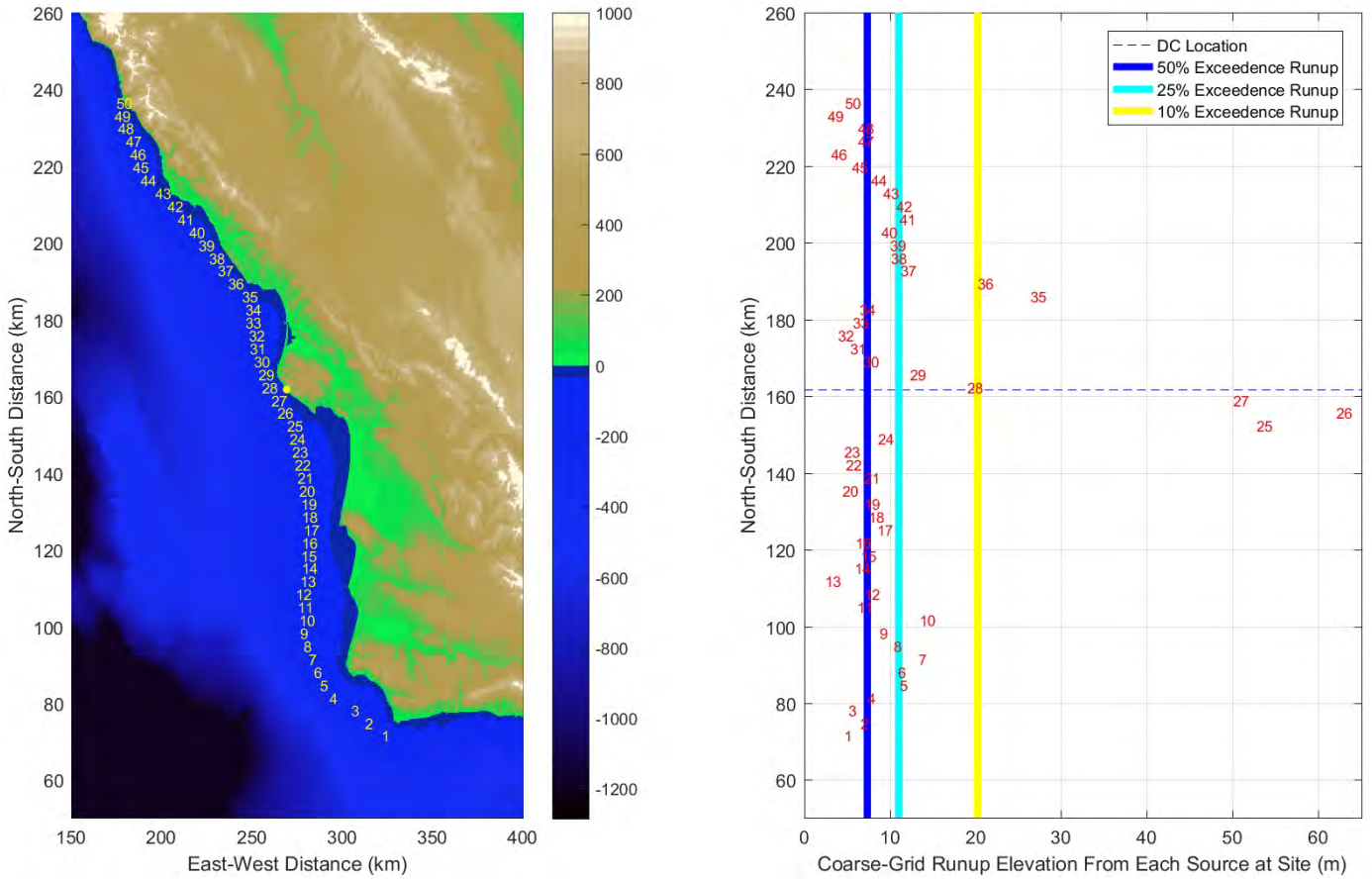

Figure 4.4.2-4: On the left are the locations of the simulated submarine failure slides, similar to that given in Figure 4.4.2-1, and on the right are maximum coarse-grid runup elevations near the DCPP site caused by each simulated slide. For example, proxy slide #10 produces a maximum runup near the DCPP site of 14 m. Also depicted are vertical bars corresponding to various exceedance runup values, where "exceedance runup" is defined as the percentage of simulations with greater coarse-grid runup, as taken from the curve shown in Figure 4.4.2-3. Note that the approximate location of the DCPP site is given by the blue dashed line. It should be noted that the tsunami results presented in this figure are based on the numerical simulation of a geologically-rare event. As such, the models relied on numerous simplifying assumptions and are based on limited site-specific data. The analysis is also replete with uncertainties regarding conceptual models for tsunami consequences and scenarios along this section of the California coastline. Thus, the results and conclusions presented in this figure should be carefully interpreted.

4.5. Local Evolution of the Tsunami near the Site

Information Submitted by the Licensee
The FHRR states that the maximum reevaluated tsunami elevation found near the DCPP SWIS is about 32.8 ft (10.0 m) (NAVD88), and the minimum flow elevation in this area is -15.7 ft (-4.8 m) (NAVD88). The SWIS, specifically the snorkel openings, is a design feature considered by the licensee to be important to safety at the South Cove location. The FHRR also mentions that the maximum runup elevation on the steep slope behind the SWIS is 62.3 ft or about 19.0 m (NAVD88). These maximum water elevations were produced by the licensee's Goleta Proxy Slide.

Taylor Engineering Technical Evaluation
In previous sections, we have examined the tsunami elevations from distant and local earthquakes, distant flank collapse, and local submarine landslides. From these investigations, it is clear that the maximum tsunami flow elevation at the DCPP site is controlled by a local submarine landslide; the SLS slide. In this section, we provide further detailed analyses of the local landslide tsunami to more precisely describe the tsunami effects at the DCPP site

We conducted a series of simulations to identify the target SLS location for the more-detailed, site-specific simulation that includes various features of the reactor site, such as the breakwaters and topography at the South Cove location. This higher-resolution, site-specific simulation provides water surface elevations for comparison to the licensee's water surface elevation estimate reported in the FHRR. The selected offshore target source location (described in subsection 4.4.2) defines the boundary condition corresponding to the incoming incipient tsunami for the site-specific simulation. The slide that produces the so-called 90% target coarse-grid runup elevation, corresponding to proxy slide #28, of 66.2 ft (20.2 m) (NAVD88) is used as the incident wave offshore for the detailed simulations.

For the site-specific modeling, we use the COULWAVE model as described in Section 3.6. Note that this is the same numerical model used for the distant and local landslide scenarios discussed in sections 4.3 and 4.4. Furthermore, the site-specific simulations use the same bathymetry and topography data as used for the SLS simulations in Section 4.3.While the bathymetry and topography data were down-sampled for the 100-m resolution Section 4.3 simulations, we used the NOAA-provided true resolution of the data, or approximately 10 m resolution, for the site-specific local tsunami modeling. For the site-specific computer simulations, a Mannings "n" coefficient of 0.025, corresponding to a smooth and straight seafloor and which we consider a reasonable estimate of bottom friction in the system, was used throughout the model domain.

Figure 4.5-1 shows snapshots of the tsunami evolution for the SLS slide at proxy location #28, in plan view, per the discussion in subsection 4.4.2. The first wave to reach the reactor site is the depression wave but, due to nonlinear shoaling, the first wave is quickly overrun by the following crest. In fact, there is minimal drainage of water from the SWIS harbor

area. The wave crest approaches as a breaking front and overtops the breakwater, which causes inundation in the South Cove area that includes the SWIS. Note that at the time of maximum runup at the SWIS location, as shown in Figure 4.5-1(d), the greatest water elevations are behind the DCPP SWIS and where water runs up the steep slope leading to the reactor powerblock terrace. The maximum runup along this slope behind the SWIS is 70.9 ft (21.6 m) (NAVD88). We remark that this maximum runup value is similar to both the near-site coarse-grid runup from the 90% SLS slide discussed in Section 4.4 of 66.3 ft (20.2 m) (NAVD88) and the maximum runup behind the SWIS from the FHRR of 62.3 ft (19.0 m) (NAVD88). However, at the SWIS location the estimated maximum wave elevation is considerably lower than the maximum runup behind it. These at-SWIS flow elevations are discussed below.

To better understand the flow elevations in the vicinity of the DCPP SWIS, we select five time series (measurements) around this particular structure. The locations selected for those time series are shown in Figure 4.5-2. These locations are chosen to provide estimates of wave height around and in the SWIS footprint. Locations 1 through 3 are situated along the SWIS curtain wall, Location 5 is near the location of the two SWIS ventilation snorkels, and Location 4 is between the curtain wall and the snorkels. Time series plots for SLS proxy slide #28 at the five different locations are displayed in Figure 4.5-3.

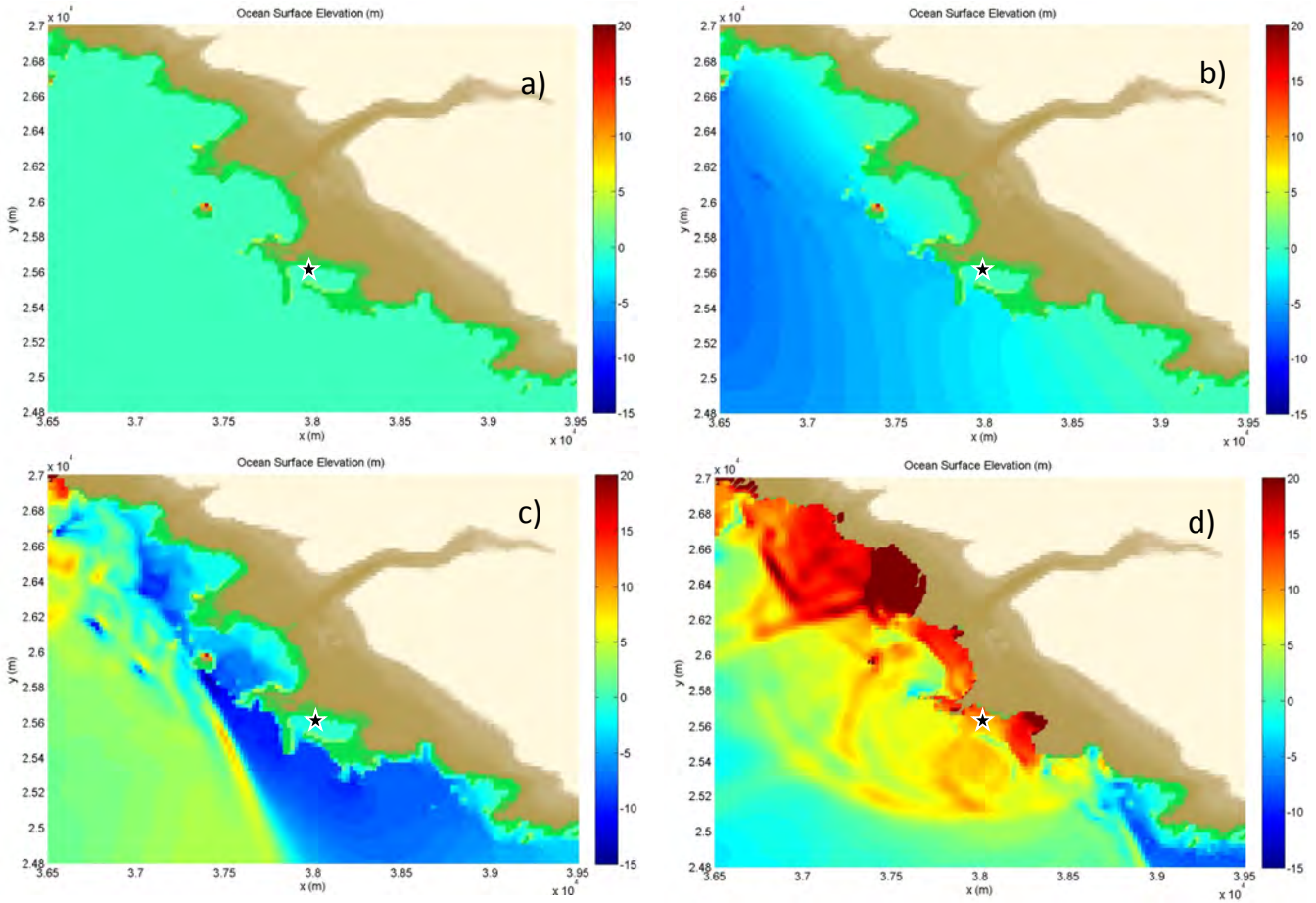

Figure 4.5-1: Snapshots of the ocean surface elevation near the DCPP site for the scenario landslide as given in Figure 4.4.2-1: a) Time =0 minutes, b) Time = 4.8 min, c) Time = 6.3 min, and d) Time=7.3 min. The star marks the South Cove SWIS. It should be noted that the tsunami results presented in this figure are based on the numerical simulation of a geologically-rare event. As such, the models relied upon numerous conservative and simplifying assumptions, and are based on limited site-specific data. The analysis is also replete with uncertainties regarding conceptual models for tsunami consequences and scenarios along this section of the California coastline. Thus, the results and conclusions presented in this figure are intended for use solely in support of this analysis.

Figure 4.5-2. An aerial image of the DCPP SWIS at South Cove, showing the five locations where time series will be extracted and discussed. Locations 1 through 3 are situated along the SWIS curtain wall, Location 5 is near the location of the two SWIS ventilation snorkels, and Location 4 is between the curtain wall and the snorkels

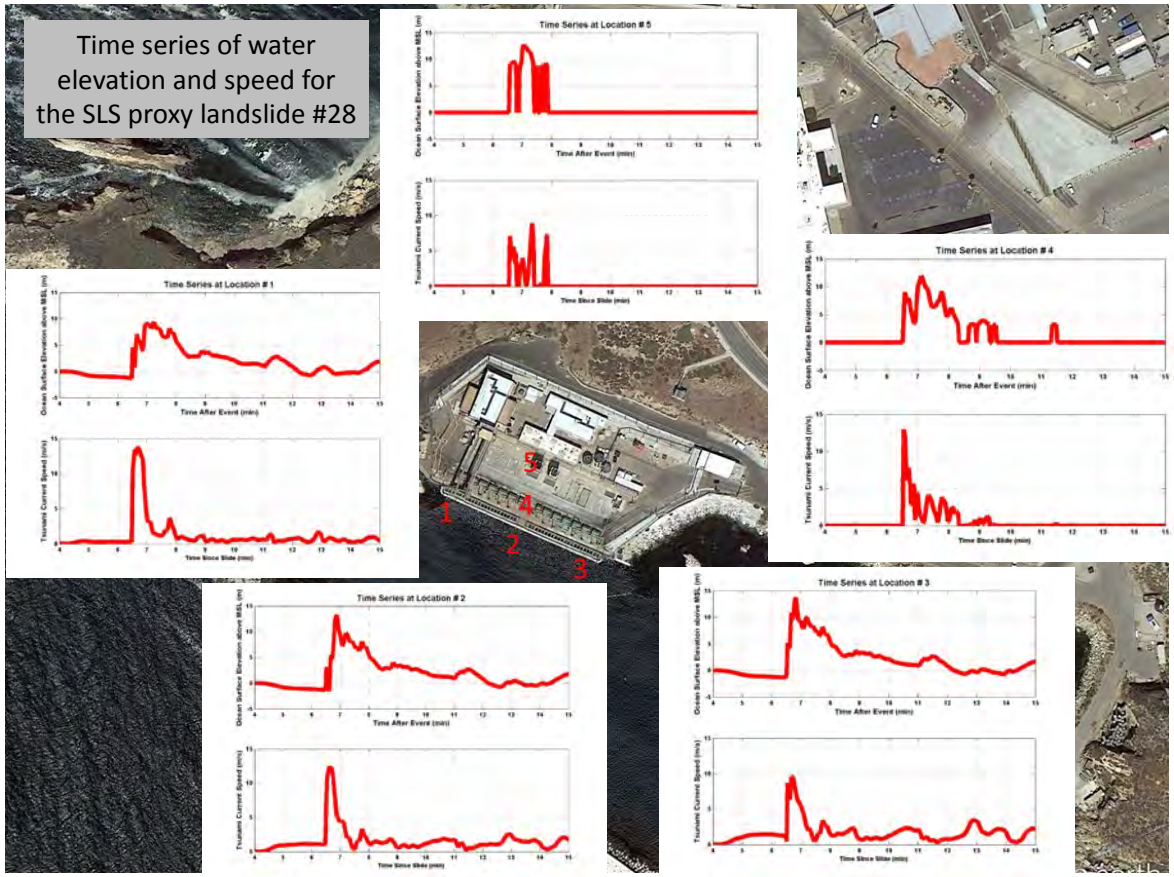

Figure 4.5-3. Time series estimates of ocean surface elevation and current speed for the maximum-elevation controlling SLS Slide source (the scenario landslide), at the five locations corresponding to the DCPP SWIS at South Cove (Figure 4.5-2); the location of each set of time series is provided in the title of the subplots. Elevations are relative to the antecedent water level. It should be noted that the tsunami results presented in this figure are based on the numerical simulation of a geologically-rare event. As such, the models relied on numerous conservative and simplifying assumptions, and are based on limited site-specific data. The analysis is also replete with uncertainties regarding conceptual models for tsunami consequences and scenarios along this section of the California coastline. Thus, the results and conclusions presented in this figure are intended for use solely in support of this analysis.

At the SWIS snorkel location (Location 5), maximum flow elevations are 39.7 ft (12.1 m) above the pre-tsunami antecedent water level. We note that the maximum water elevations along the eastern half of the curtain wall of the SWIS (Locations 2-3) are 0.5-1.0 meter higher than at the snorkels (Location 5). This spatial variation is due to the bathymetry near the SWIS and the SWIS itself, which affects the tsunami evolution. Specifically, the curtain wall acts to reflect some of the tsunami energy offshore. Accounting for the antecedent high water level, the maximum flow elevation at the SWIS snorkel intakes is 47.7 ft (14.5 m) (NAVD88). As discussed above the drawdown predicted by the local slide is not significant, at least relative to the distant earthquake source. Maximum currents near the snorkel intake pipes reach 10-13 m/s, but persist for less than one minute. Based on the 2HD site-specific analysis, the estimated PMT maximum water level from our independent analysis at the SWIS snorkel location (Location 5) is 44.7 ft (14.5 m) (NAVD88) and the estimated minimum water level at the snorkel intake pipe opening (at the same location) is -4.6 m (-15.1 ft) (NAVD88) due to the Aleutian Arc (AA-1 source) tsunami.

4.6 Overtopping of Sloping Structures

Information Submitted by the Licensee
The FHRR does not specifically address the overtopping of coastal structures.

Taylor Engineering Technical Evaluation
The predicted PMT water levels are below the SWIS snorkel opening. Furthermore, there do not appear to be any structures, such as levees or seawalls, for which an overtopping analysis is needed.

5.0 Flood Event Duration

Information Submitted by the Licensee
The FHRR does not address the duration of flooding.

Taylor Engineering Technical Evaluation
Elevated water levels are expected for up to 10 hours for the distant earthquake sources. However, the peak tsunami elevation exists for less than 30 minutes. For the local submarine landslide source, elevation water levels are expected for 10's of minutes, with peak currents existing for 1 to 2 minutes.

6.0 Hydrostatic and Hydrodynamic Forces

Information Submitted by the Licensee
The FHRR provides a force calculation for five different locations: the west-facing portion of the SWIS curtain wall (Location 2 in Figure 4.5-2), the SWIS top deck (Location 4 in Figure 4.5-2), the SWIS fore bay ceilings, the SWIS ventilation huts, and the SWIS ventilation snorkels (Location 5 in Figure 4.5-2). The FHRR finds that the tsunami loads are below the Current Licensing Basis (CLB) loads.

Taylor Engineering Technical Evaluation
Authors reviewed the analysis performed in the FHRR and agree that hydrodynamic forces associated with the tsunami are reasonable.

7.0 Debris and Water-Borne Projectiles

Information Submitted by the Licensee
The FHRR examines the impact loads of various projectiles, with weights up to 10,000 lbs. Projectile loads are calculated, but found to be less than tornado-generated missile loads.

Taylor Engineering Technical Evaluation
Authors reviewed the analysis performed in the FHRR and agree that projectile loads will be controlled by tornado. In addition, the current speeds predicted by the author's analysis are less than those found in the FHRR, and thus, authors find that the tsunami projectile loads in the FHRR are reasonable.

8.0 Effects of Sediment Erosion and Deposition

Information Submitted by the Licensee
The FHRR suggests that current speeds from the tsunami are not strong enough and/or do not have a long enough duration to cause significant erosion or deposition related damage at the site.

Taylor Engineering Technical Evaluation
The current speeds predicted by the authors analysis are less than those found in the FHRR, and thus, authors find that the tsunami erosion analysis in the FHRR is reasonable.

9.0 Conclusion

The recurrence periods of the local submarine landslide sources studied here are judged to be 100,000 years or greater, based on our current state-of-knowledge. The PMT maximum water surface elevations resulting from this analysis of submarine landslide sources (e.g., 47.7 ft (NAVD88) at the SWIS) are judged to be reasonably conservative in that they are consistent with deterministic present-day guidance and methods associated with Near Term Task Force Recommendation 2.1-flooding, and estimates of annual exceedance frequency discussed in the External Flooding Assessment Guidelines (NEI, 2016; NRC, 2016). The PMT produced a runup elevation that is therefore judged to have a frequency of exceedance of less than 1E-5/year based on available geologic evidence. Consequently, the authors judge that this independent analysis provides an appropriately-conservative deterministic scenario result, and it also provides a reasonable frequency-based estimate associated with application of the External Flooding Assessment Guidelines.

References

1. Amsden, A., Ruppel, H., Hirt, C, 1980, *SALE: a simplified ALE computer program for fluid flows at all speeds*, Technical Report LA-8095 Report, Los Alamos National Laboratories.

2. Atwater, B.F., 1987, "Evidence for great Holocene earthquakes along the outer coast of Washington State," *Science*, 236, 942-944.

3. Bailey, E.H., 1941, *Mineralogy, Petrology, and Geology of Santa Catalina Island, California* (unpub. PhD dissertation). Stanford University.

4. Balzano, A., 1998, "Evaluation of methods for numerical simulation of wetting and drying in shallow water flow models," *Coastal Engineering*, 34, 83-107.

5. Barberopoulou A., Borrero J.C., Uslu B., Kalligeris N., Goltz J.D., Synolakis C.E., Wilson R.I., 2009, "New Maps of California to Improve Tsunami Preparedness, invited feature article," *EOS Transactions AGU*, 90(16), 137-138.

6. Barberopoulou A., Borrero J.C., Uslu B., Legg M., Synolakis C.E., 2011, "A Second Generation of Tsunami Inundation Maps for the State of California," *Pure Appl. Geophys*.168, 2133-2146. (doi:10.1007/s00024-011-0293-3)

7. Becker, J. J., D. T. Sandwell, W. H. F. Smith, J. Braud, B. Binder, J. Depner, D. Fabre, J. Factor, S. Ingalls, S-H. Kim, R. Ladner, K. Marks, S. Nelson, A. Pharaoh, R. Trimmer, J. Von Rosenberg, G. Wallace, P. Weatherall, 2009, "Global Bathymetry and Elevation Data at 30 Arc Seconds Resolution: SRTM30_PLUS," *Marine Geodesy*, 32:4, 355-371, DOI: 10.1080/01490410903297766

8. Berryman K., Wallace L., Hayes G., Bird P., Wang K., Basili R., Lay T., Stein R., Sagiya T., Rubin C., Barreintos S., Kreemer C., Litchfield N., Pagani M., Gledhill K., Haller K., Costa C., 2013, "The GEM Faulted Earth Subduction Characterization Project, Version 1.0," June 2013, GEM Faulted Earth Project, available from http://www.nexus.globalquakemodel.org/gem-faulted-earth/posts.

9. Bilek, S. L., 2010, "Invited review paper: Seismicity along the South American subduction zone: Review of large earthquakes, tsunamis, and subduction zone complexity," *Tectonophysics*, 495(1), 2-14.

10. Bird P, 2003, "An updated digital model of plate boundaries," *Geochemistry Geophysics Geosystems*, 4(2). (doi:10.1029/2001GC000252)

11. Bird, P., & Kagan, Y. Y., 2004, "Plate-tectonic analysis of shallow seismicity: Apparent boundary width, beta, corner magnitude, coupled lithosphere thickness, and coupling in seven tectonic settings," *Bulletin of the Seismological Society of America*, 94(6), 2380-2399.

12. Bohannon, RG., and Gardner, J.V., 2004, "Submarine landslides of San Pedro Escarpment, southwest of Long Beach, California." *Marine Geology*, 203.3, 261-268.

13. Borrero J.C., Dolan J., Synolakis C.E., 2001, "Tsunami sources within the Eastern Santa Barbara Channel," *Geophys. Res. Lett.,* 28, 643-647. (doi:10.1029/2000GL011980)

14. Borrero J.C., Legg M.R., Synolakis C.E., 2004, "Tsunami sources in the southern California bight," *Geophys. Res. Lett*., 31, L13211. (doi:10.1029/2004GL020078)

15. Cann, L., 1985, "Slide-mudflow Fishermans Cove area, Santa Catalina Island," *In Geology of Santa Catalina Island, Santa Ana,* South Coast Geological Society, 73–81.

16. Chen, Q., Kirby, J.T., Dalrymple, R.A., Kennedy, A.B., and Chawla, A., 2000, "Boussinesq modeling of wave transformation, breaking, and runup: Part I. 2D," *Journal of Waterway, Port, Coastal, and Ocean Engineering*, 126, 57-62.

17. Cheung, K.F., Phadke, A.C., Wei, Y., Rojas, R., Douyere, Y.J.-M., Martino, C.D., Houston, S.H., Liu, P.L.-F., Lynett, P.J., Dodd, N., Liao, S., and Nakazaki, E., 2003, "Modeling of storm-induced coastal flooding for emergency management," *Ocean Engineering*, 30, 1353-1386.

18. Coombs, M.L., McGrimsey, R.G., and Browne, B.L., 2007, "Preliminary volcano-hazard assessment for the Tanaga Volcanic Cluster, Tanaga Island, Alaska," *US Geological Survey Scientific Investigations Report*, 2007-5094.

19. Daag, A.S., De los Reyes, P. J., Turbianosa, B.S., Javier, D.V., Punongbayan, R.S., 1995, "Tsunami deposits of the November 1994 Mindoro Earthquake, Philippines (abstr), Tsunami Deposits: Geological Warnings of Future Inundation." US.

Geological Survey/NOAA sponsored Conference, held on May 22-23, 1995 at the University of Washington in Seattle.

20. DeLong, S.E., Fox, P.J., and McDowell, F.W., 1978, "Subduction of the Kula Ridge at the Aleutian Ridge," *Bulletin of the Geological Society of America*, 89, 83-95.

21. Dodd, N., 1998, "Numerical model of wave run-up, overtopping, and regeneration," *Journal of Waterway, Port, Coastal, and Ocean Engineering*, 124, 73-81.

22. Duffield, W.A., Stieltjes, L., Varet, J., 1982, "Huge landslide blocks in the growth of Piton de la Fournaise, La Reunion, and Kilauea volcano, Hawaii," *Journal of Volcanology and Geothermal Research*, 12, 147-160.

23. Engebretson, D.C., Cox, A., and Gordon, R.G., 1985, "Relative motions between oceanic and continental plates in the Pacific Basin," *Geological Society of America Special Publication*, 206, 1-59.

24. Fisher, M.A., Normak, W.R., Greene, H.G., Lee, H.J., Sliter, R.W., 2005, "Geology and tsunamigenic potential of submarine landslides in Santa Barbara Channel, southern California," *Marine Geology*, 224, 1-22.

25. Flinn, E.A. and Engdahl, E.R., 1965, "A proposed basis for geographical and seismic regionalization," *Reviews of Geophysicas*, 3, 1, 123-149.

26. Flinn, E.A., Engdahl, E.R., and Hill, A.R., 1974, "Seismic and geographical regionalization," *Bulletin of the Seismological Society of America*, 64, 771-993.

27. Francis, R. D., Bohannon, R. G., and Legg M., 1998, "Geology and marine geophysics of Catalina Island and the California borderland," In *Guidebook to Field Trip #7* (R. J. Behl, ed) 94th Annual Meeting, Long Beach, Cordilleran Section of the Geological Society of America, 1-16.

28. Freymueller, J. T., and Beavan, J., 1999 "Absence of strain accumulation in the western Shumagin segment of the Alaska subduction zone," *Geophys. Res. Lett.*, 26, 3233-3236.

29. Friday D.Z., Taylor L.A., Eakins B.W., Carignan K.S., Grothe P.R., Lim E., Love M.R., 2011, "Digital Elevation Models of Port San Luis, California: Procedures, Data

Sources and Analysis," NOAA National Geophysical Data Center technical report, Boulder, CO, 28 pp.

30. Fritz, H., Hager, W., Minor, H.-E., 2001, "Lituya bay case: Rockslide impact and wave runup," *Sci. Tsunami Hazard*, 19, 2-22.

31. Fritz, H.M., Petroff, C.M., Catalan, P., Cienfuegos, R., Winckler, P., Kalligeris, N., Weiss, R., Barrientos, S.E., Meneses, G., Valderas-Bermejo, C., Ebeling, C., Papadopoulos, A., Contreras, M., Almar, R., Dominguez, J.C., and Synolakis, C.E., 2011, "Field Survey of the 27 February 2010 Chile Tsunami," *Pure Appl. Geophys*, 68(11),1989-2010 (doi:10.1007/s00024-011-0283-5)

32. Fuchs, Sir V., 1982, *Of ice and men: The story of the British Antarctic Survey*, 1943-73, Anthony Nelson, Oswestry.

33. Goldfinger C., Nelson C.H., Morey A.E., Johnson J.E., Patton J.R., Karabanov E., Gutierrez-Pastor J., Eriksson A.T., Gracia E., Dunhill G., Enkin R.J., Dallimore A., Vallier T., 2012, "Turbidite event history: Methods and implications for Holocene paleoseismicity of the Cascadia subduction zone," *U.S. Geol. Surv. Profess. Pap.* 1661-F, 170.

34. Gonzalez F.I., Geist E.L., Jaffe B., Kanoglu U., Mofjeld H., Synolakis C.E., Titov V.V., Arcas D., Bellomo D., Carlton D., 2009, "Probabilistic tsunami hazard assessment at Seaside, Oregon, for near-and far-field seismic sources," *J. Geophys. Res*., 114, C11023. (doi:10.1029/2008JC005132)

35. Gopalakrishnan, T.C., 1989, "A moving boundary circulation model for regions with large tidal flats," *International Journal for Numerical Methods in Engineering*, 28, 245-260.

36. Grantz A., Plafker G., Kachadoorian R., 1964, "Alaska's good Friday earthquake, March 27, 1964: A preliminary Geologic Evaluation," *U.S. Geological Survey report*.

37. Greene, G.H., 1991, "Offshore and onshore liquefaction at Moss Landing spit, central California—Result of the October 17, 1989, Loma Prieta earthquake." *Geology*, 19.9, 945-949.

38. Greene, H.G., Murai, L.Y., Watts, P., Maher, N.A., Fisher, M.A., Paull, C.E., and Eichubl, P., 2006, "Submarine landslides in the Santa Barbara Channel as potential tsunami sources," *Natural Hazards and Earth System Science*, 6, 63–88.

39. Grilli, S.T., Vogelmann, S., Watts, P., 2002, "Development of a 3D numerical wave tank for modeling tsunami generation by underwater landslides," *Eng. Anal. Bound. Elem.,* 26, 301-313.

40. Grilli, S.T., Watts, P., 1999, "Modeling of waves generated by a moving submerged body: Applications to underwater landslides." *Eng. Anal. Bound. Elem.*, 23, 645-656.

41. Grilli, S. T., & Watts, P., 2001, "Modeling of tsunami generation by an underwater landslide in a 3D-NWT." *In The Eleventh International Offshore and Polar Engineering Conference. International Society of Offshore and Polar Engineers*.

42. Grow, J.A. and Atwater, T., 1970, "Mid-Tertiary tectonic transition in the Aleutian Arc," *Bulletin of the Geological Society of America*, 81, 3715-3722.

43. Hampton, M.A., Karl, H.A., Murray, C.J., 2002, "Acoustic profiles and images of the Palos Verdes margin: Implications concerning deposition from the White's Point outfall," *Cont. Shelf Res*., 22, 841-857.

44. Hampton, M.A., Lee, H.J., Locat, J., 1996, "Submarine landslides." *Rev. Geophys,* 34, 33-59.

45. Hansen, J.B., and Svendsen, I.A., 1979, "Regular waves in shoaling water: Experimental data," *Univ. of Denmark Tech. Rep*. ISVA Ser., 21.

46. Hibberd, S., and Peregrine, D.H., 1979, "Surf and run-up on a beach," *Journal of Fluid Mechanics*, 95, 323-345.

47. Holcomb, R.T., Searle, R.C., 1991, "Large landslides from oceanic volcanoes," *Marine Geotechnology*, 10, 19-32.

48. Houston J., 1980. "Type 19 flood insurance study," *WES Report HL-80-18*, USACE.

49. Houston, J.R., and A.W. Garcia, 1978, "Type 16 Flood Insurance Study: Tsunami Predictions for the West Coast of the Continental United States," *U.S. Army Engineer Waterways Experiment Station, Technical Report H-78-26.*

50. Hu, K., Mingham, C.G., and Causon, D.M., 2000, "Numerical simulation of wave overtopping of coastal structures using the non-linear shallow water equations," *Coastal Engineering*, 41, 433-465.

51. Hubbard J, Shaw J.H., Dolan J., Pratt T.L., McAuliffe L., Rockwell T.K., 2014, "Structure and seismic hazard of the Ventura avenue anticline and Ventura fault, California: Prospect from large, multisegment ruptures in the western transverse ranges," *Bull. Seism. Soc. Amer.*, 105, 3, 379-439. (doi:10.1785/0120130125)

52. Imamura, F., 1996, "Simulation of wave-packet propagation along sloping beach by TUNAMI-code," in Yeh, H., Liu, P.L.F., and Synolakis, C.E., eds., *Long-Wave Runup Models,* World Scientific, 25-42.

53. Jicha, B.R., Scholl, P.W., Singer, B.S., Yogodzinski, D.M., and Kay, S.M., 2006, "Revised age of the Aleutian Island Arc formation implies high rate of magma production," *Geology*, 34, 661-664.

54. Johnson JM, and Satake K. 1997, "Estimation of seismic moment and slip distribution of the April 1,1946, Aleutian tsunami earthquake," *J. Geophys. Res.*, 102, 11765-11774.

55. Johnson, D.B., Raad, P.E., and Chen, S., 1994, "Simulations of impacts of fluid free surface with solid boundary," *International Journal for Numerical Methods in Fluids*, 19, 153-174.

56. Kalligeris, N., Montoya, L., Ayca, A., & Lynett, P., 2017, "An approach for estimating the largest probable tsunami from far-field subduction zone earthquakes," *Natural Hazards*, 89, 1, 233-253.

57. Kanamori H., 1970, "The Alaska earthquake of 1964: Radiation of long-period surface waves and source mechanism," *J. Geophys. Res.*, 75, 901-925.

58. Kanamori H., 1972, "Mechanisms of Tsunami Earthquakes," *Phys. Earth Planet. Inter.,* 6, 346-359.

59. Kennedy, A.B., Chen, Q., Kirby, J.T., and Dalrymple, R.A., 2000, "Boussinesq modeling of wave transformation, breaking and runup: I. one dimension," *Journal of Waterway, Port, Coastal, and Ocean Engineering*, 126, 39-47.

60. Kirby S., Geist E., Lee W., Scholl D., Blakely R., 2005, "Tsunami Source Characterization for Western Pacific Subduction Zones, A Preliminary Report." *USGS1 Tsunami Subduction Source Working Group*.

61. Kobayashi, N., and Wurjanto, A., 1989, "Wave overtopping on coastal structures," *Journal of Waterway, Port, Coastal, and Ocean Engineering*, 115, 235-251.

62. Korycansky, D.G., and Lynett, P.J., 2005, "Offshore breaking of impact tsunami: The Van Dorn effect revisited," *Geophysical Research Letters*, 32, doi:10.1029/2004GL021918.

63. Korycansky, D.G., and Lynett, P.J., 2007, "Run-up from impact tsunami," *Geophysical Journal International*, 170, 1076-1088.

64. Kowalik, Z., and Murty, T.S., 1993, "Numerical simulation of two-dimensional tsunami runup," *Marine Geodesy*, 16, 87-100.

65. Krastel, S., Schmincke, H.-U., Jacobs, C.L., Rihm, R., Le Bas, T.P., Alibes, B., 2001, "Submarine landslides around the Canary Islands," *Journal of Geophysical Research*, 106, 3977-3997.

66. Kuhn, G.G., 2005, "Paleoseismic features as indications of earthquake hazards in North Coastal, San Diego County, California, USA," *Engineering Geology*, 80, 115-150.

67. Lander J.F., Lockridge P.A., Kozuch M.J., 1993, *Tsunamis affecting the west coast of the United States 1806-1992*, NGDC, NOAA, U.S. Department of Commerce.

68. Lee. H.J., Normark, W.R., Greene, H.G., and Edwards, B.D., 2004, "Timing and extent of submarine landslides in Southern California." *Offshore Technology Conference*.

69. Lee, Homa. J., 2005, "Undersea landslides: extent and significance in the Pacific Ocean, an update," *Natural Hazards and Earth System Science* 5.6, 877-892.

70. Leendertse, J.J., 1987, *Aspects of SIMSYS2D: A System for Two-Dimensional Flow Computation,* The RAND Corporation R-3572-USGS.

71. Legg, M. R., and Kamerling, M. J., 2003, "Large-scale basement-involved landslides, California Continental Borderland." *Landslide Tsunamis: Recent Findings and Research Directions*. Birkhäuser Basel, 2033-2051.

72. Lenat, J.-F., Vincent, P., Bacherley, P., 1989, "The offshore continuation of an active basaltic volcano: Piton de la Fournaise (Reunion Island, Indian Ocean): Structural and geomorphological interpretation from Sea Beam mapping," *Journal of Volcanology and Geothermal Research*, 36, 1-36.

73. Leonard, M., 2010, "Earthquake Fault Scaling: Self-Consistent Relating of Rupture Length, Width, Average Displacement, and Moment Release," *Bull. Seism. Soc. Amer.*, 100(5A), 1971-1988.

74. Lipman, P.W., Lockwood, W.R., Okamura, R.T., Swanson, D.A., Yamashita, K.M., 1985, "Ground deformation associated with the 1975 magnitude-7.2 earthquake and resulting changes in the activity of Kilauea volcano, Hawaii," *U.S. Geological Survey Professional Papers*, 1276.

75. Liu, P.L.-F., Cho, Y.S., Yoon, S.B., and Seo, S.N., 1995, "Numerical simulations of the 1960 Chilean tsunami propagation and inundation at Hilo, Hawaii, in Tsuchiya," Y., and Shuto, N., eds., Tsunami: *Progress in Prediction, Disaster Prevention and Warning,* Kluwer Academic Publishers, 99-115.

76. Locat, J., Lee, H.J., Locat, P., and Imran, J., 2004, "Numerical analysis of the mobility of the Palos Verdes debris avalanche, California, and its implication for the generation of tsunamis." *Marine Geology,* 203, 269-280.

77. Loomis H.G., 1976, *Tsunami wave runup heights in Hawaii*, Hawaii Institute of Geophysics, University of Hawaii, Honolulu.

78. Løvholt, F., Pedersen, G., and Gisler, G., 2008, "Oceanic propagation of a potential tsunami from the La Palma Island," *J. Geophys. Res.*, 113, C09026, doi:10.1029/2007JC004603.

79. Lynett, P., 2006, "Nearshore wave modeling with high-order Boussinesq-type equations", *Journal of the Waterways and Harbors Division*, A.S.C.E., 132, 348-357.

80. Lynett, P., 2007, "The effect of a shallow water obstruction on long wave runup and overland flow velocity," *Journal of Waterway, Port, Coastal, and Ocean Engineering*, 133, 455-462.

81. Lynett, P., and Liu, P.L.F., 2002, "A numerical study of submarine-landslide-generated waves and run-up," *Proceedings of the Royal Society of London*, A, 458, 2885-2910.

82. Lynett, P., and Liu, P.L.F., 2006, "Three-dimensional runup due to submerged and subaerial landslides," in Mercado, A., and Liu, P.L.F., eds., *Caribbean Tsunami Hazard,* Singapore, World Scientific Publishing Co., 289-307.

83. Lynett, P., Borrero, J.C., Liu, P.L.F., and Synolakis, C.E., 2003, "Field survey and numerical simulations: A review of the 1998 Papua New Guinea tsunami," *Pure and Applied Geophysics*, 160, 2119-2146.

84. Lynett, P.J., Wu, T.-R., and Liu, P.L.-F., 2002, "Modeling wave runup with depth-integrated equations," *Coastal Engineering*, 46, 89-107.

85. MacInnes B.T., Gusman A.R., LeVeque R.J., Tanioka Y., 2013, "Comparison of earthquake source models for the 2011 Tohoku event using tsunami simulation and near field observations," *Bull. Seism. Soc. Amer.*, 103, 1256-1274.

86. Madsen, P.A., Sorensen, O.E., and Schaffer, H.A., 1997, "Surf zone dynamics simulated by a Boussinesq-type model: Part 1. Model description and cross-shore motion of regular waves," *Coastal Engineering*, 32, 255-287.

87. McAdoo, B.G., Pratson, L.F., Orange, D.L., 2000, "Submarine landslide geomorphology, US continental slope," *Marine Geology*, 169, 103-136.

88. McCaffrey R., 2008, "Global frequency of magnitude 9 earthquakes," *Geology*, 36(3), 263-266. doi: 10.1130/G24402A.

89. McGarr, A., 1965, "Excitation of seiches in channels by seismic waves," *Journal of Geophysical Research*, 70, 847-854.

90. McKenzie D. and, Jackson J. 2012, "Tsunami earthquake generation by the release of gravitational potential energy," *Earth Planetary Science Letters*, 345-348, 1-8.

91. Miller, D.J., 1960, *Giant waves in Lituya Bay, Alaska*. Geological Survey Professional Paper 354-C. U.S. Government Printing Office, Washington D.C.

92. Miller, T.P., McGrimsey, R.G., Richter, D.H., Riehle, J.R., Nye, C.J., Yount, M.E., and Dumounlin, J.A., 1998, "Catalog of the historically active volcanoes of Alaska," *US Geological Survey Open-File Report*, 98-0582.

93. Montanaro, C., and Beget, J., 2011, "Volcano collapse along the Aleutian Ridge (western Aleutian Arc)," *Natural Hazards and Earth System Science*, 11, n.3, 715-730.

94. Moore, J.G., Clague, D.A., Holcomb, R.T., Lipman, P.W., Normark, W.R., Torresan, M.E., 1989, "Prodigious submarine slides on the Hawaiian Ridge," *Journal of Geophysical Research*, 94, 17,465-17,484.

95. Moore, J.G., Krivoy, H.L., 1964, "The 1982 flank eruption of Kilauea volcano and structures of the east rift zone," *Journal of Geophysical Research*, 69, 2033-2045.

96. Moore, J.G., Normak, W.R., Holcomb, R.T., 1994, "Giant Hawaiian landslides," *Annual Reviews of Earth and Planetary Science*, 22, 119-144.

97. Morgan, J.K., Moore, G.F., Clague, D.A., 2003, "Slope failure and volcanic spreading along the submarine south flank of Kilauea volcano, Hawaii," *Journal of Geophysical Research*, 108, 2415, doi: 10.1029/2003JB002411, B9.

98. Morner, N-A., 1996, "Liquefaction and varve deformation as evidence of paleoseismic events and tsunamis, the autumn of 10430 BP case in Sweden," *Quat. Sci. Rev.*, 15, 939-948.

99. Muhs, D.R., Szabo, B.J., 1982, "Uranium-series age of the Eel Point terrace, San Clementi Island, California," *Geology*, 10, 23-25.

100. Murty, T.S., 1979, "Submarine slide-generated water waves in Kitimat Inlet, British Columbia," *J. Geophys. Res.,* 84, 7777-7779.

101. Myers, E.P., and Baptista, A.M., 1995, "Finite element modeling of the July 12, 1993 Hokkaido Nansei-Oki tsunami," *Pure and Applied Geophysics*, 144, 769-801.

102. NEI, 2016, "External Flooding Assessment Guidelines, Revision 1," NEI 16-05, June 2016, ADAMS Accession Number ML16165A176.

103. NGDC, 2015, Natural Hazards Viewer--Tsunami Events, http://maps.ngdc.noaa.gov/viewers/hazards/?layers=0, last accessed 10/30/2015.

104. Normark, W., McGann, M., and Sliter, R., 2004, "Age of Palos Verdes submarine debris avalanche, southern California," *Marine Geology*, 203,247-259.

105. NRC, 2009. "Tsunami hazard assessment at nuclear power plant sites in the United States of America," Authored by Prasad, R., Cunningham, E., & Bagchi, Nuclear Regulatory Commission. NUREG/CR-6966, PNNL-17397.

106. NRC, 2012, 10 CFR 50.54-Conditions of Licenses, https://www.nrc.gov/reading-rm/doc-collections/cfr/part050/part050-0054.html

107. NRC, 2016, Guidance for Activities Related to Near-Term Task Force Recommendation 2.1, Flooding Hazard Reevaluation; Focused Evaluation and Integrated Assessment, JLD-ISG-2016-01.

108. Okada, Y., 1985. "Surface deformation due to shear and tensile faults in a half-space," *Bull. Seismol. Soc. Am*, 75, 1135-1154.

109. Okal, E.A., Borrero J.C., Synolakis C.E., 2006, "Evaluation of tsunami risk from regional earthquakes at Pisco, Peru," *Bull. Seismol. Soc. Amer.*, 96, 1634-1648.

110. Okal, E.A., Plafker G., Synolakis C.E., Borrero J.C., 2003. "Near-Field survey of the 1946 Aleutian Tsunami of Unimak and Sanak Islands," *Bull. Seism. Soc. Amer.*, 93, 3, 1226-1234.

111. Okal, E.A., and Synolakis, C.E. 2004, "Source discriminants for near-field tsunamis," *Geophys. J. Int.*, 158, 899-912.

112. Okal, E.A., and Synolakis C.E., 2008, "Far-field tsunami hazard from mega-thrust earthquakes in the Indian Ocean," *Geophys. J. Int.*, 172, 995-1015.

113. Okal, E.A., 2008, "The excitation of tsunamis by earthquakes, in: The Sea," *Ideas and observations on progress in the study of the seas*, 15, Edited by E.N. Bernard and A.R. Robinson, 137-177, Harvard Univ. Press, Cambridge, 2008.

114. Okubo, C.H., 2004, "Rock mass strength and slope stability of the Hilina slump, Kilauea, Hawai'i," *Journal of Volcanology and Geothermal Research*, 138, 43-76.

115. Owen, M., 1980, "Design of seawalls allowing for wave overtopping," *Hydraulics Research Rep,* EX924.

116. Owen, S., Segall, P., Lisowski, M., Miklins, A., Denlinger, R., Sako, M., 2000, "Rapid deformation of the Kilauea volcano: Global positioning system measurements between 1990 and 1996," *Journal of Geophysical Research*, 105, 18,983-18,998.

117. Paris, R., Ciachetti, T., Chevalier, J., Guillou, H., Frank, N., 2011, "Tsunami deposits in Santiago Island (Cape Verde archipelago) as possible evidence of a massive flank failure of Fogos Volcano," *Sedimentary Geology*, 239, 3-4, 129-145.

118. Paskevich, V.F., Wong, F.L., O'Malley, J.J., Stevenson, A.J., 2011, "GLORIA side-scan imagery for parts of the U.S. Exclusive Economic Zone and adjacent areas," *U.S. Geological Survey Open-File Report,* 2010-1332.

119. Pedrozo-Acuña, A., Simmonds, D.J., Otta, A.K., and Chadwick, A.J., 2006, "On the cross-shore profile change of gravel beaches," *Coastal Engineering*, 53, 335-347.

120. Percival, D.B., Arcas, D., Denbo, D.W., Eble, M.C., Gica, E., Mofjeld, H.O., Spillane, M.C., Tang, L., and Titov, V.V., 2009, "Extracting tsunami source parameters via inversion of DART buoy data," *NOAA Tech. Memo.* OAR PMEL-144.

121. Petera, J., and Nassehi, V., 1996, "A new two-dimensional finite element model for the shallow water equations using a Lagrangian framework constructed along fluid particle trajectories," *International Journal for Numerical Methods in Engineering*, 39, 4159-4182.

122. Pierazzo, E., Artemieva, N., Asphaug, E., Cazamias, J., Coker, R., G.S., C., Gisler, G., Holsapple, K., Housen, K., Ivanov, B., Johnson, C., Korycansky, D., Melosh, H., Taylor, E., Turtle, E., Wuennemann, K., 2007, "The impact hydrocode benchmark

and validation project: First benchmark and validation tests," In: *Bridging the Gap II: Effect of Target Properties on the Impact Cratering Process*.

123. Plafker G., Savage J.C., 1970, "Mechanism of the Chilean earthquakes of May 21 and 22, 1960," *Geological Society of America Bulletin*, 81, 1001-1030.

124. Plafker G., 1969, "Tectonics of the March 27, 1964 Alaska earthquake," *U.S. Geol. Surv. Prof. Paper* 543-I.

125. Plafker, G., 1972, "Tectonics. In The Great Alaskan Earthquake of 1964." *Seismology and Geodesy*. 113-188, National Academy of Sciences, Washington D.C.

126. PG&E, 2016, *Diablo Canyon Power Plant Units 1 and 2 Flood Hazard Reevaluation Report*

127. Pratt, B.R., 2002, "Storms versus tsunamis: dynamic interplay of sedimentary, diagenetic and tectonic processes in the Cambrium of Montana," *Geology*, 30, 5, 423-426.

128. Raichlen, F., and Synolakis, C.E., 2003, "Runup from three dimensional sliding mass," *Long Waves Symposium*, Briggs, M., Koutitas .Ch. (Eds), 247–256, ISBN 960–243–593–3

129. Ramalho, R.S., Winckler, G., Madeira, J., Helffich, G.R., Hipolito, A., Quartau, R., Adena, K., Schaefer, J.M., 2015, "Hazard potential of volcanic flank collapses raised by new megatsunami evidence," *Science Advances*, 1, 9, e1500456, doi: 10.1126/sciadv.1500456.

130. Raubenheimer, B., 2002, "Observations and predictions of fluid velocities in the surf and swash zones," *Journal of Geophysical Research*, 107, 3190.

131. Rong Y, Jackson D.D., Magistrale H., Goldfinger C., 2014, "Magnitude Limits of Subduction Zone Earthquakes," *Bulletin of the Seismological Society of America*, 104(5). doi: 10.1785/0120130287

132. Rowland, S.M., 1984, "Geology of Santa Catalina Island." *California Geology* 37, 239–251.

133. Satake K, and Somerville P., 1992, "Location and Size of the 1927 Lompoc, California Earthquake from Tsunami Data," *Bull. Seismol. Soc. Am.*, 82, 1710-1725.

134. Satake, K., Shimazaki, K., Tsuji, Y., and Ueda, K., 1996, "Time and size of a giant earthquake in Cascadia inferred from Japanese tsunami records of January 1700," *Nature*, 379, 246-249.

135. Saville, T., 1955, *Laboratory data on wave runup and overtopping on shore structures,* U.S. Army, Beach Erosion Board, Document Service Center Technical Memo, No. 64.

136. Schaeffer, J., and Nye, C.J., 2002, *Historically active volcanoes of the Aleutian Arc, Alaska,* Division of Geological and Geophysical Surveys Miscellaneous Publications, MP-0123.

137. Shao G, Li X, Ji C, Maeda T., 2011, "Focal mechanism and slip history of the 2011 M_w 9.1 off the Pacific coast of Tohoku Earthquake, constrained with tele seismic body and surface waves," *Earth Planets Earth*, 63, 559-564.

138. Sielecki, A., and Wurtele, M.G., 1970, "The numerical integration of the nonlinear shallow-water equations with sloping boundaries," *Journal of Computational Physics,* 6, 219-236.

139. Simkin, T. and Siebert, L., 1994, *Volcanoes of the World*, 2nd Edition, Geoscience Press, Tuscon.

140. Slingerland, R.L., Voight, B, 1979, "Occurrences, properties and predictive models of landslide-generated impulse waves. Rockslides and avalanches" 2:317-397, Ed. Voight, B. *Developments in geotechnical engineering* 14B. Elsevier, Amsterdam.

141. Smith, J.R., Malahoff, A., Shor, A.N., 1999, "Submarine geology of the Hilina slump and morpho-structural evolution of Kilauea volcano," *Hawaii, Journal of Volcanology and Geothermal Research*, 94, 59-88.

142. Spaeth M.G., Berkman S.C., 1965, *The Tsunami of March 38, 1964 as Recorded at Tide Stations*, U.S. Coast and Geod. Survey.

143. Stearns, H.T., Clark, W.O., 1930, *Geology and water resources of the Kau District, Hawaii,* U.S. Geological Survey Water Supply Papers, 616.

144. Swanson, D.A., Duffield, W.A., Fiske, R.S., 1976, *Displacement of the south flank of Kilauea volcano: The result of forceful intrusion of magma into the rift zones*, U.S. Geological Survey Professional Papers, 963.

145. Synolakis, C.E., 2003, *Tsunami and Seiche, in Earthquake Engineering Handbook*, edited by Chen, W–F and Scawthorn, C., CRC Press, 9–1-9–90.

146. Tang, L., Titov, V.V., and Chamberlin, C.D., 2010, *A Tsunami Forecast Model for Hilo, Hawaii*. NOAA OAR Special Report, PMEL Tsunami Forecast Series: Vol. 1.

147. Tao, J., 1983, *Computation of wave runup and wave breaking,* Danish Hydraulics Institute.

148. Tao, J., 1984, "Numerical modeling of wave runup and breaking on the beach," *Acta Oceanologica Sinica*, 6, 692-700.

149. Taylor F.W., Briggs R.W., Frohlich C., Brown A., Hornbach M., Papabatu A.K., Meltzner A.J., Billy B., 2008, "Rupture across arc segment and plate boundaries in the 1 April 2007 Solomons earthquake," *Nat. Geosci.*, 1, 253-257.

150. Ting, F.C.-K., and Kirby, J.T., 1995, "Dynamics of surf-zone turbulence in a strong plunging breaker," *Coastal Engineering*, 24, 177-204.

151. Titov V.V., Mofjeld H.O., Gonzalez F.I., Newman J.C., 1999, *Offshore forecasting of Alaska-Aleutian subduction zone tsunamis in Hawaii,* NOAA Tech. Memo, ERL.

152. Titov V.V., and Synolakis C.E., 1995, "Modeling of breaking and nonbreaking long wave evolution and runup using VTSC-2," *J. Waterw. Port Coast Ocean Eng.*, 121, 308-316.

153. Titov V.V., and Synolakis C.E., 1998, "Numerical modeling of tidal wave runup," *J. Waterw. Port Coast Ocean Eng.*, 124, 157-171. doi:10.1061/(ASCE)0733-950X(1998)124:4(157).

154. Titov, V.V., Moore, C.W., Greenslade, D.J.M., Pattiaratchi, C., Badal, R., Synolakis, C.E., and Kanoglu, U., 2011, "A new tool for inundation modeling; community modeling interface for tsunamis (ComMIT)," *Pure Appl. Geophys.*, 168, 2121-2131.

155. Tocher, D., and Miller, D.J., 1959, "Field observations on effects of Alaskan earthquake of 10 July, 1958," *Science*, 129, 394-395.

156. Tsunami Pilot Study Working Group (TPSWG), 2006, *Seaside, Oregon Tsunami Pilot Study-Modernization of FEMA Flood Hazard Maps,* NOAA OAR Special Rep., NOAA/OAR/PMEL, Seattle, WA.

157. USGS, 2015, *U.S. Exclusive Economic Zone (EEZ), GLORIA Mapping Program*, http://coastalmap.marine.usgs.gov/gloria/, last accessed 10/30/2015.

158. Uslu, B., 2008, "Deterministic and probabilistic tsunami studies in California from near and farfield sources," *PhD thesis*, University of Southern California.

159. van de Meer, J.W., and Janssen, J.P.F.M., 1995, "Wave run-up and wave overtopping at dikes," in Kobayashi, N., and Demirbilek, Z., eds., *Wave Forces on inclined and Vertical Wall Structures,* ASCE, 1-27.

160. von Huene, R., Ranero, C. R., & Watts, P., 2004, "Tsunamigenic slope failure along the Middle America Trench in two tectonic settings," *Marine Geology*, 203, 3, 303-317.

161. Wang, X., and Liu, P. L. F., 2007, "Numerical simulations of the 2004 Indian Ocean tsunamis—coastal effects," *Journal of Earthquake and Tsunami*, 1, 03, 273-297.

162. Ward, S.N., and Day, S., 2001, "Cumbre Vieja Volcano - Potential collapse and tsunami at La Palma, Canary Islands," *Geophysical Research Letters*, 28, 17, 3397-3400.

163. Watts, A.B., and Masson, D. G., 1995, "A giant landslide on the north flank of Tenerife, Canary Islands," *Journal of Geophysical Research*, 100, 24,487-24,498.

164. Watts, P., 2004, "Probabilistic predictions of landslide tsunamis off Southern California," *Marine Geology*, 203.3, 281-301.

165. Waythomas, C.F., Miller, T.P., and Nye, C.J., 2002, "Preliminary Volcano-Hazard Assessment for Kanaga Volcano, Alaska," *US Geological Survey Open-File Report*, 02-397.

166. Waythomas, C.F., Miller, T.P., and Nye, C.J., 2003a, "Preliminary volcano hazard assessment for Great Sitkin Volcano," *US Geological Survey Open-File Report*, 03-112.

167. Waythomas, C.F., Miller, T.P., and Nye, C.J., 2003b, "Geology and late Quaternary eruptive history of Kanaga Volcano, a calc-alkaline stratovolcano in the western Aleutian Islands, Alaska," *US Geological Survey Professional Papers*, 1678, 181-197.

168. Wei, G., Kirby, J.T., Grilli, S.T., and Subramanya, R., 1995, "A fully nonlinear Boussinesq model for surface waves. Part 1. Highly nonlinear unsteady waves," *Journal of Fluid Mechanics*, 294, 71-92.

169. Weiss, R., Fritz, H., and Wuennemann, K., 2009, "Hybrid modeling of the mega tsunami runup in Lituya Bay after half a century," *Geophysical Research Letters*, 36, GL09609.

170. Weiss, R., Krastel, S., Anasetti, A., and Wuennemann, K., 2013, "Constraining the characteristics of tsunami waves from deformable landslides," *Geophysical Journal International,* 194, 1, 316-321.

171. Weiss, R., and Wuennemann, K., 2007, "Tsunami and nonlinear waves", Springer, Heidelberg, Ch. *Large waves caused by oceanic impacts of meteorites*, 237–261.

172. Weiss, R., Wuennemann, K., Bahlburg, H., 2006, "Numerical modelling of generation, propagation and run-up of tsunamis caused by oceanic impacts: model strategy and technical solutions," *Geophysical Journal International*, 167, 1, 77–88.

173. Wells D.L., and Coppersmith K.J., 1994, "New empirical relationships among magnitude, rupture length, rupture width, rupture area and surface displacement," *Bull. Seism. Soc. Amer.*, 84, 974-1002.

174. Wesson R.L., Boyd O.S., Mueller C.S., Bufe C.G., Frankel A.D., Petersen M.D., 2007, "Revision of Time-Independent Probabilistic Seismic Hazard Maps for Alaska," *U.S. Geological Survey Open-File Report* 2007-1043.

175. Wesson R.L., Frankel A.D., Mueller C.S., Harmsen S.C., 1999, "Probabilistic Seismic Hazard Maps of Alaska," *U.S. Geological Survey, Open-File Report* 99-36.

176. Wilson, B.W., and Torum, A., 1968, "Runup heights of the major tsunami on north American coasts, in: The Great Alaska Earthquake of 1964," *National Research Council (U.S.), Committee on the Alaska Earthquake*, National Academies.

177. Wilson R.I., Admire A.R., Borrero J.C., Dengler L.A., Legg M.R., Lynett P.J., McCrink T.P., Miller K.M., Ritchie A., Sterling K., Whitmore P.M., 2013, "Observations and Impacts from the 2010 Chilean and 2011 Japanese Tsunamis in California (USA)," *Pure Appl. Geophys.*, 170, 1127-1147, doi: 10.1007/s00024-012-0527-z.

178. Wilson, R., Hemphill-Haley, E., Jaffe, B., Richmond, B., Peters, R., Graehl, N., Kelsey, H., Leeper, R., Watt, S., McGann, M., Hoirup, D., Chague-Goff, C., Goff, J., Caldwell, D., and Loofbourrow, C., 2014, "The search for geologic evidence of distant-source tsunamis using new field data in California," chap. C of Ross, S.L., and Jones, L.M., eds., *The SAFRR (Science Application for Risk Reduction) tsunami scenario, U.S. Geological Survey Open-File Report* 2013–1170–C, http://dx.doi.org/10.3133/ofr20131170c.

179. Wolfe, C.J., McNutt, M.K., Detrick, R.S., 1994, "The Marquesas archipelagic apron: Seismic stratigraphy and implications for volcano growth, mass wasting, and crustal underplating," *Journal of Geophysical Research*, 99, 13,591-13,608.

180. Woo, S.-B., and Liu, P.L.-F., 2004, "A finite element model for modified Boussinesq equations. Part I: Model development," *Journal of Waterway, Port, Coastal, and Ocean Engineering*, 130, 1-16.

181. Wuennemann, K., and Lange, M., 2002, "Numerical modeling of impact-induced modifications of the deep-sea floor," *Deep-Sea Research II* 49, 669–981.

182. Wuennemann, K., Weiss, R., Hofmann, K., 2007, "Characteristics of oceanic impact-induced large water waves–re-evaluation of the tsunami hazard," *Meteoritics & Planetary Science*, 42, 11, 1893–1903.

183. Zelt, J.A., 1991, "The runup of nonbreaking and breaking solitary waves," *Coastal Engineering*, 15, 205-246.